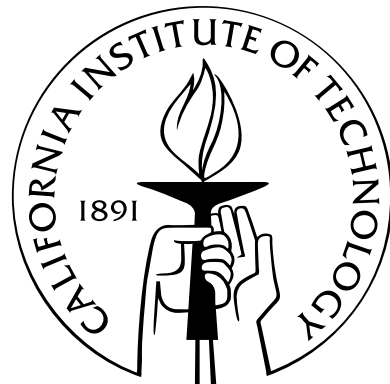


Technology Advances for Radio Astronomy

Thesis by
Damon Stuart Russell

In Partial Fulfillment of the Requirements
for the Degree of
Doctor of Philosophy



California Institute of Technology
Pasadena, California

2013
(Defended October 5, 2012)

© 2013
Damon Stuart Russell
All Rights Reserved

Acknowledgements

I am extremely grateful to Dr. Sander Weinreb, who has served as research adviser, mentor, and friend during my studies at Caltech. Dr. Weinreb opened the door for me to begin my Ph.D studies, some fifteen years after I had completed my bachelors, a gift for which I will be forever grateful. Aside from his wealth of technical knowledge, his patience, kindness, generosity, and humbleness has taught me much more than I thought possible.

To Professor A. Emami, my academic adviser, I am very grateful for the guidance provided during my course work at Caltech, as well as providing my first opportunity at IC design. This was invaluable experience to have prior to the start of my research. I would also like to thank the remaining members of my thesis committee consisting of Dr. T. Gaier, Professor A. Hajimiri, Professor A. Readhead, and Professor D. Rutledge for taking time from their busy schedules to serve on my committee.

To Professor J. Bardin, of the University of Massachusetts at Amherst, I am especially grateful for his guidance, support, and insight provided during the design of the SiGe cryogenic amplifiers contained within this work. Professor Bardin's own thesis, completed three years earlier, provided the foundation which this work was erected. I would also like to thank Dr. Jacob Kooi of Caltech for the many helpful discussions on THz mixers, which were invaluable during amplifier development.

I am very grateful to the financial support provided by The Jet Propulsion Laboratory during the completion of my course work and to Caltech during the the last three years of my residency.

I owe special thanks to Professor Readhead for the opportunity to design the cryogenic probe station now in use by his group. I would also like to thank Dr. Kieran Cleary and Dr. Rodrigo Reeves for their contributions and for their friendship and support during its construction.

I am extremely grateful to Mike Martin-Vegue, a good friend and expert machinist. He is responsible for transforming the multitude of components in the cryogenic probe station from concept to reality.

I would also like to thank my fellow group members that I have worked alongside for the last three years: Ahmed Akgiray, Hector Navarette, and Steve Smith. To Ahmed and Steve I give thanks for the many helpful technical discussions, friendship, and camaraderie shared within the laboratory. To Hector I give thanks for the expert microelectronic assembly support, during the build of the

variable-impedance noise source and low-noise amplifiers described in chapters 4 and 5 respectively.

Finally, I would like to thank my family, my wife Nayiri and daughter Sarah. Nayiri I thank for her constant encouragement and sacrifice, which has made the dream of completing my doctorate a reality. Lastly, I would like to thank Sarah for providing the motivation to complete the degree as expediently as possible.

Abstract

The field of radio astronomy continues to provide fundamental contributions to the understanding of the evolution, and inner workings of, our universe. It has done so from its humble beginnings, where single antennas and receivers were used for observation, to today's focal plane arrays and interferometers. The number of receiving elements (pixels) in these instruments is quickly growing, currently approaching one hundred. For the instruments of tomorrow, the number of receiving elements will be in the thousands. Such instruments will enable researchers to peer deeper into the fabric of our universe and do so at faster survey speeds. They will provide enormous capability, both for unraveling today's mysteries as well as for the discovery of new phenomena.

Among other challenges, producing the large numbers of low-noise amplifiers required for these instruments will be no easy task. The work described in this thesis advances the state of the art in three critical areas, technological advancements necessary for the future design and manufacturing of thousands of low-noise amplifiers. These areas being: the automated, cryogenic, probing of $\varnothing 100$ mm indium phosphide wafers; a system for measuring the noise parameters of devices at cryogenic temperatures; and the development of low-noise, silicon germanium amplifiers for terahertz mixer receivers. The four chapters that comprise the body of this work detail the background, design, assembly, and testing involved in these contributions. Also included is a brief survey of noise parameters, the knowledge of which is fundamental to the design of low-noise amplifiers and the optimization of the system noise temperature for large, dense, interferometers.

Contents

| | |
|--|-------------|
| Acknowledgements | iii |
| Abstract | v |
| List of Figures | ix |
| List of Tables | xiii |
| 1 Background and Motivation | 1 |
| 2 Cryogenic Probe Station | 10 |
| 2.1 Introduction | 10 |
| 2.1.1 Requirements | 10 |
| 2.1.2 Challenges in Cryogenic Probe Station Design | 11 |
| 2.1.3 Review of Commercially Available Stations | 13 |
| 2.2 Design | 14 |
| 2.2.1 Chuck Positioner Subassembly | 15 |
| 2.2.2 Platen Subassembly | 21 |
| 2.2.3 Refrigeration | 21 |
| 2.2.4 Chamber Design | 25 |
| 2.2.5 RF and DC Wiring | 26 |
| 2.2.6 Vacuum and Optical Systems | 26 |
| 2.3 Performance | 28 |
| 2.4 Future Improvements | 34 |
| 2.5 Summary | 35 |
| 3 Noise Parameters | 36 |
| 3.1 Introduction | 36 |
| 3.2 Background | 36 |
| 3.3 Noise Parameters R_n , G_n , and Y_{opt} | 38 |

| | | |
|----------|---|-----------|
| 3.4 | Noise Parameters T_{min} , N , and Γ_{opt} | 41 |
| 3.5 | Noise Parameters T_a , T_b , T_c , and ϕ_c | 42 |
| 3.6 | Noise Parameters $\overline{ c_1 ^2}$, $\overline{ c_2 ^2}$, and $\overline{c_1 c_2^*}$ | 45 |
| 3.7 | Which Parameter Set? | 46 |
| 4 | Noise Parameter Measurement System | 48 |
| 4.1 | Introduction | 48 |
| 4.1.1 | Background | 48 |
| 4.1.2 | Selection of Source Impedance States and Their Number | 51 |
| 4.1.3 | Wide Band Frequency Variation Method | 52 |
| 4.2 | Variable Impedance, Self-Calibrating, Noise Sources | 54 |
| 4.2.1 | Cryogenic Module | 54 |
| 4.2.2 | Ambient/Cryogenic Module | 57 |
| 4.3 | Principles of Calibration | 58 |
| 4.4 | Calibration Uncertainty | 61 |
| 4.4.1 | Random Errors | 62 |
| 4.4.2 | Systematic Errors | 63 |
| 4.4.2.1 | Errors Due to Changes in Reflection Coefficient Modulating Receiver Noise Temperature | 64 |
| 4.4.2.2 | Errors Due to Changes in Reflection Coefficient Modulating System Gain | 65 |
| 4.4.2.3 | Errors Due to Temperature Sensor Accuracy | 66 |
| 4.5 | Noise Parameter Measurement | 66 |
| 4.6 | Measurement Uncertainty | 69 |
| 4.6.1 | Random Errors | 69 |
| 4.6.2 | Systematic Errors | 69 |
| 4.7 | Cryogenic Noise Parameter Measurements | 70 |
| 4.7.1 | Module Calibration | 70 |
| 4.7.2 | Measurement Examples | 74 |
| 4.7.2.1 | Discrete SiGe HBT | 74 |
| 4.7.2.2 | Discrete LNA | 79 |
| 4.7.2.3 | MMIC LNA | 80 |
| 4.8 | Ambient Noise Parameter Measurements | 84 |
| 4.8.1 | Module Calibration | 85 |
| 4.8.2 | Measurement Examples | 91 |
| 4.8.2.1 | Ultra-Low-Noise Temperature Amplifier | 91 |

| | | |
|---------------------|---|------------|
| 4.8.2.2 | Wideband MMIC LNA module | 94 |
| 4.9 | Suggestions for Future Work | 97 |
| 4.10 | Summary | 99 |
| 5 | Low-Noise, SiGe, IF Amplifiers for THz Mixer Receivers | 100 |
| 5.1 | Introduction | 100 |
| 5.2 | Background | 101 |
| 5.2.1 | Superconducting Mixers | 102 |
| 5.2.2 | Low-Noise, IF Amplifier Design Constraints | 104 |
| 5.2.3 | Heterojunction, SiGe, Bipolar Transistors | 106 |
| 5.3 | Design of Low-Noise Cryogenic MMIC Amplifiers | 108 |
| 5.3.1 | Device Modeling | 108 |
| 5.3.1.1 | DC Measurements | 111 |
| 5.3.1.2 | Low-Frequency S-Parameter Measurements | 114 |
| 5.3.1.3 | Polynomial Fitting of DC Parameters | 117 |
| 5.3.1.4 | S-Parameter Measurements | 117 |
| 5.3.2 | Device Sizing and Bias | 119 |
| 5.3.3 | Resistive Feedback | 120 |
| 5.3.4 | On-Chip Passive Elements | 122 |
| 5.3.5 | Layout | 123 |
| 5.4 | Measurement of Cryogenic-Low Noise Amplifiers | 126 |
| 5.5 | Examples | 127 |
| 5.5.1 | WBA23. Low Power IFLNA for Large SIS Mixer Arrays | 127 |
| 5.5.2 | WBA24. Medium Power IFLNA | 133 |
| 5.5.3 | WBA25. High Power IFLNA | 139 |
| 5.6 | Suggestions for Future Work | 142 |
| 5.7 | Summary | 146 |
| 6 | Conclusions | 147 |
| Bibliography | | 148 |

List of Figures

| | | |
|------|---|----|
| 1.1 | Radio astronomy receiver technologies vs. frequency. | 3 |
| 1.2 | Noise and gain distribution of a 1-13 GHz InP MMIC @ 20 K. | 5 |
| 1.3 | Noise contributions from adjacent interferometer receiving elements. | 6 |
| 2.1 | Commercial probe station configurations. | 14 |
| 2.2 | Cutaway illustration of cryogenic probe station. | 16 |
| 2.3 | Thermal conductivities of OFHC, T6, 304-SS, and G-10 vs. temperature. | 17 |
| 2.4 | Specific heats of OFHC, T6, 304-SS, and G-10 vs. temperature. | 17 |
| 2.5 | Integrated coefficient of thermal expansion for T6, 304-SS, and G-10 vs. temperature. | 18 |
| 2.6 | Chuck positioner subassembly | 19 |
| 2.7 | Platen subassembly | 22 |
| 2.8 | Refrigeration subassembly | 24 |
| 2.9 | Photograph of cryocooler and vacuum system | 27 |
| 2.10 | Microscope image of a MMIC during cryogenic probing. | 28 |
| 2.11 | Photograph of cryostat interior. | 29 |
| 2.12 | Photograph of completed cryogenic probe station. | 30 |
| 2.13 | Temperatures within cryogenic probe station during cool down. | 31 |
| 2.14 | S-parameter and noise temperature test setups. | 32 |
| 2.15 | Probed, cryogenic S-parameters of a W-band MMIC LNA. | 33 |
| 2.16 | Probed, cryogenic noise measurements of a W-band MMIC LNA. | 33 |
| 2.17 | Cryogenic postcalibration stability. | 34 |
| 3.1 | De-embedded noise sources used in noise parameter representations. | 37 |
| 3.2 | Noise sources transferred to the input of a two-port network. | 38 |
| 3.3 | Equivalent network used for the determination of input noise temperature. | 39 |
| 3.4 | Rothe and Dahlke equivalent noise network. | 40 |
| 3.5 | Noise wave representation of a two-port. | 43 |
| 3.6 | Noise contributions from adjacent interferometer receiving elements. | 45 |
| 3.7 | Noise wave parameters represented at the input and output of a two-port network. | 46 |

| | | |
|------|--|----|
| 4.1 | Tuner based noise parameter measurement setup. | 50 |
| 4.2 | Wideband frequency variation method | 53 |
| 4.3 | Single vs. two-line mismatch network demonstration | 55 |
| 4.4 | Schematic of cryogenic, self-calibrating, variable impedance noise source. | 56 |
| 4.5 | Cryogenic, variable impedance, self-calibrating noise source module photograph | 56 |
| 4.6 | Modification of variable impedance module for use at room temperature. | 57 |
| 4.7 | Completed LLM for use at ambient and cryogenic temperatures. | 58 |
| 4.8 | Test setup and definition of calibration quantities | 59 |
| 4.9 | Noise parameter extraction algorithm | 68 |
| 4.10 | Test setup for cryogenic module calibration | 71 |
| 4.11 | Interface electronics box | 72 |
| 4.12 | Cryogenic excess noise temperature for two heater currents | 73 |
| 4.13 | Change in module reflection coefficient with heating at cryogenic temperature. | 74 |
| 4.14 | Cryogenic module calibration results | 75 |
| 4.15 | Uncertainty in the excess noise temperature from cryogenic calibration | 76 |
| 4.16 | Test setup for the measurement of noise parameters using the module | 77 |
| 4.17 | Noise parameters of NXP BFU725F at 19 K | 77 |
| 4.18 | Parameters β and g_m for NXP HBT BFU725F at 19 K | 78 |
| 4.19 | Measured vs theoretical noise parameters of NXP BFU725F HBT at 19K | 79 |
| 4.20 | Verification of NXP BFU725F HBT available gain at 19 K. | 80 |
| 4.21 | Noise parameters a for two-stage, discrete, HBT LNA at 19 K. | 81 |
| 4.22 | Verification of noise parameters for 2-stage discrete LNA at 19 K. | 81 |
| 4.23 | Noise parameters for WBA23 IC at 19 K | 82 |
| 4.24 | Noise temperature of WBA23 IC at 4.2 K with inductive compensation. | 83 |
| 4.25 | Uncertainty in noise parameter measurement of WBA23 IC | 83 |
| 4.26 | Monte Carlo sensitivity analysis of extracted noise parameters for WBA23 IC. | 84 |
| 4.27 | Test setup for module calibration at ambient temperature. | 86 |
| 4.28 | Ambient module calibration results | 88 |
| 4.29 | Noise parameters of the ambient receiver used in calibration. | 89 |
| 4.30 | Evaluation of systematic errors in the ambient calibration of the module. | 90 |
| 4.31 | Random error in ambient module calibration. | 90 |
| 4.32 | Test setup for measurement of noise parameters at ambient temperature. | 91 |
| 4.33 | Noise parameters for ambient temperature, ultra-low-noise amplifier | 92 |
| 4.34 | Tuning of Z_{opt} for an ultra-low-noise amplifier. | 93 |
| 4.35 | Verification of noise parameters for the ultra-low-noise amplifier. | 93 |
| 4.36 | Noise parameters of a wideband MMIC LNA at ambient temperature. | 94 |

| | | |
|------|---|-----|
| 4.37 | Verification of noise parameters for the wideband MMIC LNA. | 95 |
| 4.38 | Reflection error in the measured noise temperature of a wideband MMIC LNA. | 95 |
| 4.39 | Influence of reflection errors on the noise parameters of a wideband MMIC LNA. | 96 |
| 4.40 | Noise parameter uncertainty of the wideband MMIC LNA due to random errors. | 96 |
| 5.1 | Photograph of the CITST1 SiGe reticle. | 101 |
| 5.2 | Block diagram of a THz receiving element. | 102 |
| 5.3 | SIS cross section, energy band diagram, and I-V characteristics. | 103 |
| 5.4 | Simplified HEB physical structure and temperature dependence. | 104 |
| 5.5 | HBT noise model. | 107 |
| 5.6 | SiGe HBT layout and cross section | 109 |
| 5.7 | Discrete transistor evaluation fixture | 110 |
| 5.8 | Test setup used for device characterization. | 111 |
| 5.9 | DC characteristics of a $2.6 \mu\text{m}^2$ SiGe HBT at 4.2, 19, 77, and 300 K from CITST1 reticle. | 112 |
| 5.10 | Comparison of DC characteristics of SiGe HBTs from CITST1 and CITST2 reticles. . | 113 |
| 5.11 | Effects of self-heating in I_c vs. V_{ce} measurements. | 115 |
| 5.12 | Low frequency dynamic transconductance measurements. | 116 |
| 5.13 | Correction to g_m for CITST1 and CITST2 devices due to frequency dispersion | 117 |
| 5.14 | T_{min} and R_{opt} vs. J_c at 19 K. | 120 |
| 5.15 | Small signal model used for resistive feedback calculations. | 121 |
| 5.16 | Test structures for cryogenic characterization of passive components. | 122 |
| 5.17 | Substrate resistivity vs. temperature | 124 |
| 5.18 | Example of BiCMOS metal stackup and passive device location. | 125 |
| 5.19 | Cold attenuator test setup. | 126 |
| 5.20 | KAPPa conceptual packaging illustration. | 128 |
| 5.21 | WBA23 schematic and IC photograph. | 130 |
| 5.22 | WBA23 MMIC packaged within a 50Ω module. | 131 |
| 5.23 | WBA23 noise temperature at 19 K and 4.2 K physical temperatures. | 132 |
| 5.24 | WBA23 predicted noise temperature with IF matching network at 4.2 K. | 132 |
| 5.25 | WBA23 noise temperature at 19 K, CITST1 and CITST2 reticles. | 134 |
| 5.26 | WBA23 measured and simulated S-parameters at 19 K. | 134 |
| 5.27 | WBA24 schematic and IC photograph. | 135 |
| 5.28 | WBA24 MMIC packaged within a 50Ω module. | 136 |
| 5.29 | WBA24 noise temperature at 19 K. | 137 |
| 5.30 | WBA24 noise temperature vs. DC power at 19 K. | 137 |

| | | |
|------|---|-----|
| 5.31 | WBA24 measured and simulated S-parameters at 19 K. | 138 |
| 5.32 | THz array packaging concept for medium power amplifiers. | 139 |
| 5.33 | WBA25 schematic and IC photograph. | 140 |
| 5.34 | WBA25 MMIC packaged within a $50\ \Omega$ module. | 141 |
| 5.35 | WBA25 measured and simulated cryogenic S-parameters. | 142 |
| 5.36 | WBA25 measured and simulated cryogenic noise temperature. | 143 |
| 5.37 | WBA25 noise temperature at ambient temperature. | 143 |
| 5.38 | WBA25 S-parameters at ambient temperature. | 144 |
| 5.39 | WBA22 differential noise and gain at 19 K. | 145 |

List of Tables

| | | |
|-----|--|-----|
| 1.1 | Summary of proposed THz receivers | 8 |
| 2.1 | Cryogenic probe station design specifications. | 11 |
| 2.2 | Capabilities of commercially available cryogenic probe stations. | 13 |
| 2.3 | Heat loads presented to cryocooler | 29 |
| 4.1 | Calibration noise terms. | 60 |
| 4.2 | Components used within cryogenic calibration test setup. | 71 |
| 4.3 | Components used within ambient calibration test setup. | 85 |
| 5.1 | Device sizes for CITST1 and CITST2 SiGe runs. | 109 |
| 5.2 | Polynomial coefficients for β at 19 K. | 118 |
| 5.3 | Polynomial coefficients for g_m at 19 K. | 118 |
| 5.4 | Polynomial coefficients for g_m frequency dispersion correction at 19 K. | 118 |
| 5.5 | Scalable small signal model parameters. | 119 |
| 5.6 | Summary of changes to passive elements with cooling to 19 K. | 123 |
| 5.7 | WBA23 design goals and drivers | 129 |
| 5.8 | Status of SiGe MMIC designs. | 145 |

Chapter 1

Background and Motivation

The discovery of radio emission from the Milky Way in 1932, by Karl Jansky, signaled the dawn of radio astronomy. It opened up a wide spectrum of the previously unseen universe, extending from roughly 3 MHz to \sim 3 THz.¹ With this much observable bandwidth, it is no surprise that radio astronomy has contributed so broadly to our understanding of the universe and its evolution. From the discovery of the cosmic microwave background (CMB) by Penzias and Wilson in 1964, the Bell-Burnell and Hewish's discovery of pulsars in 1967, to the mysteries being currently unraveled from the data collected by Herschel-Planck,² the field of radio astronomy continues to deliver some of the most important scientific discoveries. The next generation of radio astronomy experiments will seek to answer the following questions:

- How did the cosmos evolve?
- What is involved in galaxy formation?
- How does gravity and general relativity hold up in the strong-field regime?
- Is general relativity's prediction of the existence of gravitational waves true?
- What are the origins of dark matter and dark energy?
- What is the origin and evolution of cosmic magnetism?

To answer these questions, surveys will need to be made of extremely faint radio sources over large areas of the sky. Both of these requirements are satisfied by large arrays of radio receivers; either as a network of individual antennas (interferometer) or as an array of receivers located in the focal plane of an individual collector (focal plane array). The sensitivity of either architecture being set by the radiometer equation [1]:

¹The submillimeter and far-infrared bands included.

²Herschel and Planck were launched together in 2009. Herschel is a far-infrared and submillimeter telescope with a 3.5 m mirror, designed to perform spectroscopy on distant galaxies and star forming regions. Planck is a millimeter and submillimeter telescope, with a 1.9 m primary mirror, built to study anisotropies in the CMB.

$$\Delta T = T_{sys} \sqrt{1/(N f_{BW} \tau) + (\Delta G/G)^2}, \quad (1.1)$$

where N is the number of observations, f_{BW} is the bandwidth of the observation, τ is the integration time, G and ΔG are the gain and gain stability of the receiver chain, and T_{sys} is the system noise temperature. Disregarding the effect of gain fluctuations in equation (1.1), it is immediately obvious that increasing the number of elements improves the sensitivity or reduces the integration time (improved survey speed) necessary for a given sensitivity. Aside from the merits of improved sensitivity and survey speed, very large arrays also have the following benefits:

- Large field of view. For both interferometers and focal plane arrays, increasing the number of receiving elements correspondingly increases the field of view, allowing for increased spatial coverage during a given observation.
- Improved angular resolution, λ/D , where λ is the wavelength of the observed radiation and D is the effective diameter of the telescope. The importance of this was demonstrated by Spitzer³ and more recently by the Herschel-Planck mission, whose improved sensitivity revealed a literal “carpet” of galaxies. Unfortunately, due to the small diameter of their collectors, their angular resolution is relatively poor, and many of these distant galaxies could not be resolved.

Two prime examples of such future instruments employing very large arrays are The Cornell-Caltech Atacama Telescope⁴ (CCAT) and The Square Kilometre Array⁵ (SKA). CCAT⁶ will be the most powerful sub-millimeter observatory to date, a 25 m telescope located at 5600 m on Cerro Chajnantor in the Chilean Andes. It will utilize a number of focal plane arrays including bolometers, direct detection spectrometers, and superheterodyne receivers. The SKA will be the world's largest radio telescope, consisting of a network of antennas covering 70 MHz to 50 GHz. The middle of which (SKA mid) is planned to be comprised of 3000, $\varnothing 15$ m dishes, covering 1-10 GHz and spread out over a baseline of 3000 km.

Although the scientific impact of these instruments will be enormous, their realization poses a number of significant technical challenges. Among these are the following:

- Selection of a suitable observation site. With an enormous baseline, there are few choices for suitable “radio quiet” sites for the SKA. The only current options are Australia and South Africa. For CCAT, due to atmospheric attenuation, it must be located in the thin, dry air of the Atacama desert. Both locations are remote, placing challenges in the construction of these instruments, as well as the infrastructure necessary to support them.

³Spitzer was an infrared space telescope launched in 2003, with cryogenically cooled optics. Its primary mirror was 85 cm in diameter.

⁴<http://www.ccatobservatory.org>

⁵<http://www.skatelescope.org>

⁶First light measurements expected to begin in 2018.

- Data processing. With either instrument, data volume and processing will present a huge challenge. The SKA alone will potentially generate 10 GB of processed data per second! Arrays of superconducting terahertz (THz) receivers consisting of more than 1000 pixels are planned for CCAT. With individual pixel bandwidths of ≈ 4 GHz, these instruments will require > 4 THz of bandwidth to be continuously digitized and stored during operation.
- Development and manufacturing of the large number of antennas, low-noise amplifiers (LNA), cryogenic systems, spectrometers, etc., comprising these arrays. This poses a unique challenge for two reasons: technologies must be developed to meet the performance criteria of the instrument; and they must be easily manufacturable, to make their production possible.

The work contained in this thesis seeks to advance the last item, specifically the development and manufacturing of the large numbers of LNAs that will be necessary for observations between 1 GHz and 3 THz. To do so, it advances the state of the art in three important areas: cryogenic wafer probing; cryogenic noise parameter measurement; and the development of intermediate frequency, low-noise amplifiers (IFLNA) for superconducting THz mixer receivers.

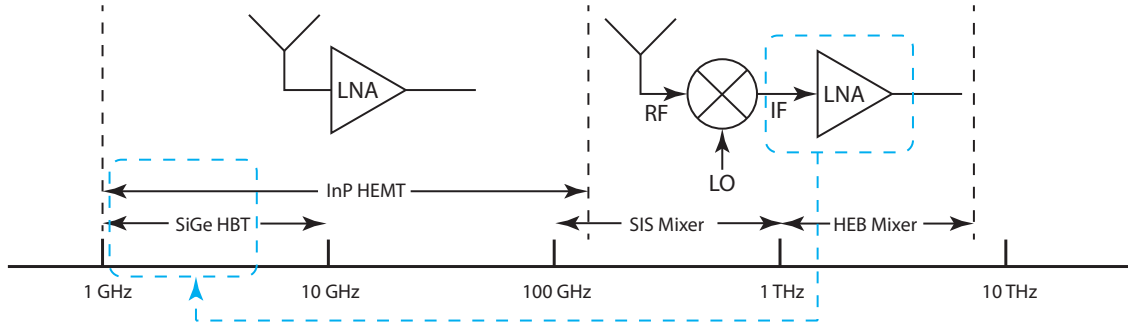


Figure 1.1: Radio astronomy receiver technologies and device types vs. frequency. Below ~ 120 GHz, InP HEMTs remain the best option for low noise and wide-bandwidth (instantaneous) observations. Above W-band, SIS mixers are utilized until ≈ 1 THz, their upper limit due to the materials involved in their construction. Above 1 THz, HEB mixers are used. Recent advancements in cooled SiGe allow it to be used as an alternative to InP in the IF amplifier following either superconducting mixer.

Figure 1.1 illustrates a simplified view of receiver and LNA technologies that may be utilized to cover this wide spectrum. Below ≈ 120 GHz, indium phosphide (InP) high electron mobility transistors (HEMT)s remain the lowest noise temperature transistors for use in cryogenic microwave and millimeter wave receiver front ends, where noise temperatures < 30 K have been reported [2], [3]. Although superconductor-insulator-superconductor (SIS) mixers are potentially lower noise options above 100 GHz, where noise temperatures of twice the quantum limit⁷ have been reported [4], they

⁷The quantum limit is $hf/k \approx 0.05 K \cdot f_{GHz}$, where h and k are the Planck and Boltzmann constants respectively, and f is frequency.

have several drawbacks: they require cooling to liquid helium (LHE) temperatures; they require complicated quasi-optical or waveguide LO distribution schemes; and they are currently limited to IF bandwidths⁸ of ≈ 10 GHz. Observations requiring low noise and wide instantaneous bandwidth will continue to depend on the performance available from InP transistors, either discretely or as part of a monolithic microwave integrated circuit (MMIC).

Unfortunately, InP has not seen the same developmental pace as technologies such as silicon, and as a result the yield of low noise InP devices, especially at cryogenic temperatures, is usually $< 50\%$.⁹ This is illustrated in figure 1.2, for a 1-12 GHz InP MMIC, designed at Caltech and manufactured by Northrop Grumman Aerospace Systems.¹⁰ The noise at 12 GHz reveals a significant spread in performance, both within a given wafer and among separate wafers. Traditionally, it has been necessary to package such devices in order to evaluate their performance cryogenically. This is especially true of devices operating at W-band (75-110 GHz), due to the difficulties imposed by wafer probing at these frequencies. The investment associated with the packaging and testing of each device dramatically increases the cost and therefore imposes practical limits on the number of devices screened for a given instrument. In addition, it is desired to speed the development of InP HEMTs, whose noise is currently ≈ 5 times the quantum limit at W-band. If radio astronomy is to use large numbers of these devices in the future, a cryogenic probe station will be necessary to quickly access their performance at frequencies up to W-band. The design and testing of such a station is the focus of chapter 2.

As the complexity of future instruments increases, an accurate understanding of the noise of the system will be necessary, as it directly limits the sensitivity of the system, per equation (1.1). To better illustrate this, consider a simple receiver, comprised of a single antenna followed by a LNA and subsequent backend electronics. The system noise temperature is given by

$$T_{sys} = T_{ant} + T_{LNA} + T_{backend}/G_{LNA} , \quad (1.2)$$

where T_{ant} is the noise temperature of the antenna, including contributions from background noise, ohmic losses, and spillover. T_{LNA} and G_{LNA} are the noise temperature and available gain of the low-noise amplifier respectively, and $T_{backend}$ is the effective noise temperature of the electronics following the LNA. T_{LNA} is a function of the impedance presented to the LNA by the antenna, Z_{ant} . In order to access the LNAs impact on the system noise temperature, due to Z_{ant} which itself may be a function of pointing, knowledge of the LNAs noise parameters are necessary. Although there are many different sets of noise parameters, they are all fundamentally equivalent. They each rely on four terms necessary to completely describe the noise of a device when presented with an

⁸For individual devices. Emerging architectures of SIS devices are pushing this limit to 20 GHz.

⁹This yield is associated with prescreened devices that have reasonable noise and DC characteristics at room temperature, before cool down.

¹⁰Northrop Grumman Aerospace Systems. One Space Park, Redondo Beach CA, 90278 U.S.A.

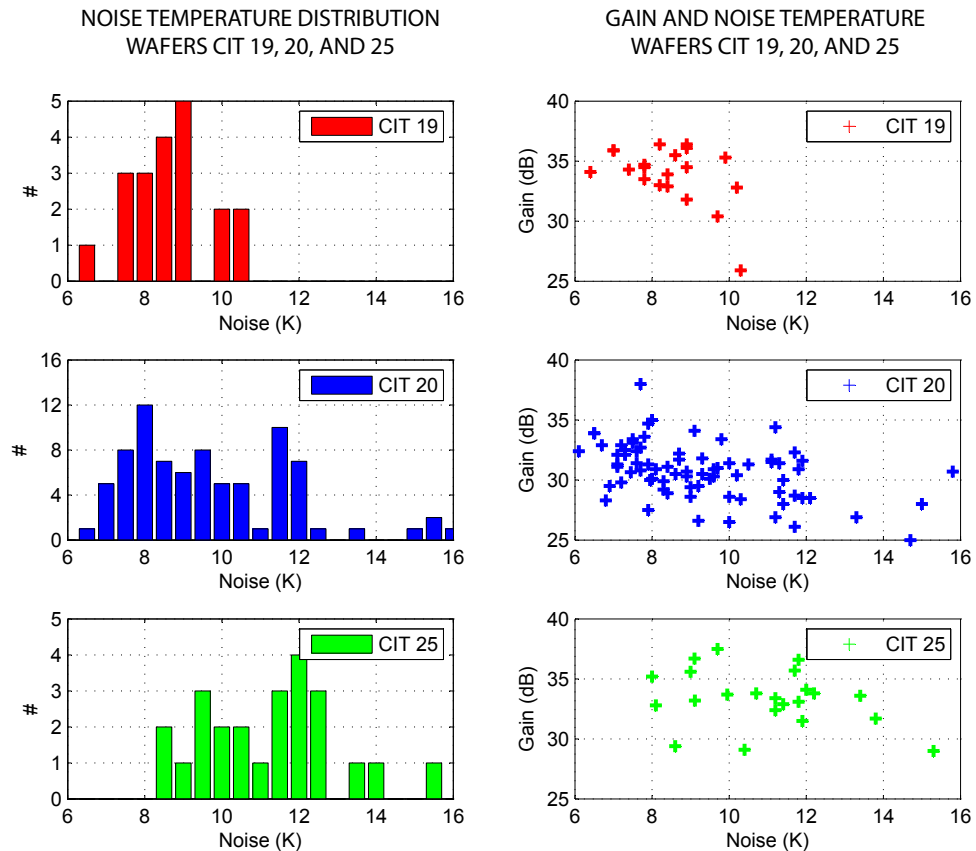


Figure 1.2: Distribution of noise and gain performance of 1-12 GHz wideband InP MMIC (p/n WBA13) amplifiers at 12 GHz, 20 K physical temperature, for three different wafers. The spread in noise temperature between devices within a wafer and between wafers is clearly evident. Data courtesy of Steve Smith, California Institute of Technology.

arbitrary source impedance, Z_s . The particular set is chosen to aide in the physical insight into a particular problem or to ease measurement. The dependence of the noise temperature, T_n on source impedance can be seen directly from noise parameter set (T_{min}, N, Z_{opt}) , through the following relation.

$$T_n = T_{min} + NT_0 \frac{|Z_s - Z_{opt}|^2}{\Re(Z_s) \Re(Z_{opt})} \quad (1.3)$$

Knowledge of noise parameters is therefore necessary to accurately determine the impact of the LNA on the system noise temperature. This can be particularly important for interferometers, where coupling may exist between closely spaced elements due to antenna spillover. In such cases the noise of a LNA from one receiver element may directly impact the noise of its neighbor. The end result being that the signal from several receivers, when combined, may contain a correlated noise component which is itself a function of antenna pointing. This is illustrated in figure 1.3, where the noise “wave” parameter set (T_a, T_b, T_c, ϕ_c) is selected as it is well suited for analysis of this problem. This is discussed further in chapter 3 where a brief introduction to noise parameters is given.

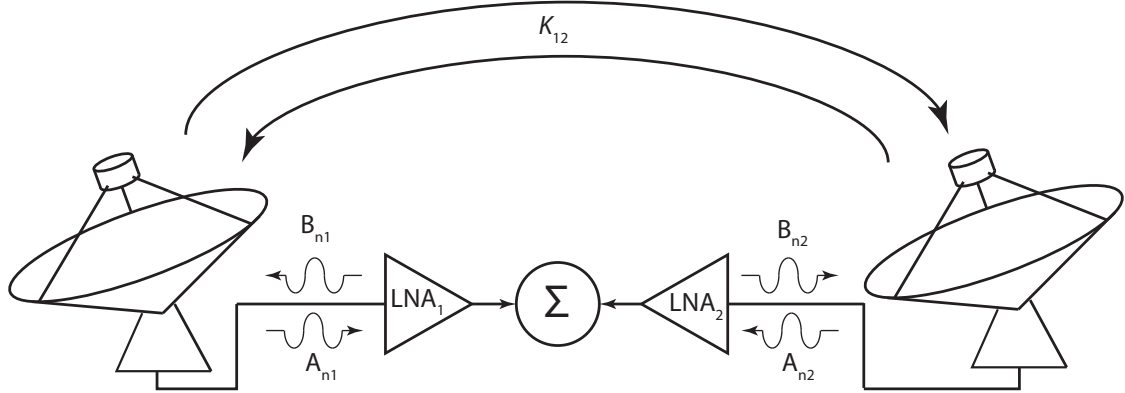


Figure 1.3: Noise contributions from adjacent interferometer receiving elements. The incident and outgoing noise waves at each LNAs input, A_n and B_n respectively, coupled with the crosstalk between antennas, results in a correlated noise component when the received signals are combined. Since the crosstalk is a function of antenna pointing, so is the additional noise. Noise waves A_n and B_n may be expressed in terms of noise parameter set (T_a, T_b, T_c, ϕ_c) , yielding a relation for T_n similar to that of equation (1.3).

Aside from accurate determination of system noise contributions, knowledge of noise parameters is also essential to LNA design. The noise of the amplifier being minimized by the proper selection of source impedance, which is frequently accomplished through impedance transformation. At room temperature, several excellent commercial systems exist for the measurement of a transistor or an amplifier’s noise parameters. However, as will be discussed further, these systems are not suitable for cryogenic noise parameter measurements, where knowledge is necessary for radio astronomy

receivers. For these reasons, the need exists for a system to cryogenically measure noise parameters. The design and calibration of such a system is covered in chapter 4.

Roughly speaking, radio astronomy observations can be broken into two categories; continuum and spectral. Continuum measurements are important for the measurement of sources where the flux is changing slowly with frequency, such as thermal and synchrotron emission. In such cases, it is advantageous to use as wide a bandwidth as possible, to increase the sensitivity of the receiver, per equation (1.1). Continuum measurements are also necessary when a large bandwidth must be instantaneously sampled, such as required for the measurement of pulsars.

Conversely, spectral measurements utilize very narrow bandwidths to resolve the emission of various atomic and molecular species from distant galaxies. The radiation occurring in specific and very narrow ranges of wavelength, usually caused by electron transitions between energy levels. The intensity of the received radiation indicating the species' abundance and its measured redshift providing information as to the velocity of the source. One of the earliest, and most famous uses of spectral analysis by radio astronomy was in the detection of the 21 cm hydrogen line by Ewen and Purcell in 1951.

Today, observation is focused on the interstellar medium (ISM) at upper millimeter (30–300 GHz) and submillimeter (0.3–3 THz) bands, for their wealth of spectral lines. Their study is particularly important in the research of galaxy formation and evolution. Aside from offering a powerful chemical diagnostic tool, whereby the presence and relative abundance of elements and molecular compounds can be detected, instruments with sufficient spectral resolution may also probe the inner workings of these galaxies. This is accomplished through observation of spectral line Doppler shifts, allowing measurement of radial velocities and yielding information as to rotational curves and mass distributions [5] within the ISM.

Unfortunately, the high frequency at which these lines exist, coupled by their strong attenuation by the earth's atmosphere has made their observation challenging. The later problem has been circumvented through observations on the Atacama desert and Mauna Kea, high altitude balloon and plane flights, and space-based instruments. The former has been solved through the advent of improved detector technologies, such as superconducting mixers, which have made detection possible. The Atacama Large Millimeter/Submillimeter Array (ALMA), currently under construction, will consist of 66 antennas, each outfitted with a number of individual superconducting receivers (pixels) to cover approximately 30–900 GHz. Alternatively, CCAT will employ a single dish, but with focal plane arrays consisting of hundreds to thousands of pixels.

Initial focal plane arrays were comprised of only a few pixels and were constructed from discrete feed-horns, mixers, and IF amplifiers [6]. Increasing the number of pixels within an array requires improvements to the packaging density and manufacturability, both of which are addressed as the level of integration increases. This was demonstrated on *SuperCam* [7], an 8×8 array operating

at 350 GHz, where feed-horns, superconducting mixers, and IF amplifiers were integrated into modular 1×8 assemblies. In order to produce more powerful instruments, even larger arrays are necessary. To satisfy the field of view CCAT alone, arrays consisting of thousands of pixels will be necessary [8]. Such instruments are already in the development phase, table 1.1 listing a few of the proposed instruments that will serve as pathfinders for future very large arrays.

Table 1.1: Summary of proposed THz receivers

| Name | Lead | Telescope | Pixels | Mixer | RF (THz) | IF (GHz) |
|-----------------------------|--|---------------------|------------------|-------|------------|----------|
| SHASTA ¹⁰ | JPL ¹¹ | SOFIA ¹² | 32 | HEB | 1.9 | 0.5–5 |
| OCAM ¹³ | UAZ ¹⁴ | SOFIA | 16 | HEB | 4.7 | 0.5–5.5 |
| GUSSTO ¹⁵ | UAZ | STO ¹⁶ | 48 | HEB | 1.45,2,4.7 | 0.5–5 |
| CHAI ¹⁷ | KOSMA ¹⁸ / CIT ¹⁹ | CCAT ²⁰ | 16, later 128 | SIS | 0.47,0.81 | 4–8 |
| KAPPA ²¹ | ASU ²² | CCAT | 16, later 1k+ | SIS | 0.675 | 0.5–4.5 |

InP HEMTs have traditionally been used for the IF amplifier following the superconducting mixer in these arrays. Phenomenal performance has been demonstrated with these amplifiers [9] both in terms of noise and power. SiGe heterojunction bipolar transistors (HBT)s, on the other hand, have shown comparable cryogenic noise performance [10], [11]. SiGe also benefits from inherent high yield, due to the maturity of silicon processing, almost a requirement for the manufacturing of arrays comprised of thousands of elements. The development of low noise, SiGe IF amplifiers for THz receivers is the focus of the work presented in chapter 5.

In summary, the three contributions detailed within this thesis are the development of a cryogenic probe station for automated testing of InP wafers; a cryogenic noise parameter measurement system and calibration methods; and low noise, low power, SiGe IF amplifiers for THz mixer receivers. Portions of this work are published in *Review of Scientific Instruments* [12], and *IEEE Transactions on Microwave Theory and Techniques* [13], [14]. The advancement of the state of the art in these areas will help pave the way for the mass production of cryogenic LNAs, which radio astronomy

¹¹Stratospheric Heterodyne Array for Spectroscopic Stratospheric THz Astronomy (SHASTA)

¹²Jet Propulsion Laboratory (JPL), Pasadena CA, U.S.A.

¹³Stratospheric Observatory for Infrared Astronomy (SOFIA). SOFIA is a 2.5 meter, submillimeter telescope, contained within a Boeing 747 flying at 14 km.

¹⁴University of Arizona (UAZ), Tucson AZ, U.S.A.

¹⁵Oxygen Camera (OCAM)

¹⁶Galactic Spectroscopic Stratosphere THz Observatory (GUSSTO)

¹⁷Stratospheric Terahertz Observatory (STO). STO is a long duration balloon experiment consisting of an 80 cm telescope providing sufficient angular resolution for resolving terahertz spectral lines from distant sources.

¹⁸Cerro-Chajnantor-Atacama-Telescope Heterodyne Array Instrument (CHAI).

¹⁹Kölner Observatorium für SubMillimeter Astronomie (KOSMA), operated by I. Physikalisches Institut, Cologne, Germany.

²⁰California Institute of Technology (CIT), Pasadena CA, U.S.A.

²¹Cornell Caltech Atacama Telescope (CCAT).

²²The Kilopixel Array Pathfinder Project (KAPPA).

²²Arizona State University (ASU), Tempe AZ, U.S.A.

requires.

Chapter 2

Cryogenic Probe Station

2.1 Introduction

As alluded to in chapter 1, evaluation of InP devices without the investment in packaging can be satisfied through the use of a cryogenic probe station. This chapter begins with a discussion of the requirements for such a station, the challenges associated with cryogenic probe station design, and discusses the capabilities of commercially available systems. It will be shown that none of the current commercial options satisfies the needs of radio astronomy, foremost of which is the ability to quickly evaluate 100 mm InP wafers. The design of a cryogenic probe station satisfying these needs is presented in section 2.2, followed by test results from the completed station in section 2.3. This chapter concludes with a brief discussion of future improvements to the station in section 2.4.

2.1.1 Requirements

The requirements of a probe station satisfying the needs of cryogenic InP testing are summarized in table 2.1, and discussed here. The minimum chuck temperature should be <20 K, to provide data relevant to the performance of the device at the physical temperature it will ultimately be operated at. Obviously, cool down time should be as short as possible, a time of <8 hours allowing the station to be cooled overnight. The high operational cost associated with the use of LHE, as will be discussed further in section 2.1.2, necessitates the use of a closed cycle (CC) cryocooler. Testing an entire InP wafer, the largest of which is currently 100 mm in diameter, is provided by a ± 50 mm range of motion in the X-Y directions. In addition, binary chuck movement¹ in the Z-direction affords step and repeat measurement capability, as the wafer may be moved relative to the probes without repositioning of the probes themselves. The entire system should be extremely stable, capable of making S-parameter and noise measurements at W-band, where the performance capabilities of InP are exploited. This allows for characterization of devices used not only in wideband

¹The chuck is in one of two positions, down for movement or up for measurement.

continuum measurements, but also for the measurement of important spectral lines such as from carbon monoxide (CO).² Commercially available cryogenic probe stations only meet a subset of these requirements, as will be discussed in section 2.1.3.

Table 2.1: Cryogenic probe station design specifications

| Parameter | Specification |
|--------------------------|---|
| Chuck Temperature | ≤ 20 K |
| Cool Down Time | ≤ 8 hrs |
| Cooler | Closed-Cycle |
| Sample Size | $\varnothing 100$ mm |
| RF Probe Range | ± 1 mm X-Y ³ |
| Chuck Range | ± 50 mm X-Y, 6.35 mm Z ⁴ |
| RF Frequency | DC-116 GHz |

2.1.2 Challenges in Cryogenic Probe Station Design

Probe station design is particularly challenging, as the system must be stable enough to position probes on feature sizes of $\sim 80 \times 80 \mu\text{m}^2$ or smaller, and do so repeatably. This is only complicated when the system must function cryogenically, as elements of the probe station must be integrated within a cryostat. Aside from the added mechanical concerns, cryogenic cooling and vacuum systems must now be integrated into the design, further complicating matters. A brief summary of the design issues associated with cryogenic probe station design are

1. Materials

- Thermal conductivity and specific heat. The thermal conductivity and specific heat of most materials are extremely strong functions of temperature, as illustrated in figure 2.3 and 2.4. This temperature dependence must be taken into account in evaluation of the heat equation, for calculations of heat load and cool down time.
- Thermal expansion. Most materials contract with a decrease in temperature, as shown in figure 2.5 for several materials commonly employed in cryogenic design. Assemblies comprised of components of different materials must be designed in such a way that the thermal contraction differential is compensated for, to provide for dimensional stability and to prevent mechanical failure.
- Emissivity. The radiative heat exchange per area, between two surfaces, is proportional to the the difference in the physical temperatures of the surfaces to the fourth power,

²CO has a rest frequency of 115.271 GHz.

³Half the largest physical dimension of the device to be measured.

⁴Binary motion for step and repeat testing.

via the Stefan-Boltzmann law. The proportionality factor is partially attributed to the emissivity of the surfaces, which is a function of the materials and their surface finishes. Emissivities can range from 0.02 for highly polished gold to >0.2 for oxidized aluminum. Thus materials and surface finishes must be carefully addressed as they greatly impact the radiative heat load presented to the cryogenic cooler.

2. Range of motion

- Chuck or platen. X-Y motion of the wafer relative to the probes, can be accomplished by either moving the chuck (probes fixed), moving the probes (chuck fixed), or moving the entire platen (chuck fixed). The larger the wafer, the larger the required range of motion.
- Probe positioners. Even with motion of the chuck or platen, the individual probes must be moved to some degree, to set their relative spacing for calibration and measurement.

3. RF “cabling.” Routing of coaxial cable or waveguide from the walls of the cryostat to the cryogenically cooled probes within poses the following challenges:

- Flexibility. All lines must be able to translate some range of motion. This range is smallest for designs which move the chuck about the probes, and largest for designs moving the platen or individual positioners.
- Repeatability. Flexing of these lines around the position used during electrical calibration⁵, introduces an error due to changes in the magnitude and phase of transmitted and reflected signals.
- Loss. RF lines from the probe (cold) to the cryostat wall (warm) must be thermally isolating, to minimize the conducted heat load on the cryogenics. Stainless steel is typically used due to its low thermal conductivity. Unfortunately, stainless steel also has high electrical loss, which may reduce the available power, of instruments used with the probe station, to levels where calibration and or measurement becomes difficult.

4. Cooling Method

- LHE is expensive⁶, and produces high operational costs for systems using open flow LHE cooling. Using a value of $l_{vap} = 4.93 \text{ cal/g}$ [15], a density of 0.125 g/mL, and a price of \$3.50/L, the operational cost is estimated to be \$4.90/(W-hr). For continuous use, a 6 W cryostat would require \$700 of LHE every 24 hours.
- Closed cycle cryocoolers, such as the Gifford McMahon (GM) cryocooler, induce vibration from the movement of their internal displacer which is challenging to isolate from the

⁵This is particularly true for S-parameter measurements.

⁶Although the price varies regionally, a conservative estimate is \$3.50/liter.

probes and chuck. Pulse tube cryocoolers are mechanically quieter as they do not use a displacer, but do not have the same cooling capacity as their GM counterparts.⁷

2.1.3 Review of Commercially Available Stations

Table 2.2: Capabilities of commercially available cryogenic probe stations

| Parameter | Requirement | Lakeshore (CRX-4K) | Cascade (PMC) | Cascade (PAC-200) |
|---------------------------------|-------------------|--------------------|-------------------|-------------------|
| Chuck Temperature (K) | ≤ 20 | 4.5 | 4.2 | 4.2 |
| Cool Down Time (hrs) | ≤ 8 | ≤ 2 | not stated | not stated |
| Cooler | C-C ⁸ | C-C ⁸ | LHe ⁸ | C-C ⁸ |
| Sample Size (mm) | $\varnothing 100$ | 51 | 200 | 200 |
| Probe Range (X-Y-Z)(mm) | $\pm 1^9$ | $\pm 25, 12.5, 9$ | ± 12.5 | ± 12.5 |
| Chuck Range (X-Y)(mm) | ± 50 | none | ± 100 | ± 100 |
| Automation Capability | yes | no | no | ?? ¹⁰ |
| RF Frequency Range (GHz) | DC-116 | DC-67 | N/C ¹¹ | N/C ¹¹ |

Table 2.2 lists the performance capabilities of several cryogenic probe stations, commercially available from Lakeshore Cryotronics¹² and Cascade-Microtech.¹³ Simplified mechanical schematics of both systems are illustrated in figure 2.1. These systems are available with either closed-cycle or open-flow cryocoolers, capable of chuck temperatures of 4.2 K. Unfortunately, neither system is well suited for cryogenic probing at millimeter wave frequencies, as will be explained.

As seen at the top of figure 2.1, the Lakeshore system mounts its probe positioners external to the cryostat through bellows. This allows the use of an extremely small cryostat, helping to lower the radiative heat load, but has several disadvantages. The primary of which is that each probe must be moved during testing of multiple devices, a time-intensive process for a large numbers of devices. Secondly, long probe arms are necessary to connect the positioners (exterior to the cryostat) to the probes within. As the stiffness of the probe arm is proportional to the cube of its length, this makes the probes sensitive to vibration coupled in through their probe positioners.¹⁴

Cascade-Microtech's manual (PMC) and semiautomated (PAC-200) solve some of these issues. These systems place the probe positioners within the cryostat,¹⁵ shortening the probe arms sig-

⁷Sumitomo's GM cryocooler p/n SRDK-415D has a cooling capacity of 1.5W at 4.2 K, while its pulse tube cooler, p/n SRP-082B has a capacity of 1.0 W at 4.2 K.

⁸C-C=Closed Cycle, LHe=Liquid Helium.

⁹Required probe range of motion is ~ 1 mm, half the largest physical dimension of the devices to be measured.

¹⁰Although the system does have step and repeat capability through movement of its platen, it is not clear if the RF cabling to the platen would be able to translate the necessary distance of ± 50 mm.

¹¹Not configured for RF measurements.

¹²Lakeshore Cryotronics, Inc. 575 McCorkle Blvd., Westerville OH, 43082, U.S.A.

¹³Cascade Microtech, Inc. 9100 SW Gemini Dr., Beaverton OR, 97008, U.S.A.

¹⁴This is of particular concern if a closed-cycle cryocooler is to be used.

¹⁵The manual station uses control rods for positioner actuation, while the semiautomated system uses electrical actuators.

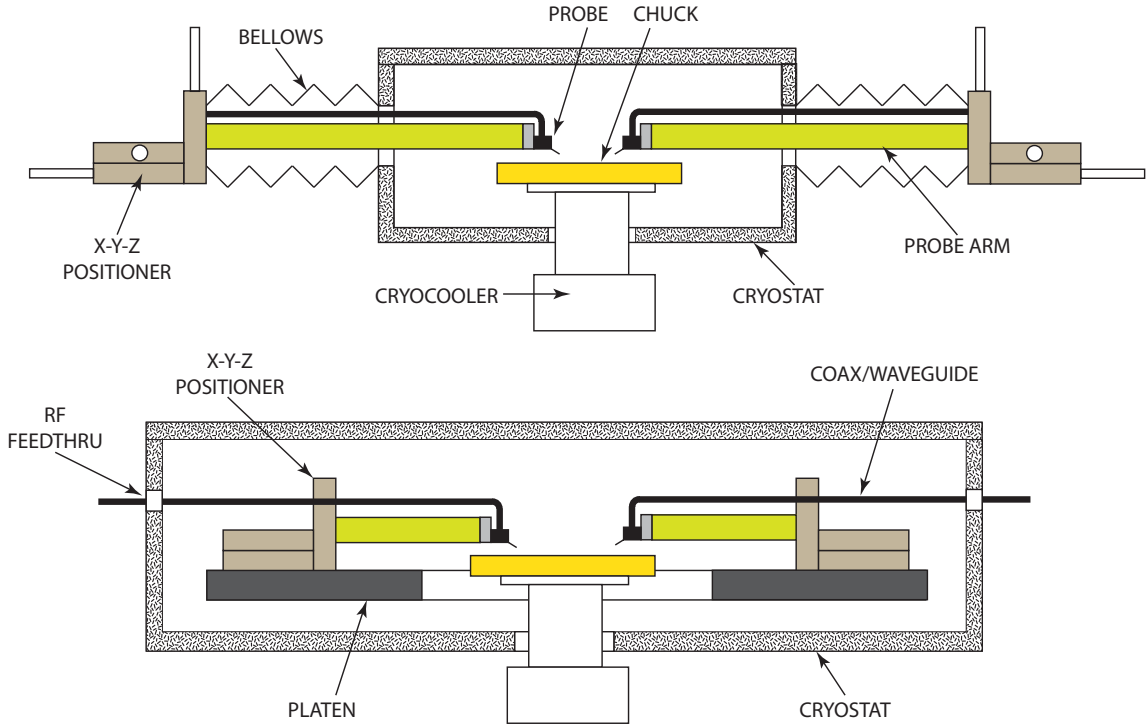


Figure 2.1: Simplified diagrams of two commercial cryogenic probe station configurations. (*Top*) Lakeshore Cryotronics mounts the probe positioners outside of the cryostat through bellows. (*Bottom*) Cascade-Microtech system places the probe positioners inside the cryostat, actuated by control rods or electrical actuators. On its semiautomated system, the PAC-200, the platen is able to move in 3 dimensions, allowing the probes to be moved across the wafer without individual repositioning. In both cases the RF cabling connected to the probe must translate the full range of motion.

nificantly. In addition, the platen within the PAC-200 is capable of movement in 3 dimensions, allowing the probes to be stepped across the chuck without individual repositioning. Unfortunately, any RF cabling must translate with the probes. This requires a significant amount of flexing of these lines, for testing across large wafers, as one end is fixed to the vacuum feedthrough within the cryostat's wall. Although coaxial line may be potentially used at lower frequencies, waveguide may be required at millimeter wave due to the output power limitations of instruments such as vector network analyzers (VNA) used with the station.

2.2 Design

To overcome these limitations, the following design strategies were utilized in the development of the station presented in this work.

1. Chuck range of motion in X-Y-Z. Motion in X-Y allows devices to be quickly tested without repositioning of the probes. It also minimizes the motion the probes relative to the cryostat

wall, and therefore the amount of flexing required of the RF cabling. Binary Z motion¹⁶ allows for step and repeat measurement capability.

2. Location of all positioners (chuck and probe) within the cryostat and electrically actuated. This allows the use of short (stiff) probe arms, reducing susceptibility to mechanically induced vibration. Electrical actuation removes the use of bulky control rods, simplifying the design and allowing for computer controlled automation.
3. Maintain all positioners at room temperature. This allows commercial positioners to be incorporated, such as utilized by the semiconductor and optics manufacturing industries.
4. Mechanically isolate the cyrocooler from the probe station through the use of a bellows and flexible heat straps linking the cryocoolers cold fingers to the probes and chuck.

In order to improve the serviceability of the station, as well as allowing rapid reconfiguration, the station is comprised of three subassemblies, illustrated in figure 2.2 and described as follows:

Chuck positioner subassembly. Moves the $\varnothing 114$ mm chuck over a ± 50 mm range in X and Y and pistons the chuck 6.35 mm in Z. It is rigidly mounted to the floor of the cryostat.

Platen subassembly. Holds up to 4 probe positioners, each with ± 6.35 mm range of motion in X, Y and Z. It is mounted to the chuck positioner via adjustable standoffs.

Refrigeration subassembly. Provides cooling of the chuck and probes through the use of flexible oxygen-free copper (OFC) heat straps. The first stage of its cryocooler shields the second stage cold finger assembly and also cools the radiation shield surrounding the chuck. It requires partial disassembly for integration with the other subassemblies.

The sections to follow detail the design of the subassemblies and components comprising the probe station. Equations are provided that give quick physical insight into design trade-offs and limitations. Calculations rely on the use of temperature-dependent values of thermal conductivity, heat capacity, and thermal expansion from NIST's¹⁷ cryogenic materials database [16]. The temperature dependence of these properties are illustrated in figure 2.3–2.5 for oxygen-free high conductivity copper (OFHC), 6061-T6 aluminum alloy (T6), type 304 stainless steel (SS), and glass-reinforced epoxy laminate (G10); materials which are employed in the construction of the probe station.

2.2.1 Chuck Positioner Subassembly

The chuck positioner is shown in figure 2.6. Two vacuum compatible, translation stages with 100 mm range (p/n UTSPPV6 from Newport¹⁸), are used to provide X–Y motion for the chuck assembly,

¹⁶Binary motion implies the chuck is one of two states; down for motion in X and Y or up, placing the wafer in contact with the probes for measurement.

¹⁷National Institute of Standards and Technology (NIST), Boulder CO, 80305 U.S.A.

¹⁸Newport Corporation, 1791 Deere Ave, Irvine CA, 92606 U.S.A.

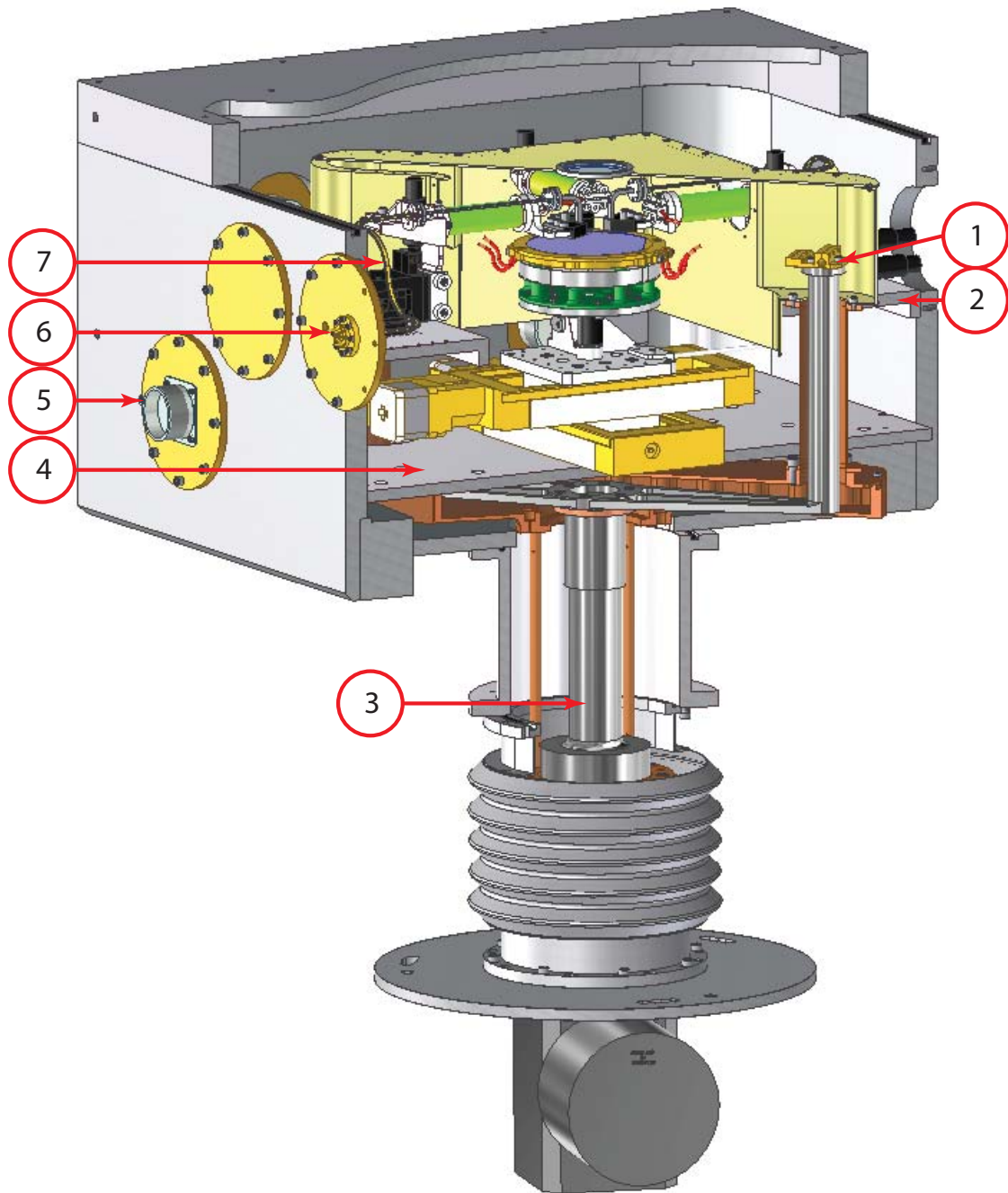


Figure 2.2: Cutaway illustration of the probe station subassemblies and components. (1) Cold finger strapping bracket, (2) platen subassembly, (3) refrigeration subassembly, (4) chuck positioner subassembly, (5) DC vacuum feedthru for motorized stage control, (6) WR-10 vacuum feedthrough, and (7) WR-10 service loop. Chamber external dimensions are 609.6 mm × 609.6 mm × 355.6 mm.

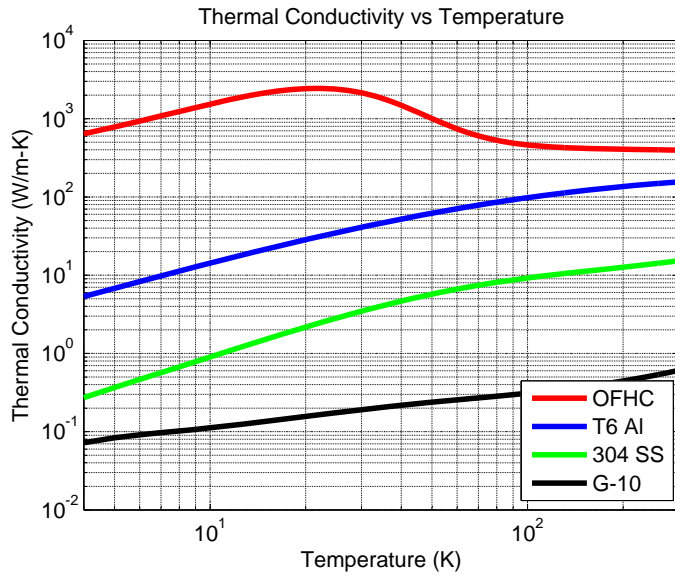


Figure 2.3: Thermal conductivities [16] of OFHC, G-10, and 304 stainless steel as a function of temperature. Note that there are 4 orders of magnitude between the thermal conductivity of G-10 (thermal insulator) and OFHC (thermal conductor) at cryogenic temperatures. The effect of the conductivity peak in OFHC, combined with its drop in specific heat with temperature, can be seen in the temperature data presented in figure 2.13, where there is a sudden drop in temperatures at ≈ 3.5 hours from the start of the cool down.

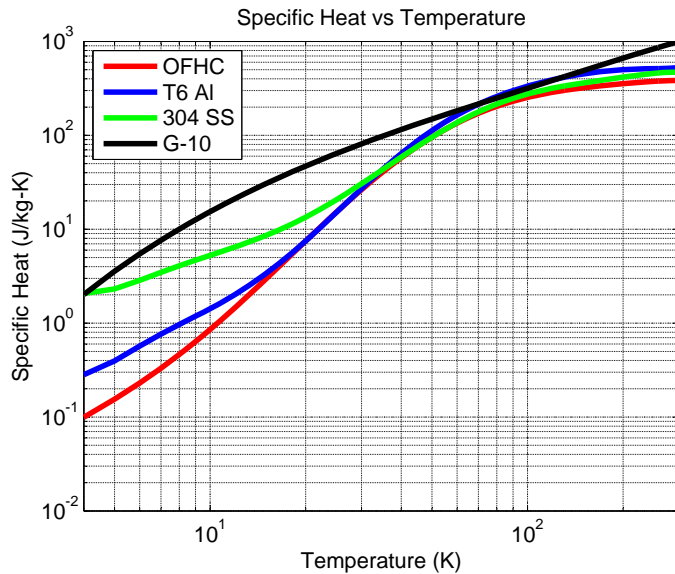


Figure 2.4: Specific heat [16] of OFHC, G-10, and 304 stainless steel as a function of temperature. The specific heat is the amount of energy required to change 1 kg of a given substance by 1 K.

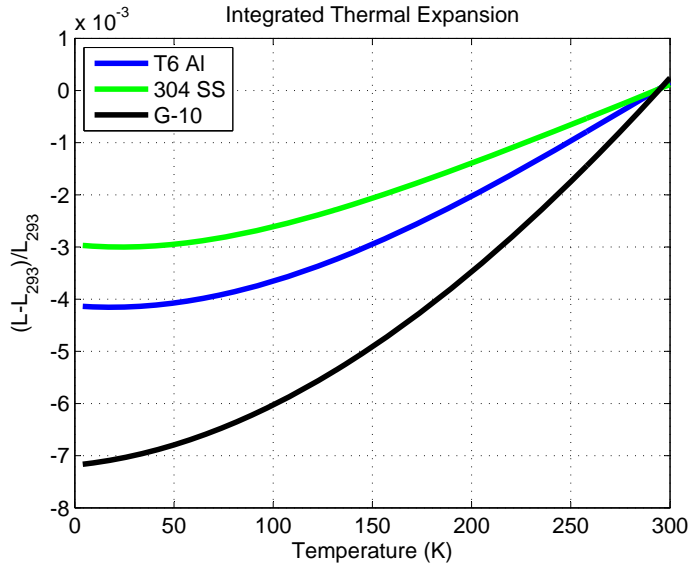


Figure 2.5: Integrated coefficient of thermal expansion [16] of T6, 304-SS, and G-10 as a function of temperature. It is defined as the change in length of an object relative to its length at 290° K. This quantity is easier to measure than the coefficient of thermal expansion itself.

shown at the bottom of the same figure. The translation stages are mounted to a 9.5 mm thick plate machined from 6061 T-6 aluminum. This plate is bolted to the floor of the cryostat with vented 1/4-20 fasteners. The use of vented fasteners avoids a “virtual leak,” whereby air trapped at the bottom of a blind tapped hole slowly escapes between the gap of the internal and external threads. The plate is polished and plated with electroless nickel to reduce its emissivity, and therefore minimize the radiant heat load presented to the cooled components of the probe station. At each corner of the chuck positioner subassembly there is an adjustable standoff, for planarity adjustment of the platen subassembly above it. The standoffs have 3/4-32 UN threads, allowing for ≈ 0.8 mm of vertical displacement per revolution of their adjusters.

The chuck assembly, shown in the bottom of figure 2.6 is mounted to the top translation stage. It uses a stepper motor (Lin Engineering¹⁹) and ball-spline bearing assembly prepared for vacuum use (THK²⁰ p/n LF10-3.34LES) to provide binary motion of the chuck in the Z-direction. This is accomplished by mounting a custom cam lobe to a stepper motor, which rides against a roller bearing mounted to the bottom of the chuck base. Rotating the stepper motor 90° raises the chuck base approximately 6.35 mm, equal to the lift of the cam lobe. One of the benefits of using a stepper motor in this configuration is that it can be stalled without risk of damage to the motor. This allows the use of a cam stop, providing repeatable vertical displacement of the chuck. A G-10 spacer is used to isolate the chuck base (room temperature) from the chuck (<20 K) above. The conducted heat

¹⁹Lin Engineering, 16245 Vineyard Blvd, Morgan Hill CA, 95037 U.S.A.

²⁰THK America, 200 E. Commerce Dr., Schaumburg IL, 60173 U.S.A.

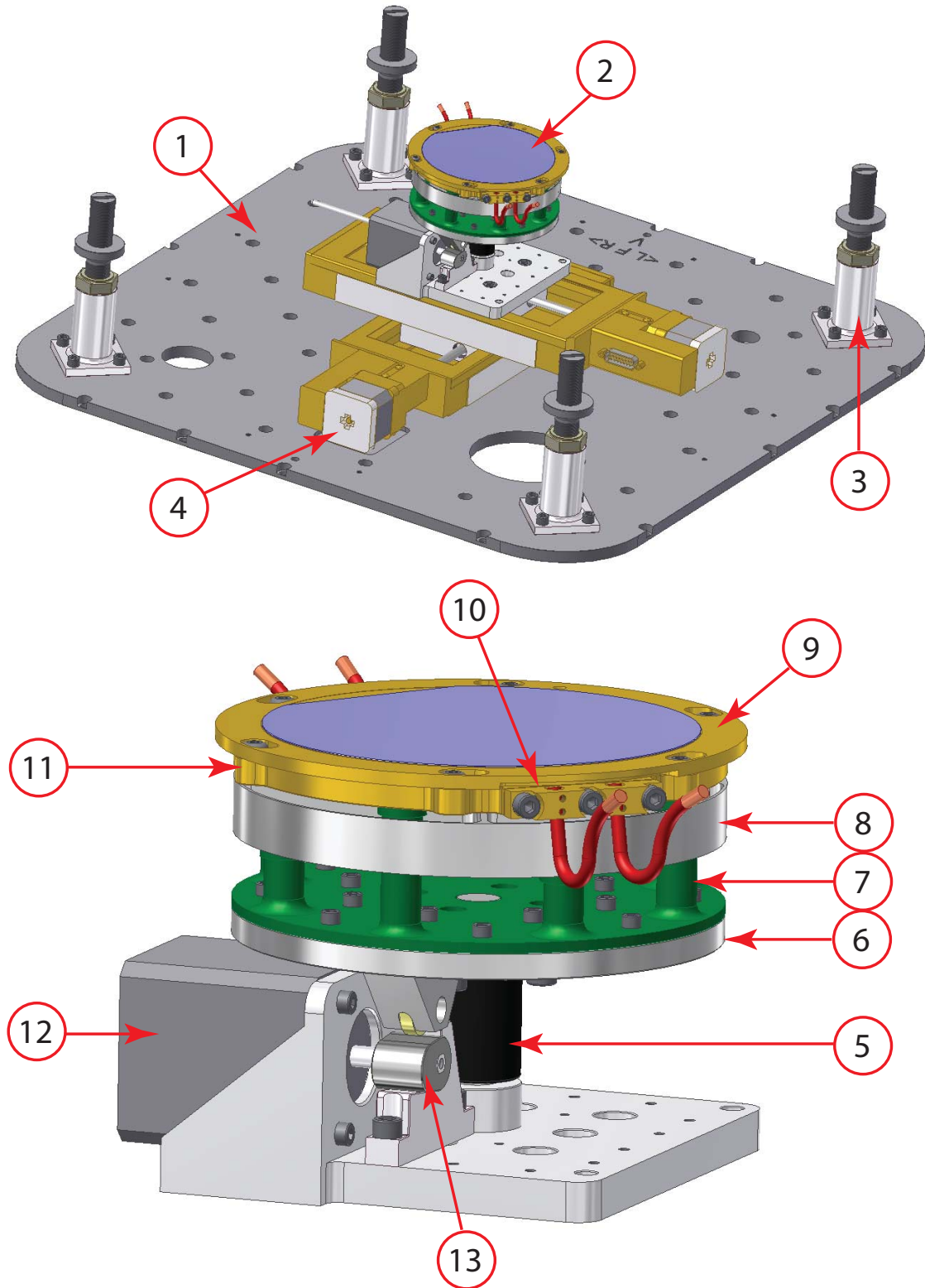


Figure 2.6: (*Top*) Chuck positioner subassembly. (1) Mounting plate, (2) chuck assembly, (3) platen mounts, and (4) 100 mm translation stage. (*Bottom*) Chuck assembly. (5) Ball-spline bearing, (6) chuck base, (7) G-10 isolator, (8) radiation shield, (9) wafer holder, (10) brackets for 8 gauge OFC cable (routed to cold fingers), (11) chuck, (12) stepper motor, and (13) cam lobe.

load through the G-10 spacer is calculated using the temperature-dependent thermal conductivity of G-10, shown in figure 2.3, with the following relation:

$$P_{cond} = \frac{A_{norm}}{l} \int_{T_1}^{T_2} k(T) dT, \quad (2.1)$$

where, A_{norm} is the area of the G-10 isolator normal to the conducted heat flow (84 mm^2) and l is the length (28 mm), resulting in a conducted heat load of 332 mW.

Additional standoffs on the G-10 spacer are used to mount a radiation shield to minimize the thermal load from the chuck base. Radiated power between the two surfaces, with areas A_2 and A_1 , may be calculated using [17]

$$P_{rad} = \epsilon_{12} F_{12} A_1 (T_2^4 - T_1^4), \quad (2.2)$$

where the effective emissivity, ϵ_{12} , and configuration factor, F_{12} , depend on the materials and geometry of these two surfaces. For large parallel plates, $F_{12} = 1$ and ϵ_{12} is given by

$$\epsilon_{12} = \frac{A_2 \epsilon_1 \epsilon_2}{A_2 \epsilon_2 + A_1 \epsilon_1 (1 - \epsilon_2)}. \quad (2.3)$$

Equations 2.2 and 2.3 may be used to estimate the radiated heat load from the top of the heat shield to the bottom of the chuck, given that both are polished, gold plated surfaces ($\epsilon_1 = \epsilon_2 = .03$). The resulting heat load is 72 mW. Additional relations for ϵ_{12} and F_{12} , for different geometries, can be found in introductory texts on heat transfer [18]. These relations quickly become complicated, and the large parallel plate example is well suited for quick estimates of radiated heat load. A heater located on the stepper motor mounting plate ensures that the temperature of the stepper motor, ball spline bearing, and translation stages are maintained above 283 °K, their minimum operating temperature (due to internal clearances that must be maintained). The temperature is monitored by a silicon diode temperature sensor (p/n DT-470-CU-13 from Lakeshore-Crytronics) and the heater controlled via a PID temperature controller (Model 336, also from Lakeshore Cryotronics).

Gold plated OFHC is used for the chuck itself, ensuring temperature uniformity. A silicon diode temperature sensor is affixed to the bottom for monitoring purposes. Mounting points are included at the outer perimeter of the chuck so that a wafer holder may be utilized, allowing wafers to be quickly exchanged. The thermal path between the chuck and cold fingers of the cryogenic system is established with 4 flexible heat straps manufactured from 8-gauge²¹ oxygen-free copper (OFC). Two of these straps are mounted to each side of the chuck through OFHC brackets, into which the OFC cables are soldered.

²¹≈3.3 mm in diameter

2.2.2 Platen Subassembly

The platen assembly of figure 2.7 holds up to 4 probe positioner assemblies, shown at the top of the same figure. They are bolted to a common 10 mm thick aluminum plate which is mounted above the chuck positioning assembly through the adjustable standoffs previously mentioned. The probe positioners themselves are from Quater²²(p/n XYZ500MIMT), with ± 6.35 mm of travel in X-Y-Z. Attached to the positioner is the probe arm holder, which supports the probe arm, itself machined from thermally insulating G-10 rod. The probe arm has an outer diameter 22.9 mm, wall thickness of 2.54 mm, and is 76.2 mm in length. Its thermal conduction may be calculated using (2.1) along with the temperature dependent thermal conductivity of G-10, shown in figure 2.3. This results in a 280 mW heat load per probe arm. The probe arm holder also allows for adjustment of probe planarity, through manual adjustment of two 2-56 fasteners in its base. If desired, these 2-56 locations can be counter bored for the mounting of linear actuators (such as p/n TRA6PPV6 from Newport), should automated probe planarity adjustment be needed in the future. The probe holder at the end of the G-10 probe arm is machined from OFHC, polished, and plated with electroless nickel. It is connected to the cryocooler's cold fingers through the same 8-gauge OFC straps used to connect the chuck.

For the W-band measurements presented in Section 2.3, a 127 mm length of WR-10 SS waveguide (wall thickness 0.254 mm) is connected between the probe positioner (warm) and probe (cold). The length of the waveguide was optimized for its thermal load and equalization of its thermal expansion, relative to that of the G-10 probe arm. Each waveguide yields a conducted heat load of 52 mW. Although methods exist to plate WR-10 waveguide with one to two skin depths of gold [19][20], thereby lowering the electrical loss, this increases the thermal load. Fortunately, the VNA used with the probe station, shown in Section 2.3, has adequate power at W-band so that the electrical loss of the unplated waveguide could be accommodated.

2.2.3 Refrigeration

The design of the refrigeration subsystem is centered around Sumitomo's²³ RDK-415D, Gifford McMahon (GM) cryocooler, capable of cooling 1.5 W at 4.2 K. The subassembly is shown in figure 2.8. The base of the cryocooler attaches to the bottom of the cryostat through a bellows which provides mechanical isolation. Mounting of the cryocooler to the probe station's steel frame is accomplished with a bracket cushioned with rubber mounts, to help dampen the cryocooler's vibration. The cooler's second stage is shielded by its first stage via a manifold system, which is also used to mount the radiation shield enclosing the entire chuck assembly. All cold finger assemblies were machined from OFHC, polished, and plated with electroless nickel (emissivity ≈ 0.1). The emissivity of

²²Quater Research and Development, PO Box 8824, Bend OR, 97708 U.S.A.

²³Sumitomo Cryogenics of America, 456 Oakmead Parkway, Sunnyvale CA, 94085 U.S.A.

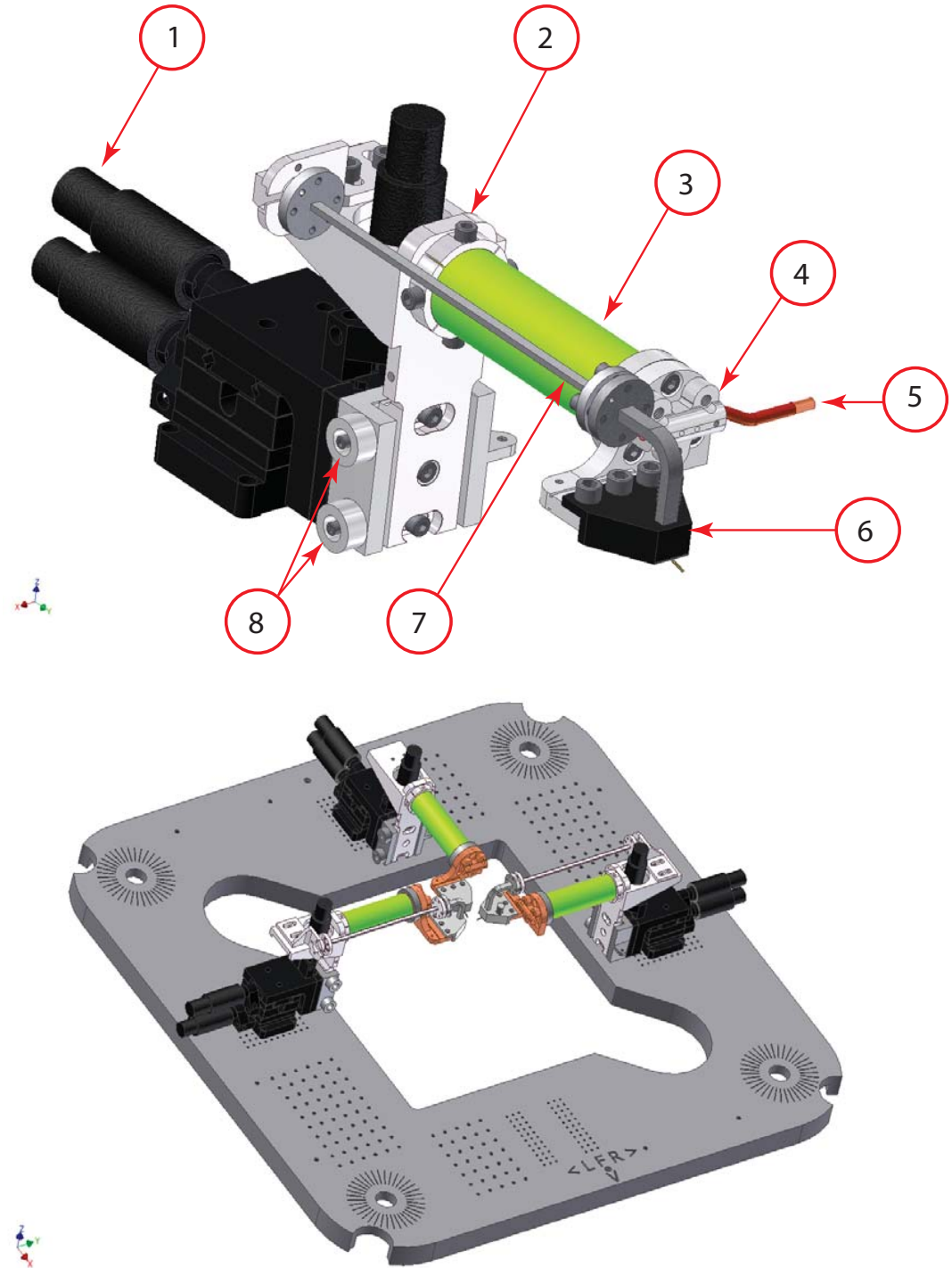


Figure 2.7: (Top) Probe positioner subassembly. (1) Quater XYZ500MIMT positioner, (2) probe arm holder, (3) G-10 probe arm, (4) probe holder (connected to the cold fingers with 8 gauge OFC cable (5)), (6) WR-10 to CPW probe, (7) WR-10 stainless steel waveguide, and (8) 2-56 screws used for probe planarity adjustment. Items (6) and (7) may be replaced with different combinations of waveguide/coaxial line and probe for measurements over different frequency ranges. (Bottom) Platen subassembly is comprised of up to 4 probe positioner assemblies (3 shown) mounted to a 10 mm thick aluminum plate.

electroless nickel is three times that of gold, but is much less expensive and offers excellent corrosion resistance.²⁴

The design of the cold fingers was optimized for a trade-off between thermal resistance and cool-down time. Increasing the cross-sectional area of the cold fingers lowers the temperature differential across them,²⁵ but increases their cooling time due to the increased heat capacity. To estimate the cool-down time, data from NIST's cryogenic materials database [16] was again used as the specific heat of most materials is a strong function of temperature. The cool-down time may be estimated using

$$t_{cool} = m \int_{T_1}^{T_2} \frac{c_v(T)}{P_{cool}(T)} dT, \quad (2.4)$$

where m is the mass of OFHC to be cooled and $c_v(T)$ is its specific heat. $P_{cool}(T)$ is a function of the heat load on the cryocooler, and is therefore a function of component temperature within the cryostat. An analytical expression for $P_{cool}(T)$ is not available, and this quantity was instead assumed to be constant for the purpose of estimation. Using a value of 15 W at 10 K, from the cryocooler's load map, the station is estimated to reach <20 K in 4.1 hours. The actual cool-down time to 20 K is 3.5 hours, as shown in figure 2.13.

The use of indium foil and Apiezon-N grease [21], [22] was not found to improve the thermal resistances of bolted joints within the refrigeration subassembly. It is reasoned that this is due to the quality of the machining, polishing, and plating of these components, fabricated by MVI.²⁶ The only exception was the inclusion of indium foil between the cryocooler's 2nd stage and its cold finger assembly, which was found to make a modest improvement of 0.2 K.

The vibration analysis of the Sumitomo cryocooler was investigated by Tomaru et al. [23], who determined that the two dominant sources of cryocooler vibration are due to its displacer and He pressure oscillations within the cold stages. Here, the cryocooler's vibration is mitigated in part by the use of the bellows and rubber mounts previously mentioned. In addition, the OFC heat straps, from the probe arms and chuck to the cold fingers, help to provide additional isolation. These cables are mounted to the cold fingers through OFHC brackets into which the heat straps are soldered. Vibration coupled to the chuck and probe arms has not yet been measured, but it is estimated that the differential displacement is $\sim 4 \mu\text{m}$ (the resolution of the optical system) as movement of the probes relative to chuck is barely visible under high magnification.

²⁴If left unplated, these surfaces would eventually oxidize, causing the emissivity, and therefore heat load on the cooler, to change with time

²⁵From the interface with the second stage of the cold head to the point at which the thermal straps connect, leading to the chuck and probes.

²⁶MVI Engineering and Manufacturing, 5772 Crown Dr., Mira Loma CA, 91752 U.S.A.

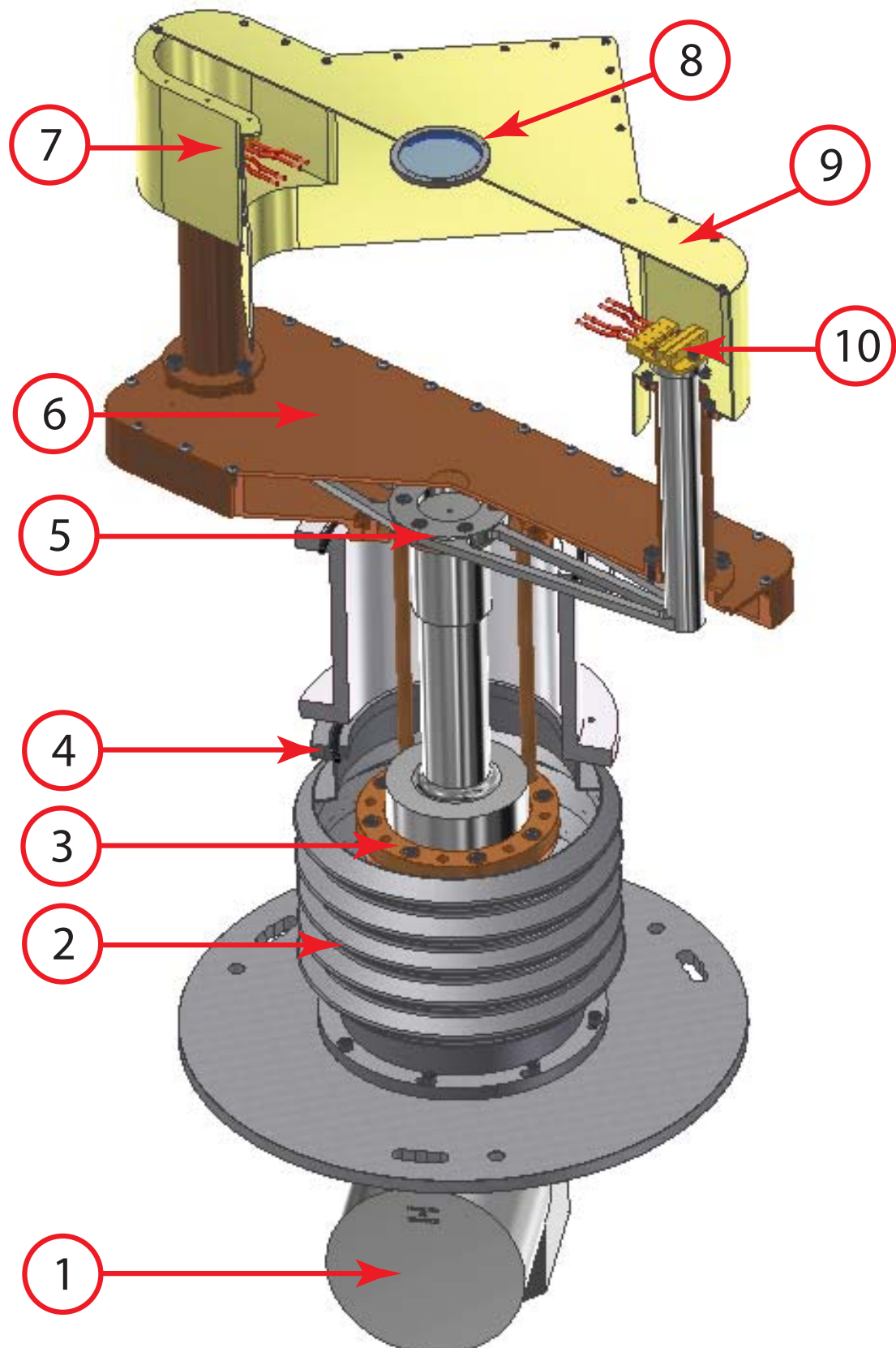


Figure 2.8: Cutaway view of refrigeration subassembly. (1) Sumitomo GM Cryocooler, (2) bellows, (3) 1st stage cold finger assembly (two of the cold fingers have been removed to aide illustration), (4) o-ring gland with o-ring, (5) 2nd stage cold finger assembly, (6) 1st stage manifold, (7) radiation shield (bottom), (8) IR reflecting window, (9) radiation shield (top), and (10) OFHC brackets and heat straps that connect cold fingers to chuck and probes.

2.2.4 Chamber Design

The cryostat's chamber was machined out of M-1 aluminum "mold" plate from Alpase.²⁷ The mechanical properties of M-1 are similar to that of 6061-T6 aluminum (Young's modulus = 74 GPa for M1 plate and 69 GPa for 6061-T6), but M-1 has a lower cost and is more readily available in large sizes. The chamber could have been fabricated from welded plate, as is common for large cryostats, but fabrication costs were estimated to be five times that of the machined version. The chamber interior dimensions measure 572 mm \times 572 mm \times 238 mm. Its walls need to be thick enough to maintain a suitable safety factor between stress on the chamber and the yield strength of the material the chamber is constructed from. Approximate relations for the maximum deflection, δ , and stress, S , for rectangular plates are given by [24], [25]

$$\delta = \kappa \frac{L^4 \Delta P}{E t^3}, \quad (2.5)$$

$$S = \beta \frac{L^2 \Delta P}{t^2}, \quad (2.6)$$

where, κ and β are dimensionless factors depending on the aspect ratio of the plate and how its edges are supported ($\kappa = 0.0443$ and $\beta = 0.28$ for simply supported square plates), L is the rectangle's shorter dimension, ΔP is the pressure differential, E is Young's modulus, and t is the thickness. The largest calculated deflection is 3.4 mm occurring in the cryostat's lid (machined from 12.7 mm thick 6061-T6 plate instead of M-1 aluminum plate). The corresponding stress is 58 MPa, yielding a safety factor of > 4 when compared to the yield strength. The measured deflection of the lid under high vacuum was ≈ 2 mm, indicating that the above relations were slightly conservative. The majority of the chamber's floor is 51 mm thick, to minimize deflection which would potentially bind the 100 mm translation stages of the chuck positioner subassembly. The interior of the chamber is polished and plated with electroless nickel, reducing the radiation load to the cold components and offering a surface that is easily cleaned.

All interfaces were sealed with the use of Parker o-rings from Valley Seal.²⁸ They were manufactured from Butyl or Viton, depending on availability, with a selected shore hardness of 75. O-ring glands were designed according to the guidelines provided in Parker's o-ring handbook [26]. During assembly, all o-rings were treated with a light coat of vacuum grease prior to installation, providing lubrication for proper seating during pump down by allowing them to move within their glands.

²⁷Alpase, 9750 Seaaca St, Downey CA, 90241 U.S.A.

²⁸Valley Seal Company, 6430 Varial Ave., Suite 106, Woodland Hills CA, 91367 U.S.A.

2.2.5 RF and DC Wiring

The WR-10 service loops (items (4) and (10) in figure 2.11) connect the output of the SS WR-10 waveguides (item (7) in figure 2.7) to WR-10 vacuum feedthrus mounted in the cryostat wall (item (6) in figure 2.2). These were manufactured by Custom Microwave²⁹ out of gold-plated, thin wall coin silver waveguide, providing enough flexibility for the probe positioners to articulate through their range of motion. The vacuum feedthrus were procured from Aerowave³⁰ and are similar in design to those used within ALMA's³¹ band-6 cartridge [27].

All temperature sensors, actuators, and device bias lines were wired to 37 pin hermetic feedthrus (p/n DSTBFH-28-21PP-110 from Detoronics³²). To reduce thermal loading from the temperature sensor and device bias lines, 32-gauge phosphor bronze wire was used (p/n QL-32 from Lakeshore Cryotronics) due to its low thermal conductivity. Actuator wiring, for the chuck and probe positioners, utilize 28-gauge, kapton insulated, shielded, twisted pair wiring (p/n 100692 from Accu-Glass³³). Kapton insulation was chosen to reduce outgassing from the cable assemblies.

2.2.6 Vacuum and Optical Systems

The vacuum system for the probe station was designed by Dr. Rodrigo Reeves of Caltech, the details of which can be found in [12]. It is built around a turbo-molecular pump (p/n (Turbo-V 301 Navigator)) provided by Varian Inc. (now Agilent Technologies³⁴). The use of a turbo-molecular pump eliminates concerns of contamination through the back streaming of pump oil, which is possible with a roughing pump. figure 2.9 illustrates the vacuum gauge and pump connections at the bottom of the cryostat. Vacuum levels of ≈ 1 mTorr are reached in 15 min, and $10 \mu\text{Torr}$ after several hours of pumping.

The optical system must provide the ability to select either a wide field of view (for movement during step and repeat testing) or high magnification (for actual probing). Both of these requirements were met with the system designed by Dr. Kieran Cleary of Caltech, also detailed in [12]. It consists of a Navitar³⁵ zoom system and PAXcam5³⁶ digital microscope camera. Under low magnification, a 13.8 mm field of view is obtained and a resolution of $\sim 4 \mu\text{m}$ under high magnification. The camera peers through a vacuum window (p/n ISOVPZ63QTCRSV from VACOM³⁷) mounted in the cryostat's lid. To limit IR heating of the chuck from the camera's light source, an IR reflecting window is mounted in the top of the chuck's radiation shield (see item 9 of figure 2.8). Figure 2.10

²⁹Custom Microwave Inc., 24 Boston Ct., Longmont CO, 80501 U.S.A.

³⁰Aerowave Inc., 344 Salem St., Medford MA, 02155 U.S.A.

³¹Atacama Large Millimeter Array (ALMA), www.almaobservatory.org.

³²Detoronics Corp. 10660 E. Rush St., El Monte CA, 91733 USA.

³³Accu-Glass Products, Inc. 700 Arroyo Ave., San Fernando CA, 91340 U.S.A.

³⁴Agilent Technologies, 5301 Stevens Creek Blvd., Santa Clara CA, 95051 U.S.A.

³⁵Navitar Inc., 200 Commerce Dr., Rochester NY, 14623 U.S.A.

³⁶PAXcam, 707 N. Iowa Ave., Villa Park IL, 60181 U.S.A.

³⁷VACOM Vakuum Komponenten & Messtechnik GmbH, Gabelsgergerstraße 9, 07749 Jena, Germany

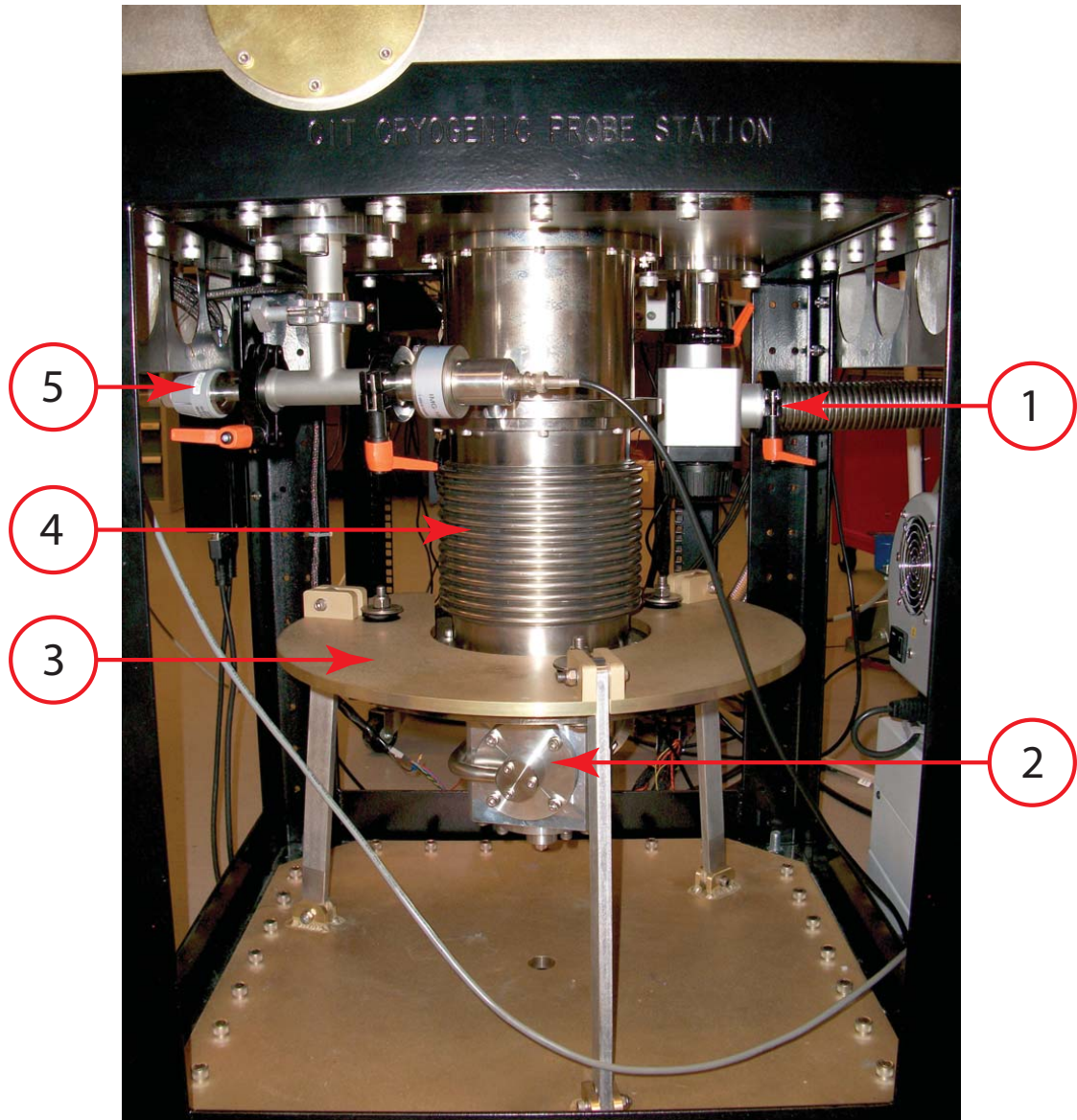


Figure 2.9: Bottom view of cryostat showing mounting of Sumitomo cryocooler and vacuum ports. (1) KF40 connection to Varian vacuum pump, (2) Sumitomo cryocooler, (3) cryocooler mounting plate, (4) bellows, and (5) KF25 vacuum-tee for mounting of low and high range vacuum gauges.

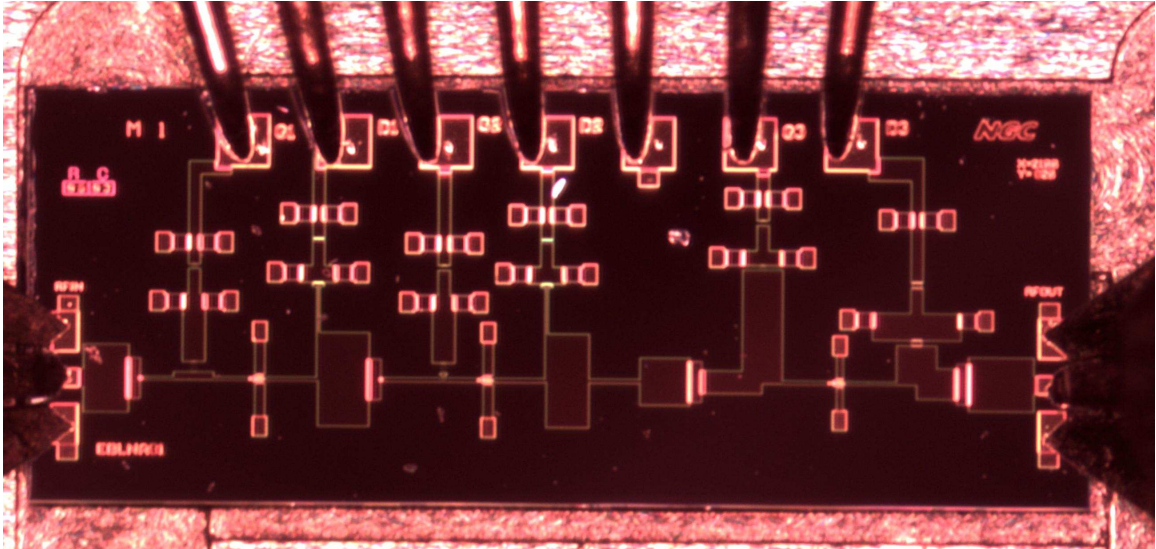


Figure 2.10: Image taken with the probe stations PAXcam5 digital camera during cryogenic probing. The MMIC is an EBLNA81 amplifier [3]. WR-10 CPW probes can be seen at the left and right of the photo, with the DC probe at the top. Photo courtesy of Dr. Kieran Cleary, Caltech.

shows the image of a W-band MMIC LNA obtained with the optical system during cryogenic probing.

2.3 Performance

Photographs of the completed station are shown in figure 2.11 and 2.12. Temperatures at various locations within the cryostat versus cool down time are illustrated in Figure 2.13, where it can be seen that the chuck temperature reaches <20 K in under 4 hours. From the final chuck temperature of 18.6 K and the load map of the Sumitomo cryocooler, it is estimated the total heat load on the cooler is ≈ 6 W. Of this, 1.3 W is accounted for due to conduction and radiation as summarized in table 2.3. The remaining 4.7 W heat load is due to radiative coupling between the cryostat floor (298 K) and chuck (18.6 K) part of which is reflected off of the bottom of the radiation shield that surrounds the chuck. Although the chuck reaches <20 K in under 4 hours, it takes 8 hours to stabilize to within ± 0.1 K, as preferred for noise measurements. This is likely again due to radiative coupling between the chuck and its radiation shield, as the shield is made out of thin aluminum and takes longer to cool down than the OFHC components that comprise the majority of the refrigeration system.

Instrumentation for the S-parameter and noise temperature measurement setups used with the cryogenic probe station are detailed in [12], developed by Dr. Rodrigo Reeves and Dr. Kieran Cleary. These setups are illustrated in figure 2.14, where the physical temperatures are provided to

³⁸Conducted

³⁹Radiated

⁴⁰Estimated from temperature data from completed station. Includes radiation shield surrounding chuck.

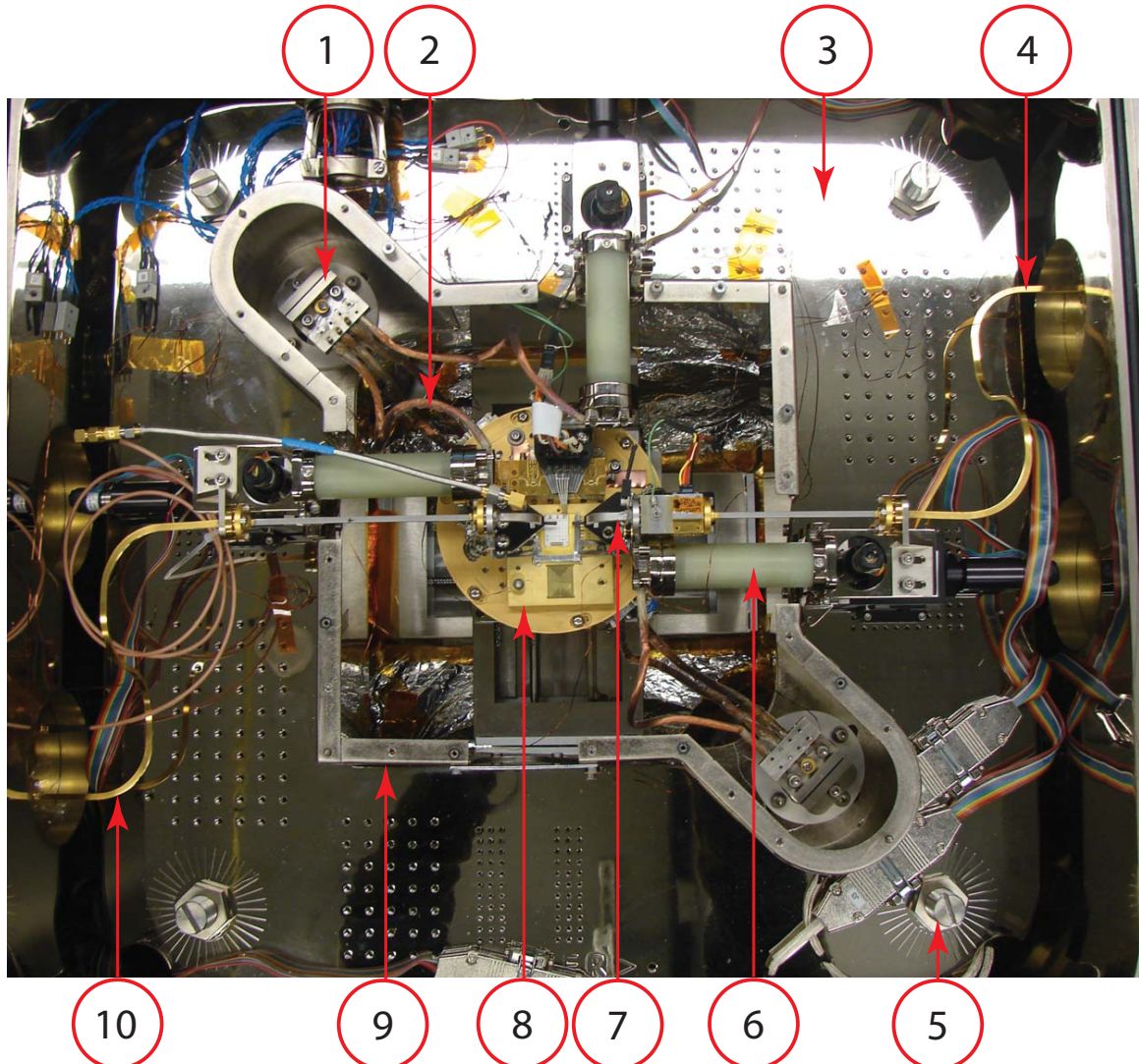


Figure 2.11: Top-down photograph of the inside of the cryostat. (1) Cold finger heat strap brackets and (2) straps, (3) platen subassembly, (4) WR-10 output service loop, (5) adjustable standoffs for platen height and planarity adjustment, (6) probe positioner subassembly, (7) WR-10 probe, (8) chuck, (9) chuck radiation shield, and (10) WR-10 input service loop.

Table 2.3: Heat loads presented to cryocooler

| Path | Material/Finish | Heat Load | Mode |
|------------------------------|---------------------|--------------|------------|
| Probe Arms ³⁸ | G10 | (3) x 280 mW | Conduction |
| Waveguides ³⁸ | Stainless Steel | (2) x 52 mW | Conduction |
| Chuck Isolator ³⁸ | G10 | 332 mW | Conduction |
| Heat Shield ³⁹ | Polished, Au plated | 74 mW | Radiation |
| Chamber ^{39,40} | Polished, Ni plated | 4700 mW | Radiation |

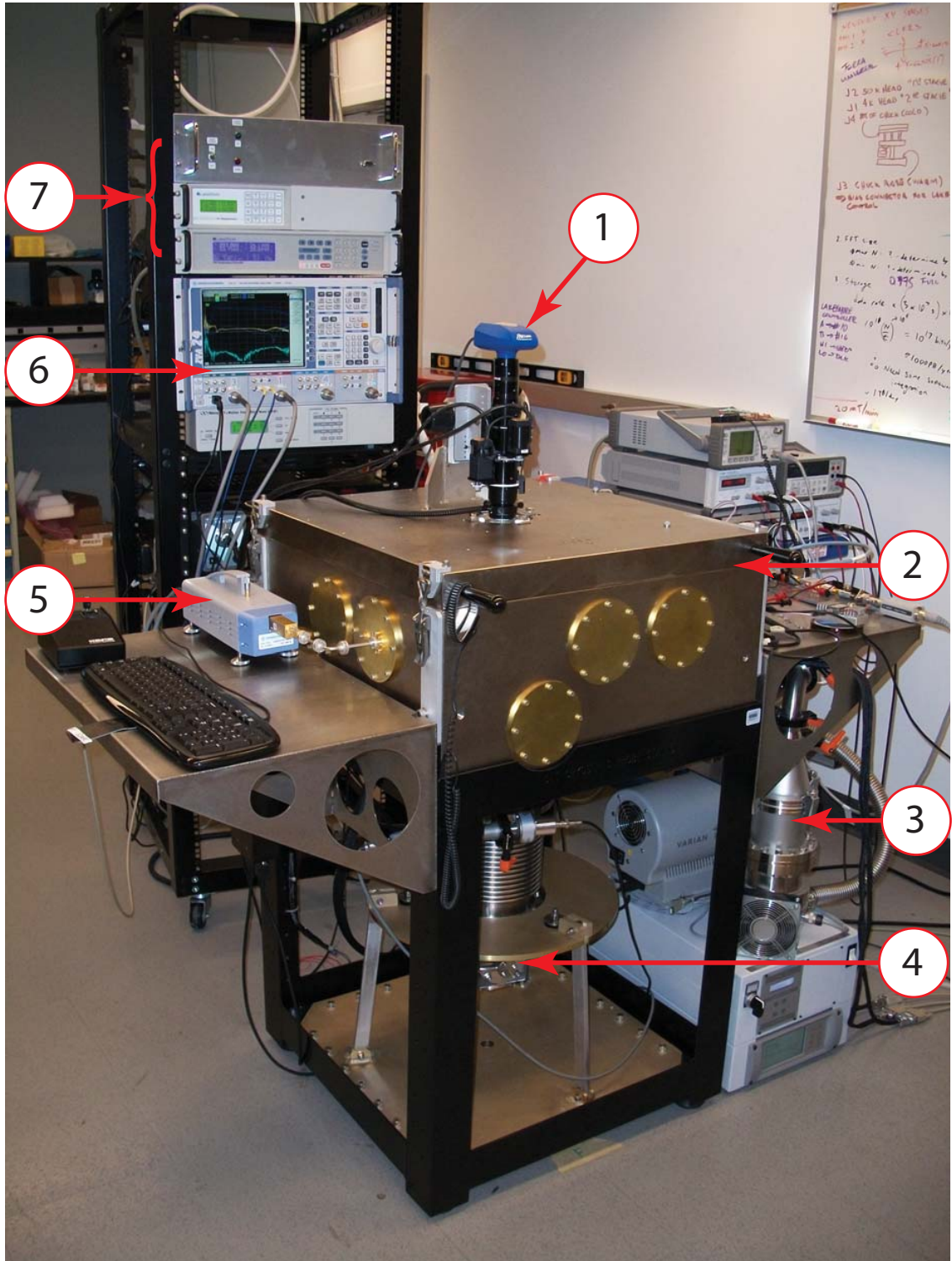


Figure 2.12: Completed cryogenic probe station, located in the Cahill Center for Astronomy and Astrophysics at Caltech. (1) Microscope and camera, (2) cryostat, (3) vacuum pump, (4) cryocooler, (5) millimeter-wave head, (6) VNA, and (7) stepper motor, heater, and temperature sensor electronics.

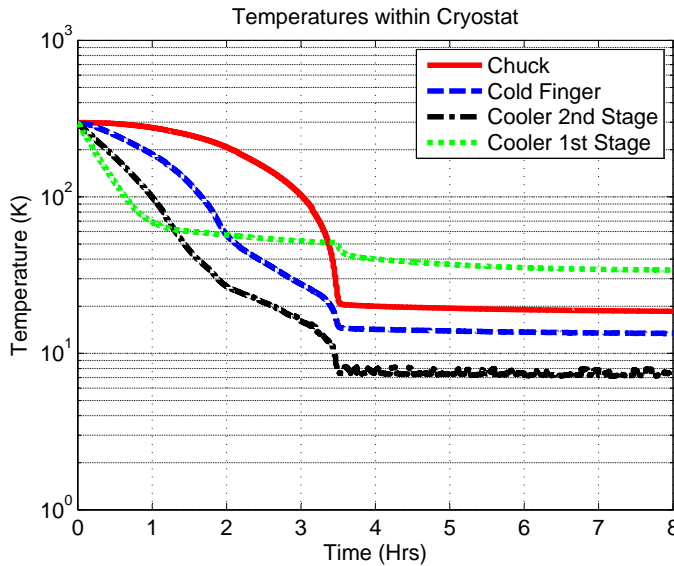


Figure 2.13: Temperatures within cryostat during cool down. The chuck reaches <20 K in under 4 hours. Final temperatures are: 18.6 K for the chuck; 13.5 K for the 2nd stage cold finger assembly; 6.8 K at the 2nd stage of the cryocooler; and 34 K at the 1st stage of the cryocooler, all reached after 8 hours from the beginning of cool down. From the final stage temperatures, the load on the cryocooler's second stage is estimated to be ≈ 6 W.

help illustrate thermal paths within the measurement chain. The RF probes stabilize at a slightly higher temperature than the chuck, due in part from the difference in the number of thermal straps connecting them to the cold fingers (one strap is used for connection of each probe, versus four used to connect the chuck). The probe's temperature does not appear to be effecting that of the chuck,⁴¹ possibly due to the high thermal impedance presented by the materials and small contact area of the WR-10 CPW probes used. Typical W-band S-parameter and noise temperature measurements obtained with these setups are shown in figure 2.15 and 2.16.

Possibly the best illustration of the stations cryogenic probing capability is shown in figure 2.17. This measurement was made by landing the probe connected to port 1 of the VNA on a CS-5 calibration short, seven times, once an hour. The measurement reveals a combined drift (probe station and VNA) of 0.04 dB over 7 hours. This corresponds to a calibration error of ≈ 45 dB, which is over an order of magnitude better than required for MMIC testing purposes. The result also suggests that the station may be stable enough for measurements above W-band, where InP MMICs have been demonstrated up to 500 GHz [28].

⁴¹By comparison of the chuck temperature with and without the probes landed.

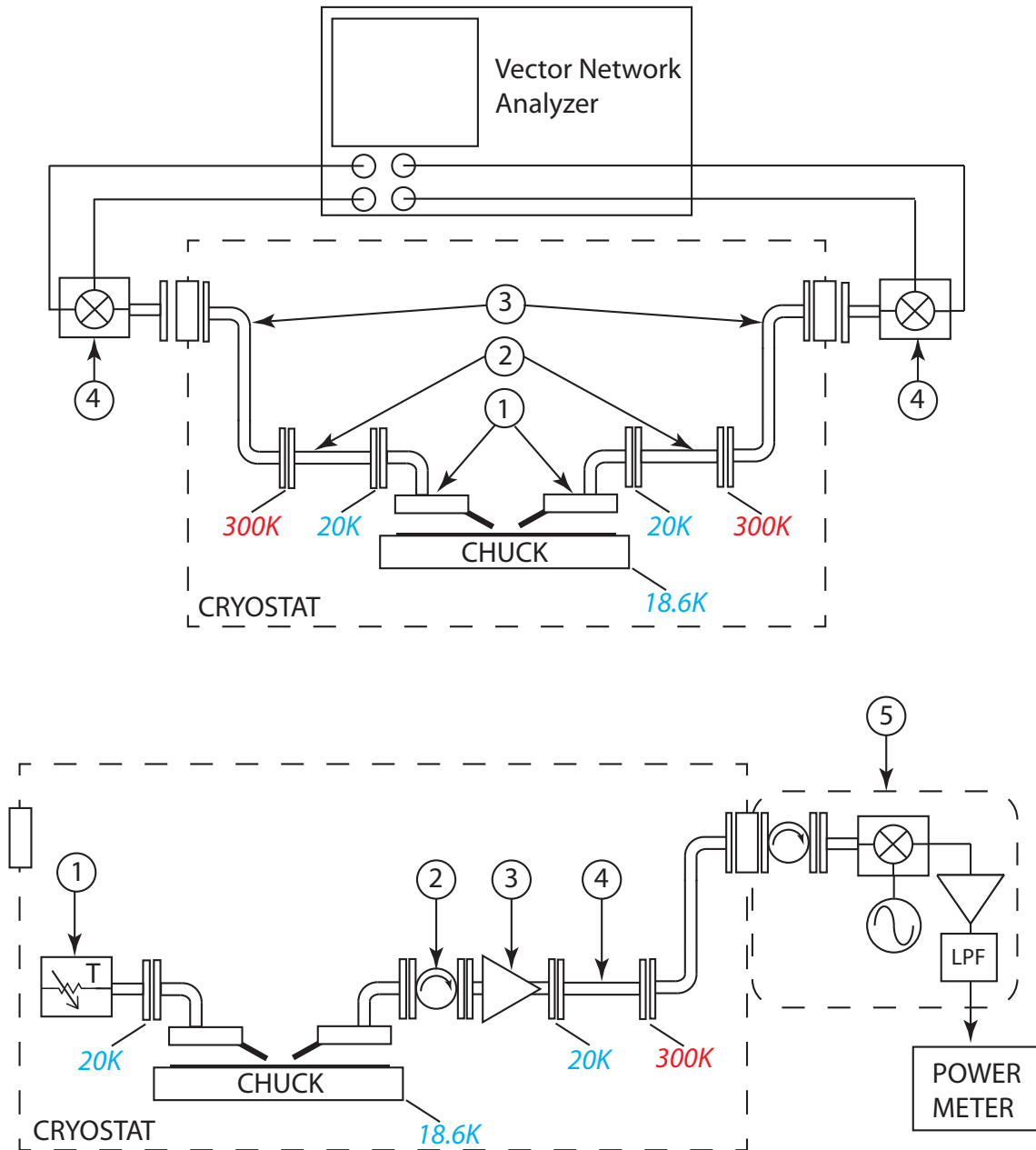


Figure 2.14: (Top) S-parameter test setup. (1) WR-10 probes, (2) SS WR-10 waveguides, (3) WR-10 service loop, and (4) millimeter-wave heads. (Bottom) Noise temperature test setup. (1) Variable temperature load, (2) cooled isolator, (3) cooled preamplifier, (4) SS WR-10 waveguide, and (5) down conversion block. Physical temperatures are indicated to help illustrate thermal paths within the measurement chain.

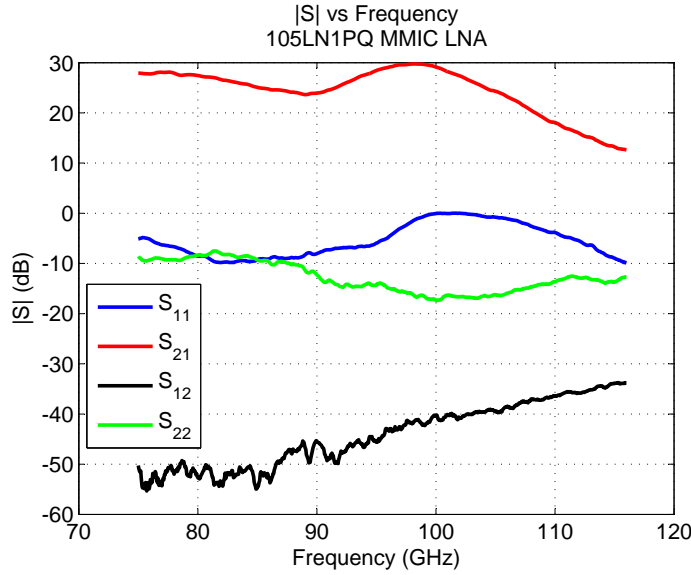


Figure 2.15: Probed, cryogenic S-parameters of a 4-stage InP MMIC LNA, p/n 105LN1PQ [2]. Bias conditions are $V_g=200$ mV, $V_d=750$ mV, and $I_d=10$ mA. Data courtesy of Dr. Rodrigo Reeves, Caltech.

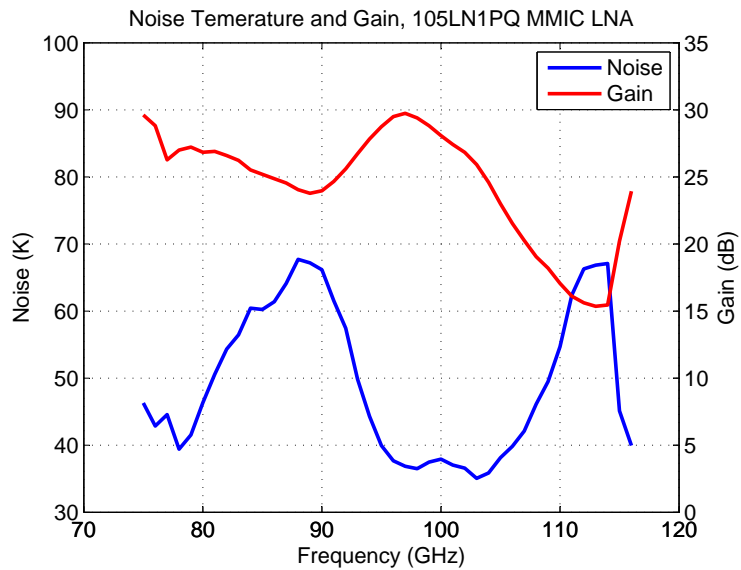


Figure 2.16: Probed, cryogenic noise and gain measurements of the 105LN1PQ MMIC LNA. Noise measurements were made using a variable temperature termination at the input of the LNA. Bias conditions are equivalent to those listed in figure 2.15.

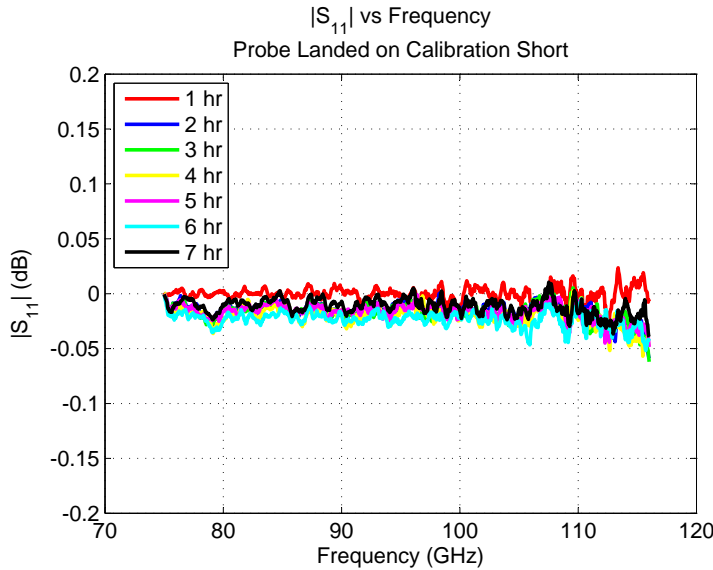


Figure 2.17: Cryogenic postcalibration stability, measured with a VNA. A probe was landed on a GGB CS-5 short calibration structure, then raised and relanded between measurements. Each trace corresponds to a measurement taken at 1-hour intervals, drifting from 0 dB to 0.04 dB in 7 hours. This corresponds to a calibration error of \approx 45 dB, which is at least an order of magnitude better than required for current MMIC testing purposes.

2.4 Future Improvements

The cryogenic probe station is currently being utilized to screen W-band MMIC LNAs for several projects within radio astronomy. The station will be updated in the near future for DC–67 GHz measurements, replacing the WR-10 waveguide and feedthrus with stainless steel UT-47 coaxial cable from Micro-Coax⁴² and V100 hermetic glass beads from Anritsu.⁴³ No degradation to the temperature performance is expected, as it is currently limited by radiative coupling between the cryostat's floor and chuck.

It is estimated that any future improvements to the minimum chuck temperature will be limited to a decrease of \approx 4 K. Increasing the cross section of the cold fingers connected to the cryocooler's second stage will reduce the chuck temperature at the cost of increased cool-down time. Altering the chuck radiation-shield's (item 8 in figure 2.8) material and finish may have the largest impact, as it is suspected that the majority of the radiative load incident on the chuck is reflected off the radiation shield. For the time being, the current minimum chuck temperature of 18.6 K is sufficient for cryogenic InP screening purposes.

⁴²Micro-Coax, 206 Jones Blvd, Pottstown PA, 19464 U.S.A.

⁴³Anritsu Corporation, 490 Jarvis Dr., Morgan Hill CA, 95037 U.S.A.

2.5 Summary

The design and performance of a cryogenic probe station satisfying the needs of InP MMIC screening for radio astronomy has been demonstrated. These needs were shown not to be satisfied by commercially available probe stations, a review of the capabilities of which were presented. The unique challenges in cryogenic probe station design were discussed, along with the novel design approach utilized in the station described here. Design details were then presented, with expressions provided that allow quick physical insight to the design trade-offs and limitations involved. Performance of the station was next demonstrated with S-parameter and noise temperature measurements at W-band. The station not only meets all of its performance goals, but costs almost a factor of 10 less than the only commercial option satisfying the majority, but not all of the design requirements.

Chapter 3

Noise Parameters

3.1 Introduction

In this chapter, several noise parameters “sets” will be summarized. Their understanding is critical in the comprehension of the work presented in chapter 4, as well as in the design of the LNAs in chapter 5. Following a brief review of electrical noise, the noise parameter set of Rothe and Dahlke [29] will be presented. As several other sets of noise parameters trace their origins to those of Rothe and Dahlke, it is beneficial to review their derivation. Noise parameter sets suitable for design work at higher frequencies will then presented, including the hybrid set (T_{min} , N , and Γ_{opt}) used throughout the remainder of this work. The chapter concludes with a brief discussion on the selection of the appropriate set of noise parameters.

3.2 Background

Noise is fundamental property of, and is present in, every physical system. It manifests itself in the statistical fluctuations of physical quantities, as dictated by quantum mechanics and the corpuscular nature of matter. The main sources of noise within electrical circuits are

- **Thermal noise**¹ is due to the random (Brownian) motion of charged carriers. Its power spectral density² is flat³ with frequency and equal to $4kTR$ (V^2Hz^{-1}) where, k is Boltzmann’s constant and T and R are the physical temperature and resistance of the object respectively.
- **Shot noise** is due to the finite nature of electric charge. It is associated with the motion of charged carriers across a potential barrier and has power spectral density equal to $2qI_{DC}$ (A^2Hz^{-1}). Where q is the electron charge and I_{DC} is the average or DC current. Shot noise also has a flat frequency spectrum.

¹Also referred to as Johnson or Nyquist noise.

²Noise content in a 1 Hz bandwidth.

³For $hf \ll kT$, where h and k are the Planck and Boltzmann constants and f is frequency.

- **1/f noise** describes any noise process whose power spectrum is inversely proportional to frequency. More generally, its power spectrum is inversely proportional to f^α , with α lying between 1 and 2. It is caused by traps within the device, formed from defects at the interface between semiconductor layers and within the bulk semiconductor itself.
- **Avalanche noise** is found in semiconductors with a large applied field. Carriers accelerated by a field can gain enough energy to dislodge an electron-hole pair upon impact. These new carriers can themselves gain enough energy to dislodge additional carrier pairs. In transistors this effect is more commonly referred to as impact ionization. For bipolar transistors, the effect can be seen in the base-collector junction which is typically reverse biased.

Electrical circuits, may contain hundreds of different noise generators, of the types listed above. To aide in analysis, it is beneficial to de-embed these noise sources into a set of parameters, analogous to network parameters $[Y]$, $[Z]$, $[ABCD]$, $[S]$, etc., commonly used in circuit analysis. These de-embedded noise sources form “noise parameters.” They allow calculation of the noise contribution of the network from knowledge of the noise parameters, external terminating impedances, and its network parameters alone. In some noise parameter representations, only the noise parameters and source impedance are needed for noise calculations.

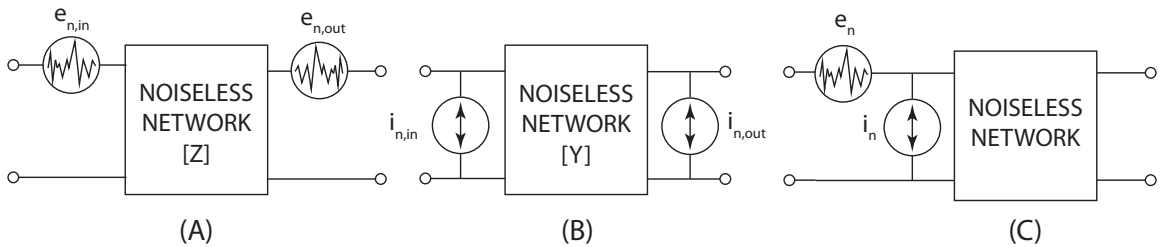


Figure 3.1: Noise sources de-embedded from their original noisy networks, used in the determination of equivalent noise parameter representations. (A) Thevenin, (B) Norton, and (C) composite network referred to the the input, originally proposed by Rothe and Dahlke [29]. Associated with each set of noise sources is a (complex) correlation coefficient, ρ . Rothe and Dahlke’s model is particularly useful as it frees noise calculations from the knowledge of the network’s parameters.

The formulation of noise parameters transform an original “noisy network” into two networks: one containing the noise contributions of the original network; and a “noiseless” network, the original network with all internal noise sources removed. For a two-port network, only four noise parameters are necessary to completely describe the noise behavior of the original noisy network, regardless of the number of internal noise sources. Although there are many different “sets” of noise parameters, all are equivalent with the appropriate transformations, as they all originate from the same physical processes. figure 3.1 shows several different representations of noise parameters, de-embedded from their original noisy networks. These parameters are formed by two external, de-embedded noise

sources whose Fourier coefficients are represented by their mean square values $|\bar{X}|^2$ and $|\bar{Y}|^2$, and (complex) correlation coefficient $\rho = \overline{XY^*}/\sqrt{|\bar{X}|^2|\bar{Y}|^2}$. It is implicitly assumed that all noise sources are wide-sense stationary, their expected values denoted by an overbar “ $\bar{\cdot}$ ”.

3.3 Noise Parameters R_n , G_n , and Y_{opt}

Subfigures A and B of figure 3.1 utilize noise sources at input and output of their noiseless network, the noise contribution of the network determined from these sources, the networks [Y] or [Z] parameters, and terminating admittances or impedances. Rothe and Dahlke were first to suggest the noise equivalent circuit of figure 3.1 C, where both noise sources are referred to the input of the network, freeing noise calculations from knowledge of network parameters.

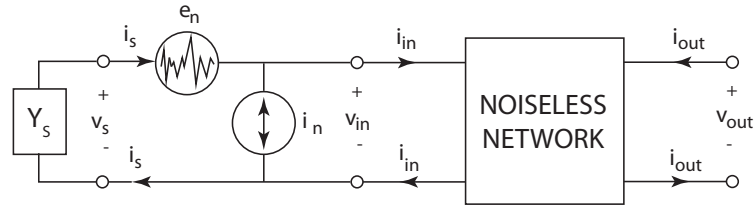


Figure 3.2: Series noise voltage and shunt noise current, transferred to the input of the two-port network.

The network of figure 3.1C is repeated in figure 3.2, illustrating nodal voltages and currents for the derivation to follow. The correlation coefficient between noise sources e_n and i_n is defined by

$$\rho = \frac{\overline{i_n e_n^*}}{|\bar{i_n}|^2 |\bar{e_n}|^2}, \quad (3.1)$$

where i_n may now be broken into two components, one correlated and one uncorrelated with e_n , denoted by $i_{n,c}$ and $i_{n,\perp}$ respectively.

$$i_n = i_{n,c} + i_{n,\perp} \quad (3.2)$$

The correlation admittance, Y_{corr} , is thus defined as

$$\begin{aligned} i_{n,c} &= Y_{corr} e_n \\ Y_{corr} &= \rho \sqrt{\frac{|\bar{i_n}|^2}{|\bar{e_n}|^2}} \\ &= \frac{\bar{i_n} \bar{e_n^*}}{|\bar{e_n}|^2}. \end{aligned} \quad (3.3)$$

The relations for the source voltage, v_s , and current, i_s , may then be expressed as

$$v_s = v_{in} + e_n , \quad (3.4)$$

$$\begin{aligned} i_s &= i_{in} + i_{n,\perp} + Y_{corr}e_n \\ &= i_{in} + i_{n,\perp} + Y_{corr}(v_s - v_{in}) . \end{aligned} \quad (3.5)$$

Equations (3.4) and (3.5) are represented schematically in figure 3.3, where it should be noted that Y_{corr} does not generate thermal noise. The beauty of the approach taken by Rothe and Dahlke is that the two correlated noise sources, e_n and i_n , have now been broken up into two independent sources and a (complex) correlation admittance. This eases the calculation of the input noise temperature, T_n , which is now determined. T_n is defined to be the equivalent physical temperature of the source, when connected to a noise free equivalent of the original network, which yields the same available noise power as the original noisy network. The noise output power may be determined by short circuiting the output of figure 3.3 and determining the output current contribution from each noise source.

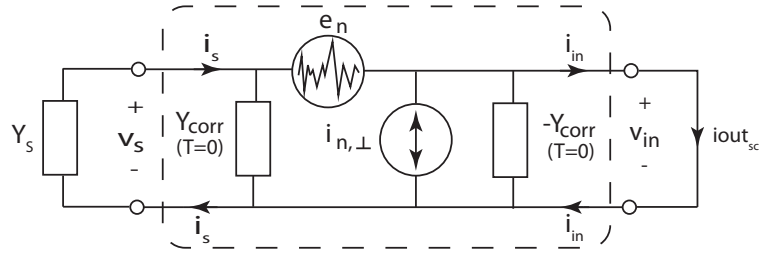


Figure 3.3: Rothe and Dahlke equivalent noise network used in the determination of input noise temperature. The output is short circuited and i_{out} determined for noise sources e_n and $i_{n,\perp}$. Y_{corr} does not generate thermal noise.

$$kT_n\Delta f = \frac{|\overline{i_{n,\perp}}|^2 + |\overline{e_n}|^2 (Y_s + Y_{corr})}{4\Re(Y_{out})} , \quad (3.6)$$

where Nyquist's relation [30] for the available noise power from a body at physical temperature T_n has been utilized, $P_{av} = kT_n\Delta f$ ⁴, to define the temperature of the source. Nyquist's relation can also be used to define the noise resistance and conductance of e_n and $i_{n,\perp}$ respectively, both evaluated at the standard noise temperature of $T_0 = 290$ K, by definition.

⁴This is an approximation of the power spectral density across a conductor at temperature T , $P(f) = hf/(e^{hf/kT} - 1)$. This is valid for $hf \ll kT$, where h and k are Planck's and Boltzmann's constants respectively, and f is frequency.

$$R_n = (4kT_0)^{-1} \overline{|e_n|^2} \quad (3.7)$$

$$G_n = (4kT_0)^{-1} \overline{|i_{n,\perp}|^2} \quad (3.8)$$

The noise parameter set (R_n , G_n , and Y_{corr}) is thus formed.⁵ equation (3.7) and (3.8) may then be substituted into (3.6) to arrive at an expression for T_n in terms of (R_n , G_n , and Y_{corr}).

$$T_n = \frac{T_0}{G_s} (G_n + R_n |Y_s + Y_{corr}|^2) \quad (3.9)$$

It is immediately apparent that T_n is a function of the source admittance, $Y_s = G_s + jB_s$, and that the noise may be minimized by the proper selection of Y_s . The minimum noise temperature, and source conductance at which this occurs, is determined by taking the appropriate partial derivative, $\frac{\partial T_n}{\partial G_s}$, of equation (3.9), with $B_s = -B_{corr}$.

$$Y_{s,min} = \sqrt{\frac{G_n}{R_n} + G_{corr}^2 - jB_{corr}} \quad (3.10)$$

$$T_{min} = 2T_0 R_n (G_{corr} + G_{s,min}) \quad (3.11)$$

Using these results, equation (3.9) is often reexpressed as

$$T_n = T_{min} + T_0 \frac{R_n}{G_s} |Y_s - Y_{opt}|^2, \quad (3.12)$$

$$Y_{opt} = Y_{s,min}. \quad (3.13)$$

This reveals the relationship between T_n and the distance between Y_s and Y_{opt} on the admittance plane. The final representation of Rothe and Dahlke's noise equivalent circuit is shown in figure 3.4.

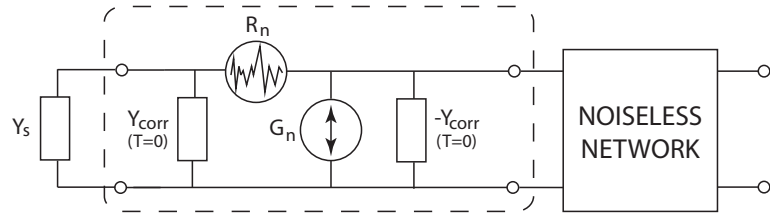


Figure 3.4: Final noisy network de-embedded from original network with internal noise sources. R_n and G_n are defined at the standard noise temperature of $T_0=290$ K.

⁵Roth and Dahlke also proposed the equivalent set (r_n, g_n, Z_{corr}) , where a correlation impedance is defined instead of an admittance.

3.4 Noise Parameters T_{min} , N , and Γ_{opt}

Equation (3.12) may be transformed into the hybrid parameter set (T_{min} , N , and Γ_{opt}), suitable for use at microwave frequencies, by substitution of the relations for the source and optimum source reflection coefficients

$$\begin{aligned}\Gamma_s &= \frac{Y_0 - Y_s}{Y_0 + Y_s} , \\ \Gamma_{opt} &= \frac{Y_0 - Y_{opt}}{Y_0 + Y_{opt}} .\end{aligned}$$

Where $Y_0 = 1/Z_0$ is the characteristic admittance. Following simplification, (3.12) is transformed into

$$T_n = T_{min} + 4T_0 R_n G_{opt} \frac{|\Gamma_{opt} - \Gamma_s|^2}{(1 - |\Gamma_{opt}|^2)(1 - |\Gamma_s|^2)} . \quad (3.14)$$

It was first proposed by Lange [31], that the noise resistance R_n , in (3.14), should be replaced with a constant that is invariant under lossless impedance transformation. Lange revealed that this constant is $N = R_n \Re(Y_{opt})$, which upon substitution into (3.14) becomes

$$T_n = T_{min} + 4T_0 N \frac{|\Gamma_{opt} - \Gamma_s|^2}{(1 - |\Gamma_{opt}|^2)(1 - |\Gamma_s|^2)} . \quad (3.15)$$

These noise parameters and relation for T_n will be referenced through the remainder of this work. Z_{opt} , the optimum generator impedance, will be used interchangeably with Γ_{opt} in future discussions of noise parameters in chapter 4, to provide physical insight into measured results, Γ_{opt} and Z_{opt} being related by

$$Z_{opt} = Z_0 \frac{1 + \Gamma_{opt}}{1 - \Gamma_{opt}} .$$

It is helpful to view the factor $4T_0 N$ of equation (3.15) as a “sensitivity factor,” by which T_n is raised above T_{min} by the distances between Γ_{opt} and Γ_s . Pospieszalski [32],[33],[34] has shown that certain limits for the ratio of $4T_0 N$ to T_{min} exist for field effect transistors (FET) and heterojunction bipolar transistors (HBTs). The first limit can be seen from inspection of equation (3.11) and stems from the fact that the correlated portion of the noise current cannot be greater than the total noise current itself. At T_{min} , where $Y_s = Y_{opt}$, this implies that $G_{opt} \geq G_{corr}$. The following limit is therefore set:

$$\begin{aligned}T_{min} &\leq 2T_0 R_n (2G_{opt}) , \text{ or} \\ 1 &\leq \frac{4NT_0}{T_{min}} .\end{aligned}$$

Pospiesalski has also shown that both FETs and HBTs belong to a class of networks for which $\Re(\rho) \geq 0$, whose effects can be seen by recasting equation (3.11) in the following form.

$$\begin{aligned} T_{min} &= 2T_0 R_n (G_{corr} + G_{s,min}) \\ &= 2T_0 (R_n \Re(\rho) \sqrt{\frac{|i_n|^2}{|e_n|^2}} + R_n \Re(Y_{opt})) \\ &= 2T_0 (\Re(\rho \sqrt{R_n g_n}) + N) \end{aligned} \quad (3.16)$$

$$= 2T_0 (R_n |Y_{opt}| \Re(\rho) + N) , \quad (3.17)$$

from which it can be seen than $4NT_0/T_{min} \leq 2$. Taken together, the following limits are set on the quantity $4NT_0/T_{min}$

$$1 \leq \frac{4NT_0}{T_{min}} \leq 2 . \quad (3.18)$$

This provides a convenient gauge of the quality of measured noise parameters. Parameters for which N and T_{min} conspire to fall outside of which are in error. This relation will be used in chapter 4 to qualify noise parameters determined using a self-calibrating, variable-impedance network.

3.5 Noise Parameters T_a , T_b , T_c , and ϕ_c

At microwave frequencies it is natural to devise a set of noise parameters with a wave nature. Penfield [35] first constructed a set of such parameters based on the original derivations of Rothe and Dahlke [29]. The noise waves, one incident to the two port and the other traveling away from its input, as shown in figure 3.5, were defined to be uncorrelated through the use of a complex normalization impedance. Meys [36] later used the wave representation of Penfield, but did not require the ingoing, A_n , and outgoing,⁶ B_n , waves to be uncorrelated, and instead related them to the characteristic impedance Z_0 . They are related to e_n and i_n of section 3.3 through

$$\begin{aligned} A_n &= -\frac{e_n + Z_0 i_n}{2\sqrt{\Re(Z_0)}} , \\ B_n &= \frac{e_n + Z_0^* i_n}{2\sqrt{\Re(Z_0)}} . \end{aligned}$$

The input noise temperature due to A_n and B_n can be determined by calculating the total power incident on the network shown in figure 3.5.

⁶Relative to the input of the two-port.

$$\begin{aligned}
P_{noise} &= \overline{|A_n + B_n \Gamma_s|^2} \\
&= \overline{|A_n|^2} + |\Gamma_s|^2 \overline{|B_n|^2} + 2\Re(\Gamma_s \overline{A_n^* B_n})
\end{aligned} \tag{3.19}$$

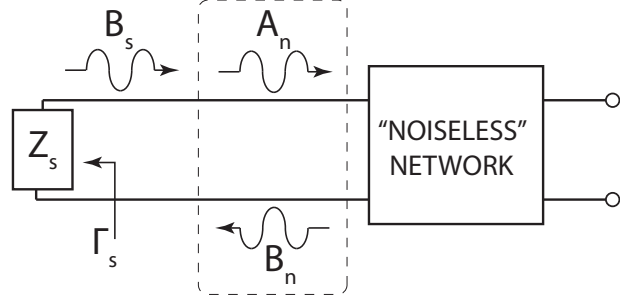


Figure 3.5: Noise wave representation originally constructed by Meys [36]. A_n and B_n are the ingoing and outgoing noise waves, relative to the network's input. B_s is the noise wave from the source, used for calculation of the input noise temperature, T_n .

The same incident power would be produced by a source of strength,

$$|B_s|^2 = P_s(1 - |\Gamma_s|^2) . \tag{3.20}$$

Therefore, T_n may be determined by equating equation (3.19) and (3.20), and using Nyquist's formula for the available spectral power from the source at physical temperature T_n , $P_s = kT_n$,

$$kT_n(1 - |\Gamma_s|^2) = \overline{|A_n|^2} + |\Gamma_s|^2 \overline{|B_n|^2} + 2\Re(\Gamma_s \overline{A_n^* B_n}) , \tag{3.21}$$

or

$$T_n = \frac{T_a + |\Gamma_s|^2 T_b + 2 |\Gamma_s| T_c \cos(\phi_s + \phi_c)}{1 - |\Gamma_s|^2} , \tag{3.22}$$

where

$$\begin{aligned}
T_a &= \frac{\overline{|A_n|^2}}{k}, \\
T_b &= \frac{\overline{|B_n|^2}}{k}, \\
T_c &= \frac{\overline{|A_n^* B_n|}}{k}, \\
\phi_c &= \angle(\overline{A_n^* B_n}), \\
\phi_s &= \angle(\Gamma_s).
\end{aligned}$$

Equation 3.22 provides quick insight into the fundamental mechanism of noise matching in LNA design. The minimum noise temperature is achieved by the proper selection of Γ_s by which the correlated portion of B_n is reflected off of the source, and causes maximum destructive interference with A_n . The required argument of Γ_s to do so is $\phi_{opt} = \pi - \phi_c$, resulting in

$$T_n = \frac{T_a + |\Gamma_s|^2 T_b - 2 |\Gamma_s| T_c}{1 - |\Gamma_s|^2}. \quad (3.23)$$

The required modulus of Γ_s may be determined by taking the appropriate partial derivative of (3.23), setting it equal to zero, and solving for $|\Gamma_s|$. The appropriate root of the resulting equation is selected so as to make $|\Gamma_s| = 0$ when A_n and B_n are uncorrelated, since reflecting any portion of B_n only adds to the noise ($\Gamma_s = \Gamma_{opt} = 0$ in this case). Finally, equation (3.22) may be put into a form similar to (3.15).

$$T_n = T_{min} + T_f \frac{|\Gamma_s - \Gamma_{opt}|^2}{1 - |\Gamma_s|^2}, \quad (3.24)$$

where

$$\begin{aligned}
|\Gamma_{opt}| &= \frac{1}{2T_c} \left(T_a + T_b - \sqrt{(T_a + T_b)^2 - 4T_c^2} \right), \\
\phi_{opt} &= \pi - \phi_c, \\
T_f &= \frac{T_c}{|\Gamma_{opt}|}, \\
T_{min} &= T_f - T_b.
\end{aligned}$$

The use of noise wave parameters is very useful in understanding the system noise penalty incurred in interferometers consisting of dense arrays of radio telescopes. In such configurations, crosstalk between antenna elements maybe an issue depending on the spillover of the antennas, itself a function of pointing. A simple two element example of which is shown in figure 3.6. The corresponding crosstalk noise temperatures are

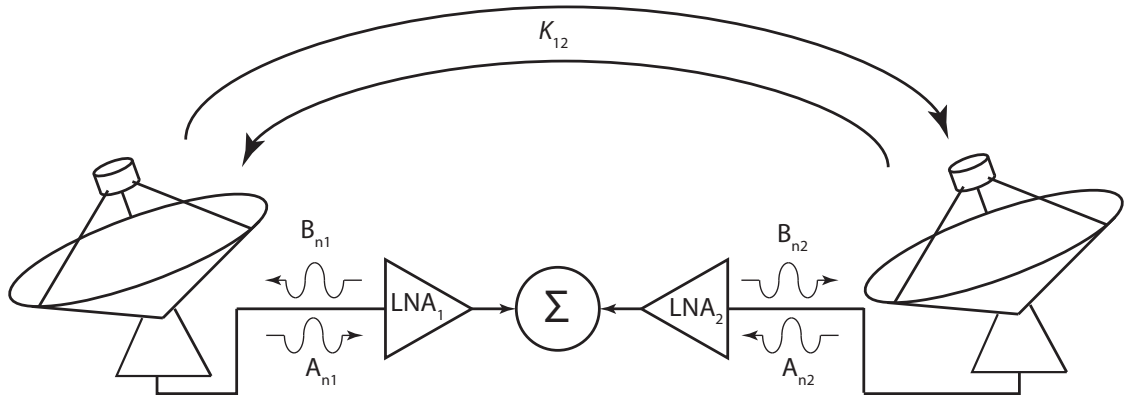


Figure 3.6: Noise contributions from adjacent interferometer receiving elements. The incident and outgoing noise waves at each LNAs input, A_n and B_n respectively, coupled with the crosstalk between antennas, results in a correlated noise component when the received signals are combined. Since the crosstalk is a function of antenna pointing, so is the additional noise.

$$\begin{aligned}
 T_{x,12} &= \kappa_{1,2} \overline{|B_{n,2} + S_{11,2} A_{n,2}|^2} \\
 &= \kappa_{1,2} \left(T_{b,2} + |S_{11,2}|^2 T_{a,2} + 2T_{c,2} |S_{11,2}| \cos(\phi_{11,2} + \phi_{c,2}) \right), \\
 T_{x,21} &= \kappa_{1,2} \overline{|B_{n,1} + S_{11,1} A_{n,1}|^2} \\
 &= \kappa_{1,2} \left(T_{b,1} + |S_{11,1}|^2 T_{a,1} + 2T_{c,1} |S_{11,1}| \cos(\phi_{11,1} + \phi_{c,1}) \right),
 \end{aligned}$$

where $\kappa_{1,2}$ is the available gain between antenna elements one and two, a function of the pointing of both antennas. The total noise temperature at the summing junction contains both correlated and uncorrelated noise components from each receiver. Minimizing the system noise temperature is no longer a matter of optimizing the interaction of an antenna with its own LNA. Further complicating matters is that system noise, in general, changes with antenna pointing. In the future, as the density of array elements increases, accurate knowledge of the noise parameters will be necessary to minimize system noise temperature.

3.6 Noise Parameters $\overline{|c_1|^2}$, $\overline{|c_2|^2}$, and $\overline{c_1 c_2^*}$

Noise parameters may also be represented by waves c_1 and c_2 , emanating from the input and output of the device respectively, as shown in figure 3.7. This set of noise parameters, introduced by Wedge and Rutledge [37], is related to those of Meys through the following relations:

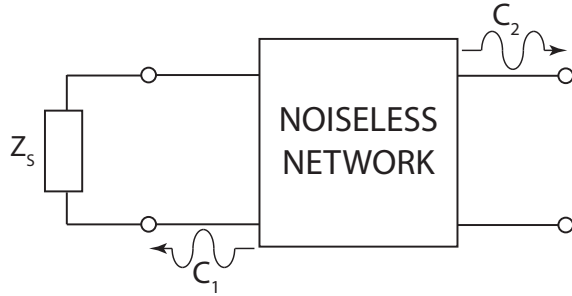


Figure 3.7: Noise wave parameters represented at the input and output of a network.

$$\overline{|c_1|^2} = \overline{|B_n + S_{11}A_n|^2}, \quad (3.25)$$

$$\overline{|c_2|^2} = |S_{21}|^2 \overline{|A_n|^2}, \quad (3.26)$$

$$\overline{c_1 c_2^*} = S_{21}^* \overline{A_n^* B_n} + S_{11} S_{21}^* \overline{|A_n|^2}. \quad (3.27)$$

Nyquist's relation may be used with equation (3.25)–(3.27) to define corresponding noise temperatures. A noise parameter measurement system, suitable for use at microwave frequencies, was developed by Wedge and Rutledge [38] to measure these parameters. It uses circulators instead of tuners within its test setup, therefor having the benefit of no moving parts and the associated repeatability aspects. One additional attractive feature is that $\overline{|c_1|^2}$ and $\overline{|c_2|^2}$ may be verified through simple power measurements at the input and output of the device respectively. NIST uses such techniques to verify noise parameters [39] measured at its facility.

3.7 Which Parameter Set?

The question naturally arises, “which noise parameter set should be used?” There is no simple answer, as it depends largely on how these parameters are to be used or measured. Those of Rothe and Dahlke are well suited at analog frequencies such as in operational amplifier (OPAMP) analysis. In this regime distributed effects may be ignored and noise measurements may be made with dynamic signal analyzers and oscilloscopes.⁷ At higher frequencies, where wavelengths become comparable to circuit dimensions, the other noise parameters sets introduced here become important, if not necessary to use. The salient point is that all noise parameters are de-embedded representations of the physical noise sources within a device or circuit. As they all originate from the same physical mechanisms, transformations between sets may be performed to satisfy a particular measurement,

⁷Assuming that the noise to be measured has been suitably amplified to place it well above the noise floor of the instrumentation.

design, or analysis need.

Chapter 4

Noise Parameter Measurement System

4.1 Introduction

Chapter 3 introduced several different representations of noise parameters, the hybrid set (T_{min} , N , and Γ_{opt})¹ used specifically in the remainder of this work. In this chapter, a system suitable for the measurement of noise parameters at cryogenic and ambient temperatures will be presented. Background is first provided on noise parameter measurement methods and their application at cryogenic temperatures. Of these, the wide-band-frequency-variation (WBFV) method's use of variable impedance noise sources is particularly attractive, as will be discussed. Two different variable impedance, self-calibrating, noise sources will then be presented in section 4.2; the first designed for cryogenic temperatures and the second for both ambient and cryogenic temperatures. Principles used in the calibration of these modules are presented in section 4.3, including an analysis of systematic and random errors. The techniques developed are not unique to the calibration of these modules and may, in general, be applied to any noise source. The description of noise parameter measurements made using these modules, and the corresponding measurement uncertainty analysis, then follows. Sections 4.7 and 4.8 provide calibration and measurement examples at cryogenic and ambient temperatures for a number of different devices. These results are compared against theory and independent measurements. Future work and improvements to the system are presented in Section 4.9.

4.1.1 Background

The measurement of noise parameters, using the method originally proposed by R. Q. Lane [40] in 1969, is to linearize the equation for the noise factor, reexpressed here in terms of input noise temperature, T_n , as

¹ Z_{opt} will be used interchangeably with Γ_{opt} , where $\Gamma_{opt} = (Z_{opt} - Z_0)/(Z_{opt} + Z_0)$.

$$T_n = T_{min} + T_0 \frac{R_n}{G_s} |Y_s - Y_{opt}|^2 , \quad (4.1)$$

$$= A + B(G_s + \frac{B_s^2}{G_s}) + C \frac{1}{G_s} + D \frac{B_s}{G_s} , \quad (4.2)$$

where

$$T_{min} = A + \sqrt{4BC - D^2} , \quad (4.3)$$

$$R_n = \frac{B}{T_0} , \quad (4.4)$$

$$G_{opt} = \frac{\sqrt{4BC - D^2}}{2B} , \quad (4.5)$$

$$B_{opt} = \frac{-D}{2B} . \quad (4.6)$$

Factors (A,B,C, and D) may be thought of as an additional “hybrid” set of noise parameters. The noise temperature is measured at a number of known source admittances ($Y_s = G_s + jB_s$), at a given frequency, the resulting measurements expressed as

$$\begin{bmatrix} T_{meas_1} \\ T_{meas_2} \\ \vdots \\ T_{meas_n} \end{bmatrix} = \begin{bmatrix} 1 & G_{s_1} + B_{s_1}^2/G_{s_1} & 1/G_{s_1} & B_{s_1}/G_{s_1} \\ 1 & G_{s_2} + B_{s_2}^2/G_{s_2} & 1/G_{s_2} & B_{s_2}/G_{s_2} \\ \vdots & \vdots & \vdots & \vdots \\ 1 & G_{s_n} + B_{s_n}^2/G_{s_n} & 1/G_{s_n} & B_{s_n}/G_{s_n} \end{bmatrix} \cdot \begin{bmatrix} A \\ B \\ C \\ D \end{bmatrix} , \quad (4.7)$$

or

$$[T] = [\Psi] \cdot [A] . \quad (4.8)$$

The different admittance states are achieved through the use of a microwave tuner [40], a combination of tuner and varactor [41], switched impedances [42], or the WBFV [43]. An example of a typical test setup using a tuner is shown in figure (4.1). Although only 4 noise temperature measurements (at unique values of Y_s) are necessary to determine A, B, C , and D from equation (4.7), >16 are usually necessary in practice to reduce the effects of measurement uncertainty. The noise parameters are then determined through a linear least squares fit,

$$[A] = ([\Psi]^T [\Psi])^{-1} [\Psi]^T [T] , \quad (4.9)$$

or weighted linear least squares fit,² corresponding to

²The use of a weighted least squares fit is useful when one or more of the measurements is suspect.

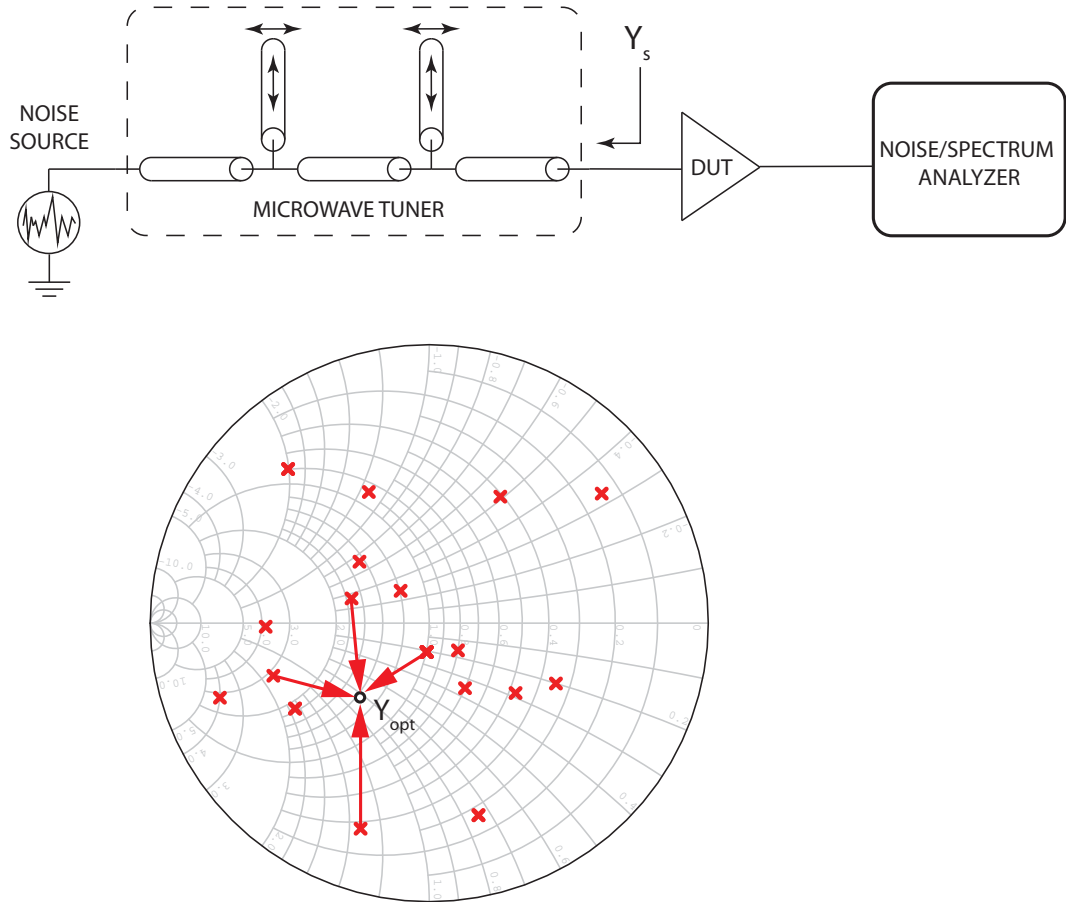


Figure 4.1: (Top) Typical test setup used in the measurement of a DUT's noise parameters. The tuner is adjusted to present the DUT with a number (>16 in practice) of different admittance states, the noise temperature recorded at each of these. (Bottom) Illustration of the measured admittance states, as viewed on a Smith Chart. Arrows represent the distance from each state, Y_s , to Y_{opt} , corresponding to term $|Y_s - Y_{opt}|$ in Equation (4.1).

$$[A] = ([\Psi]^T [W] [\Psi])^{-1} [\Psi]^T [W] [T] . \quad (4.10)$$

Finally, $[A] \rightarrow [T_{min}, R_n, Y_{opt}]$ through the use of Equations (4.3)-(4.6). This process must be repeated for each frequency that the noise parameters are to be determined. Although initially a time intensive process, this routine was soon automated [41], and now several excellent automated noise parameter test sets are available from companies such as Maury Microwave.³

4.1.2 Selection of Source Impedance States and Their Number

The question naturally arises, how many source impedance (admittance) states should be measured and at what value? Unfortunately, no rigorous quantitative solution exists to this problem, due to the number of factors involved. Several observations may be made however. To do so, we will use the expression for T_n , introduced in chapter 3, repeated here for convenience,

$$T_n = T_{min} + 4NT_0 \frac{|\Gamma_s - \Gamma_{opt}|^2}{(1 - |\Gamma_s|^2)(1 - |\Gamma_{opt}|^2)} . \quad (4.11)$$

Caruso [44] demonstrated that equation (4.11) can be linearized, similar to equation (4.1), using the following expansion,

$$T_n = a + b \frac{1}{1 - |\Gamma_s|^2} + c \frac{|\Gamma_s| \cos(\angle \Gamma_s)}{1 - |\Gamma_s|^2} + d \frac{|\Gamma_s| \sin(\angle \Gamma_s)}{1 - |\Gamma_s|^2} , \quad (4.12)$$

where

$$T_{min} = a + \frac{b + \Delta}{2} , \quad (4.13)$$

$$N = \Delta 4T_0 , \quad (4.14)$$

$$|\Gamma_s| = \sqrt{\frac{b - \Delta}{b + \Delta}} , \quad (4.15)$$

$$\angle \Gamma_s = \arctan 2\left(\frac{d}{c}\right) . \quad (4.16)$$

The corresponding measurements, at multiple values of Γ_s , may be expressed in matrix form as

$$\begin{bmatrix} T_{meas_1} \\ T_{meas_2} \\ \vdots \\ T_{meas_n} \end{bmatrix} = \begin{bmatrix} 1 & \frac{1}{1 - |\Gamma_{s_1}|^2} & \frac{|\Gamma_{s_1}| \cos(\angle \Gamma_{s_1})}{1 - |\Gamma_{s_1}|^2} & \frac{|\Gamma_{s_1}| \sin(\angle \Gamma_{s_1})}{1 - |\Gamma_{s_1}|^2} \\ 1 & \frac{1}{1 - |\Gamma_{s_2}|^2} & \frac{|\Gamma_{s_2}| \cos(\angle \Gamma_{s_2})}{1 - |\Gamma_{s_2}|^2} & \frac{|\Gamma_{s_2}| \sin(\angle \Gamma_{s_2})}{1 - |\Gamma_{s_2}|^2} \\ \vdots & \vdots & \vdots & \vdots \\ 1 & \frac{1}{1 - |\Gamma_{s_n}|^2} & \frac{|\Gamma_{s_n}| \cos(\angle \Gamma_{s_n})}{1 - |\Gamma_{s_n}|^2} & \frac{|\Gamma_{s_n}| \sin(\angle \Gamma_{s_n})}{1 - |\Gamma_{s_n}|^2} \end{bmatrix} \begin{bmatrix} a \\ b \\ c \\ d \end{bmatrix} , \quad (4.17)$$

³Maury Microwave, 2900 Inland Empire Blvd., Ontario CA, 91764 U.S.A.

or

$$[T] = [X] \cdot [a] . \quad (4.18)$$

Caruso pointed out that the values of Γ_s selected for measurement should obey the following conditions:

1. They should avoid being of equal magnitude \rightarrow circle on the Smith Chart.
2. They should avoid being of equal phase \rightarrow a straight line on the Smith Chart.
3. They should enclose Z_{opt} .

Condition 1 above leads to each element of column 2 of $[X]$ being identical. Columns 1 and 2 are therefore related by a constant factor, making determination of $[a]$ impossible. Similarly, condition 2 makes columns 3 and 4 of $[X]$ related by constant factor, $\cot(\angle\Gamma_s)$, again preventing a solution. Although condition 3 is not strictly necessary for solution of (4.9) or (4.10), it becomes increasingly important as random errors within the measurement increase.

4.1.3 Wide Band Frequency Variation Method

Unfortunately, variable impedance noise sources relying on mechanical or electromechanical tuning of the impedance are not well suited for the measurement of cryogenic noise parameters, for the following reasons:

- They cannot be cryogenically cooled due to the tight tolerances and materials involved in their design.
- Locating the variable impedance unit outside of the cryostat degrades the accuracy of the measurement for two reasons: the uncertainty associated with loss and physical temperature of the transmission line between the tuner (warm) and DUT (cold); and the attenuation of this transmission line decreases the spread in the constellation of admittances (refer to figure (4.1), collapsing them inward toward Y_0).

Robert Hu [43] demonstrated a novel method for noise parameter measurement, where the tuner in figure 4.1 is replaced by a mismatch at the end of a transmission line. The transmission line and mismatch automatically sweep out a constellation of impedances with frequency. Its simplicity and absence of moving parts makes it ideally suited for application to cryogenic measurements. The method relies on the noise parameters being locally constant over the frequency interval $\nu/2l$, where ν is the speed of propagation within the transmission line, and l is its physical length. The measurement of such a network at many points over a frequency sampling window of width $\nu/2l$, together

with a separate matched noise measurement ($\Gamma_s = 0$), result in $[X]$ being overdetermined, and a solution of (4.18) possible. The measurement is illustrated graphically in figure 4.2. One drawback with the mismatch network used in this example is that it does not satisfy condition 1 presented in Section 4.1.2 and therefore requires the separate matched load measurement. This necessitates two cool downs for cryogenic measurements,⁴ adding to measurement time. The system of equations for the different mismatched and matched measurements is given by equation (4.19) using expressions (4.12)-(4.16). Each measurement point corresponds to a different frequency within the sampling window. $T_{mis,x}$ represent the mismatch network measurements and $T_{50,y}$ the corresponding matched measurements.

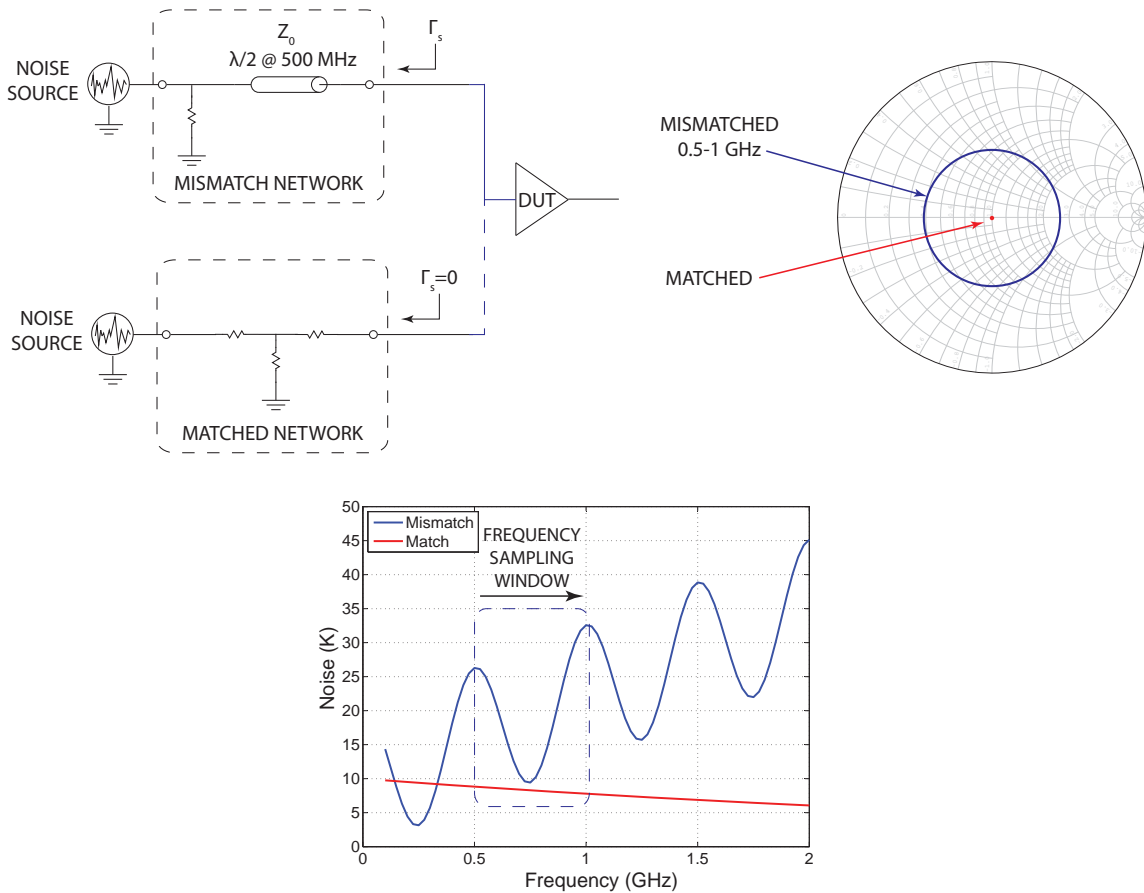


Figure 4.2: In the WBFV the measurement of multiple tuner settings (ref figure 4.1) is replaced by the measurement of two networks: a mismatch at the end of a length of transmission line; and a matched network. The frequency sampling window, 500 MHz wide in this example, is moved across the data, populating the T and X matrices in (4.19). The noise parameters are calculated at the center of the window, 750 MHz for the case shown. The matched measurement is required in the example above because the mismatch network itself does not encode enough information into $[\chi]$.

⁴Alternatively, a switch could be used to select mismatch or matched measurements. The repeatability of a mechanical switch or the loss and noise sources within a solid-state switch must then be addressed.

$$\begin{bmatrix} T_{mis_1} \\ T_{mis_2} \\ \vdots \\ T_{mis_n} \\ T_{50_1} \\ T_{50_2} \\ \vdots \\ T_{50_n} \end{bmatrix} = \begin{bmatrix} 1 & \frac{1}{1-|\Gamma_{s_1}|^2} & \frac{|\Gamma_{s_1}| \cos(\angle \Gamma_{s_1})}{1-|\Gamma_{s_1}|^2} & \frac{|\Gamma_{s_1}| \sin(\angle \Gamma_{s_1})}{1-|\Gamma_{s_1}|^2} \\ 1 & \frac{1}{1-|\Gamma_{s_2}|^2} & \frac{|\Gamma_{s_2}| \cos(\angle \Gamma_{s_2})}{1-|\Gamma_{s_2}|^2} & \frac{|\Gamma_{s_2}| \sin(\angle \Gamma_{s_2})}{1-|\Gamma_{s_2}|^2} \\ \vdots & \vdots & \vdots & \vdots \\ 1 & \frac{1}{1-|\Gamma_{s_n}|^2} & \frac{|\Gamma_{s_n}| \cos(\angle \Gamma_{s_n})}{1-|\Gamma_{s_n}|^2} & \frac{|\Gamma_{s_n}| \sin(\angle \Gamma_{s_n})}{1-|\Gamma_{s_n}|^2} \\ 1 & 1 & 0 & 0 \\ 1 & 1 & 0 & 0 \\ \vdots & \vdots & \vdots & \vdots \\ 1 & 1 & 0 & 0 \end{bmatrix} \begin{bmatrix} a \\ b \\ c \\ d \end{bmatrix} \quad (4.19)$$

4.2 Variable Impedance, Self-Calibrating, Noise Sources

As alluded to earlier, the mismatch circuit in Section 4.1.3 does not encode enough information into $[X]$, making measurement of the network alone insufficient for noise parameter determination. Fortunately, a simple modification to the mismatch network may be made that does allow for determination of noise parameters through measurement of a single network. This is accomplished by placing a second open or short-circuited transmission line,⁵ of length $2l$ at the end of the original line, length l . This is illustrated schematically in figure 4.3 along with the impedances swept out in a frequency interval $\nu/2l$, compared against the previous single line network.

4.2.1 Cryogenic Module

The modified network, together with an internal noise source, bias-tee, heater, and temperature sensor were integrated into a single module, the simplified schematic for which is shown in figure 4.4. The noise source is comprised of a MP3X8260 noise diode from M-Pulse Microwave⁶ yielding ~ 25 dB excess noise ratio (ENR)⁷ at 295K, when biased at 10 mA. It is followed by a 20 dB fixed attenuator, p/n ATN3580-20 from Skyworks.⁸ The attenuator is necessary since the diode impedance changes drastically between off (unbiased) and on (~ 10 mA) conditions, which would lead to a large systematic error being introduced in the calibration of, and measurements made with, the module. These systematic errors are covered in more detail in sections 4.4 and 4.6. The bias-tee is comprised of two 20 $\text{k}\Omega$, 0201 size resistors in shunt with the main transmission line. One of these resistors is used for the bias, the other to sense the resulting voltage, thus removing knowledge of the resistors value from determination of the sourced voltage. AC coupling between noise diode, attenuator, and

⁵An open circuited line was selected for the network to be described, as it simplifies integration of a bias-tee with the network.

⁶M-Pulse Microwave, 576 Charcot Ave., San Jose CA, 95131 U.S.A.

⁷ $ENR = 10\log_{10}(T_{excess}/290)$, where T_{excess} is the difference between the available noise temperature and the physical temperature.

⁸Skyworks Solutions, Inc., 20 Sylvan Rd., Woburn MA, 01801 U.S.A.

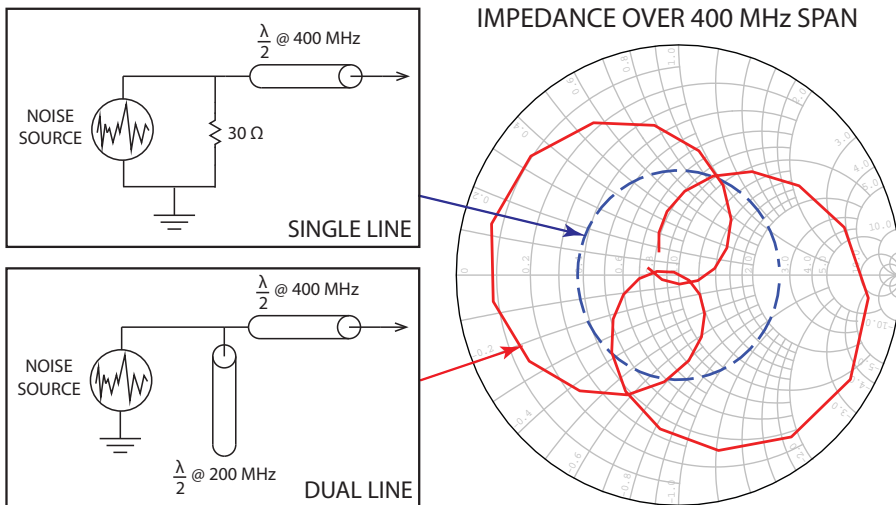


Figure 4.3: Single vs. two-line network demonstration. The single line mismatch varies only the phase over a frequency sampling window, while the two-line network varies both phase and magnitude. This is essential for determination of noise parameters from measurement of the network alone.

bias-tee is accomplished through 47 pF metal-insulator-semiconductor (MIS) capacitors, also from Skyworks.

The $\lambda/2$ lines are realized using 50Ω copper clad, coaxial cable, p/n UT-85 from Micro-Coax.⁹ These lines are approximately 45.7 and 22.9 cm long, designed for a frequency sampling window¹⁰ of 400 MHz. The ends of the lines are soldered to a 0.5 mm thick printed circuit board (PCB) made from Rogers¹¹ RO4350 dielectric ($\epsilon_r = 3.48$). The junction between the PCB and coaxial lines was designed with Ansoft's HFSS electromagnetic simulator to yield a reflection coefficient of less than -20 dB through 12 GHz. This helps ensure that the impedance response of the module is dominated by the interaction of the $\lambda/2$ lines, and not from parasitic reflections.

All circuitry is enclosed in an isothermal module measuring 5 x 6.35 x 3.5 cm, shown in figure 4.5. To allow for self-calibration, a 50Ω , 50 W heater and silicon diode temperature sensor (p/n's HTR-50 and DTR-470-CU-13-1.4L respectively) from Lakeshore Cryotronics are integrated within the module. The temperature sensor is calibrated by Lakeshore Cryotronics and has a stated accuracy of ± 12 mK. This is necessary to reduce error in the determination of the modules excess noise temperature, as will be discussed in sections 4.4 and 4.6. To ensure that the physical temperature of the internal components match the measured temperature, care was taken in the placement and

⁹Micro-Coax, 206 Jones Blvd., Pottstown PA, 19464 U.S.A.

¹⁰One complete revolution of the Smith Chart.

¹¹Rogers, Advanced Circuit Materials Division, 100 S. Roosevelt Ave., Chandler AZ, 85226 U.S.A.

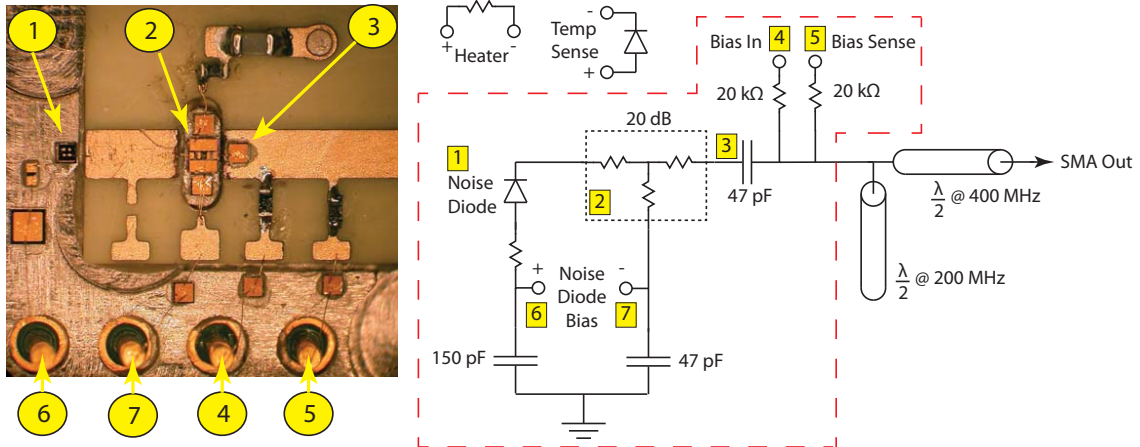


Figure 4.4: (Left) Photograph of noise diode, attenuator, and bias-tee portion of variable impedance, cryogenic noise source, indicated in schematic on right by dashed red box. (Right) Simplified schematic. $\lambda/2$ lines are 50 Ω , copper clad, coaxial lines, p/n UT-85 from Micro-Coax. Temperature sensor and heater allow for self-calibration of the module's excess noise temperature.

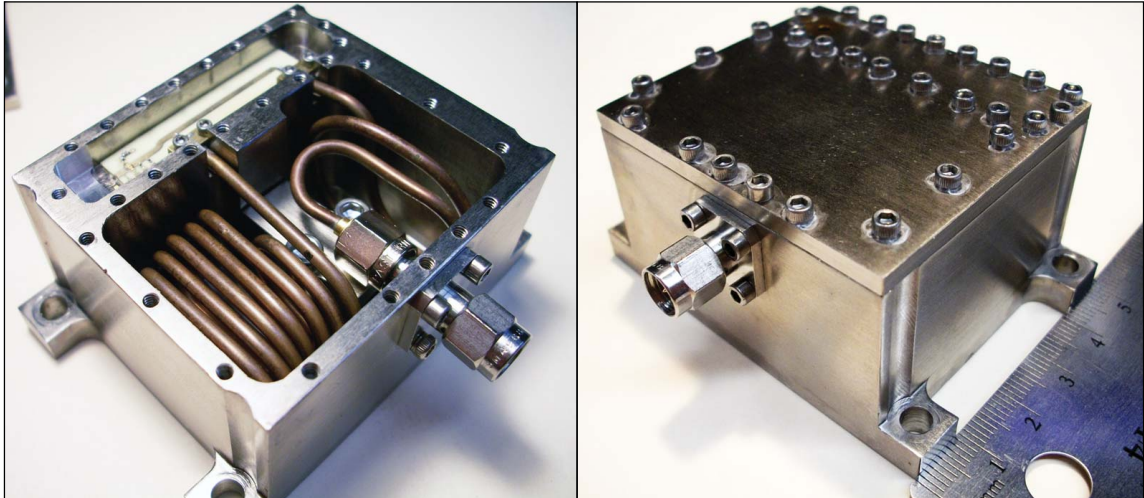


Figure 4.5: Photographs of the cryogenic, variable impedance, self calibrating noise source, herein referred to as the long line module (LLM). (Left) Photograph with top cover removed, revealing the $\lambda/2$ coaxial lines, 180° at 200 MHz (front pocket) and 400 MHz (back pocket). The cavity containing the noise diode, attenuator, and bias-tee is in the upper left corner. (Right) Exterior of the LLM. The module dimension's are 5 \times 6.35 \times 3.5 cm. Output connector is SMA male. Bias, heater, and temperature sensor signals are routed through a 15-pin μ D connector at the back of the module (not shown).

mounting of the components. The attenuator is mounted on a pedestal machined into the housing, protruding through an aperture in the PCB. In addition, the heater is located low in the module, close to the baseplate, to ensure that no temperature gradient exists in the area where the internal circuitry is located. The completed module is shown in figure 4.5 and is herein referred to as the long line module (LLM).

4.2.2 Ambient/Cryogenic Module

The only limitation with the use of the previous module at higher temperatures is in its calibration. As will be discussed in the following sections, the calibration process requires a sizable difference in the measurement of Y-factor for “cold” and “hot” measurement states to reduce the effects of measurement uncertainty. This is relatively easy to achieve at cryogenic temperatures but difficult at ambient temperature. As will become clear later, a more reasonable approach is to calibrate the internal noise source separately, without the effect of the mismatch network, using the methods detailed in section 4.3. The determination of the excess noise temperature for the entire module requires measurement of the mismatch networks S-parameters and subsequent calculation of its available gain. Multiplying the internal noise source’s excess noise temperature by the available gain of the mismatch network provides the excess noise temperature at the module’s output.¹²

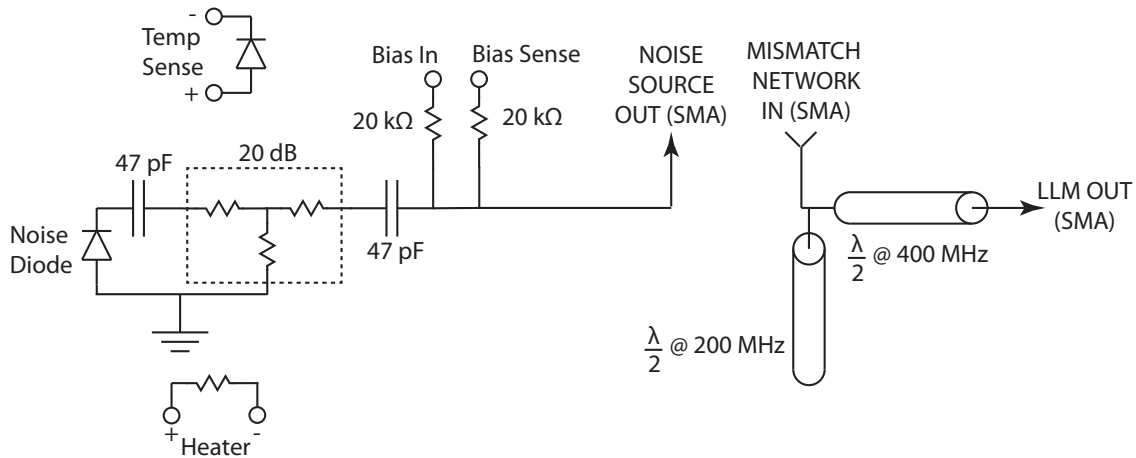


Figure 4.6: Modification of LLM for use at room temperature. Two additional SMA connectors, *Noise Source Out* and *Mismatch Network In* have been added to the cryogenic module to allow for separate calibration of the internal noise source and mismatch network.

The module described above is shown in figure 4.7. Two additional SMA connectors were added to the cryogenic module, at the output of the noise source and input of the mismatch network, to allow for separate calibration of these respective elements. The housing material was changed

¹²The underlying assumption is that the internal noise source and mismatch network are at the same physical temperature.

from aluminum to OFHC to ensure that the assembly would be isothermal, as calibrations would be performed at ambient temperature and pressure, and convection would therefore play a role. Gold plating was utilized, in place of the nickel plating of the cryogenic module, to minimize RF losses. Aside from these changes, the module is largely identical to the cryogenic module described earlier. Although calibration and noise measurement results are presented for this module at room temperature only, nothing precludes its use cryogenically.

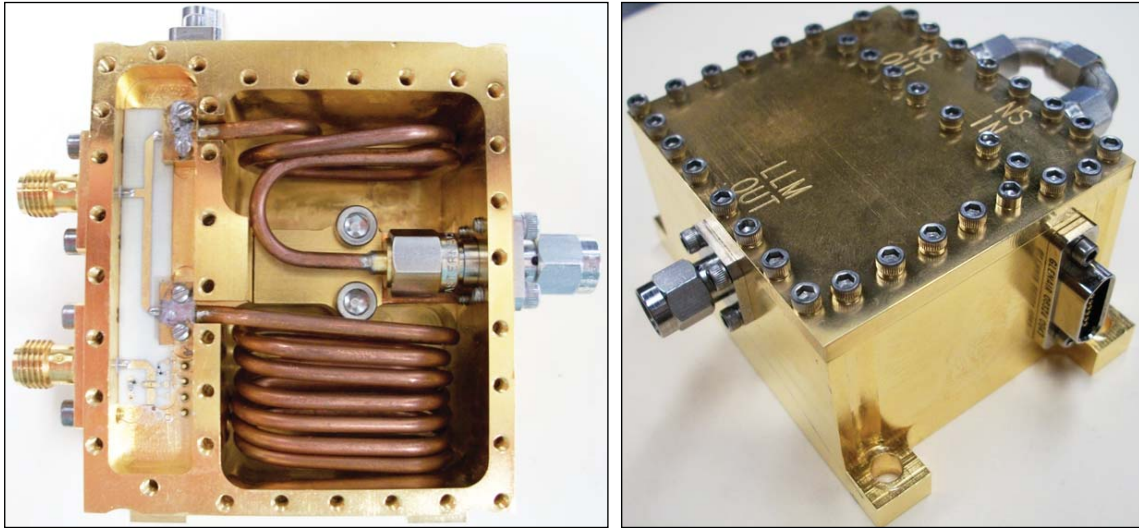


Figure 4.7: Completed LLM for use at ambient and cryogenic temperatures. (*Left*) Top-down view of LLM with cover removed. The internal noise source is at the bottom left of the photo and is identical to that shown in figure 4.4. Connectors are provided for the noise source output and mismatch network input, shown at the left of the photo. After calibration these ports are connected to one another with a pair of 90° SMA adapters. (*Right*) Photograph of completed module. 15-pin μ D connector on side of module routes DC bias, temperature sensor, and heater control lines.

4.3 Principles of Calibration

Noise source calibration is traditionally measured in two ways; by comparison to measurements made with terminations held at different physical temperatures, or by comparison against a noise source calibrated with the former method. For the measurement of extremely low noise devices, it is beneficial to calibrate the noise source directly, removing the uncertainty involved when transferring the calibration from one noise source to another. To do so, the calibration scheme presented here uses Nyquist's theorem [30], which states that the available noise power P_{av} from a passive network is equal to $kT_{phy}\Delta f$, for $hf/kT_{phy} \ll 1$, where k is Boltzmann's constant, h is Planck's constant, and T_{phy} is the physical temperature of the network.

By changing the physical temperature of the LLM (internal noise diode off), the resulting change

in noise power can be used to determine the noise of the receiver, T_{rx} , used in the module's calibration. Once T_{rx} is determined, the excess noise of the internal noise diode, referred to the module output terminals, can be measured by turning the internal noise diode on and off. The entire calibration sequence can be performed without disconnecting the LLM from the receiver.

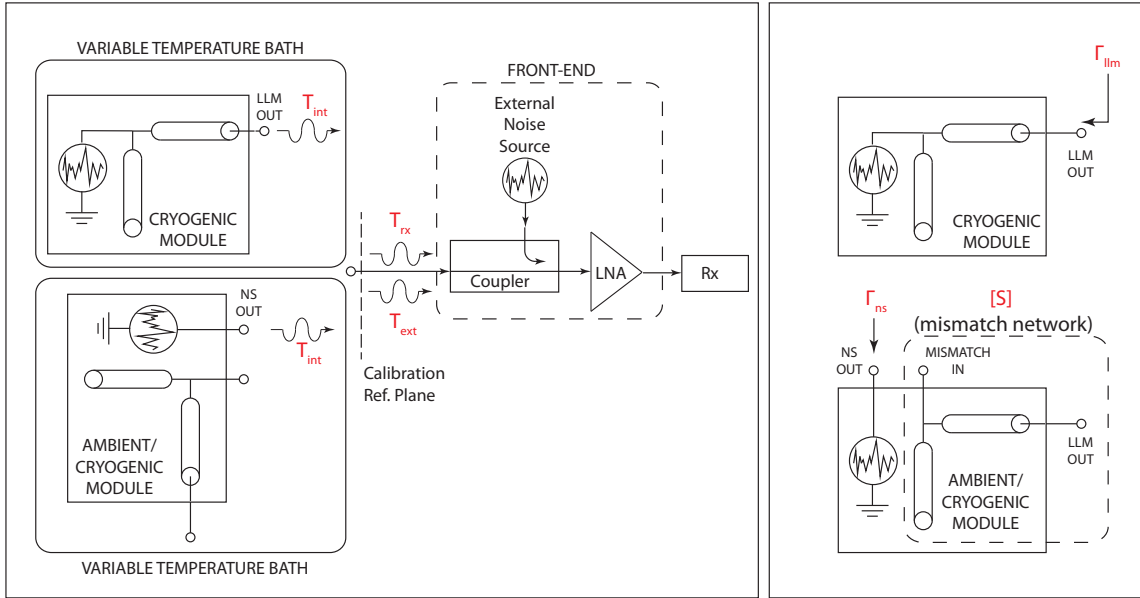


Figure 4.8: (Left) Test setup and definition of calibration quantities for the thermal calibration of the LLM. For the cryogenic module T_{int} is defined at the output of the LLM and for the ambient/cryogenic module it is defined at the output of its internal noise source (through a separate connector). In both cases, T_{int} is the excess noise equal to the difference between the noise source “on” and “off” states. T_{rx} and T_{ext} are used in the determination of T_{int} . (Right) Definition of calibration quantities measured by a VNA. For the cryogenic module only Γ_{llm} is measured, while for the ambient/cryogenic module both Γ_{ns} and the S-parameters of the mismatch network are measured.

This method requires that T_{rx} be constant during the calibration procedure. Unfortunately heating and cooling of the module is slow, and the gain of the receiver will fluctuate during this time. To remove the error introduced by gain fluctuations, the signal from an external noise source is injected with a coupler, placed in front of the receiver's LNA. This allows the cold and hot measurements of the receiver's calibration to be made as ratios (Y-factors), of the external noise source on and off, in each temperature state. These Y-factors are independent of receiver gain and are thus more stable than receiver output powers. This test setup is illustrated on the left of figure 4.8. The coupler, LNA, and external noise source are referred to as the “frontend.” The receiver used in all measurements is an Agilent N8975A Noise Figure Analyzer (NFA), which pulses the external noise source on and off to directly output Y-factor.

Following measurements of the LLM at cold and hot physical temperatures (internal noise source off), the module's heater is turned off and the module allowed to stabilize at its cold temperature

state. A Y-factor measurement is then made while switching the internal noise source on and off, with the external noise source off. This allows for determination of the excess noise temperature of the internal noise source, T_{int} . As shown in figure 4.8, T_{int} is defined at the output of the LLM for the cryogenic module and at the output of the noise source for the ambient/cryogenic module. The measured Y-factors for each of the three calibration states are given in relations (4.20) below, in terms of the calibration terms defined in table 4.1.

$$\begin{aligned} Y_c &= \frac{T_{cold} + T_{ext} + T_{rx}}{T_{cold} + T_{rx}} \\ Y_h &= \frac{T_{hot} + T_{ext} + T_{rx}}{T_{hot} + T_{rx}} \\ Y_{ns} &= \frac{T_{int} + T_{ns} + T_{rx}}{T_{ns} + T_{rx}} \end{aligned} \quad (4.20)$$

Table 4.1: Calibration noise terms.

| Term | Definition |
|-----------|---|
| Y_c | Y-factor with LLM cold, external noise source firing ¹³ |
| Y_h | Y-factor with LLM hot, external noise source firing ¹³ |
| Y_{ns} | Y-factor with LLM cold, internal noise source firing ¹³ |
| T_c | Physical temperature of LLM cold |
| T_h | Physical temperature of LLM hot |
| T_{ns} | Physical temperature of LLM when firing internal noise source ¹⁴ |
| T_{int} | Excess noise temperature of LLM ¹⁵ |
| T_{ext} | Noise temperature of external noise source ¹⁵ |
| T_{rx} | Noise temperature of frontend+receiver ¹⁵ |

Since there are only three unknowns, T_{int} may be determined.

$$T_{int} = (Y_{ns} - 1)(T_{ns} + T_{rx}) , \quad (4.21)$$

where

$$T_{rx} = \frac{(Y_h - 1)(T_{hot}) - (Y_c - 1)(T_{cold})}{Y_c - Y_h} . \quad (4.22)$$

Since the available noise temperature from the LLM, with internal noise diode off, is equal to its physical temperature, accurate knowledge of the module's temperature is necessary. The systematic and random components of this error are analyzed in Sections 4.4. To mitigate these, the modules internal temperature sensor is continuously logged during measurement of each of the calibration

¹³50% duty cycle.

¹⁴~0.8 K and 0.2 K higher than T_c at cryogenic and ambient temperatures respectively, due to the added 50 mW heat load present when the internal noise diode is fired at 50% duty cycle.

¹⁵Referenced to the output of the LLM for the cryogenic module, and to the output of the internal noise source for the ambient/cryogenic module.

states, to track any temperature fluctuations.

Following determination of T_{int} , separate measurements are performed with a VNA, as defined on the right of figure 4.8. For the cryogenic module, the reflection coefficient of the output of the LLM, Γ_{llm} , is measured. This measurement, along with T_{int} determined from the thermal calibration, are written to a calibration file for the module. For the ambient/cryogenic module, the reflection coefficient of the internal noise source, Γ_{ns} , and the S-parameters of the mismatch network are measured. The excess noise temperature at the output of the ambient/cryogenic module is then calculated,

$$T'_{int} = T_{int}G_{av} , \quad (4.23)$$

where

$$\begin{aligned} G_{av} &= \frac{1 - |\Gamma_{ns}|^2}{|1 - S_{11}\Gamma_{ns}|^2} |S_{21}|^2 \frac{1}{1 - |\Gamma_{llm}|^2} , \text{ and} \\ \Gamma_{llm} &= S_{22} + \frac{S_{21}S_{12}\Gamma_{ns}}{1 - S_{11}\Gamma_{ns}} . \end{aligned} \quad (4.24)$$

Both T'_{int} and Γ_{llm} are written to a calibration file for this module as well. It should be noted that both the measurement of Γ_{llm} for the cryogenic module and Γ_{ns} for the ambient/cryogenic module are done with the internal noise source in its off (unbiased) state. The error caused by the finite difference between Γ_{ns} in on and off states will be analyzed in Sections 4.4.2 and 4.6.2.

4.4 Calibration Uncertainty

Measurement uncertainty is due to a combination of random and systematic errors. *Random* errors appear as fluctuations in a measurement, regardless of how well the particular experiment is controlled. If the physical mechanisms for these errors arise from wide-sense stationary processes, then the uncertainty (error) in a measurement may be improved by increasing the number of samples. The random errors addressed in this work are the result of electrical noise. *Systematic* errors arise from biases in the measurement, the resulting uncertainty *cannot* be improved with increasing the number of measurements. Such errors may be due to drifts within instruments, unwanted reflections, offsets within sensors, etc. In most cases the effects of systematic errors may be removed from a measurement.

In this section the random and systematic errors associated with the calibration of the LLM are discussed and their effect on the uncertainty in the excess noise temperature, T_{int} . Only those errors

that are fundamental to the calibration method will be discussed. Errors inherent to the specific piece of test equipment used, such as dynamic range errors from the receiver, will not be assessed. Although T'_{int} for the ambient/cryogenic module is determined from the thermal calibration and from VNA measurements, only those errors associated with the thermal calibration will be analyzed.¹⁶ The resulting errors in T_{int} , $\Delta T_{int,ran}$ and $\Delta T_{int,sys}$, will be evaluated for the cryogenic and ambient calibrations presented in Sections 4.7.1 and 4.8.1.

4.4.1 Random Errors

This first order analysis will consider the following quantities as sources of random error in the calibration of the LLM:

1. Y-factor measurements Y_{ns} , Y_c , and Y_h .
2. Temperature measurements T_{ns} , T_c , and T_h .

For the Y-factor measurements, it will be assumed that measurement uncertainty is limited by the noise from the LLM and that of the frontend/receiver combination (refer to figure 4.8). The uncertainty in a single measurement of T_{on} or T_{off} ($Y = T_{on}/T_{off}$) is given by [45]

$$\Delta T_{on,off} = \frac{T_{on,off}}{\sqrt{\Delta f \tau}} , \quad (4.25)$$

where T_{on} and T_{off} are the noise temperatures with the internal (Y_{ns} measurement) or external noise source (Y_c and Y_h measurements) in its on and off states, Δf is the resolution bandwidth of the receiver, a N8975A NFA from Agilent, set to 4 MHz for all measurements reported here, τ is the integration time for a single measurement of T_{on} or T_{off} , and is fixed at 16 mS within the NFA.

Assuming that errors within the measurements Y_{on} and Y_{off} are uncorrelated, their corresponding uncertainties may be root-sum-squared [46], where it is assumed there are N averages of a Y-factor measurement at a given frequency.

$$\begin{aligned} \Delta Y &= \sqrt{\left[\frac{\Delta T_{on}}{\sqrt{N}}\right]^2 \cdot \left[\frac{\partial Y}{\partial T_{on}}\right]^2 + \left[\frac{\Delta T_{off}}{\sqrt{N}}\right]^2 \cdot \left[\frac{\partial Y}{\partial T_{off}}\right]^2} \\ &= \sqrt{\frac{2}{\Delta f \tau N}} Y \end{aligned} \quad (4.26)$$

Random errors within the temperature sensor measurements are the result of electrical noise from the temperature sensor and its readout electronics. For the Lakeshore Cryotronics silicon diode used

¹⁶It is assumed that the errors in the VNA measurements are small enough as to not significantly impact the overall uncertainty.

in the LLM, the uncertainty is ± 12 mK.¹⁷ The total temperature measurement uncertainty (sensor and readout electronics) is on the order of ± 50 mK.

The uncertainty in T_{int} is analyzed by first evaluating the sensitivity factors, from the appropriate partial derivatives of equations (4.21) and (4.22), thus determining how the various errors will propagate. Assuming all measurement errors are independent, the individual contributions may be combined root-sum-square. Following simplification, and assuming that the uncertainties of temperature measurements are all equal to ΔT_{phy} , the uncertainty in T_{int} due to random errors within the Y-factor and temperature measurements is given by

$$\Delta T_{int,ran} = \frac{Y_{ns} - 1}{(Y_c - Y_h)^2} \sqrt{\gamma_t^2 + \gamma_{ch}^2 + \gamma_{ns}^2} , \quad (4.27)$$

where

$$\begin{aligned} \gamma_t^2 &= \Delta T_{phy}^2 2 (Y_c - Y_h)^2 (Y_c^2 + Y_h^2 - Y_c Y_h - Y_c - Y_h + 1) , \\ \gamma_{ch}^2 &= (T_h - T_c)^2 \left(\Delta Y_c^2 [1 - Y_h]^2 + \Delta Y_h^2 [Y_c - 1]^2 \right) , \\ \gamma_{ns}^2 &= \Delta Y_{ns}^2 \left(\frac{T_{ns} + T_{rx}}{Y_{ns} - 1} \right)^2 (Y_c - Y_h)^4 . \end{aligned}$$

Note that the random error is inversely proportional to $\Delta Y_{ch}^2 = (Y_c - Y_h)^2$. This reveals why it is critical to maintain a sizable difference in Y-factor, between cold and hot calibration states, for low random error.

4.4.2 Systematic Errors

Systematic errors associated with calibration of the LLM include

1. Changes in the reflection coefficient of the LLM, Γ_{llm} , leading to two errors:
 - (a) Modulation of T_{rx} , per equation (4.11). Heating of the module produces a change in Γ_{llm} (Γ_{ns} for the ambient/cryogenic module) and therefore an error introduced in the determination of T_{rx} .
 - (b) A change in system gain between T_{on} and T_{off} Y-factor measurement components. There is a small change in Γ_{llm} when the internal noise source of the module is switched between its off and on states, resulting in the additional error.

¹⁷Lakeshore states the uncertainty in their temperature sensors as a combination of sensor repeatability and accuracy, the latter of which is determined by how the sensor is calibrated. The repeatability of the sensor is defined here as the random component of the sensor uncertainty. The accuracy is defined as a systematic error and is discussed in the next section.

2. Knowledge of the module's physical temperature. Temperature sensor readings contain an offset that depends on how the sensor is calibrated and (for Lakeshore silicon diode sensors) the bias current at which they are operated at.
3. Temperature variations within the LLM. The calibration scheme presented here assumes that the module is isothermal. Finite thermal resistances within the LLM reduce this homogeneity through conduction, convection,¹⁸ and radiation.
4. Drifts in the noise temperature of the external noise source, usually associated with fluctuations in temperature.
5. Linearity of the frontend's LNA and that of the receiver.

The systematic errors analyzed here will only be associated with the first two cases. It is assumed that the other sources of error can be minimized through careful attention during construction of the test setup, and the selection and configuration of the measurement equipment. The systematic errors described in the next three sections are combined to yield the cumulative systematic error,

$$\Delta T_{int,sys} = \Delta T_{int,\Gamma_s,T_{rx}} + \Delta T_{int,\Gamma_s,G_t} + \Delta T_{int,temp} . \quad (4.28)$$

4.4.2.1 Errors Due to Changes in Reflection Coefficient Modulating Receiver Noise Temperature

For the cryogenic module, changes occur in Γ_{llm} between the different states of the calibration, for the ambient/cryogenic module these changes appear in Γ_{ns} . In this analysis, we will define the corresponding reflection coefficient for the different modules simply as Γ_s to simplify the derivations that follow. To analyze the effects of changes in Γ_s on T_{rx} , equation (4.11) is recast in terms of Z_s and Z_{opt} (of the frontend/receiver combination used in the calibration) through substitution of $Z_s = Z_0(1 + \Gamma_s)/(1 - \Gamma_s)$, yielding

$$T_n = T_{min} + \frac{NT_0}{Z_0} \frac{|Z_s - Z_{opt}|^2}{R_{opt}} . \quad (4.29)$$

Changes in T_n are due to changes in Z_s from heating and cooling of the module and switching between the on and off states of its internal noise source. These changes are determined through evaluation of equation (4.29) at each of these states. The corresponding relations are

¹⁸For room temperature measurements only. The vacuum level at which the cryogenic measurements are made is high enough that convection may be ignored.

$$\begin{aligned}\Delta T_{rx,HotCold} &= \frac{NT_0}{Z_0 R_{opt}} \left[|Z_{s,hot}|^2 - |Z_{s,cold}|^2 + 2(R_{opt}(R_{s,cold} - R_{s,hot}) + X_{opt}(X_{s,cold} - X_{s,hot})) \right], \\ \Delta T_{rx,OnOff} &= \frac{NT_0}{Z_0 R_{opt}} \left[|Z_{s,on}|^2 - |Z_{s,off}|^2 + 2(R_{opt}(R_{s,on} - R_{s,off}) + X_{opt}(X_{s,on} - X_{s,off})) \right].\end{aligned}$$

If $Z_{opt} \approx Z_0$, then the above relations may be simplified to

$$\Delta T_{rx,HotCold} \approx \frac{NT_0}{Z_0^2} \left[|Z_{s,hot}|^2 - |Z_{s,cold}|^2 + 2Z_0(R_{s,cold} - R_{s,hot}) \right], \quad (4.30)$$

$$\Delta T_{rx,OnOff} \approx \frac{NT_0}{Z_0^2} \left[|Z_{s,on}|^2 - |Z_{s,off}|^2 + 2Z_0(R_{s,on} - R_{s,off}) \right]. \quad (4.31)$$

These errors enter into the measurement of Y_h and Y_{ns} (ref. equation (4.20)) during calibration as follows

$$Y_h = \frac{T_{hot} + T_{ext} + T_{rx} + \Delta T_{rx,HotCold}}{T_{hot} + T_{rx}},$$

$$Y_{ns} = \frac{T_{int} + T_{ns} + T_{rx} + \Delta T_{rx,OnOff}}{T_{ns} + T_{rx}}.$$

The net effect is to put a systematic error in the determination of T_{int} amounting to

$$\Delta T_{int,\Gamma_s,T_{rx}} = \frac{(Y_{ns} - 1)(Y_h - 1)}{Y_c - Y_h} \Delta T_{rx,HotCold} - \Delta T_{rx,OnOff}. \quad (4.32)$$

This error could be removed if the noise parameters of the receiver were known. Section 4.8.1 estimates this, and other systematic errors, for the ambient module calibration, where the noise parameters of the frontend/receiver are measured and in turn used to estimate (4.32).

4.4.2.2 Errors Due to Changes in Reflection Coefficient Modulating System Gain

Another systematic error, introduced by the change in reflection coefficient of the LLM, manifests itself in a mismatch in system gains during T_{on} and T_{off} measurements of Y_{ns} . equation 4.20 assumes that these gains are equal, and therefore cancel out. In reality, the finite change of the reflection coefficient between on/off states requires an additional correction term to be added to Y_{ns} as follows:

$$Y'_{ns} = Y_{ns} \frac{G_{t,on}}{G_{t,off}}. \quad (4.33)$$

Where $G_{t, on}$ and $G_{t, off}$ are the transducer power gains¹⁹ for the on and off states respectively. If the input match of the frontend is low and its reverse isolation high, then equation (4.33) may be approximated by

$$Y'_{ns} \approx Y_{ns} \frac{1 - |\Gamma_{s, on}|^2}{1 - |\Gamma_{s, off}|^2} .$$

This translates to an error in T_{int} equal to

$$\Delta T_{int, \Gamma_s, G_t} = Y_{ns} \left(\frac{|\Gamma_{s, off}|^2 - |\Gamma_{s, on}|^2}{1 - |\Gamma_{s, on}|^2} \right) (T_{rx} + T_{ns}) . \quad (4.34)$$

Although there is a similar error produced by the external noise source switching between on and off states, this error is usually much smaller due to the presence of the coupler and attenuation added between the noise source and coupled arm. It is therefore ignored in this analysis.

4.4.2.3 Errors Due to Temperature Sensor Accuracy

As stated earlier, temperature readings contain a systematic error in addition to their random component. This temperature offset could arise from thermal resistance in the mounting of the sensor, the sensor bias,²⁰ and the way the sensor is calibrated. The net effect of the uncertainty on T_{int} is

$$\Delta T_{int, temp} = \frac{(Y_h - 1) \Delta T_{hot} - (Y_c - 1) \Delta T_{cold}}{Y_c - Y_h} + \Delta T_{ns} . \quad (4.35)$$

It should be noted that if the temperature measurements are related to their true values by a constant offset ($\Delta T_{temp} = \Delta T_{hot} = \Delta T_{cold} = \Delta T_{ns}$) then $\Delta T_{int, temp} = 0$.

4.5 Noise Parameter Measurement

Once the LLM has been calibrated, it can be used to measure the noise of a DUT with the LLM at its input. While the thermal calibration is slow, due to the heating, cooling, and associated number of averages used during calibration,²¹ the measurement proceeds quickly as the internal noise source is used for Y-factor measurements. The noise temperature is determined from the measured Y-factor by:

¹⁹Defined as the ratio of delivered power to available power.

²⁰For Lakeshore silicon diodes this is with a 10 μ A current source.

²¹For the measurements presented in this chapter, 100 averages were used during cryogenic calibration and 999 averages (the limit of the NFA) during ambient calibration.

$$\begin{aligned}
T_{meas} &= \frac{T_{int} - (Y - 1) T_{llm}}{Y - 1} && \text{for cryogenic module measurements.} \\
T_{meas} &= \frac{T'_{int} - (Y - 1) T_{llm}}{Y - 1} && \text{for ambient/cryogenic module measurements.}
\end{aligned} \tag{4.36}$$

Where T_{llm} is the physical temperature of the respective module, which is continually logged during Y-factor measurement. The noise parameters are determined from these measurements, and knowledge of $T_{int}(T'_{int})$ and Γ_{llm} contained within the module's calibration file. This is done through "extraction," where the weighted least squares method presented in section 4.1.3 is utilized. Due to the impedance variation presented by the LLM, the matched (T_{50}) measurements are no longer necessary and are removed from the matrix formulation of equation (4.19). This work processes the calibration and measurement files through an extraction algorithm written in Matlab, based on a weighted least squares fit across a 400 MHz frequency-sampling window, moved across the data. The simplified algorithm for the extraction routine is shown in figure 4.9. To mitigate dynamic range errors (from the frontend and receiver) and systematic errors (imposed by the changes in Γ_{llm} in on and off states), a variable Y-factor threshold, Y_{thr} , is used. Y-factors less than this value are excluded from the calculation of noise parameters. Doing so also removes discontinuous points in the measured noise temperature from use in the extraction, which aides in the least squares fitting process. Y_{thr} is determined by varying its value during successive extractions to obtain the best possible fit between measured and calculated noise temperatures. This is done by minimizing the error between the measured noise temperature and that calculated using the extracted noise temperatures and equation (4.11), evaluated as a function of frequency and Γ_{llm} ,

$$\Delta T_{error} = T_{meas} - T_{n,calc} . \tag{4.37}$$

The use of Y_{thr} , combined with the removal of frequencies where radio frequency interference (RFI) is present, reduces the number of points within a frequency-sampling window by roughly 30% for the cryogenic measurements and 13% for the ambient measurements presented in this work.

Following extraction of the noise parameters, de-embedding is performed if necessary, to either remove reactive parasitics (such as bond wire inductance) or electrical length (such as for a device mounted within a 50 Ω fixture). Since T_{min} and N are invariant under lossless transformation, only Γ_{opt} requires adjustment. At this time Z_{opt} is determined from Γ_{opt} to provide additional physical insight into the extracted parameters.

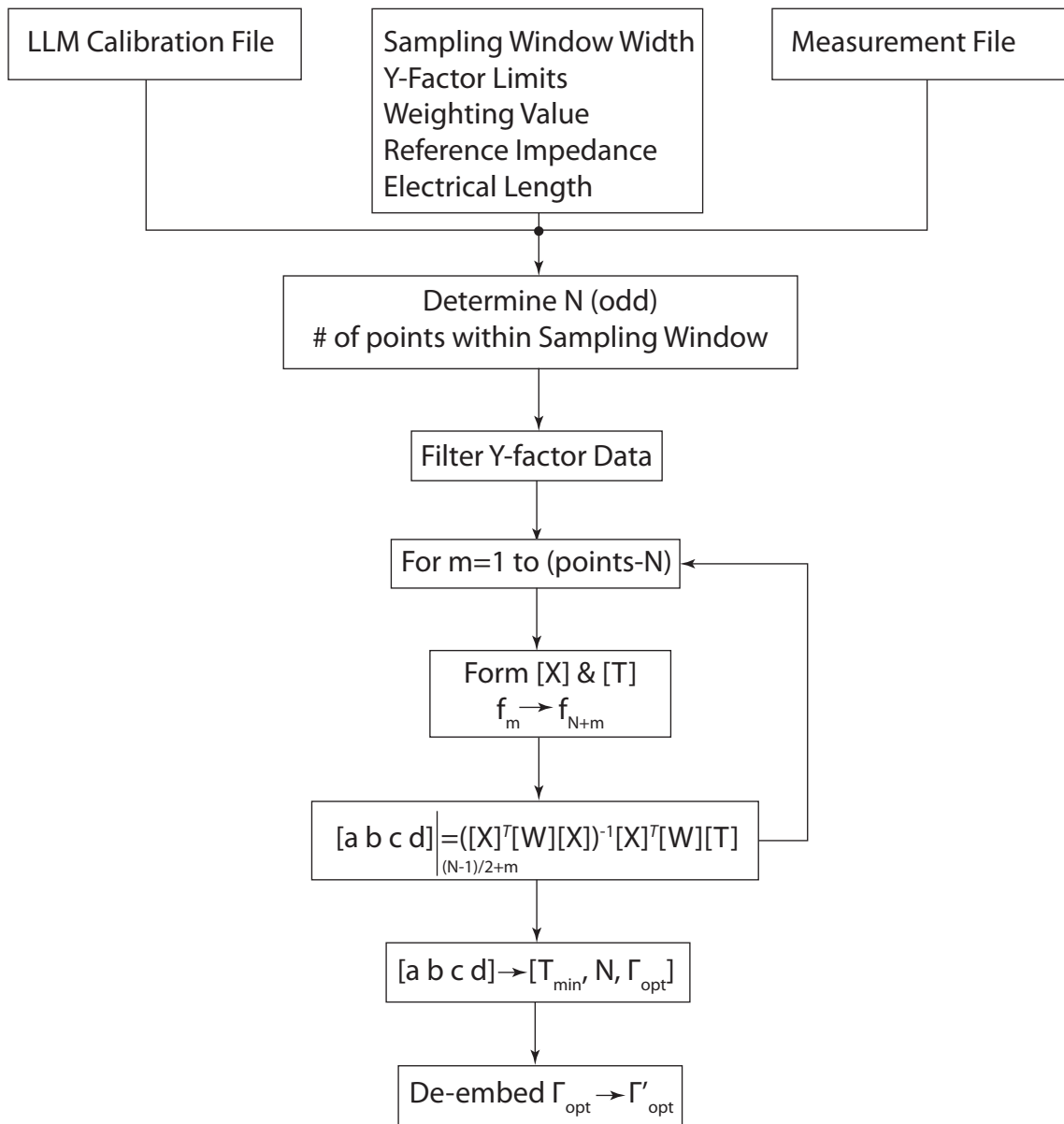


Figure 4.9: Noise parameter extraction algorithm.

4.6 Measurement Uncertainty

4.6.1 Random Errors

The procedure from Section 4.4.1 can be used to evaluate the random error associated with the measured noise temperature of a device, when driven by the LLM. The corresponding uncertainty in the measured noise temperature, $\Delta T_{meas,ran}$, is

$$\Delta T_{meas,ran} = \sqrt{\Delta T_{int}^2 \left(\frac{1}{Y_{dut}-1} \right)^2 + \Delta T_{phy}^2 + \Delta Y_{dut}^2 \left(\frac{T_{int}}{Y_{dut}-1} \right)^2}, \quad (4.38)$$

where T_{int} is replaced by T'_{int} if the ambient/cryogenic LLM is used. Note that the uncertainties due to ΔT_{int} and ΔY_{dut} are inversely proportional to $(Y_{dut}-1)$, one of the reasons to filter out extremely low Y-factors from the extraction.

4.6.2 Systematic Errors

The systematic measurement errors in the measurement are similar to those introduced in section 4.4.2. They are comprised of errors due to the change in reflection coefficient of the LLM, between on and off states, and from the error involved in the temperature measurement of the LLM. Reflection errors are again broken into two components: modulation of the noise temperature, now of the DUT; and changes to the system gain. The error corresponding to the modulation of the devices noise temperature is given in equation (4.39). Like the corresponding error in the calibration of the LLM, this error can be estimated, but not completely accounted for.

$$\begin{aligned} \Delta T_{meas,\Gamma_{llm},T_{dut}} = & \frac{1}{Y_{dut}-1} \frac{NT_0}{Z_0 R_{opt}} \left[|Z_{llm,on}|^2 - |Z_{llm,off}|^2 + \dots \right. \\ & \left. 2(R_{opt}(R_{llm,on} - R_{llm,off}) + X_{opt}(X_{llm,on} - X_{llm,off})) \right] \end{aligned} \quad (4.39)$$

The second error, caused by the change in system gain from Γ_{llm} changing between on and off states, is given by

$$\Delta T_{meas,\Gamma_{llm},G_t} = T_{int} \frac{1-M}{Y_{dut}^2 - Y_{dut}(1+M) + M}, \quad (4.40)$$

where M is the ratio of transducer gains between on and off states. Unlike the calibration, where S_{11} of the frontend is small through the proper selection of coupler and LNA, the same can not generally said about the DUT. If the reverse isolation of the device is sufficiently high, however, M can be approximated as

$$M \approx \frac{1 - |\Gamma_{llm, on}|^2}{|1 - S_{11}\Gamma_{llm, on}|^2} \frac{|1 - S_{11}\Gamma_{llm, off}|^2}{1 - |\Gamma_{llm, off}|^2}. \quad (4.41)$$

Systematic errors in the measurement of the LLM's physical temperature, $T_{llm, temp}$, during the measurement routine introduces an error equal to $\Delta T_{meas, temp} = -\Delta T_{llm}$. This is seen from evaluation of $\partial/\partial T_{llm}$ operating on equation (4.36). The total systematic error is a sum of the three errors above.

$$\Delta T_{meas, sys} = \Delta T_{meas, \Gamma_{llm, T_{dut}}} + \Delta T_{meas, \Gamma_{llm, G_t}} + \Delta T_{meas, temp}. \quad (4.42)$$

4.7 Cryogenic Noise Parameter Measurements

In this section, the calibration of and measurements made with the cryogenic LLM are presented, using the methods developed in Sections 4.3 and 4.5.

4.7.1 Module Calibration

The test setup used in the calibration of the cryogenic LLM is shown in figure 4.10. The LLM and frontend (excluding the external noise source) are mounted in a cryostat, cooled by a CTI-350 cold head from Brooks Automation.²² The cold plate attached to the second stage of the cold head, along with the brackets mounting the various components, are machined from OFHC to ensure that good thermal conductivity is achieved. Due to the mass of OFHC used in the test setup, temperature fluctuations are small and slowly changing. Because of this, the heater within the LLM was operated open-loop, the LLM's internal temperature sensor continually sampled to track any small, but finite, temperature changes. The various components comprising the test setup are listed in table 4.2.

The measurement is automated through a custom routine written in Matlab. Communications with the NFA are handled over GPIB, while control of the interface electronics box (IEB) is handled over USB. The block diagram and photos of the IEB are provided in figure 4.11. At its heart is a USB controlled, model U3 LabJack,²⁹ whose digital IO, ADCs, and DACs are used for noise source selection (internal or external), temperature monitoring, and temperature control respectively.

Preliminary cryogenic reflection coefficient measurements of the LLM reveal that it has sufficient variability to present the DUT with a wide spread of impedances to ~ 12 GHz. In addition, its

²²Brooks Automation Inc., 15 Elizabeth Drive, Chelmsford MA, 01824 U.S.A.

²³Krytar. 1288 Anvilwood Ave., Sunnyvale CA 94089 U.S.A.

²⁴Agilent Technologies, 5301 Stevens Creek Blvd., Santa Clara CA 95051 U.S.A.

²⁵California Institute of Technology, Pasadena CA 91125. Contact Steve Smith (steves@caltech.edu) for additional information.

²⁶Mini-Circuits, P.O. Box 350166, Brooklyn NY, 11235 U.S.A.

²⁷Keithly Instruments Inc., 28775 Aurora Rd., Cleveland OH, 44139 U.S.A.

²⁸SSI Cable Corp., 820 E. Hiawatha Blvd., Shelton WA, 98584 U.S.A.

²⁹LabJack Corp. 3232 S Vance St., Suite 100, Lakewood CO, 80227 U.S.A.

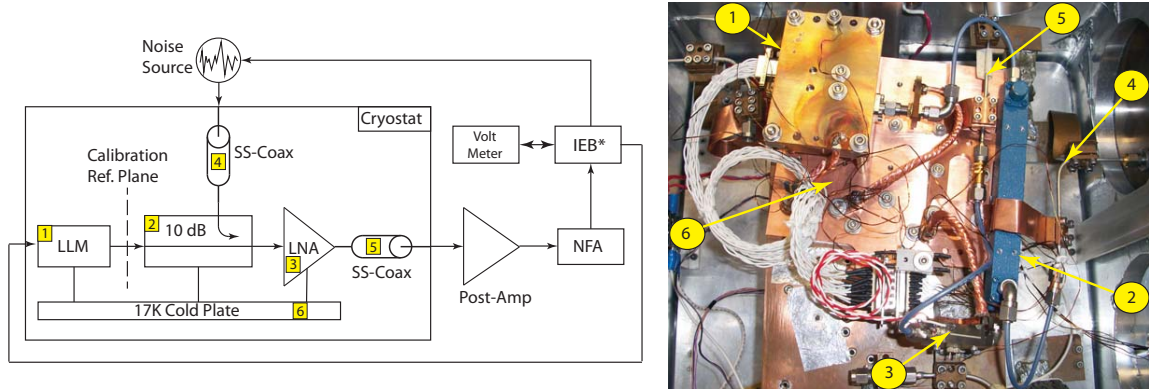


Figure 4.10: Test setup for the cryogenic calibration of the LLM. Components, listed in table 4.2 are mounted in a small cryostat cooled by a CTI-350 cold head. Thermal isolation of RF lines into and out of the cryostat is accomplished through the use of stainless steel coaxial lines, items 4 and 5. Both the interface electronics box (IEB) and NFA are computer controlled (not shown) through a custom routine written in Matlab.

Table 4.2: Components used within cryogenic calibration test setup.

| Component | Manufacturer | Description |
|-----------------------|-----------------------------|---|
| Coupler | Krytar ²³ | p/n 1831, 90° hybrid, 1–18 GHz |
| External Noise Source | Agilent ²⁴ | p/n 346C, 0.01–26.5 GHz, 15 dB (nominal) ENR |
| LNA | CIT ²⁵ | CITLF4, 0.5–4 GHz, <8K noise, 30dB gain |
| Post-amplifier | Mini-Circuits ²⁶ | ZVA-183, 0.7–18 GHz, 25 dB gain |
| NFA | Agilent | N8975A |
| IEB | Custom | Interface Electronics Box (IEB) described in text |
| Voltmeter | Keithley ²⁷ | Model 2001 |
| RF Thermal Breaks | SSI ²⁸ | Custom 15 cm coaxial cables, SMA connectors. |

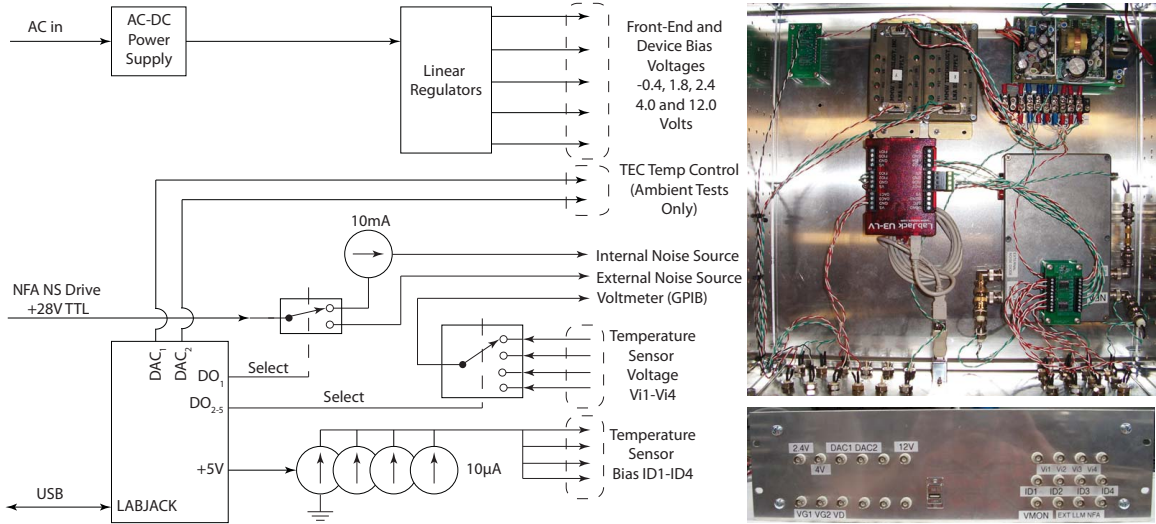


Figure 4.11: Interface electronics box (IEB) used for the calibration of and measurements made with the LLM. The box controls noise source selection (external or internal), temperature monitoring, temperature control, and device bias. (Right) Top down photo of IEB with cover removed. (Bottom right) Front panel of IEB.

internal noise source was designed to provide sufficient excess noise temperature beyond 12 GHz. Instead of calibrating over this entire range, calibration and measurements were done with an upper limit of 4 GHz, below which the noise parameters of devices to be measured were quickly changing. The LLM was thus calibrated from 0.750 to 4.0575 GHz, in 7.5 MHz steps. The presence of strong RFI in the lab below 900 MHz, combined with the low frequency limit of the coupler used, limited our ability to calibrate down to the LLM's theoretical limit of 400 MHz. All Y-factor measurements were performed with the NFA set for 100 averages and 4 MHz of resolution bandwidth.

The measurement of Γ_{llm} with a VNA requires an additional cryogenic cool down and is error prone, thus deserving special attention. This is due to the fact that the VNA calibration must be done at room temperature,³⁰ while the actual measurement of Γ_{llm} is made at cryogenic temperature. The cooling of the coaxial cable between the LLM and the interior wall of the cryostat leads to two errors:

1. Decrease in physical loss of the cable materials. Metal loss is the dominant factor and roughly proportional with temperature. This leads to an amplitude error in the measurement of Γ_{llm} , as the path loss of the cooled section of coaxial cable decreases with cooling.
2. Phase change in the cable due to the temperature dependence of the dielectric constant within the cable. Although the metal outer and inner conductor contract with temperature, the effect

³⁰The calibration cannot be done cryogenically due to possible damage to the calibration components, particularly the broadband load.

of the increasing dielectric constant of the polytetrafluoroethylene (PTFE) is stronger. This leads to phase being added to the measurement.

Following measurement of Γ_{llm} cryogenically, the errors above were evaluated by placing a short at the end of the cable, and taking measurements at both room and cryogenic temperatures. From the change in amplitude and phase of S_{11} , the errors introduced by the coaxial cable were determined and removed from the measurement of Γ_{llm} .

During the calibration sequence, several cross-checks were made, to ensure that additional systematic errors did not enter into the sequence. The first of these was to calibrate T_{int} using two different values of heater current, 112.5 and 140 mA, resulting in 6 and 9 K³¹ of heating respectively. The values of T_{int} should be in good agreement, with the lower heater current determination of T_{int} having more ripple, as predicted by equation (4.27). This is in fact found to be the case, as illustrated in figure 4.12. As a result, the higher heater current was used in the final determination of T_{int} .

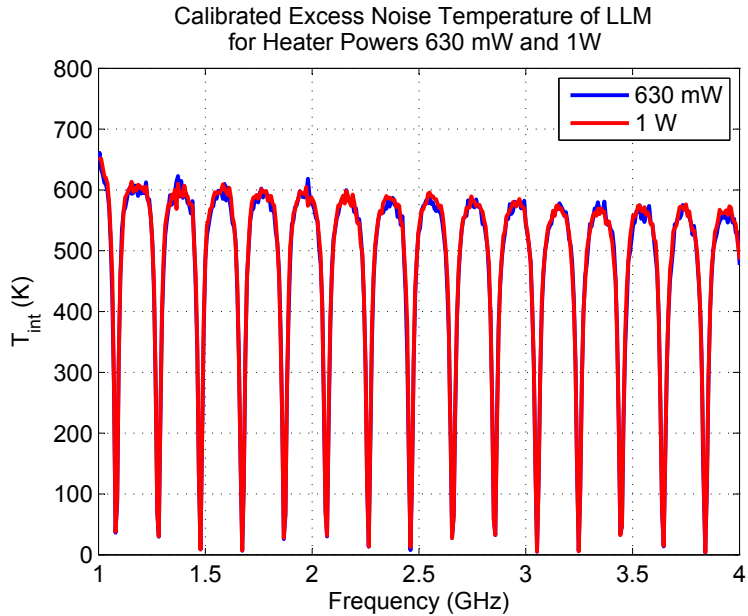


Figure 4.12: T_{int} for heater currents of 112.5 (27.5 K module temperature) and 140 mA (30.5 K module temperature). The agreement between the two is very good, with the value determined at 112.5 mA having slightly more ripple, due to the lower value of ΔT_{ch} .

The second check was to verify that Γ_{llm} does not change appreciably between the cold and hot measurement states. If such a change were to occur, T_{rx} would not be constant for the reasons described in Section 4.4.2. To gauge this effect, Γ_{llm} was measured with the LLM cold (21.5 K)

³¹Higher heater currents were not used, due to the limited current carrying capability of the cryogenic wire used within the cryostat.

and hot (30.5 K). The difference between the two states is shown in figure 4.13, where it is seen that the change in Γ_s is less than -45 dB to 4 GHz, and less than -35 dB to 12 GHz. Results from the modules calibration are shown in figure 4.14. T_{int} and Γ_{llm} (complex) are written to a calibration file for use during noise parameter measurement.

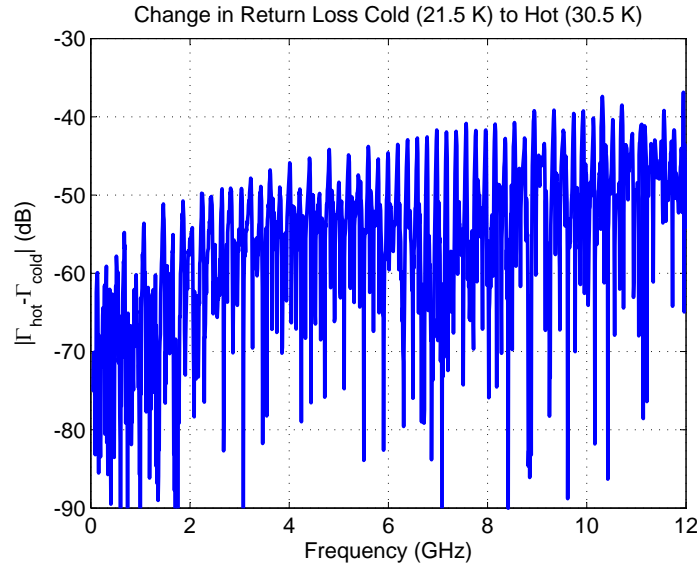


Figure 4.13: Change in LLM reflection coefficient with heating from 21.5 K (0 mA heater current) to 30.5 K (140 mA heater current).

In order to determine the effects of random errors on the measurement, equation (4.27) was evaluated to reveal that ΔT_{int} is on the order of 0.8%, or ± 7 K, over most of the calibration range. This is illustrated in the top figure of figure 4.15. To put this in perspective, the stated uncertainty of Agilent's noise sources is 3.5%, four times greater than that of the calibration results reported here. Measured values of T_{int} between 1.68 and 1.86 GHz were then fitted with a 7th-order polynomial to help illustrate how well the calculated uncertainty of ± 7 K matches measurement. This is shown in the bottom figure of figure 4.15 where it is seen that the ripple in the measurement of T_{int} is in good agreement with the calculated uncertainty.

4.7.2 Measurement Examples

4.7.2.1 Discrete SiGe HBT

NXP's³² SiGe HBT (p/n BFU725F) was mounted in a coaxial fixture so that its noise parameters could be measured with the LLM. The packaged device and test setup are shown in figure 4.16. Measuring the Y-factor of the device at multiple bias levels provided an opportunity to test the ability of the LLM and extraction routine in determining values of Z_{opt} distant from 50Ω . At low

³²NXP Semiconductors, 60 5656 AG Eindhoven, Netherlands.

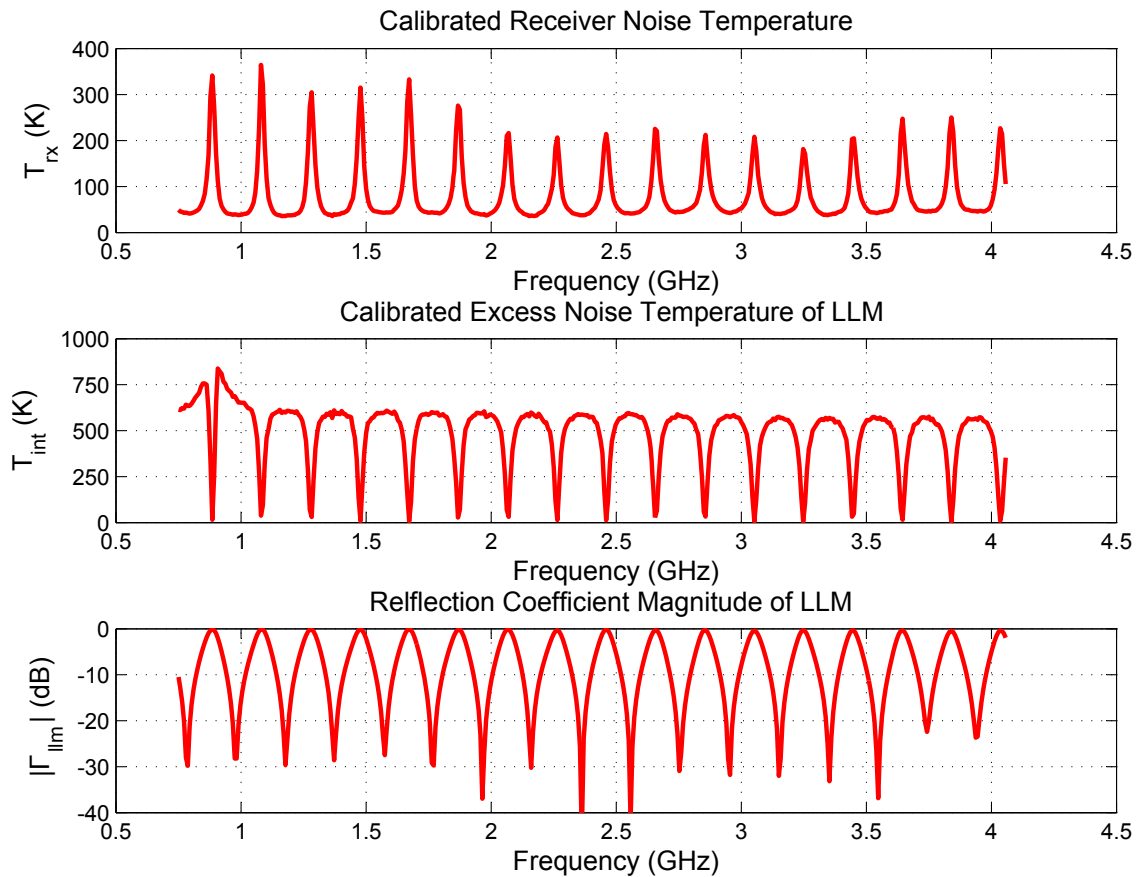


Figure 4.14: Long line module calibration results. (Top) T_{rx} as determined with a 140 mA heater current. (Middle) T_{int} , excess noise temperature, referenced to output terminals of LLM. (Bottom) Reflection coefficient magnitude presented by the LLM.

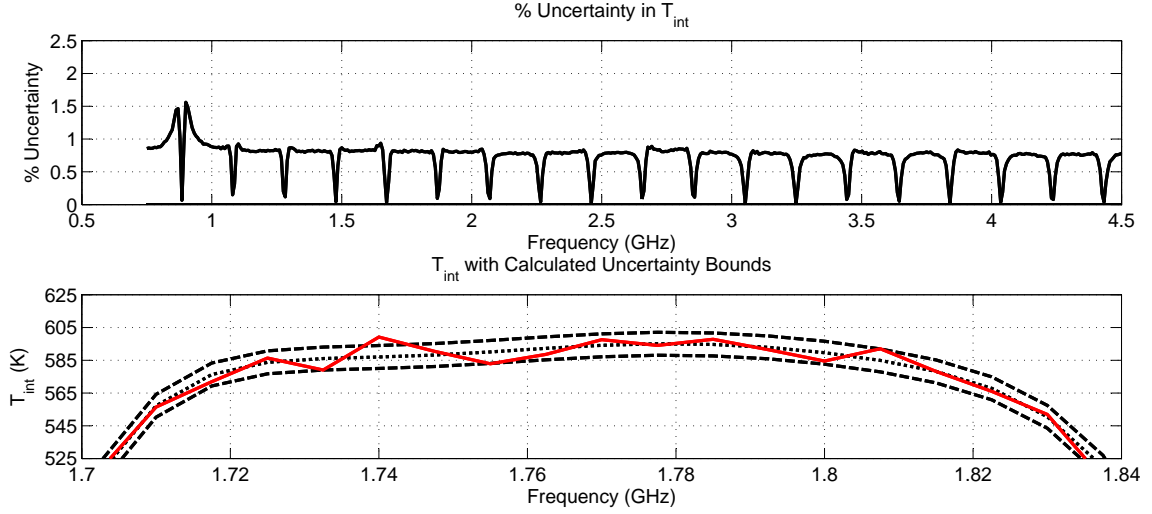


Figure 4.15: (Top) Percent error in T_{int} evaluated using (4.27). The error is approximately 0.8%, or ± 7 K, over most of the band. (Bottom) T_{int} data, from the middle plot of figure 4.14, with 7th order polynomial fit between 1.68 and 1.86 GHz, which the calculated uncertainty bounds have been superimposed. The calculated uncertainty is in good agreement with the ripple in the measurement of T_{int} .

levels of collector current and at low frequency, the impedance presented by the LLM is too distant from Z_{opt} . As a result, the extraction algorithm is not able to determine the noise parameters in this regime. This occurred for $I_c < 5$ mA. The noise parameters for collector currents of 5, 9, and 15 mA are plotted in Fig 4.17. All measurements were made with a collector to emitter voltage of 1 V. A reference plane extension of 68.5 pS was applied to Z_{opt} , corresponding to the distance between the fixtures SMA connector and base lead of the NXP device.

The factor $4NT_0/T_{min}$ was calculated and verified to be between 1 and 2, as Pospieszalski has shown to be necessary [47]. To provide additional verification of the noise parameters, the results were compared against theoretical calculations of T_{min} , N , and Z_{opt} [10].³³

$$T_{min} = T_a \sqrt{\frac{1}{\beta_{dc}}(1 + \kappa) + \kappa(\frac{f}{f_t})^2}, \quad (4.43)$$

where

$$\kappa = 2g_m(r_b + r_e), \quad (4.44)$$

and

$$N = \frac{1}{2} \frac{T_a}{T_0} \sqrt{\frac{1}{\beta_{dc}}(1 + \kappa) + \kappa(\frac{f}{f_t})^2}, \quad (4.45)$$

³³Alternate forms of these expressions may be found in [47].

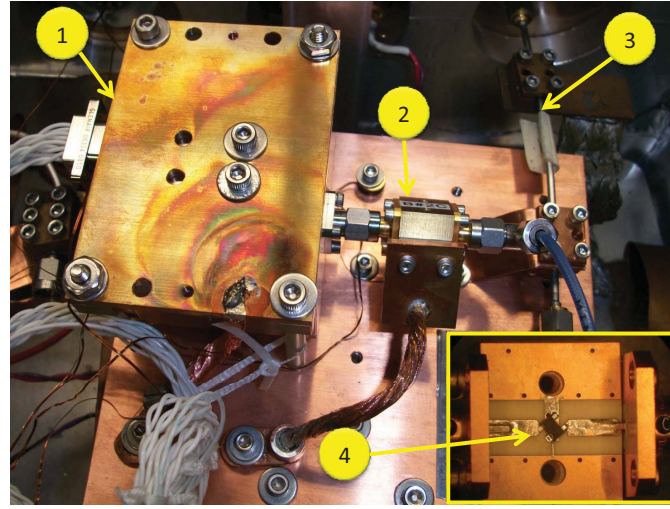


Figure 4.16: Photograph of SiGe HBT measurement setup. (1) LLM is underneath a OFHC plate, which is heat strapped to the cold head. (2) Packaged HBT. (3) Output, stainless steel coax, (4) Inset photograph of test fixture with cover removed. The NXP HBT is at the center of the inset photo.

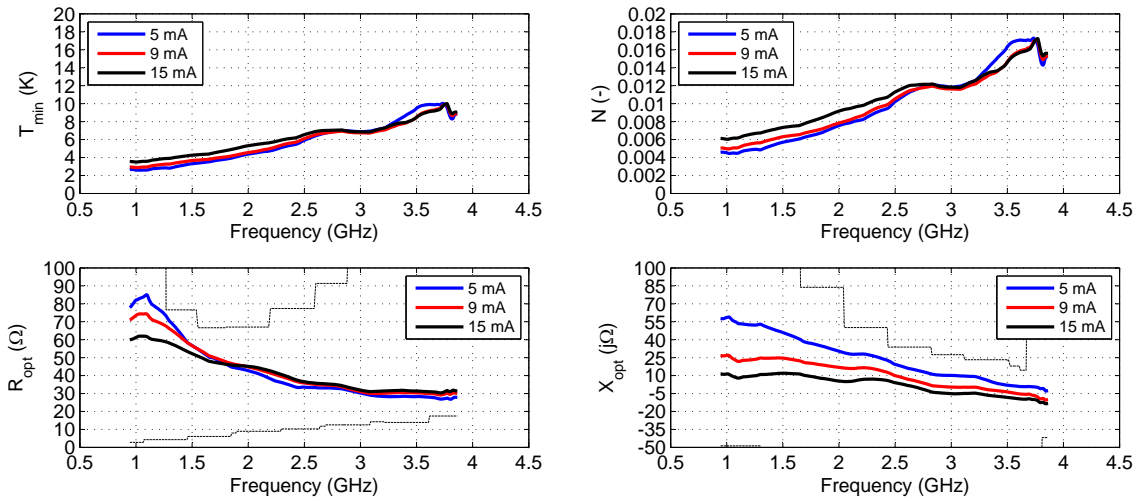


Figure 4.17: Noise Parameters, at 19 K, for NXP SiGe HBT (p/n BFU725F) at $I_c = 5, 9$, and 15 mA, with $Y_{thr} = 10$. A box car average, 54 points points long, has been used to smooth the extracted noise parameters. Plotted in black, on the plots of R_{opt} and X_{opt} , are the maximum and minimum values of resistance and reactance presented by the LLM during the measurement.

$$R_{opt} = \frac{\beta_{dc}}{g_m(1 + \beta_{dc}(f/ft)^2)} \sqrt{\frac{1}{\beta_{dc}}(1 + \kappa) + \kappa(\frac{f}{f_t})^2}, \quad (4.46)$$

$$X_{opt} = \frac{\beta_{dc}}{g_m} \frac{f/ft}{1 + \beta_{dc}(f/ft)^2}. \quad (4.47)$$

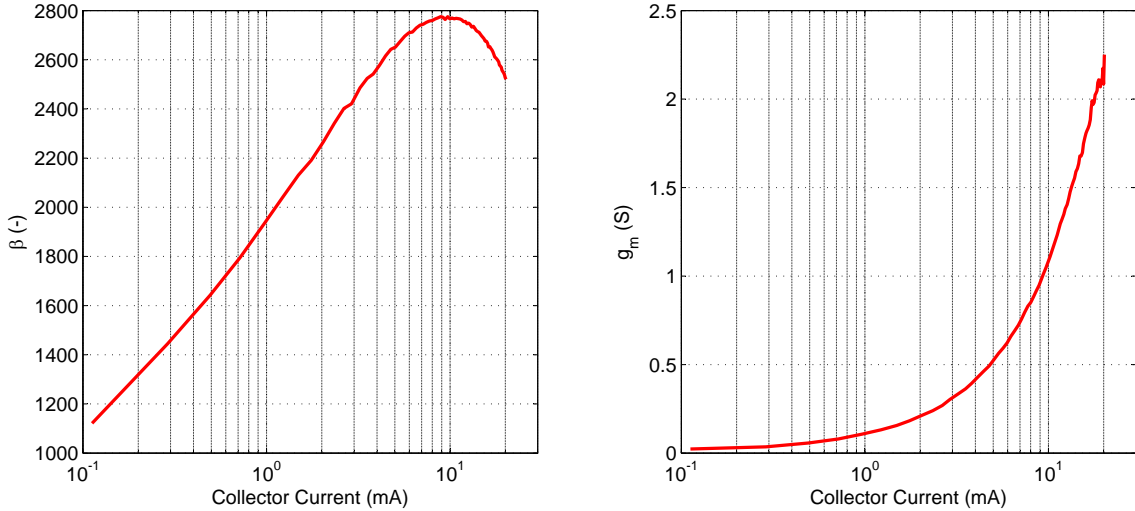


Figure 4.18: Measured DC characteristics for NXP HBT BFU725F at 19 K. (Left) $\beta = I_c/I_b$ and (Right) $g_m = \Delta I_c/\Delta V_{be}$.

The more commonly used noise parameter, R_n [31] is given by

$$R_n = N/\Re(1/Z_{opt}). \quad (4.48)$$

β , and g_m were determined experimentally on the HBT with DC measurements, using the bias-tie internal to the LLM, the results shown in figure 4.18. The S-parameters were then measured and f_t estimated for each bias level. Values of r_b and r_e were taken from the small signal model provided by NXP. The theoretical noise parameters are calculated and overlaid with the measured results, as shown in figure 4.19. There is good agreement between the measured and theoretical noise parameters, even though the theoretical calculations do not take into account additional packaging parasitics or changes in r_b and r_e due to temperature. It is believed that the differences between measured and theoretical values are due to the lack of knowledge of the component values within the actual small-signal model of the transistor at cryogenic temperatures.

The LLM measurements also allow calculation of the available gain, G_{av} , of the transistor. This requires a separate measurement of the backend noise of the post-amp and receiver used in the test setup (item 5 onward in figure (4.10)). G_{av} is calculated by use of the following relation:

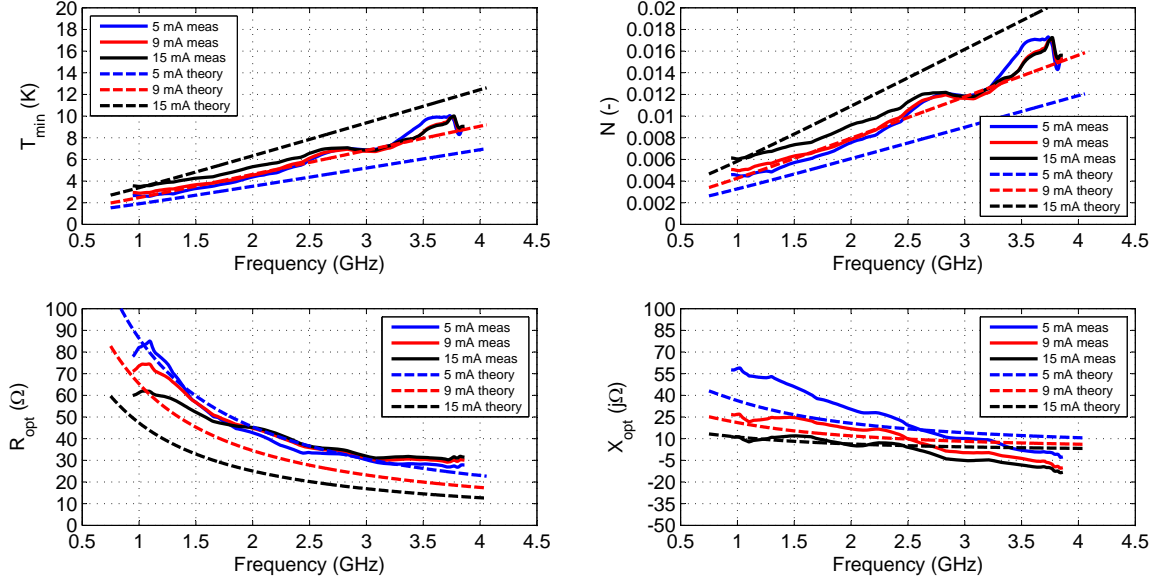


Figure 4.19: Measured (solid) and theoretical (dashed) noise parameters of NXP SiGe HBT. The theoretical values were determined with relations (4.43) through (4.47) and with DC measurements made at 19 K.

$$G_{av} = \frac{P_{on,dut} - P_{off,dut}}{P_{on,be} - P_{off,be}} \frac{T_{excess,be}}{T_{int}}, \quad (4.49)$$

where $P_{on,dut}, P_{off,dut}$ and $P_{on,be}, P_{off,be}$ represent the measured noise powers of the DUT and backend respectively. $T_{excess,be}$ is the excess noise temperature of the noise source used in the measurement of $P_{on,be}$ and $P_{off,be}$. To illustrate this, G_{av} of the transistor for frequencies where $|\Gamma_s|^2 < -20$ dB were plotted against a separate measurement of $|S_{21}|^2$, using a VNA. This is shown in figure 4.20. The agreement is again quite good, the comparison providing validation as to the calibration's determination of T_{int} .

These measurements required a correction for the noise of the post-amp (uncooled) and NFA. Future cryogenic measurements will employ a cooled pre-amplifier, immediately following the device under test. This greatly reduces the correction necessary for back end noise, and will allow for better determination of T_{min} (of the device itself) through extraction.

4.7.2.2 Discrete LNA

A two-stage LNA, using the NXP BFU725F transistor [48], was then measured cryogenically at a bias current of 11.7 mA. Following noise parameter measurement, the amplifier's 50 Ω noise was measured using the cold attenuator method [49],[50].³⁴ The physical temperature of the LNA for both measurements was 19 K.

³⁴The uncertainty in this noise measurement is estimated to be ±1 K.

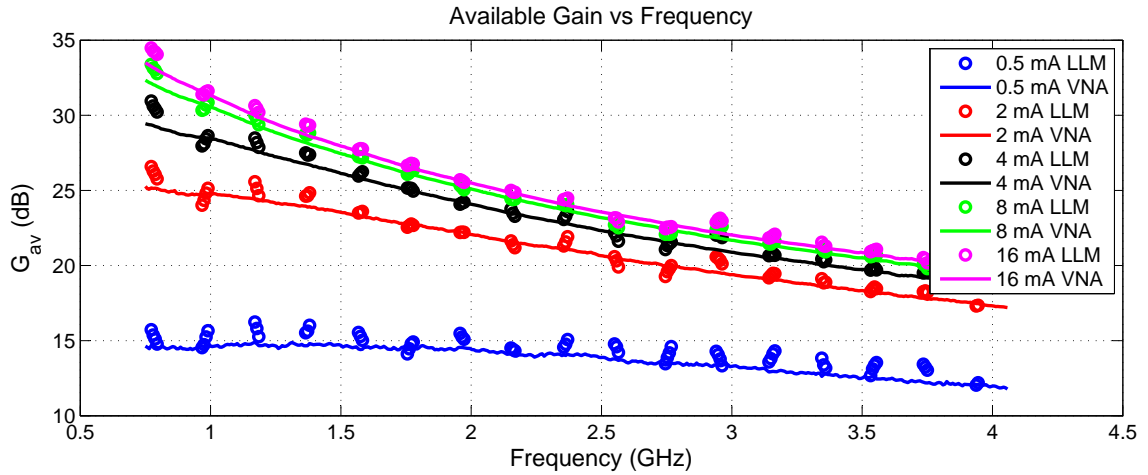


Figure 4.20: Measured available gain, G_{av} , for $Z_s \approx 50 \Omega$, using LLM (circles) and VNA (solid lines) for the NXP HBT at 19 K. G_{av} for the LLM is plotted every 200 MHz, at points where $|\Gamma_{lum}| \leq -20 \text{ dB}$

The results of the noise parameter measurements are shown in figure 4.21. The noise temperature and available gain of the LNA when driven by a 50Ω source, T_{50} and G_{av50} respectively, were then calculated from these measurements and compared against those from the cold attenuator method. figure 4.22 reveals good agreement between measurements using the two methods, with less than 2 K difference in T_{50} across most of the measurement band. G_{av} for the two methods is also in good agreement, with less than 0.5 dB difference in gain from 1 to 4 GHz. The factor $4NT_o/T_{min}$ was calculated and verified to be between 1 and 2. It is plotted along with comparisons of T_{50} and G_{av50} in figure 4.22.

4.7.2.3 MMIC LNA

The final cryogenic noise parameter measurement presented was performed on a low power, low noise, packaged WBA23 SiGe MMIC described in section 5.5.1. This amplifier was designed to interface with a superconductor-insulator-superconductor (SIS) mixer which itself presents $\approx 135 \Omega$ generator resistance in parallel with 300 fF. When operated at $< 2 \text{ mW}$ of DC power, the MMIC needs a fairly large value of source inductance to compensate its value of X_{opt} . Measurements were completed at 19K with the MMIC packaged in a 50Ω module, the noise parameters shown in figure 4.23. These measurements indicate that a 5.1 nH inductor in series with the MMIC input will compensate X_{opt} at 2.2 GHz (the reactance presented by the inductor is illustrated by the dashed line in figure 4.23). Noise measurements were then completed at 4.2 K, the actual physical temperature that the SIS and MMIC will be operated at, in a small liquid helium dewar using the cold attenuator method. The results are shown in figure 4.24, for the case with and without a 5.1 nH inductor included at the input

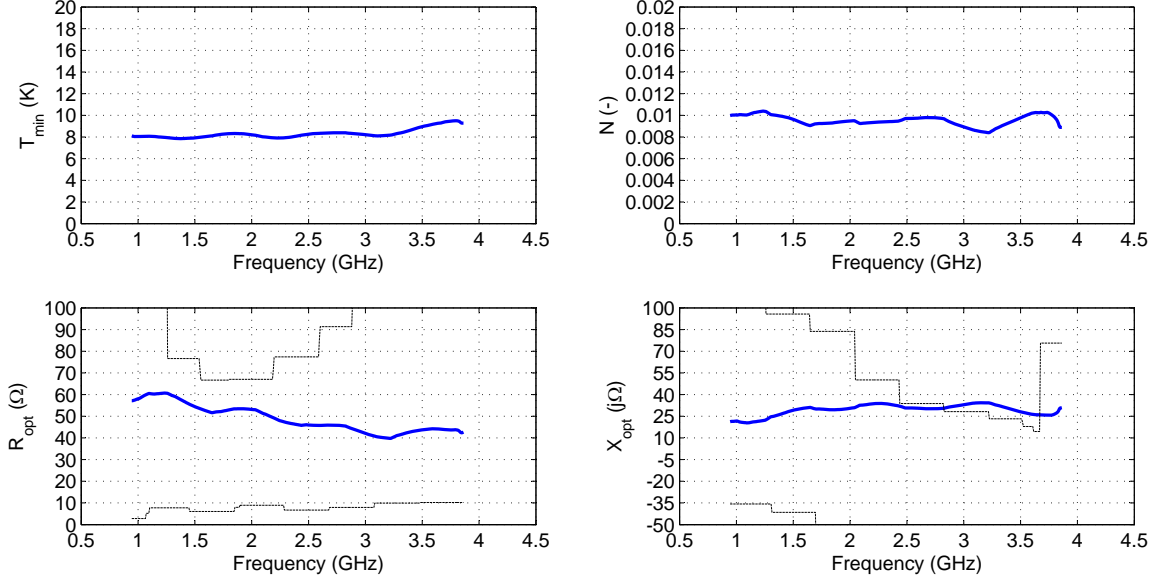


Figure 4.21: Noise parameters for the discrete LNA at 19 K, with $Y_{thr}=10$ used during extraction. A box car average, 54 points long, has been used to smooth the extracted noise parameters. Plotted in black, on the plots of R_{opt} and X_{opt} , are the maximum and minimum values of resistance and reactance presented by the LLM during measurement.

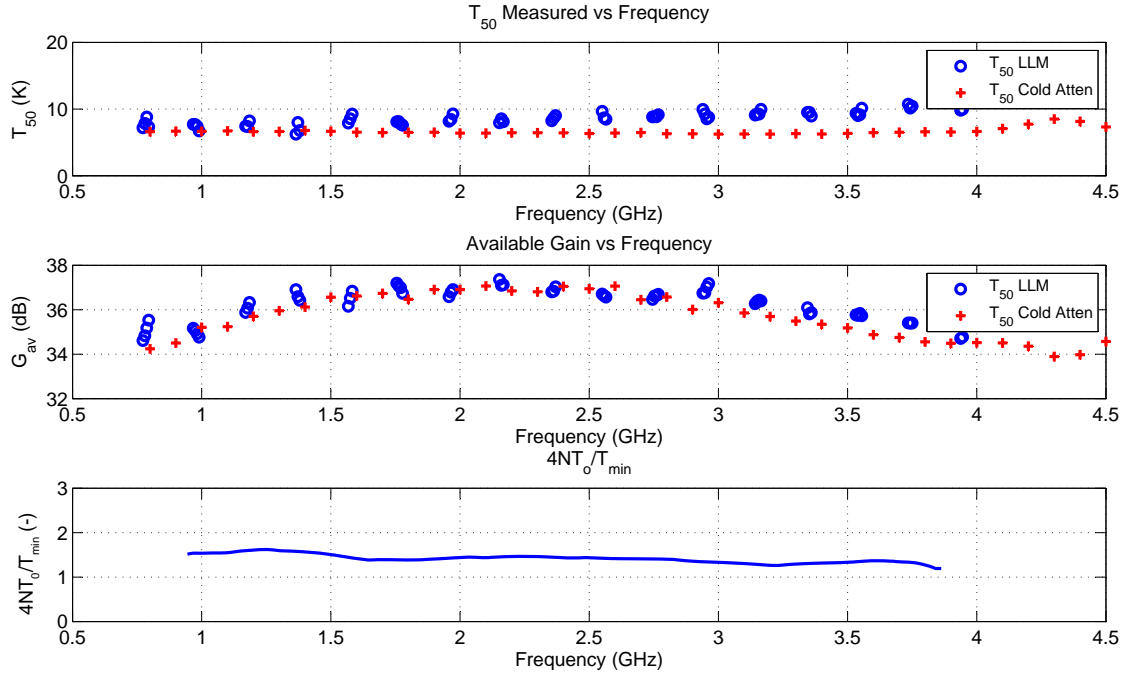


Figure 4.22: Verification of noise parameters for the discrete LNA, $V_{cc}=1.9$ V at 11.7 mA, 19 K physical temperature. (Top) Plot shows calculated T_{50} from measured noise parameters vs. that measured using the cold attenuator method. (Middle) Plot reveals calculated G_{av} ($50\ \Omega$ source impedance) vs. that measured using the cold attenuator method. (Bottom) Plot is the factor $4NT_0/T_{min}$ which has been shown by Pospieszalski to lie between 1 and 2 [47].

of the MMIC's $50\ \Omega$ module. X_{opt} is compensated at ≈ 2.6 GHz, slightly higher than the predicted value of 2.2 GHz. Some of the discrepancy may be because the noise parameter measurements were completed at a higher physical temperature of 19 K (the 4.2 K dewar was physically too small to complete noise parameter measurements at 4.2 K directly).

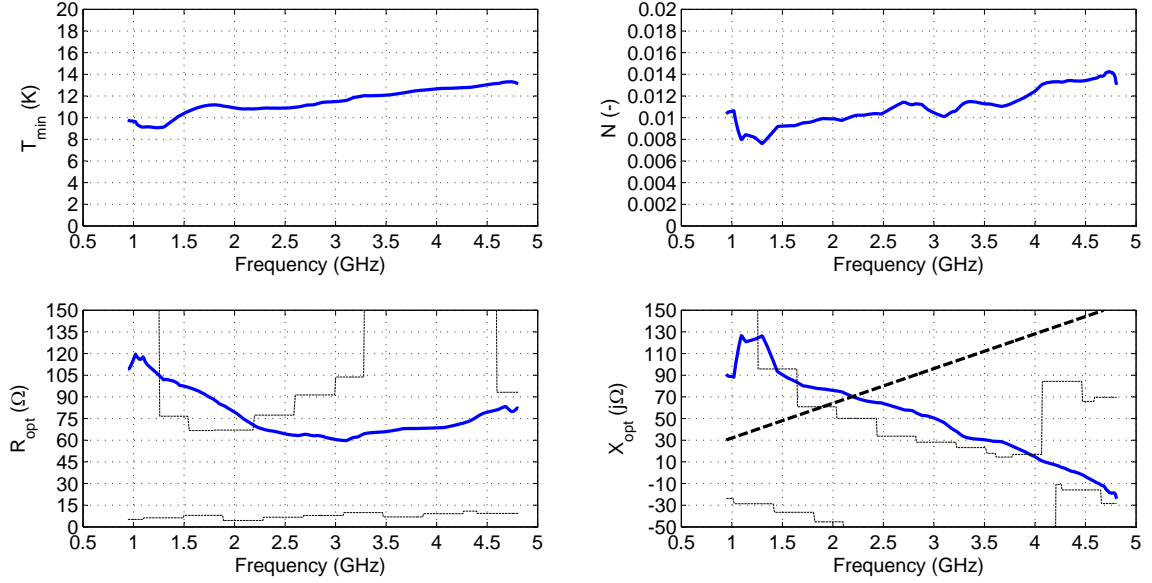


Figure 4.23: Noise parameters of WBA23 low power MMIC, measured at 19 K physical temperature. This MMIC is from the CITST1 reticle fabricated by ST-Microelectronics, described in section 5.5.1. It is biased at $V_{cc} = 1.289\text{ V}$ @ 1.5 mA. The dashed black line, in the plot of X_{opt} represents the reactance presented by a 5.1 nH inductor. The intersection of X_{opt} and this line indicates that X_{opt} will be compensated at 2.2 GHz if the inductor is placed in series with the MMIC's input.

The evaluation of the random errors, provided by equation (4.38), for the measurement of the low power MMIC is shown in figure 4.25. Frequencies where $Y_{dut} \geq 10$ are indicated in black. The uncertainty is $< \pm 0.7\text{ K}$ for measurement frequencies where the Y-factor ≥ 10 . A Monte-Carlo analysis was then performed to determine what effect this error would have on the noise parameter extraction.³⁵ figure 4.26 shows the variability in the extracted noise parameters after 100 Monte Carlo runs. The simulation was performed by adding $\pm 0.7\text{ K}$ of random noise to the measured noise temperature of the low power MMIC, for each noise parameter extraction. The results are presented as percent change in the noise parameters shown previously in figure 4.23. This analysis reveals that the uncertainty in the noise parameters is low, $\leq 2.5\%$ over most of the band. The only exception is ΔX_{opt} above 4 GHz, the reason for which being due to it's normalization by X_{opt} , which crosses 0 at ≈ 4.25 GHz.

³⁵It was assumed that the VNA measurement of the modules reflection coefficient, Γ_{llm} , was of sufficient accuracy to not appreciably impact the results of this analysis.

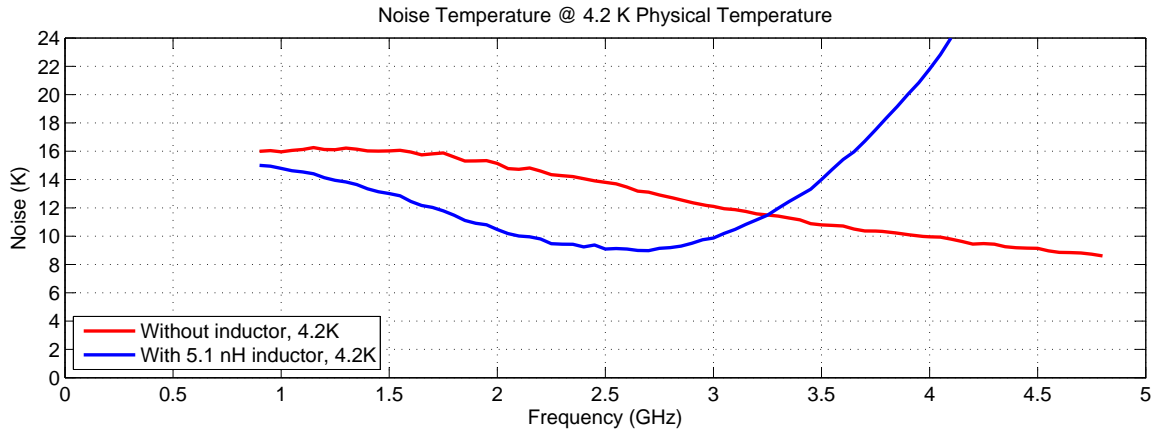


Figure 4.24: Measured noise temperature at 4.2 K with and without a 5.1 nH inductor at the input of the low power MMIC. X_{opt} should be compensated at 2.2 GHz based on the extracted noise parameters measured at 19 K.

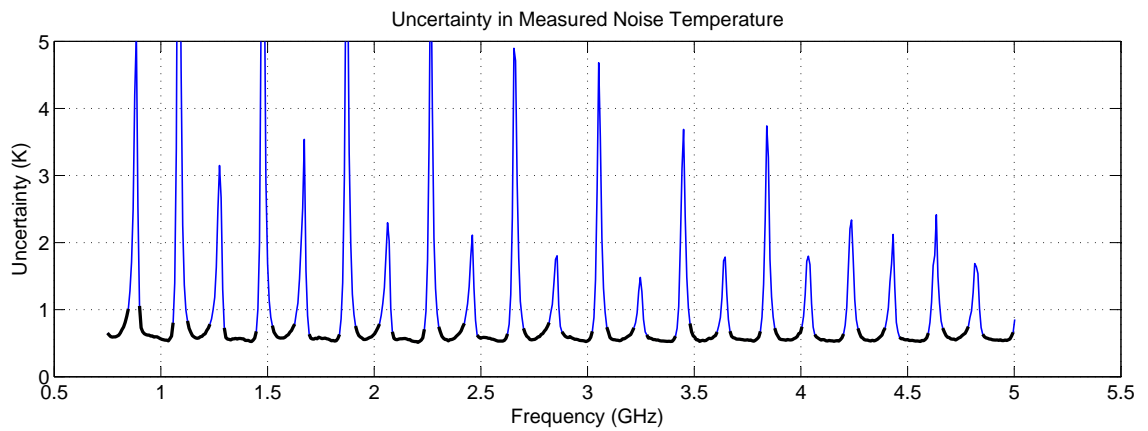


Figure 4.25: Uncertainty in the measured noise temperature of the low power MMIC, using equation (4.38). Black segments indicate noise temperatures where $Y_{meas} \geq 10$. Frequencies with Y-factors below this limit (higher measured noise) were not used in the extraction.

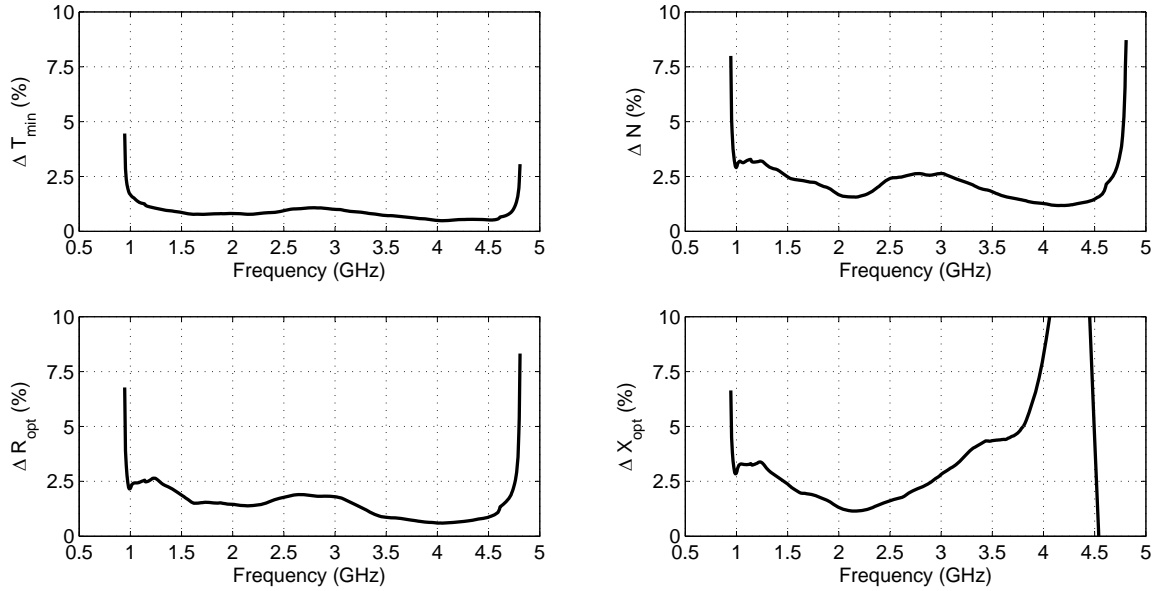


Figure 4.26: Monte Carlo analysis of the sensitivity of the low noise MMIC noise parameter extraction to ± 0.7 K of random noise on the measurement. The increase in ΔX_{opt} is due to its normalization by X_{opt} , which crosses 0 at ≈ 4.25 GHz (refer to figure 4.23).

4.8 Ambient Noise Parameter Measurements

At cryogenic temperatures metals have low loss and amplifiers benefit from low levels of thermal noise and higher gain. All of these factors make it relatively easy to get a sizable change in Y-factor (ΔY_{ch}) with a moderate change (9 K) increase in module temperature. The results are low calibration and measurement errors. At room temperature the opposite is true, and the calibration requires on the order of ~ 40 K change between cold and hot states to produce enough change in Y-factor, as will be shown. Even so, if the module were to be calibrated at the LLM output as done cryogenically, the change in Y-factor would remain extremely small at frequencies where the LLM is highly reflective, as the noise wave exiting the frontend³⁶ reflects off of the LLM and is reincident upon it, further diminishing the Y-factor. Isolators could be used, inserted between the LLM and frontend, but this is of limited benefit. Their own loss increases the noise temperature of the receiver, thus reducing Y-factor. As most isolators are relatively narrow band, such a setup would potentially require many isolators to cover a given range of frequencies. At ambient temperature it becomes beneficial, if not necessary, to use the LLM described in Section 4.2.2, as the excess noise temperature of the internal noise source, T_{int} , can be calibrated independently of the mismatch network. This solves the problem of low Y-factor caused by high reflection, as the internal noise source itself is relatively well matched. The mismatch network may be characterized separately with a VNA. Following both measurements, the internal noise source is connected to the input of the mismatch network, and T'_{int}

³⁶Refer to Section 3.5 for a discussion on noise waves.

for the overall module is calculated through the use of equation (4.23) and (4.24).

A consequence of a higher temperature separation between cold and hot calibration states, ΔT_{ch} , is that the measurement is more susceptible to systematic errors caused by changes in the reflection coefficient. Calibrating the internal noise source independently of the mismatch network helps here as well. If forced to calibrate at the output of the mismatch network, the calibration would be especially prone to errors induced by the phase change of the PTFE coaxial cables forming the mismatch network.

4.8.1 Module Calibration

Due to the increased physical temperature and larger ΔT_{ch} required, the internal heater within the ambient LLM module is not sufficient to produce the required temperature change. Two thermoelectric coolers³⁷ (TECs) are used in place of the heater and cold-head used in the cryogenic measurements. The first TEC is used to regulate the temperature of the LLM from slightly above ambient (300 K) to 340 K. The second TEC is used to maintain the temperature of the frontend components, again comprised of a coupler, external noise diode, and LNA. The TECs and frontend components are housed in a sealed enclosure³⁸ to limit the effects of convection currents on component temperatures. The completed test setup and listing of components are shown in figure 4.27 and table 4.3 respectively.

Table 4.3: Components used within ambient calibration test setup.

| Component | Manufacturer | Description |
|-----------------------|-----------------------------|---|
| Temperature Sensor | Lakeshore Cryotronics | p/n DT-470-CU-11 |
| Coaxial Cable | Astrolab ³⁹ | p/n minibend-2.5 |
| Coupler | Krytar | p/n 1831, 90° hybrid, 1–18 GHz |
| External Noise Source | Agilent | p/n 346C-KO1, 1–50 GHz, 20 dB (nominal) ENR |
| NFA | Agilent | N8975A |
| Voltmeter | Keithley | Model 2001 |
| IEB | Custom | Interface Electronics Box |
| LNA | CIT | WBA25, 1–6 GHz, ≈80 K noise, 25 dB gain |
| TEC Unit | TE Technology ⁴⁰ | p/n CP-031 |
| TEC Controller | TE Technology | p/n TC-36-25-RS232 |
| TEC Power Supply | TE Technology | p/n PS-12-8.4 |

The first calibration step is to determine the excess noise temperature of the internal noise source, T_{int} . This is done by hooking the receiver directly to the noise source output of the ambient/cryogenic module and performing the calibration routine outlined in Section 4.3. figure 4.27 reflects this setup,

³⁷Although somewhat misleading by their name, the “coolers” are bidirectional, allowing them to both run at a higher and lower temperature, relative to their baseplate temperature.

³⁸The enclosure is fitted around the TEC elements so that their heat sinks and fans are exterior to the enclosure.

³⁹Astrolab Inc., 4 Powder Horn Dr., Warren NJ, 07059-5105 U.S.A.

⁴⁰TE Technology Inc, 1590 Keane Dr., Traverse City MI, 49696-8257 U.S.A.

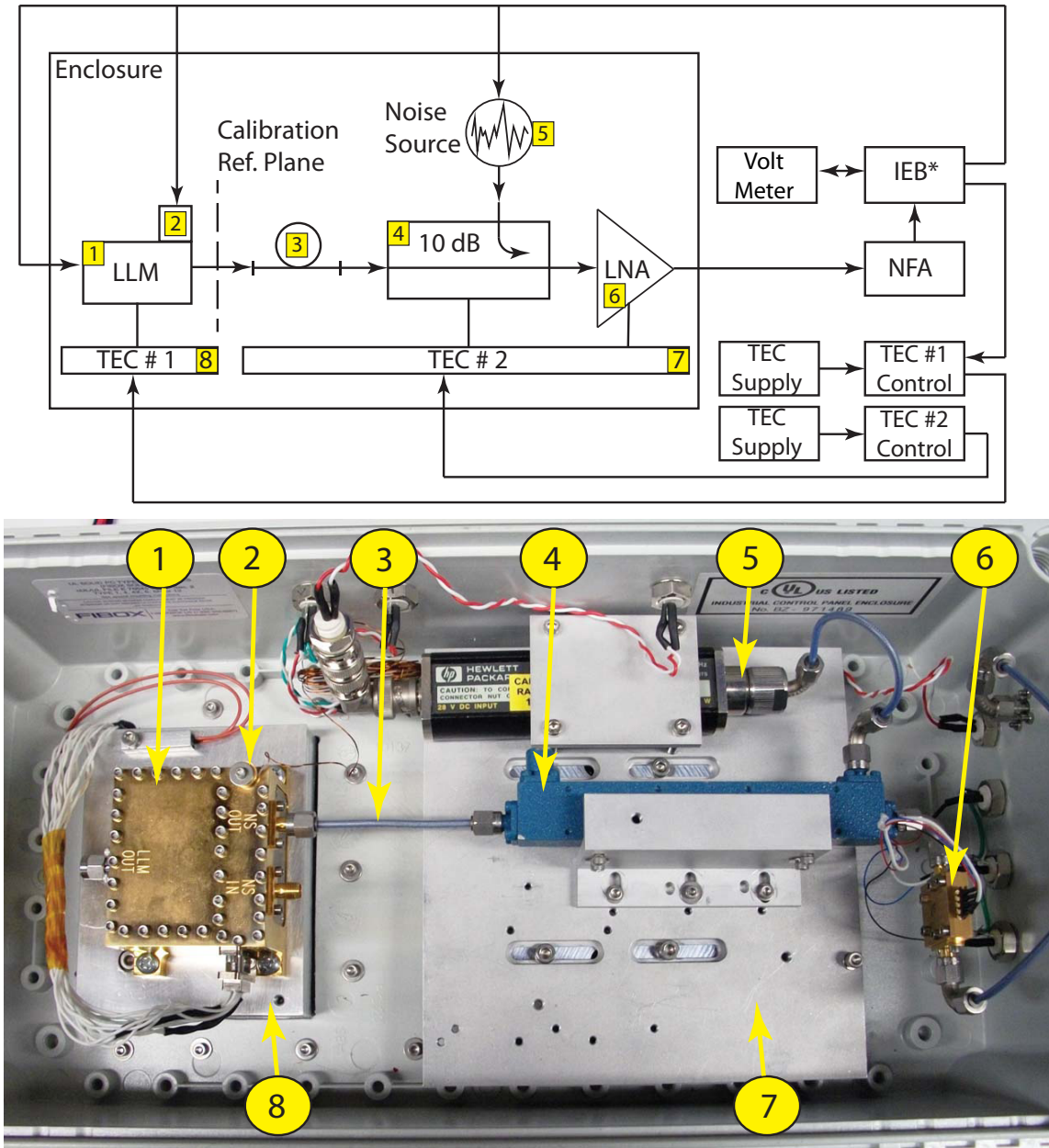


Figure 4.27: Test setup for module calibration at ambient temperature. (1) LLM Module, (2) temperature sensor, (3) coaxial cable, (4) 10 dB coupler, (5) external noise source (with 3 dB attenuator), (6) low noise amplifier (described in Section 5.5.3 and biased at $V_{cc1}=2.84$ V, 30 mA, and $V_{cc2}=1.37$ V, 15 mA), (7) receiver TEC plate, and (8) LLM TEC plate. Details for these components are provided in table 4.3.

where the module is calibrated with the same 7.5 MHz frequency grid as used earlier. The maximum number of sweep points within the NFA is 401, resulting in a maximum of 3 GHz per sweep. Y_{ns} , Y_c , and Y_h measurements are thus performed for the first 3 GHz of calibration bandwidth, the unit then returned to 300 K and the next measurement sequence initiated for the next 3 GHz band. Due to limitations in the noise temperature of the LNA and loss of the coupler, it was difficult to obtain an adequate value of Y_{ch} above 7 GHz. The ambient calibration was therefore only performed to 6.75 GHz.

Following determination of T_{int} , the S-parameters of the mismatch network are measured. The SMA-SMA adapter used to connect the noise source output to the mismatch network input is included in this measurement. The measurement is made at 300 K physical temperature with the same frequency spacing as the measurements for T_{int} . The excess noise temperature of the completed module, T'_{int} , is then determined using equation (4.23) and (4.24), as previously mentioned.

The results of the calibration are shown in figure 4.28 where T_{rx} , T_{int} , T'_{int} , and Γ_{llm} are shown. It is believed that a systematic error within the test setup produced the error of ~ 70 K in the determination of T_{rx} . The source of this error is yet unknown, and is currently under investigation. A separate measurement of T_{rx} was made using the NFA and smart noise source (SNS). This measurement, along with the thermal calibration determination of T_{rx} , is shown at the top of figure 4.28. The fact that the required offset is repeatable for successive calibration runs leads to the conclusion that the error is systematic and not random. Further investigation has revealed that problem originates from a 1.3% error in the measurement of Y_h . It was initially thought that this error was caused by a temperature gradient down the coaxial line connecting the LLM to the frontend (item 3 in figure 4.27). This effect, however, is small and would result in an overestimation of T_{rx} . Subsequent measurements, with the LLM removed from the setup, and a $50\ \Omega$ termination at the input of the coupler, suggest that the problem may be due to a ground loop from the LLM's TEC module effecting the ENR of the external noise source. This is based on the observation that the error in Y_h persists even when the LLM is removed from the setup, and the normal calibration routine executed. In such a scenario, one would expect Y_h and Y_c to be equal. Regardless of the actual mechanism, further work is necessary to remove this error from measurement. The fundamental approach, however, is sound.

As discussed in Section 4.4.2, systematic errors are introduced in the calibration due to changes in reflection coefficient, Γ_{ns} in this case. These errors are analyzed next and correspond to the following mechanisms:

1. Change in $\Delta\Gamma_{ns}$, due to heating of the module during calibration. This produces a change in T_{rx} between cold and hot calibration states. This change, $\Delta\Gamma_{ns,hotcold}$, is shown in the top of figure 4.30.

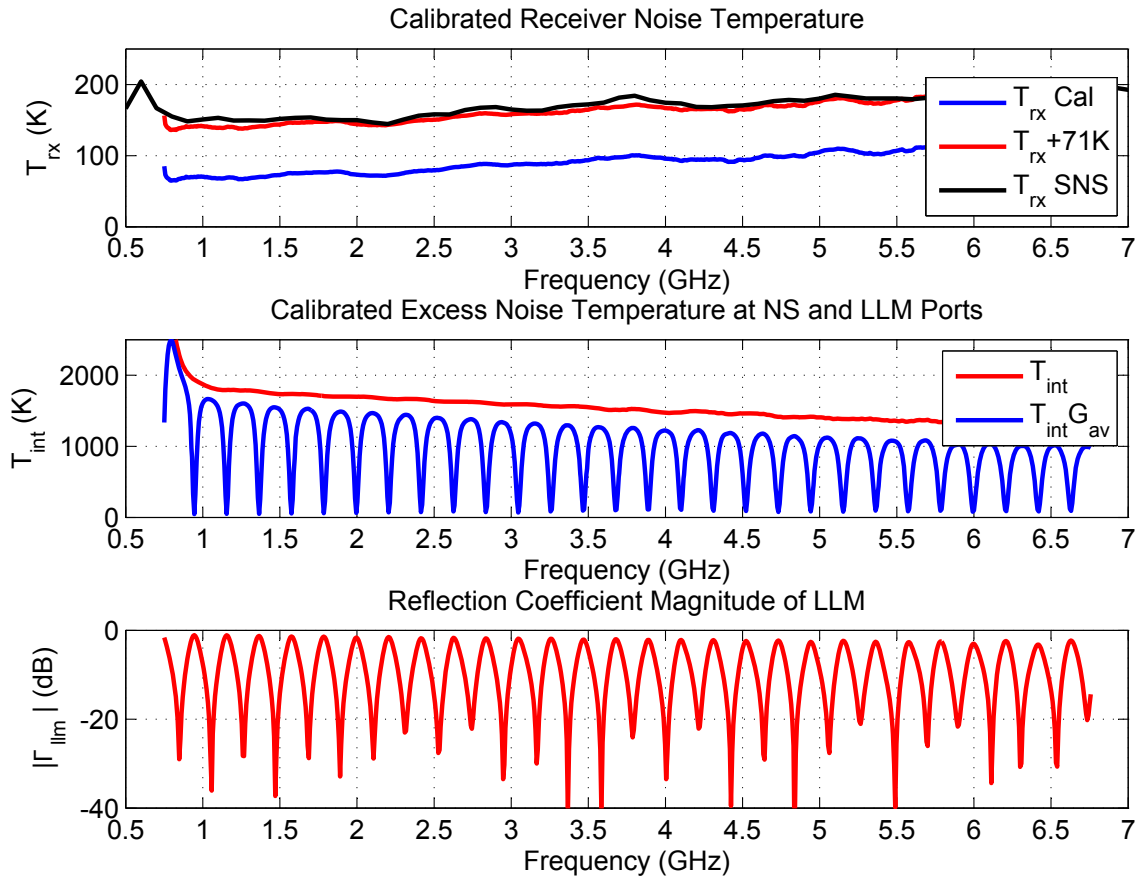


Figure 4.28: LLM ambient calibration results. (Top) Calibrated receiver noise temperature. T_{rx} was roughly one-half as large as determined with an independent noise temperature measurement. It is believed this is due to a systematic error within the test setup that is not currently understood. The offset between the two is 71 K, independent of frequency and repeatable. (Middle) Calibrated excess noise temperature T_{int} at the NS and LLM outputs, with the static 71 K correction in T_{rx} used in its determination. (Bottom) Reflection coefficient magnitude at the LLM output port.

2. Change in $\Delta\Gamma_{ns}$, with internal noise source in its on and off positions. This produces an error in the determination of T_{int} due to changes in T_{rx} and a change in the system gain during on and off measurement states of Y_{ns} . This change is defined as $\Gamma_{ns, onoff}$, the measurement of which is also shown at the top of figure 4.30.

In order to justify use of equation (4.30) and (4.31) in equation (4.32), the noise parameters of the receiver used during calibration were extracted, the results shown in figure 4.29. These measurements indicate that Z_{opt} is $\sim 50 \Omega$ over frequency, as required. N was then treated to a third-order polynomial fit and used to estimate $\Delta T_{int,\Gamma_s,T_{rx}}$. Similarly, the S-parameters of the frontend were measured, verifying that equation (4.34) could be utilized due to its low return loss and high reverse isolation. $\Delta T_{int,\Gamma_{ns},G_t}$ and $\Delta_{int,\Gamma_s,T_{rx}}$ were thus evaluated, the results of these systematic errors shown at the bottom of figure 4.30.

Systematic errors due to temperature measurements were not evaluated, due to lack of a secondary temperature sensor with sufficient accuracy. It is believed that this error is $\leq 0.1\%$, from the accuracy of the calibration of the Lakeshore Cryotronics silicon diode integrated into the module.

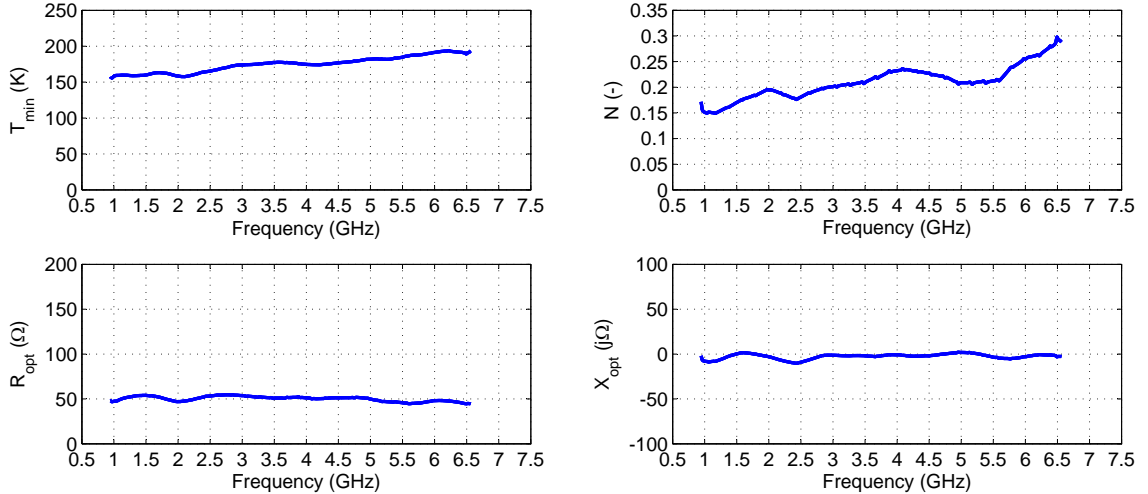


Figure 4.29: Noise parameters of the receiver used during ambient calibrations, as portrayed in figure 4.27. Z_{opt} is sufficiently close to 50Ω justifying use of equation (4.30) and (4.31) in equation (4.32).

equation (4.27) was used to determine the random error in the calibration, the results shown in figure 4.31. The low uncertainty of $\sim 0.5\%$ over most of the band comes at the cost of added calibration time due to averaging. Section 4.9 discusses alternatives to the greater number of averages, through development of a new receiver. It is believed that a total calibration uncertainty (systematic +random) of $< 1\%$ can be achieved.

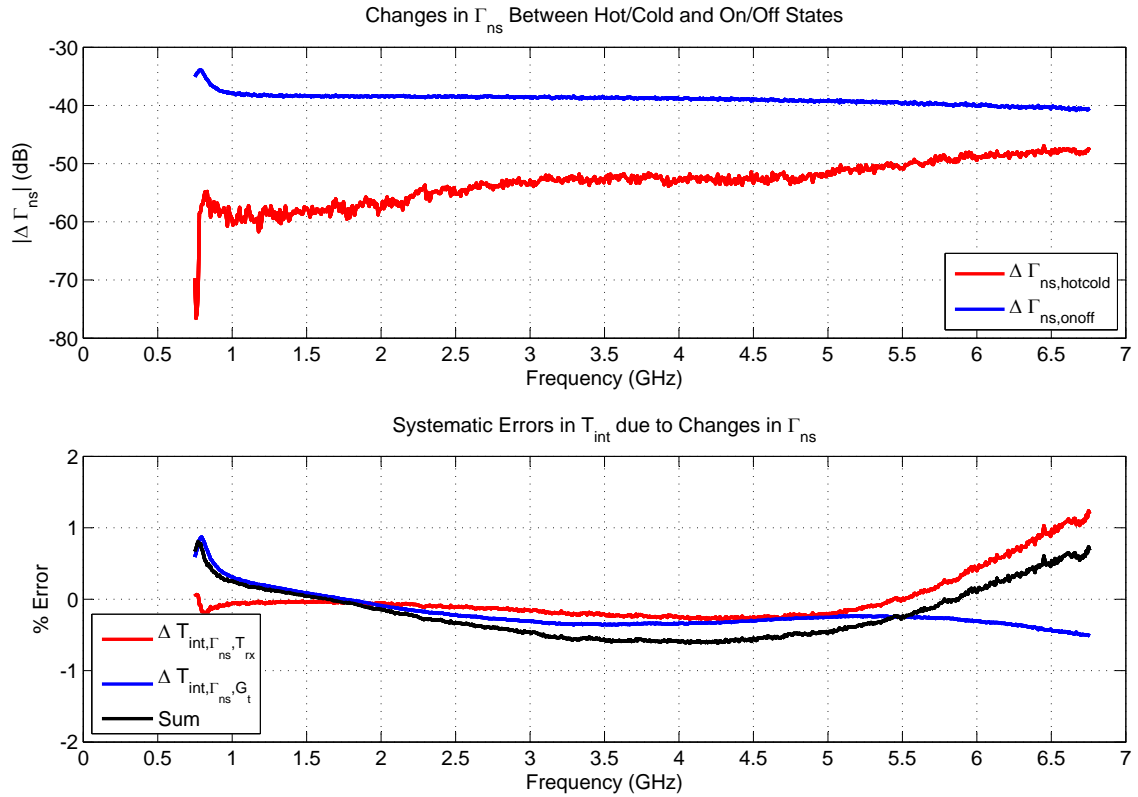


Figure 4.30: Evaluation of systematic errors in the ambient calibration of the LLM. (Top) Changes in Γ_{ns} between hot and cold calibration states and on and off states of the internal noise source. (Bottom) Corresponding systematic errors. Even without compensation, the cumulative systematic error due to changes in reflection coefficient is $\leq 0.5\%$ over most of the calibration band.

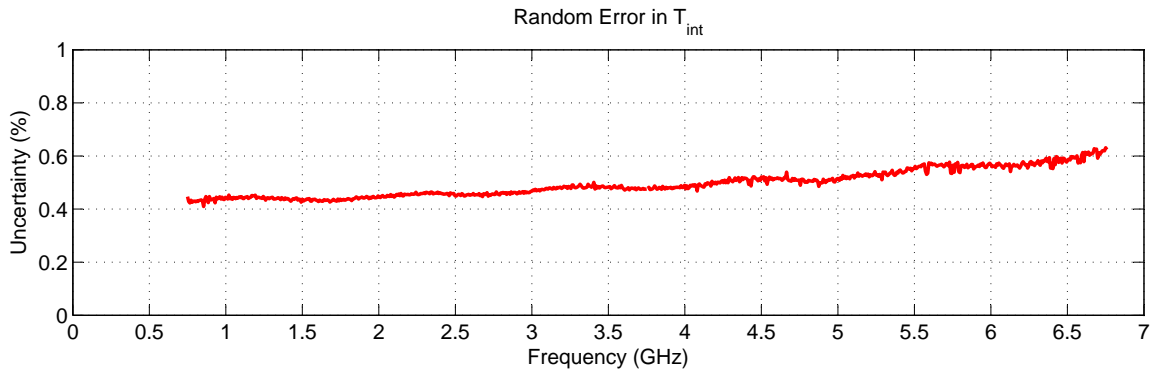


Figure 4.31: Random error in the ambient calibration of the LLM, following correction for the systematic error in T_{rx} . The increase in uncertainty at higher frequencies is due to the increased noise temperature of the LNA and loss of the coupler used in the frontend.

4.8.2 Measurement Examples

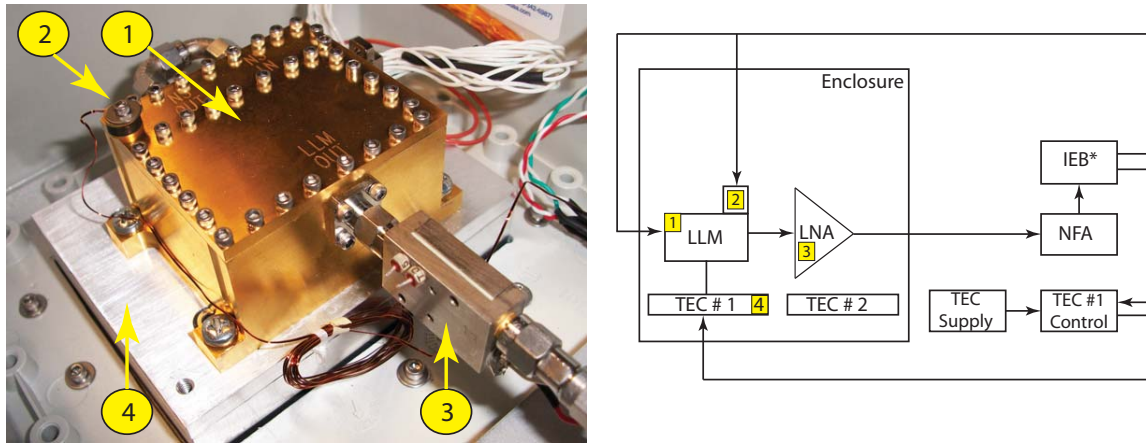


Figure 4.32: Test setup for measurement of noise parameters at ambient temperature. (1) LLM, (2) External temperature sensor (used in conjunction with LLM's internal sensor), (3) DUT (LNA), and (4) TEC plate. The second TEC plate is unused during noise parameter measurements.

The noise parameters of two LNAs were measured to evaluate the performance of the room temperature LLM and its calibration. Both measurements utilize the setup shown in figure 4.32. The DUT is connected directly to the output of the LLM and the Y-factor measured with the NFA uncorrected. Measurements were made at the same 7.5 MHz frequency grid as the calibration, with 16 averages per measurement. The resulting measurement time, for 802 points, was ≈ 10.7 minutes.

4.8.2.1 Ultra-Low-Noise Temperature Amplifier

The first measurement was performed on an ultra-low-noise temperature amplifier, designed at Caltech by Dr. Sander Weinreb [51]. This amplifier provides more than an octave of bandwidth (0.6–1.6 GHz), and a noise temperature of < 25 K at ambient temperature. The amplifier was mounted in the test setup shown in figure 4.32 and its noise parameters measured, shown in figure 4.33 for a bias of $V_g = -0.4$ V at $0.11 \mu\text{A}$, $V_d = 1.5$ V at 82 mA. Since the lowest calibration frequency was 750 MHz, the lowest frequency available for the reported noise parameters is 950 MHz. The noise parameters above this frequency show that R_{opt} is $\sim 50 \Omega$ over most of the band. X_{opt} , however, reveals that further improvement is possible through a matching network either external or internal to the module. To investigate compensation within the module, 64.8 pS of electrical length was de-embedded from Z_{opt} ,⁴² corresponding to a 6 mm distance behind the amplifiers SMA input connector. The corresponding value of Z_{opt} is provided by the black traces in figure 4.34. At 1.2 GHz, $Z_s = Z_{opt}$ if a 33 Ω resistor and 2.7 nH inductor are placed in series, 6 mm behind the input of the amplifier. This modification to the amplifier is shown on the left of figure 4.34. The

⁴² T_{min} and N are invariant under lossless impedance transformation.

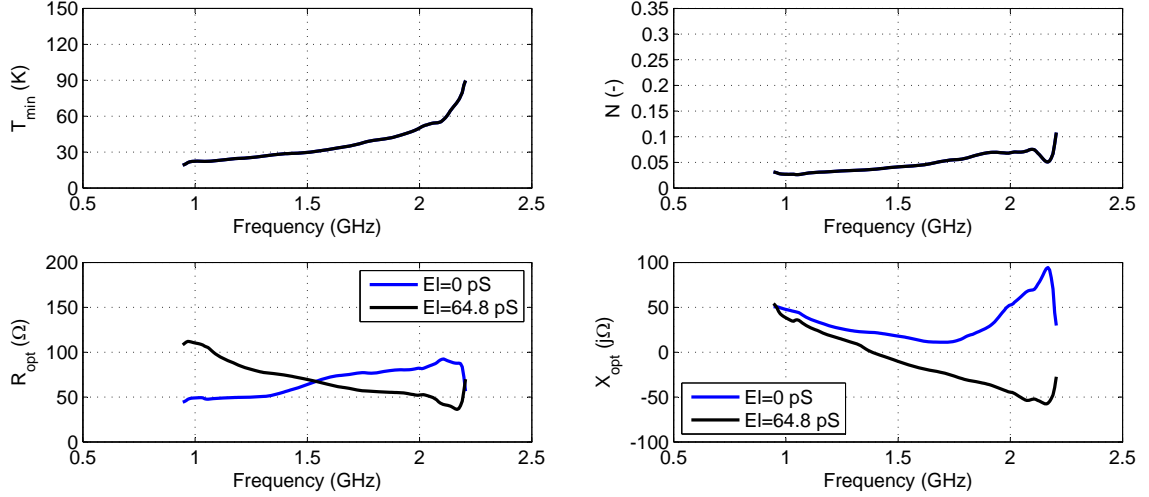


Figure 4.33: Noise parameters for ambient temperature, ultra low noise amplifier. Bias conditions were $V_g = -0.4$ V at $0.11 \mu\text{A}$, $V_d = 1.43$ V at 74 mA . R_{opt} and X_{opt} are provided at the reference plane of the input connector (blue trace) and with 64.8 pS of electrical length de-embedded (black trace). The de-embedded values are used to determine the appropriate matching network to be integrated within the amplifier so that $Z_s = Z_{opt}$ at 1.2 GHz .

noise temperature was then measured and compared against that without the network, the results shown on the right of the same figure. The measured noise temperature must be corrected, however, to remove the noise introduced by the series resistor. This is accomplished through combining the Friis noise equation with the noise contribution of the series resistor and its available gain:

$$T_n = \left(T_{meas} - \frac{R}{R_s} T_{phy} \right) \frac{R_s}{R_s + R},$$

where R is the series resistor, T_{phy} is the physical temperature of the resistor, $R_s = \Re(Z_s)$, and T_{meas} is the measured noise temperature with the resistor included. The results reveal that the noise is minimized at 1.2 GHz , in very good agreement with the predictions made from the extracted noise parameters.

To provide further validation of the noise parameters, separate measurements of the amplifiers noise temperature were made with an Agilent 50Ω noise source, previously calibrated against a liquid nitrogen (LN2) load [51]. The results from these measurements are compared against calculations from the measured noise parameters, of the noise temperature of the amplifier when presented by a source impedance of 50Ω , as shown in the top of figure 4.35. The results from 0.95 to 1.5 GHz are in good agreement. Beyond this the two separate, the reason being that the measurement made with the LLM was made without the NFA calibrated, for reasons previously discussed. The use of a low noise post amplifier could be used in the future to reduce the backend noise contribution, in place of NFA calibration. The factor $4NT_0/T_{min}$, shown in the bottom of figure 4.35 is between 1

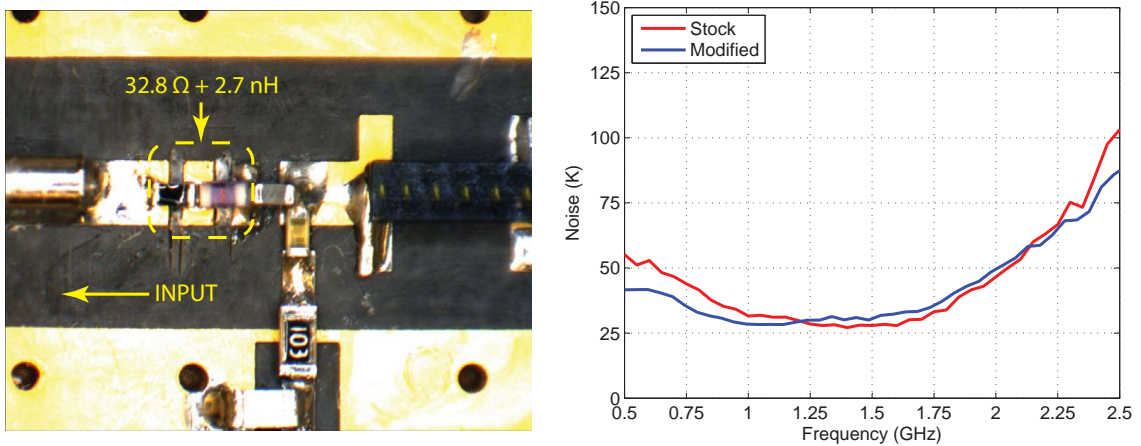


Figure 4.34: Verification of noise parameters for the ultra-low-noise amplifier. (Left) Close-up of amplifier input, where a 32.8Ω and 2.7 nH inductor have been placed in series to match Z_{opt} at 1.2 GHz. (Right) Measured input noise temperature of the amplifier, before and after modification to its input, with the noise of the resistor removed from the measurement. T_n is minimized at ≈ 1.2 GHz, as predicted.

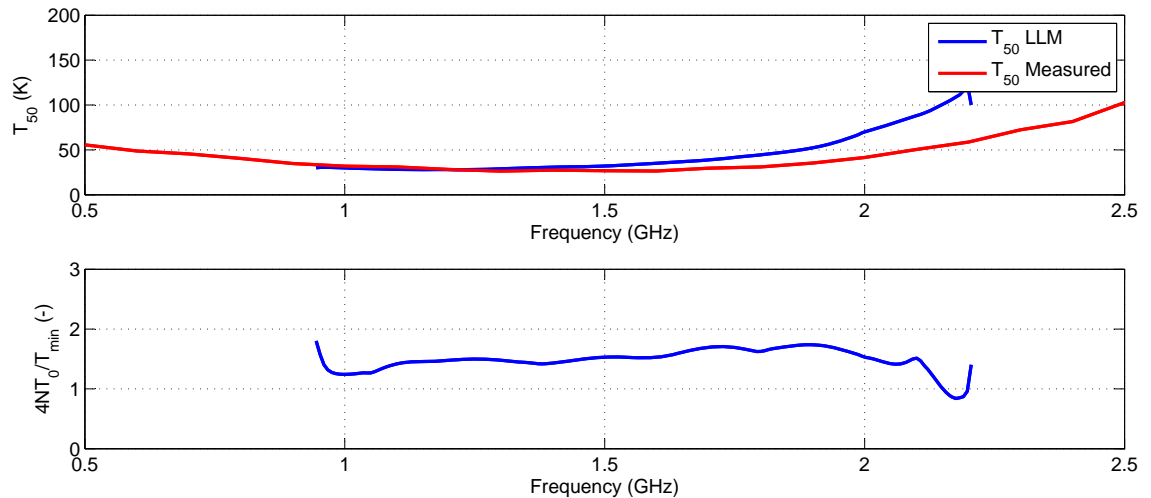


Figure 4.35: Verification of noise parameters for the ultra-low-noise amplifier. (Top) Comparison of the calculation of T_{50} determined from the measured noise parameters and that from a separate measurement using a 50Ω noise source. The LLM measurement is uncorrected for the noise of the NFA, leading to the deviation between the two measurements at higher frequency as the gain of the amplifier decreases. (Bottom) Verification that the ratio $4NT_0/T_{min}$ lies between 1 and 2.

and 2 as required.

4.8.2.2 Wideband MMIC LNA module

In order to further demonstrate the capabilities of the system, a wide-band InP amplifier [52], was measured at ambient temperature from 0.750 to 6.7575 GHz, the results provided in figure 4.36. Validity of these noise parameters was tested by using them to compute the noise temperature with a $50\ \Omega$ source, compared against that measured using an Agilent NFA and SNS. The results between the two measurements are in good agreement, as observed in the top of figure 4.37. There is no deviation between the two measurements, as was with the case for the ultra-low-noise amplifier, due to the amplifier's high gain (~ 30 dB). Shown at the bottom of figure 4.37 is the factor $4NT_0/T_{min}$, verified to be between 1 and 2.

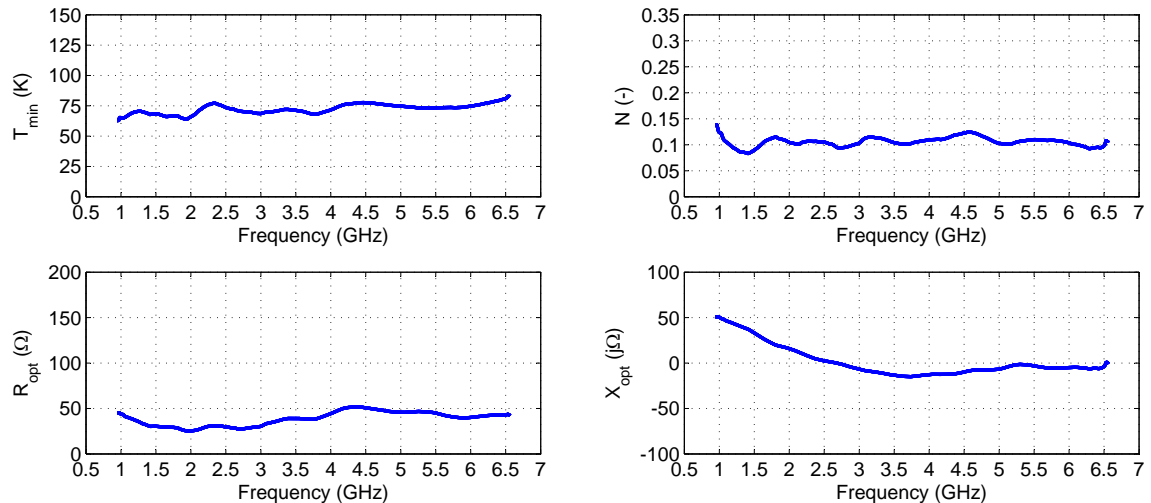


Figure 4.36: Noise parameters for the wide-band MMIC LNA module at ambient temperature. Bias conditions are $V_{g1}=-0.4$ V, $V_{g2}=-0.4$ V, $V_d=1.8$ V at 50 mA.

These measurements, combined with separate S-parameter measurements of the LNA, were used to evaluate the systematic errors in the measurement, per equation (4.42). The contribution from the change in system gain, due to the change in reflection coefficient between on and off states (equation (4.40)), dominates in this case. This systematic error is shown in figure 4.38. The error is large ($\sim 7\%$), but the effect on the extracted noise parameters is fairly small due to several factors:

1. Several of the largest peaks, at lower frequencies, are disregarded as they correspond to frequencies where $Y_{dut} < 1.25$, which were not used during the extraction through the appropriate setting of Y_{thr} .
2. The systematic error cycles above and below zero several times within a sampling window (400

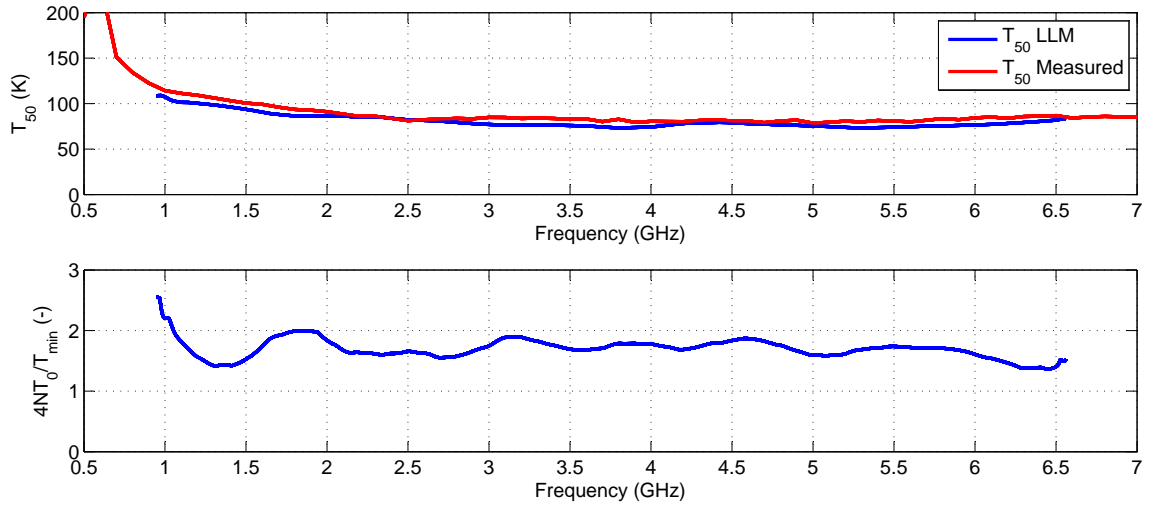


Figure 4.37: Verification of noise parameters for the wideband MMIC LNA. (Top) Comparison of T_{50} from calculations using the measured noise parameters and from a separate measurement using a 50Ω noise source. (Bottom) Verification that $4NT_0/T_{min}$ lies between 1 and 2.

MHz). This cyclical error is averaged across the sampling window, thus leading to a decreased impact on the noise parameters.

The effect of the systematic error is shown in figure 4.38, compared against the noise parameters extracted without compensation for this error. The results reveal only a small susceptibility to systematic error.

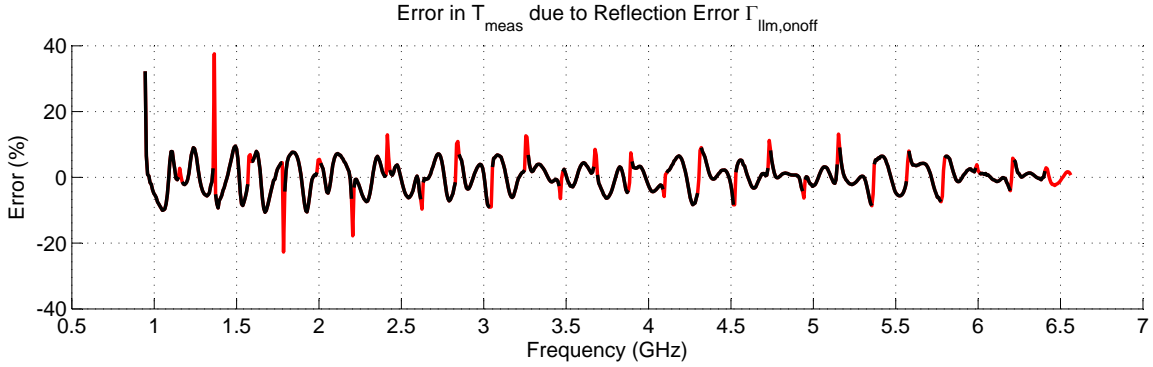


Figure 4.38: Reflection error, caused by the change in impedance of the LLM between on and off states of its internal noise source, in the measured noise temperature of the wideband MMIC LNA. The *black* regions of the trace indicate frequencies where $Y_{meas} > 1.25$, the threshold used for the Y-factors used in the extraction.

Finally, equation (4.38) was used to analyze the effect of random error on the measurement, a combination of uncertainties from the LLM calibration, measured Y-factor of the DUT, and

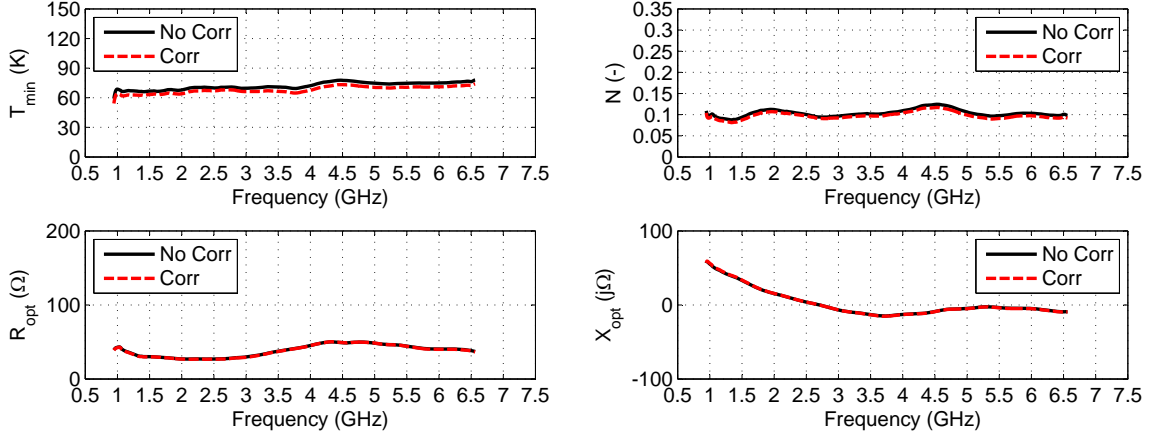


Figure 4.39: Influence of reflection errors, between on and off states of the LLM, on the extracted noise parameters for the wideband MMIC LNA. *Black* traces are noise parameters without correction and *red* traces are noise parameters with correction applied to the measured Y-factors. The correction only effects T_{min} and N to a small degree.

temperature sensor uncertainties. The effect on the noise parameters was again calculated using Monte Carlo analysis, the results shown in figure 4.40 after 100 simulation runs. They indicate that the percentage error is extremely low, <2% over the majority of the measurement range. ΔX_{Opt} increases periodically, a result of the normalization by X_{Opt} which crosses 0 at several points (refer to figure 4.36).

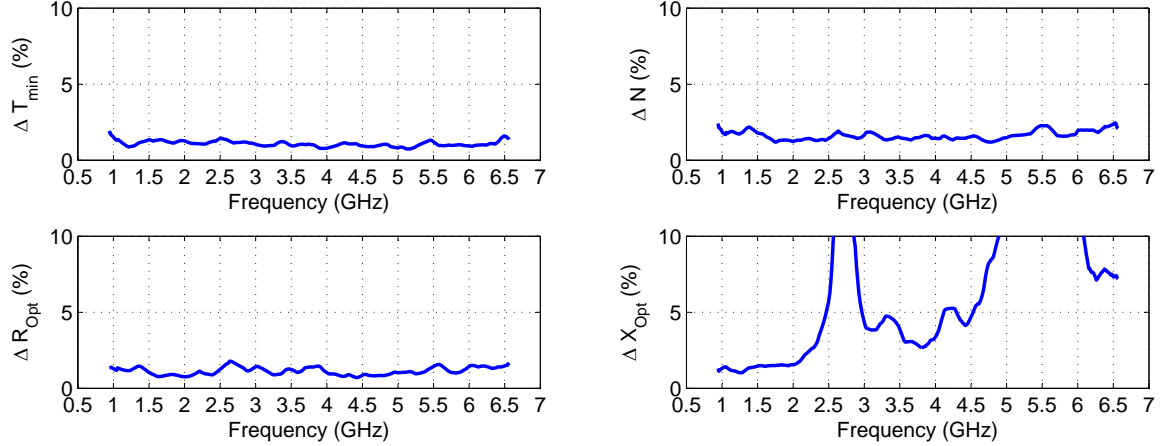


Figure 4.40: Noise parameter uncertainty of the wideband MMIC LNA due to random errors. The uncertainty is <2% over most of the band with the exception of ΔX_{opt} . The increase in ΔX_{opt} is due the normalization of the error, as X_{opt} is ~ 0 at 2.6 and 5.5 GHz (refer to figure 4.36)

4.9 Suggestions for Future Work

Although both modules can be calibrated to at least 12 GHz, this has not yet been done, due mainly to the availability of a wideband, LNA over this frequency range, for use in the frontend during calibration. In addition to low noise, this amplifier should also well matched, to reduce systematic errors as discussed in section 4.4.2. In the near term, a combination of LNAs may be necessary. Below \sim 5 GHz, SiGe LNAs may be used were the use of resistive feedback allows for improved low frequency match, as will be discussed in chapter 5. Above this frequency, InP HEMT based amplifiers have suitable return loss, and lower noise than their current SiGe HBT counterparts. A similar LNA should follow the DUT during noise parameter measurements, if the same NFA is continued to be used in uncorrected mode. This will reduce the backend noise contribution, especially for DUTs with low gain.

The receiver is another area for possible improvement. Although the Agilent N8975A NFA is a powerful instrument, it does have several limitations that come to light when used with the LLM and its calibration scheme. The first of these is in the limited adjustability of its resolution bandwidth (RBW). While 4 MHz is suitable for the cryogenic module described in this work, a larger RBW would be desired if a higher frequency module where to be designed, say with smaller line lengths utilized in the mismatch network. Larger RBW would also be useful in the thermal calibration of the current ambient/cryogenic module. As T_{int} is measured at the output of the internal noise source, the frequency response is relatively flat. Increasing RBW beyond 4 MHz is possible in such a scenario, allowing for increased measurement speed or lower measurement uncertainty.

Similarly, adjustability in the integration time of the receiver would also be a welcome addition. This would provide a separate “knob” to optimize measurement speed and uncertainty. It is currently fixed at 16 mS within the NFA, no doubt driven by the gain stability of its receiver, some assumption of the gain stability of the DUTs to be measured, and the settling time (on/off transitions) of the solid state noise sources used with the NFA.

The limits of bandwidth and integration time with existing NFA’s could be greatly improved by multichannel digital spectrometer processing. One frequency at a time is measured by the NFA so that the time between 16 mS integrations is several seconds when hundreds of frequency points are measured. For example, a combination of digital spectrometer analyzing, with 400 MHz of bandwidth and 4 MHz resolution, and stepped by a local oscillator in 400 MHz steps would allow for a factor of 100 improvement in either the integration time or the time per measurement.

Full adjustability of the attenuators used within the RF and IF signal paths of the receiver would also be welcome. The NFA automatically updates these to keep its square law detector within its linear range. Measurements with low Y-factor, and therefore high measured noise temperature, are not used during the noise parameter extraction process due to their inherent uncertainty. It may

therefore be beneficial to use a lower value of RF/IF attenuation for improved sensitivity where the Y-factor is large, sacrificing linearity at low Y-factors which are disregarded anyway.

Work on the numerical methods used with the extraction algorithm is also an area to be addressed. Hu [43] revealed that some of the ripple contained on the extracted noise parameters can be attributed to spectral harmonics created by moving a rectangular sampling window across the measured noise temperature data. This is somewhat expected, as the extraction algorithm effectively convolves the sampling window (rectangular pulse) with the measured noise temperature data. Hu suggested the use of a triangular frequency-sampling window which would reduce the presence of these harmonics in the extracted parameters. The uncertainty analysis performed in section 4.6, however, revealed that the random component of error in the measured noise temperature is inversely proportional to $(Y_{dut} - 1)$. It is beneficial, therefore, to “weight” measurements with a larger Y-factor more strongly than those with a low Y-factor. This is the reason why weighting was used in the extraction algorithm, but it is yet to be determined what the resulting numerical effects are on the noise parameters.

Improvement to the low frequency performance of the LLM could also be addressed. It is currently limited by the AC coupling capacitors used to bias the internal noise source and in the bias-tee. Extremely broadband RF blocking capacitors are now available from companies such as AVX.⁴³ While these work superbly at ambient temperature, their large temperature dependence would likely preclude their use cryogenically.

The attenuator value used within the cryogenic module could be increased. figure 4.14 reveals that T_{int} is ≈ 600 K, likely a factor of 10 higher than is actually required for DUTs with noise temperatures < 20 K. This would provide two benefits: a reduction in systematic errors due to changes in Γ_{llm} between on and off states; and a reduced susceptibility to linearity errors, both within the receiver and DUT itself.

Finally, there remains development work to be performed on the mismatch network within the LLM. One of its limitations is that its impedance constellation is not able to continuously enclose Z_{opt} , of the DUT, over a broad frequency range. The periodic response of the LLM moves counter-clockwise about the Smith Chart, often much more rapidly than Z_{opt} . Therefor, there exist ranges of frequencies where Z_{opt} is not enclosed. This becomes more important as the random measurement error increases, as enclosure of Z_{opt} helps to lower the susceptibility to these errors. Exacerbating the situation is the electrical length that may be added due to packaging, ahead of the first device contained therein.

⁴³AVX p/n GX01ZD103PATD-500. AVX Corporation. 1 AVX Blvd., Fountain Inn, SC 29644, U.S.A.

4.10 Summary

In this chapter, a cryogenic-ambient noise parameter measurement system has been presented. It utilizes a variable impedance noise source allowing noise parameter determination from its measurement alone, unlike previous networks that required an additional “matched” measurement. The construction of two modules, one suitable for use at cryogenic temperatures only and the other for operation at both ambient and cryogenic temperatures, have been presented. Principles detailing their calibration and related measurement uncertainties were presented next. The novel, self-calibrating scheme allows for measurement of the LLM’s excess noise temperature with only a single cryogenic cool down. This approach is not unique in use with the LLM and may, in principle, be adapted to the calibration of any noise source. Details were then provided for the noise parameter extraction algorithm written for the system, and a discussion of corresponding uncertainties. The last two sections presented examples of cryogenic and room temperature calibrations and noise parameter measurements made with the LLM. Uncertainties were evaluated and shown to have cumulative values roughly half that of commercially available noise sources. Measurements were compared against theory and independent measurement, with very good agreement between the two.

Chapter 5

Low-Noise, SiGe, IF Amplifiers for THz Mixer Receivers

5.1 Introduction

In this chapter, SiGe, intermediate-frequency low-noise amplifiers (IFLNAs) for use with superconducting mixers are discussed and several designs presented. Background material is first provided on superconducting mixers, the design requirements imposed on the IFLNA, and SiGe heterojunction bipolar transistors (HBTs). Design of cryogenic SiGe amplifiers follows in section 5.3 beginning with a discussion on HBT modeling. Although the majority of the material presented is focused toward monolithic microwave integrated circuit (MMIC) implementation, it is equally applicable to discrete amplifiers as well. The measurement of cryogenic LNAs using the cold attenuator method is then discussed, including the corresponding uncertainties. Several examples of IFLNAs are presented next, where the trade offs in noise temperature and bandwidth vs. DC power consumption are explored. Section 5.6 discusses future work on SiGe IFLNAs.

The MMICs and discrete HBTs discussed in this chapter were fabricated on a commercial 130 nm BiCMOS9MW process from ST Microelectronics.¹ Bardin² [10] compared cooled SiGe from five different manufacturers³ and found that from ST-Microelectronics offered the best cryogenic performance. The work presented here is based on two wafer runs, herein referred to as CITST1 and CITST2, from ST Microelectronics. These runs were processed through Circuits Multi-Projects⁴ (CMP), the reticle for CITST1 shown in figure 5.1.

Bardin provided the initial small signal models for these designs, based on his characterization of ST-G4 experimental devices. Run CITST1 used a standard BiCMOS9MW process, β and g_m for these devices being lower than expected. This difference is attributed to the use of the standard SiGe

¹ST Microelectronics,12 rue Jules Horowitz B.P. 217, Grenoble 38019, France.

²Ph.D. 2009, California Institute of Technology.

³NXP, IBM, Jazz, IHP, and ST-Microelectronics

⁴CMP, 46 Avenue Felix Viallet, 38031 Gernoble Cedex, France.

process, rather than the experimental process utilized in the manufacturing of the ST-G4 devices previously characterized. The discrete devices from the CITST1 run were subsequently characterized and a new small signal model produced, and was used for the design of the MMICs contained on the second run, CITST2. β enhancement was requested for the CITST2 run, in hopes of obtaining devices that approached the ST-G4 performance. Although β was almost twice as high as the earlier CITST1 run, the transconductance was unfortunately lower. It will be shown in Section 5.2.3 that maximizing both β and g_m is essential for minimization of HBT noise temperature.

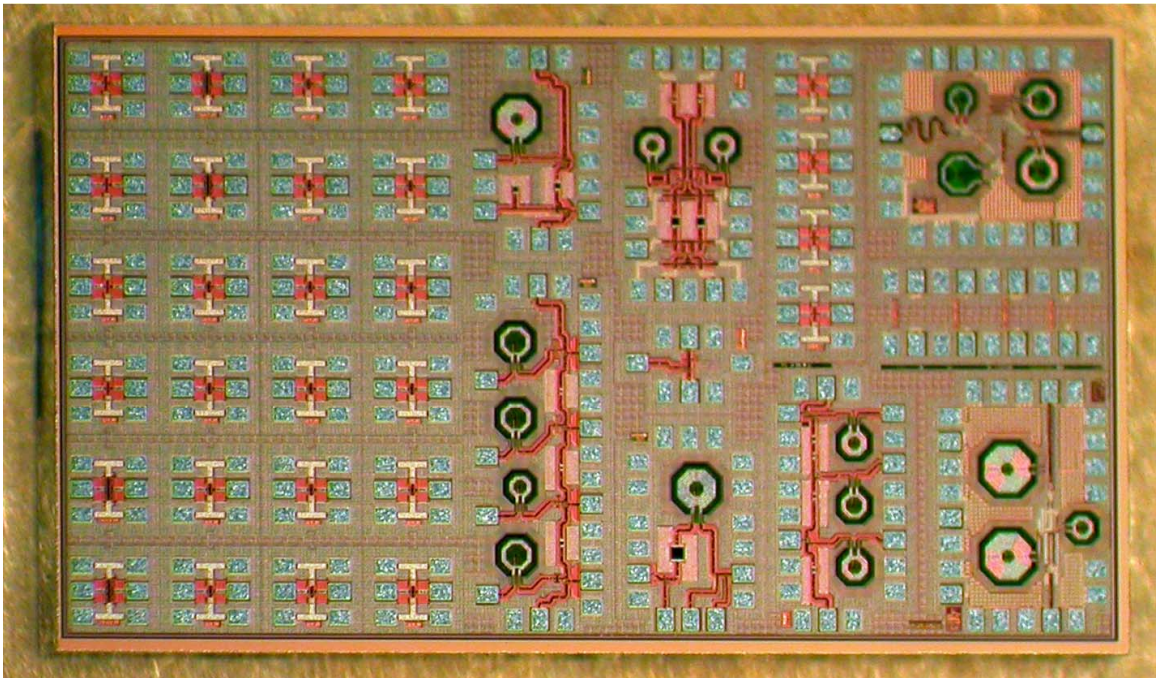


Figure 5.1: Photograph of the CITST1 SiGe reticle. Dimensions are $4.1 \text{ mm} \times 2.3 \text{ mm}$. Discrete HBTs with emitter areas of 1.3 , 2.6 , 9.75 , and $31.6 \mu\text{m}^2$ are on the left of the reticle, IFLNA designs on the right. “Dicing streets,” or distance between adjacent devices, are $100 \mu\text{m}$. The CITST2 reticle is similar in size and layout. A summary of IFLNA designs included in these reticles can be found in table 5.8.

5.2 Background

Based on spectroscopies need for high sensitivity and spectral resolution ($\lambda/\Delta\lambda$) of up to 10^6 [53], heterodyne receivers are employed with large focal plane arrays of superconducting mixers. These mixers are either superconducting-insulator-superconducting (SIS) or hot-electron-bolometers (HEB), cooled to liquid helium (LHE) temperatures. figure 5.2 illustrates the block diagram of one of the individual receiver elements, or pixels, contained within an array. The local-oscillator (LO) is multiplexed either quasi-optically or by a network of waveguide splitters and couplers to the array’s

pixels. Up to several terahertz, the LO can be sourced by a microwave oscillator followed by a chain of diode multipliers. Output powers of up to $3 \mu\text{W}$ at 1.7 GHz have been reported [54], whereas the LO power required by SIS and HEB mixers is on the order of 0.1 to $1 \mu\text{W}$ per device. Above this frequency, quantum cascade lasers have been demonstrated [55], and show promise of providing the LO power necessary to pump large terahertz arrays.

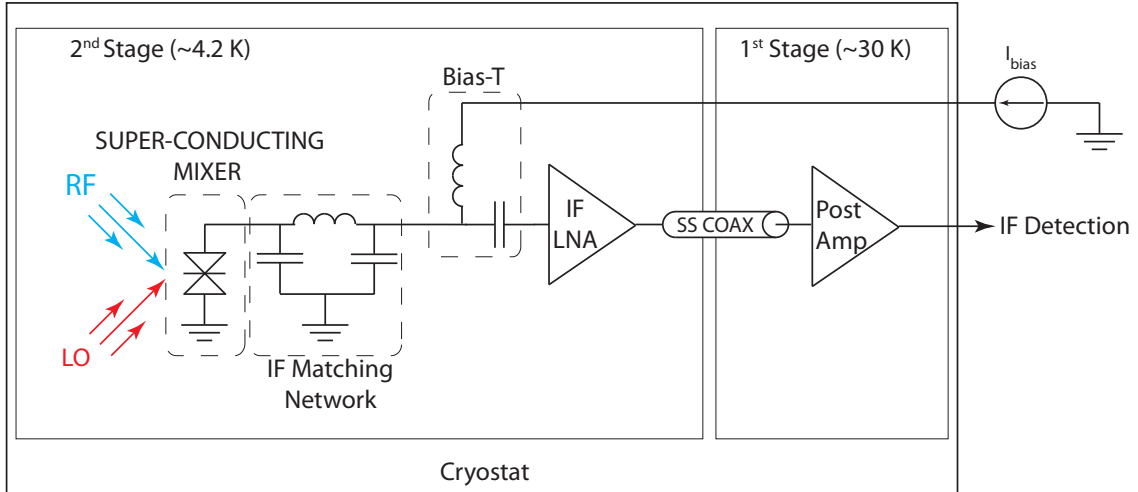


Figure 5.2: Block diagram of a THz receiver element, or pixel. The LO is distributed either quasi-optically or through a network of waveguide splitters and couplers. The superconducting mixer is cooled to LHE temperatures, either through liquid cryogens or with a mechanical cryocooler. Additional gain is provided following the IFLNA, which is either cooled if the IFLNA has low gain or at room temperature if the IFLNA gain is large (~ 30 dB). Thermal isolation between temperature stages may be achieved with the use of SS coaxial line.

5.2.1 Superconducting Mixers

Zmuidzinas [56] provides an excellent review of the SIS mixers, their operation and physical limitations summarized here. SIS mixers are employed from approximately 100 GHz to 1.4 THz, with sensitivities of twice the quantum limit⁵ for frequencies well below the superconducting energy gap. They are employed either individually or as a balanced pair. Typical construction consists of an extremely thin layer, 5–20 Å thick, of Al_2O_3 and AlN sandwiched between two superconductors, Nb and/or NbTiN . The bandgap of the superconductor, 2Δ , sets a fundamental limit on the upper frequency of operation. Below the bandgap, photons may assist in the tunneling of electrons across the junction. Above the bandgap, the superconducting junction behaves as a metal, electrons passing freely in either direction. For junctions comprised of Nb only, this limit corresponds to ≈ 680 GHz. The use of NbTiN for at least one of the superconductors, combined with special fabrication techniques, allows for an upper frequency of ≈ 1.4 THz [57].

⁵ $h\nu/k$ or ~ 0.05 K/GHz

Although the thin junction is necessary for tunneling, it leads to a significant capacitance. For a $\sim 1 \mu\text{m}^2$ junction, the junction capacitance is on the order of 100 fF, depending on the particular materials system. This, coupled with the normal resistance, R_n , of the junction, imposes another limit on the upper RF frequency the mixer is operated at. Although series inductance can be added to resonate the junction capacitance, the Q of this inductance decreases with increasing frequency, ultimately limiting noise and conversion loss. Packaging of the device adds additional parasitic capacitance, particularly at the device's IF port.⁶ This may account for 100–200 fF alone. For a device with 300 fF total capacitance seen by the IF port and $50 \Omega R_n$, the resulting IF bandwidth is limited to 10.6 GHz.

Without applied bias, only photons with energy greater than the superconductor bandgap, 2Δ , may provide electrons with enough energy to tunnel across the barrier between the superconducting electrodes. Application of a DC bias, V_{dc} , to the junction lowers this threshold by an amount qV_{dc} , where q is the electron charge. With the lowered barrier, photons with energy $hf \geq 2\Delta - qV_{dc}$ may participate in photon assisted tunneling. This is illustrated in figure 5.3 where a simplified construction diagram, band diagram, and I-V characteristics of a SIS junction are shown. To suppress the Josephson effect, where a DC current can exist within the junction without the application of an applied field, a DC magnetic field is supplied to the junction.

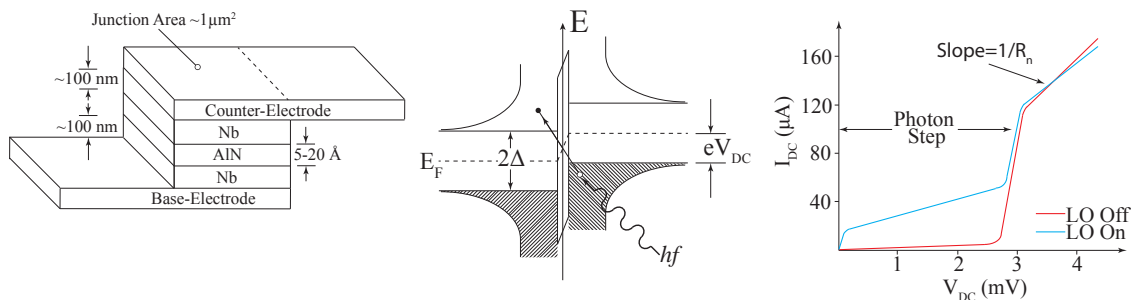


Figure 5.3: (Left) Simplified SIS junction showing typical superconductor and insulating layer thicknesses. The base and counter electrodes are wiring layers. The junction itself is typically deposited on a thin quartz substrate, which may also contain the mixer's waveguide probes, series inductance, and IF filter. (Middle) SIS energy band diagram. Application of a DC bias to the electrodes reduces the offset between conduction and valence bands on either side of the junction. Electrons with energy $hf \geq 2\Delta - qV_{dc}$ may tunnel across the thin insulating layer, through absorption of incoming radiation. (Right) Junction I-V characteristics. The photon step corresponds to $hf/q = 2.8 \text{ mV}$ at 680 GHz for Nb junctions. Above this frequency the superconductor behaves as a metal.

Fortunately, HEB mixers do not have these same physical constraints and are able to operate well above the frequency limits of the SIS junctions. In addition, they require very little LO power, $\sim 0.1 \mu\text{W}$ [58] is typically required, about a factor of 10 lower than their SIS counterparts. The devices are

⁶A low-pass filter for the mixer's IF port is usually integrated with the SIS junction, fabricated on the same substrate. Parasitic bond pad capacitance is therefore not seen by the mixer at THz frequencies.

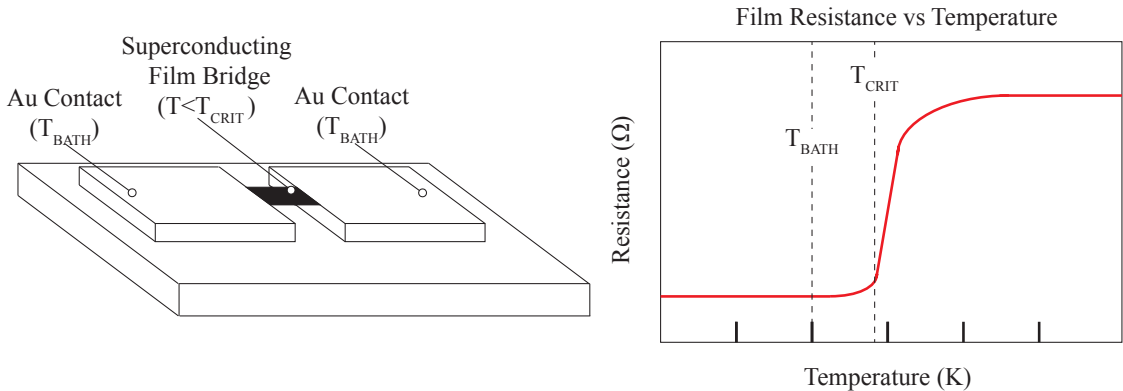


Figure 5.4: (Left) Simplified HEB physical structure. A superconducting film bridge is placed between the two electrodes of the device. The entire structure is immersed in a bath temperature, T_b , below the critical temperature, T_{cr} , of the superconducting element. (Right) Resistance across the superconducting film bridge versus temperature. The application of DC and LO power to the structure raises the temperature of the superconductor close to its critical temperature. Application of a small amount of RF power raises the temperature of the film slightly, but produces a large change in its resistance. This strong nonlinear behavior aids in mixing efficiency.

constructed from a thin film of superconductor, bridging a narrow gap between the two electrodes of the device. The entire mixer resides in a bath temperature, T_b , below the critical temperature, T_{cr} , of the superconductor. DC bias and LO power are applied to increase the junction's temperature close to the superconductor's critical temperature. Incident photons with sufficient energy, hf , to increase the junction temperature above the critical temperature, produce a large change in the resistance of the device. This strong nonlinearity aids in the IF mixing efficiency. There are however two drawbacks to HEB mixers, their slow thermal response and higher noise than their SIS counterparts. Although much improved over its bolometer predecessors, the thermal capacity of the junction and its thermal conductivity to the surrounding bath limit its bandwidth to ~ 4 GHz, for state of the art devices. Additionally, the noise of these devices is about a factor of 20 times the quantum limit, an order of magnitude above that of SIS mixers [56].

5.2.2 Low-Noise, IF Amplifier Design Constraints

Referring to figure 5.2, the mixer is followed by an IFLNA which is also cooled, to lower its own noise. The noise temperature of this amplifier should be minimized, as the conversion gain of superconducting mixers is typically in the neighborhood of -8 dB (DSB). The effect of low conversion gain can be seen in the effective system noise temperature [59],⁷

$$T_{Sys, DSB} = T_{Ant} + T_{DSB} + T'_{IF}/(2G_{conv}) , \quad (5.1)$$

⁷Not accounting for losses due to the optics in front of the mixer

where the double side band noise temperature, T_{DSB} , is comprised of contributions from the antenna noise temperature, T_{Ant} , and the effective input noise temperature of the IF chain, T'_{IF} . T'_{IF} is itself comprised of the IFLNA noise and the noise of the backend electronics, T_{BE} , which follow it. Like $T_{Sys,DSB}$ above, T'_{IF} is calculated using the Friis noise equation [1], where G_{IF} is the available gain of the IFLNA.

$$T'_{IF} = T_{IF} + \frac{T_{BE}}{G_{IF}} \quad (5.2)$$

Inspection of (5.1) and (5.2) reveals a trade-off in the design of the LNA following the mixer. Its noise should be minimized and its gain maximized. Unfortunately, increasing the gain also increases the power dissipation of the IFLNA, which itself should be minimized if the amplifier is to be mounted immediately next to the mixer at the same physical temperature. IFLNAs with higher power dissipation may be used if thermally isolated from the mixer, through the use of a short section of stainless steel coaxial line, for example. This packaging option is explored further in section 5.5.2. To ease assembly, integration with the mixer is preferred, as it simplifies the assembly and eliminates any unwanted phasing of reflections between the mixer and amplifier that might occur within the IF band. Minimizing the power dissipation also reduces the burden on the design of the cryogenics and the number of cryocoolers necessary. Alternatively, for balloon flights such as STO (refer to table 1.1), minimizing the power dissipation allows for longer flight times, as liquid cryogens are consumed at a slower rate.

In addition to low noise and power dissipation, the amplifier should have be well matched,⁸ either by itself, or through the use of a matching network between the mixer and IFLNA. This is particularly important for HEB mixers, as some portion of the reflected power from the LNA is absorbed by the superconducting film bridge, thus raising its temperature, an effect known as thermoelectric feedback [60]. A low return loss also flattens the gain response of the mixer/amplifier combination, reducing the amount of gain compensation that may be necessary. Although an isolator may be used between mixer and IFLNA, this both complicates and increases the size of the assembly, as well as adding to the noise. IFLNAs with low return loss are therefore preferred.

Finally, to aide in integration, the amplifier should be as small as possible, and require few external components, so that the spacing between pixels may be made as small as possible.⁹ Integrating the mixer's bias-tee and the IF matching network within the IFLNA further reduces the envelope of the electronics and eases the manufacturing of very large arrays of terahertz receivers.

⁸ ≤ -10 dB is usually sufficient.

⁹Ideally, all components would fit within the footprint of the mixer's feed.

5.2.3 Heterojunction, SiGe, Bipolar Transistors

Traditionally, superconducting arrays have used III-V devices, such as InP and GaAs, for the IF LNA [7]. Although they provide remarkable cryogenic noise performance, they have the following limitations:

1. Poor low frequency return loss. Although SIS devices may use a higher IF frequency, such as 4–8 GHz, the time constant associated with HEB mixers limits their upper IF frequency to \sim 4 GHz. Below this range, the return loss of HEMTs are relatively poor. Isolators or balanced amplifiers are required in this case.
2. Low yield. As described in the introduction, the yield of InP devices is currently very low, \sim 50%. Very large THz receiver arrays would require the testing of a significant number of devices. This would be a daunting task, even with the benefits of automated cryogenic wafer probing, using the system described in chapter 2.

These problems are alleviated with the use of SiGe HBTs that offer similar noise performance to InP HEMTs for frequencies less than \approx 5 GHz but have inherent high yield due to the maturity of Si processing. Resistive feedback may be used between the base and collector of HBTs, simplifying biasing and improving the low frequency return loss over what is attainable with their FET counterparts. The use of SiGe HBT's, as part of a BiCMOS process, also allows the benefits of additional metal layers¹⁰ and a wide variety of passive components.

Bardin [10] studied cooled SiGe extensively, and found that its exceptional noise performance was due primarily to the dramatic increase in β and g_m with cooling. Inspection of the equivalent small signal noise model, shown in figure 5.5, for the HBT reveals why these improvements with cooling are so important. For now, C_{be} and C_{bc} are ignored, as the low frequency noise behavior of the HBT will be determined. The equivalent noise temperature, for the common-emitter configuration, may be calculated by comparing the short circuited current at the output, due to the generator resistance, to that from each of the device's internal noise sources [11], [61]. These internal noise sources are uncorrelated and thus add as mean squares to the device noise temperature, T_n . The individual components of which are summarized below, where it is assumed that $\beta \gg 1$ and $R_g/\beta \ll 1/g_m$.

¹⁰6 metal layers are available in the BiCMOS9mw process from ST-Microelectronics, compared with only 2-3 metal layers commonly used in InP processing

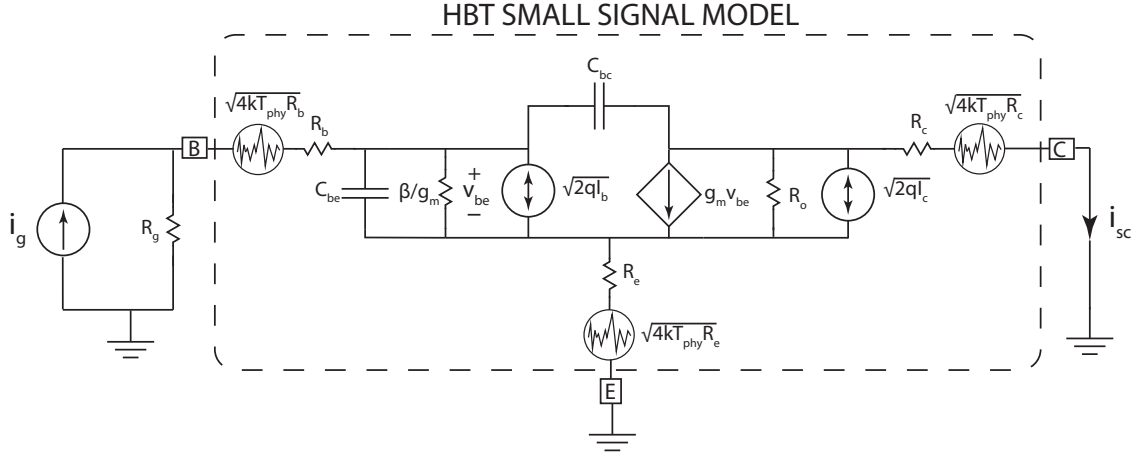


Figure 5.5: HBT noise model. T_{phy} is the physical temperature of the device. R_b , R_c , and R_e generate thermal noise while the base and collector currents generate shot noise. The effective noise temperature is calculated by determining the contribution of each noise source to $|\overline{i_{sc}}|^2$, the expected value, of the magnitude squared, of the short circuit output current. This is compared to that due to the generator (source), i_g .

$$\begin{aligned}
 T_{n,R_b} &= T_{phy} \frac{R_b}{R_g} \\
 T_{n,R_c} &= T_{phy} \frac{R_c}{R_o^2} (1/g_m + R_e)^2 \frac{R_g + R_b}{R_g^2} \\
 T_{n,R_e} &= T_{phy} \frac{R_e (R_g + R_b)}{R_g^2} \\
 T_{n,I_b} &= \frac{qI_c}{2k\beta} (R_g + R_b) \\
 T_{n,I_c} &= \frac{qI_c}{2kR_g^2} (1/g_m + R_e)^2 (R_g + R_b)
 \end{aligned}$$

Since the collector to emitter resistance, R_o , is usually $>1 \text{ M}\Omega$, the noise contribution from R_c can be ignored. The remaining terms are combined in equation (5.3) to form the total, low frequency, noise contribution from the HBT¹¹. The term on the left represents the contribution due to base and collector shot noise, and that on the right corresponds to thermal noise of internal resistances.

$$T_n = \frac{qI_c}{2k} (R_g + R_b) \left(1/\beta + \left(\frac{1/g_m + R_e}{R_g} \right)^2 \right) + T_{phy} \left(\frac{R_b}{R_g} + R_e \frac{R_g + R_b}{R_g^2} \right) \quad (5.3)$$

It is immediately obvious that increasing both β and g_m reduces the shot noise contributions from the base and collector. R_b is the other dominant noise source and can be partially minimized

¹¹Note that 1/f noise processes, such as generation-recombination noise, has not been included here. It is assumed that their spectral components are negligible at 500 MHz, the lowest frequency the IFLNAs are operated at.

through careful layout.¹² R_e should also be minimized, for although its own noise contribution is small, its effect on gain increases the contribution from the collector shot noise.

5.3 Design of Low-Noise Cryogenic MMIC Amplifiers

In this section, the design of cryogenic LNAs is discussed, starting with device characterization. Although much of the work here is geared toward MMIC implementation, the concepts and approaches taken are equally applicable to discrete amplifier design as well. Both the characterization and designs to follow focus on HBTs in the common-emitter configuration.

5.3.1 Device Modeling

Device modeling, or characterization, is essential to low noise amplifier design. The goal being the production of an accurate, scalable, small signal model for the transistor, which can be used in conjunction with a circuit simulator such as AWR's Microwave Office (MWO). The HBT's small signal model was revealed earlier in figure 5.5, the determination of its element values presented in this section. The first-order modeling approach presented will be shown to provide accurate estimates of device performance in the DC–8 GHz range, sufficient for the design of the IFLNAs presented here. More advanced modeling techniques are described in detail by Bardin [10], yielding highly accurate device performance estimation at much higher frequencies.

The device models presented are based on characterization of the discrete transistors contained within the CITST1 and CITST2 reticles. Their simplified device structure and summary of sizes (device areas) and configurations is provided in figure 5.6 and table 5.1 respectively. Each of these devices was mounted in a coaxial fixture for characterization, an example of which is shown in figure 5.7. Figure 5.8 illustrates the test setup used in the DC and RF characterization of these devices, its configuration discussed in further detail in the following sections. The characterization sequence is as follows:

1. DC measurements of device current gain, $\beta = I_c/I_b$, and transconductance, $g_m = \partial I_c/\partial V_{be}$. Additional measurements are made of I_c vs. V_{ce} at multiple values of base current to determine at which point device self-heating occurs. It is necessary to operate a device below this power level, at least in the first stage of an amplifier, to ensure that the noise is minimized. Self-heating increases the device physical temperature, which in turn increases the noise.
2. Low frequency response of S_{21} measured to determine if g_m derived from DC (static g_m) measurements is consistent with that determined vs. frequency (dynamic g_m).

¹²This can be done by routing the interconnects on the top metal layers within the IC, and using multiple vias to connect down to the base contact.

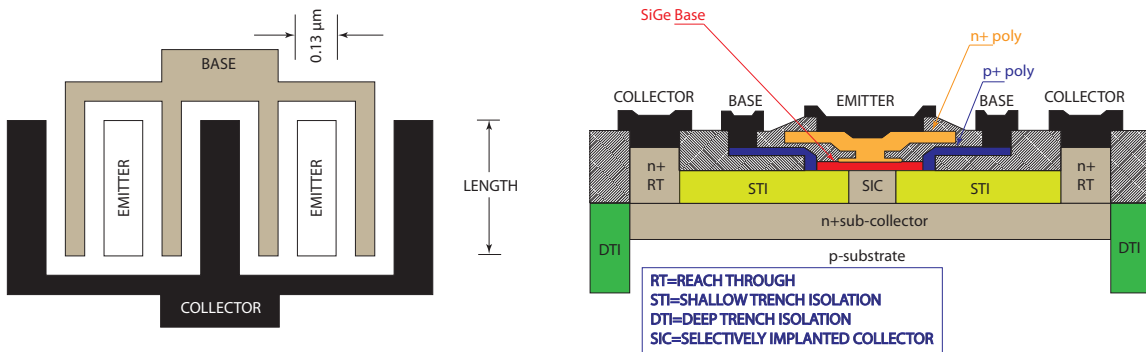


Figure 5.6: (Left) Top view of HBT ‘C-B-E-B-C’ layout for a transistor comprised of two emitter contacts (stripes). (Right) Simplified cross section of HBT C-B-E-B-C construction.

| Run | Emitter Stripes | Stripe Length | Devices in | Device Size |
|--------|-----------------|---------------|------------|-----------------|
| - | # | μm | # | μm ² |
| CITST1 | 1 | 10 | 1 | 1.3 |
| CITST1 | 2 | 10 | 1 | 2.6 |
| CITST1 | 5 | 15 | 1 | 9.75 |
| CITST1 | 5 | 12 | 4 | 4 x 7.8 = 31.2 |
| CITST2 | 2 | 9.62 | 1 | 2.5 |
| CITST2 | 4 | 9.62 | 1 | 5.0 |
| CITST2 | 5 | 15 | 1 | 9.75 |
| CITST2 | 5 | 12 | 4 | 4 x 7.8 = 31.2 |

Table 5.1: Devices sizes for CITST1 and CITST2 SiGe runs evaluated within this work. The 31.2 μm^2 devices are formed from 4 smaller devices, wired in parallel. All emitter stripes are 0.13 μm wide.

3. Polynomial fits of g_m and β from DC and low frequency S_{21} measurements.
4. S-parameters measured at multiple collector currents. This data is subsequently fit to the scalable small signal model in figure 5.5. This assumes that the devices to be characterized are reasonably consistent in their emitter stripe lengths.¹³

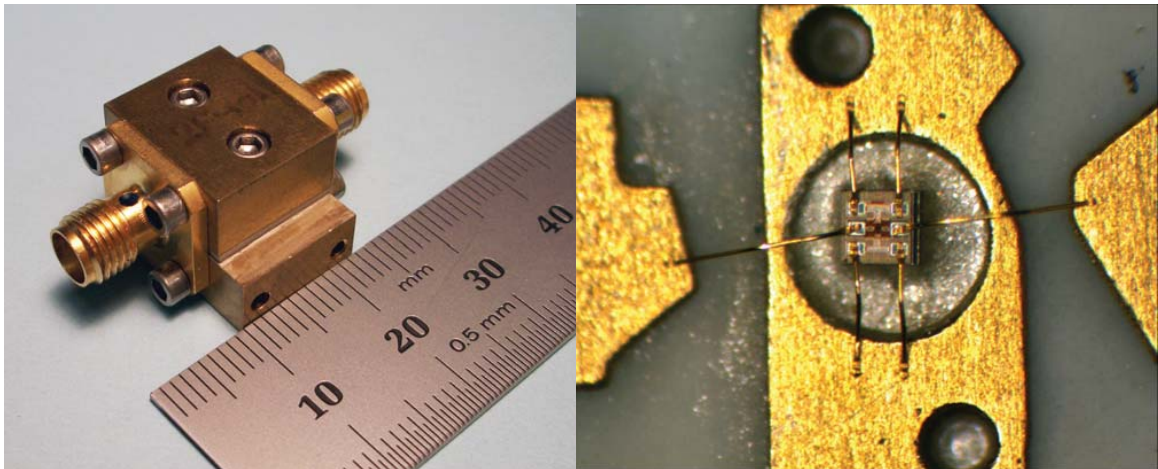


Figure 5.7: (Left) Fixture for DC and RF characterization of discrete HBT devices at 4.2, 19, 77, and 300 K physical temperatures. (Right) Wire bonding diagram of the HBT mounted within a $\varnothing 1$ mm via at the center of the fixtures printed circuit board. The base and collector terminals are the middle left and right bonding pads respectively. Remaining pads are for the emitter, which is tied to chassis. HBT die size is approximately $400 \mu\text{m} \times 400 \mu\text{m}$.

These measurements were completed at 300, 77, 19, and 4.2 K using the following methods:

- 4.2 K. With the use of a small LHE cooled cryostat manufactured by Infrared Laboratories.¹⁴
- 19 K. Using a cryostat cooled by a Brooks Automation CTI-350 cold head.
- 77 K. By immersing the fixture and thermally isolating stainless steel coaxial lines in a LN2 filled styrofoam container.

Although DC measurements were carried out at each of the cryogenic temperatures, S-parameter measurements were only carried out at 19 K. As will be shown, there was no visible change in DC parameters with cooling from 19 to 4.2 K. It is assumed that the remaining small signal elements will remain relatively unchanged as well.

¹³Device size is altered by adjusting stripe length and/or by the number of stripes hooked in parallel (sharing common base, collector, and emitter terminals).

¹⁴Infrared Laboratories. 1808 E. 17th Street, Tucson AZ, 85719 U.S.A.

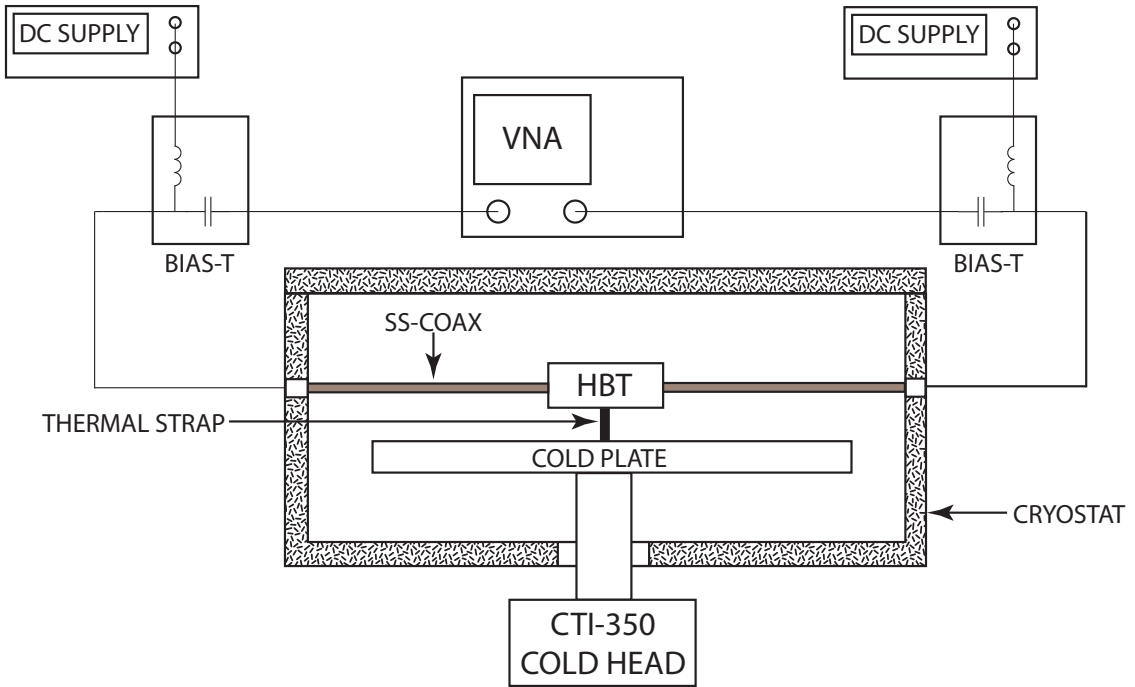


Figure 5.8: Test setup used in the characterization of the discrete HBT's listed in table 5.1. DC bias is routed through the bias-tees internal to the VNA. During DC measurements the power of the VNA is disabled, to remove its effect on the measurement.

5.3.1.1 DC Measurements

The first set of DC measurements performed are of β and g_m , taken by sweeping I_b and measuring the resulting V_{be} and I_c of the device. These measurements were performed at $V_{bc}=0$ V, to emulate bias levels when resistive feedback between the base and collector is employed.¹⁵ At ambient temperature, the resulting V_{ce} voltage is ≈ 0.8 V, and at cryogenic temperatures it is ≈ 1.0 V. The data from these measurements on the CITST1 reticle is shown in figure 5.9. What is particularly interesting is that both β and g_m are unchanged between 4.2 and 19 K. This implies that the shot noise contributions from base and collector should also be unchanged between these two temperatures. As a result, any improvements in transistor noise with cooling should be due only to thermal noise from the base and emitter resistances.¹⁶ Also apparent is the dramatic increase in both β and g_m with cooling, increasing by a factor of 36 and 2.7 respectively. It should be noted that g_m is slightly underestimated using the measurement scheme described above, due to the emitter resistance, R_e . g_m measured in this way is lower than the true g_m by a factor of $(1 + g_{m0}R_e)^{-1}$, were g_{m0} is the true transconductance. This may be partly due to the drop off of the slope of g_m for $I_c > 10$ mA, as seen in figure 5.9.

¹⁵The use of resistive feedback results in a small voltage drop between collector and base, but the β of the devices is so high as to make this drop negligible.

¹⁶As described in section 5.2.3, the contribution from the collector resistance is so small that it may be ignored.

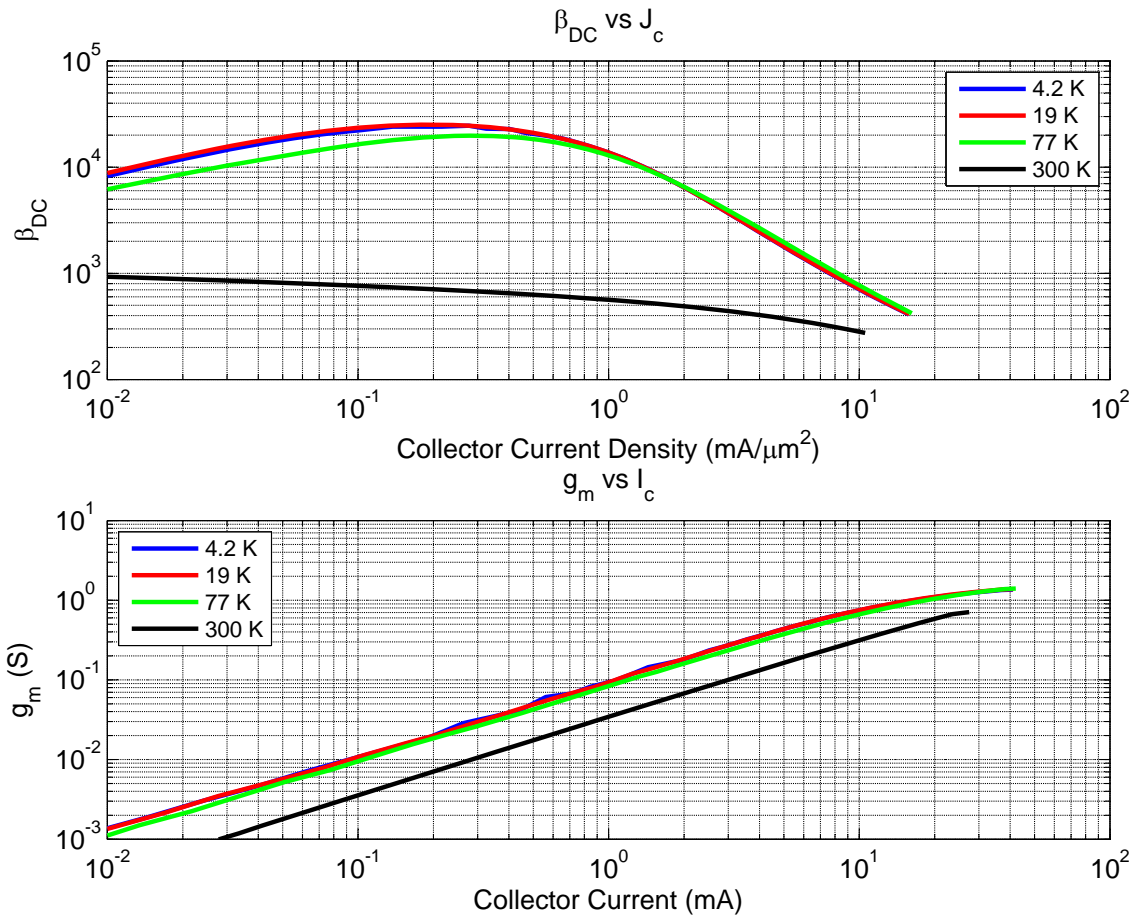


Figure 5.9: Measured DC characteristics of a $2.6 \mu\text{m}^2$ SiGe HBT at 4.2, 19, 77, and 300 K from the CITST1 reticle. (Top) $\beta = I_c/I_b$ and (Bottom) $g_m = \partial I_c/\partial v_{be}$. Note that β and g_m do not change with cooling from 19 to 4.2 K. The shot noise contributions should therefore remain constant between these two temperatures, any improvement to the noise temperature being due to thermal noise only.

Figure 5.10 compares β and g_m for HBTs for the different devices included within the CITST1 and CITST2 reticles. The increase in β with the CITST2 reticle is clearly apparent, along with the shift in its peak value from a collector current density of $0.2 \text{ mA}/\mu\text{m}^2$ to $1 \text{ mA}/\mu\text{m}^2$. Unfortunately, the increase in β was accompanied by a drop in g_m . The following observations may also be made from inspection of figure 5.10:

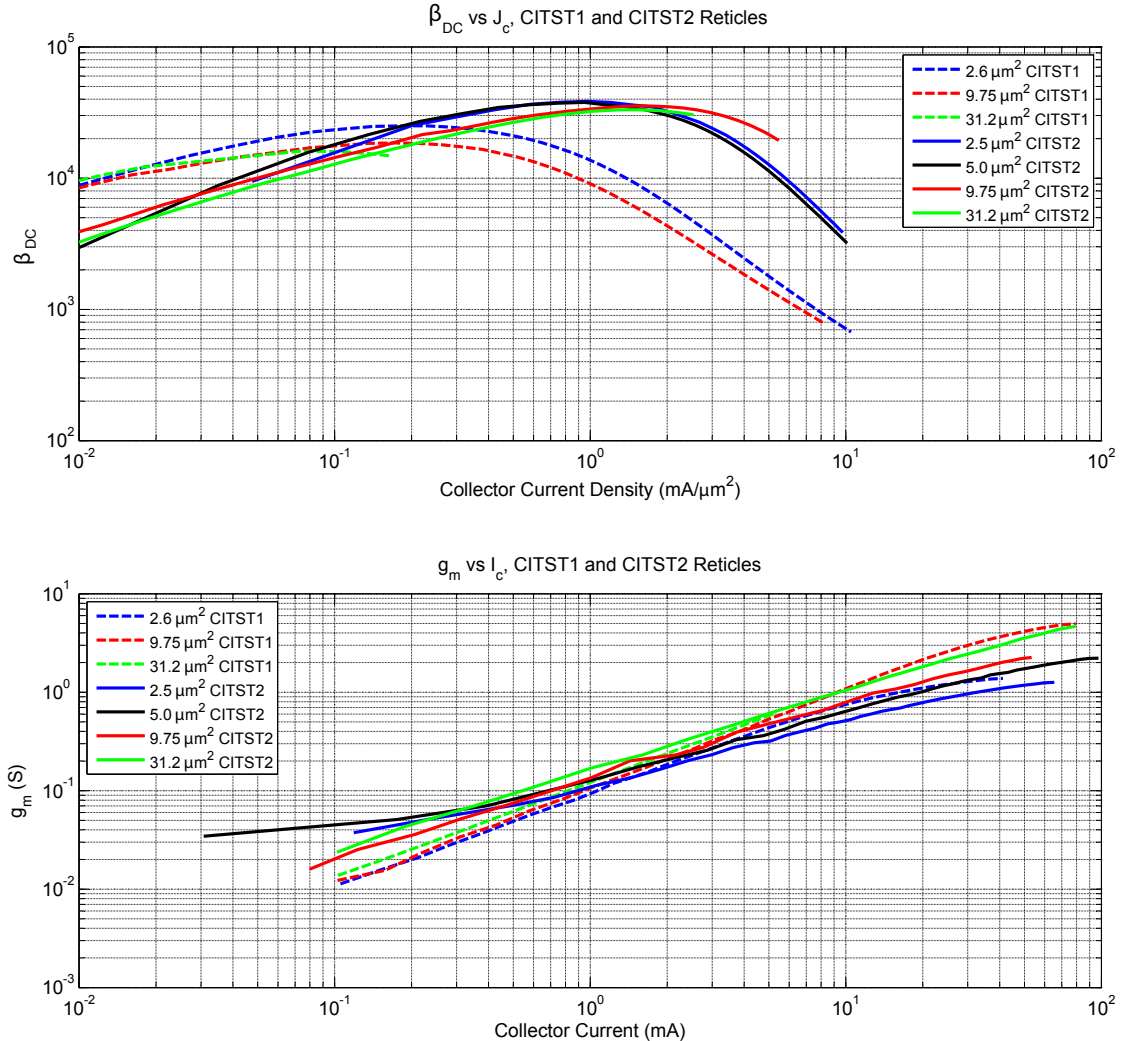


Figure 5.10: Comparison of DC characteristics of SiGe HBTs from CITST1 and CITST2 reticles at 19 K. (Top) Peak β is higher by a factor of 1.5 with the CITST2 run, at a current density almost an order of magnitude greater than that of the CITST1 run. (Bottom) g_m is higher at lower collector currents for the CITST2 devices, with an inflection point corresponding to a current density of $0.58 \text{ mA}/\mu\text{m}^2$ for the $2.5 \mu\text{m}^2$ device and smaller for the larger devices.

1. Peak β is larger for smaller devices, within a given reticle. This is likely due to the fact that these devices are constructed from fewer emitter stripes (refer to figure 5.6 and table 5.1), the net contribution of leakage between adjacent stripes therefore being minimized.

2. g_m is larger for the CITST2 devices at collector current densities less than $\approx 0.50 \text{ mA}/\mu\text{m}^2$. T_{min} for these devices, as will be shown, unfortunately reaches a minimum at current densities of $1 \text{ mA}/\mu\text{m}^2$. The benefit of higher β from the CITST2 reticle has therefore been diminished by a decrease in g_m . At high I_c , the g_m for a given I_c is lower for the CITST2 devices. The collector shot noise contribution to the noise temperature is reduced by a factor of g_m^2 , the lower g_m for a given value of I_c therefore results in a higher noise.
3. Ideally, g_m should only depend on the total collector current through the device, and should therefore be independent of device size. Figure 5.10 reveals, however, that g_m is in fact higher for larger devices. The contribution from R_e plays only a small role in this discrepancy. Other mechanisms responsible for this effect, such as high injection, heterojunction barrier effects [62], should be investigated further.

The above observations suggest that it is beneficial to run a greater number of emitter stripes, for a given device area. This reduces β somewhat, but the improvement to the noise due to g_m is greater. To investigate the effects of self-heating, DC I-V curves of I_c vs V_{ce} are measured at several different values of base current. Self-heating can be seen in the droop of the I_c - V_{ce} characteristics in Figure 5.11, for a $9.75 \mu\text{m}^2$ device. The negative slope in the traces for which the power dissipation $P_{DC} = I_c V_{ce} > 8 \text{ mW}$ indicates that self-heating is occurring. It is attributed to the asymmetry in the ideality factors of the base-emitter and base-collector junctions, the temperature rise effecting collector currents more than base currents [63]. Device power dissipation should therefore be kept below $\approx 0.82 \text{ mW}/\mu\text{m}^2$ to avoid the effects of self-heating. This limit is somewhat conservative for two reasons:

- The calculation is based on the device geometry for the $9.75 \mu\text{m}^2$ device, which is comprised of 5 emitter stripes. The stripes at the center of the device are likely at a higher temperature due to the contribution from their neighbors. Devices with fewer stripes may be able to handle higher power densities as a result.
- I_c is exponentially dependent on temperature, while the noise from R_b is only linearly dependent on physical temperature. Although heating may be present in the IV characteristics, its contribution on the noise may be negligible.

5.3.1.2 Low-Frequency S-Parameter Measurements

If dynamic and static g_m were equal, then this measurement step would not be necessary. Unfortunately for the HBT's characterized here, this was found out not to be the case. This effect is better known as transconductance frequency dispersion, and has been studied extensively in III-V field effect devices [64], [65], [66]. Only limited research has been done into the effect in SiGe [67].

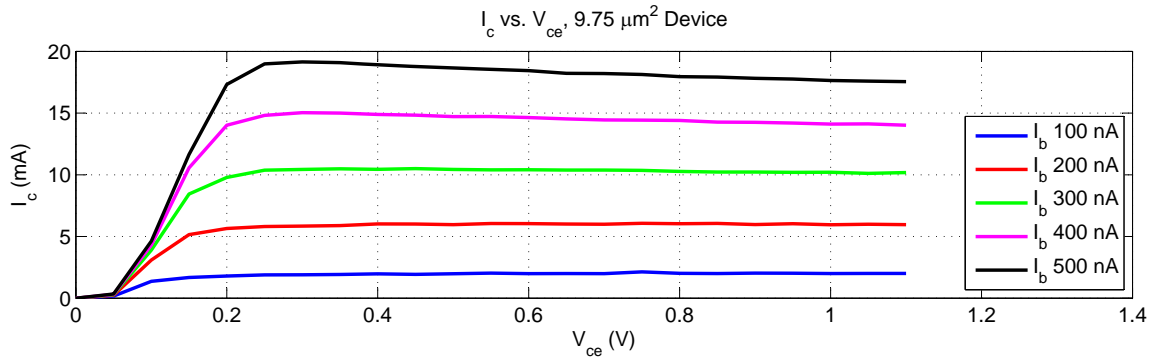


Figure 5.11: Self-heating effects observed in measured I_c vs V_{ce} characteristics, at a 19 K baseplate temperature. The droop in I_c vs V_{ce} at ~ 8 mW points to self-heating for this $9.75 \mu\text{m}^2$ device, or ~ 2.1 mW for the smaller $2.6 \mu\text{m}^2$ device used in the WBA23 MMIC described in section 5.5.1.

It is attributed to “fast traps” existing both at the surface and within the bulk of the device. The end result being an associated frequency response of g_m , ultimately leading to degradation below its value determined from DC measurements. To put this effect in the correct context, consider the ultimate noise limit of an HBT, where all parasitic resistances are now zero and β is infinite, resulting in no base shot noise. Inspection of equation (5.3) reveals that the resulting input noise temperature is

$$T_n = \frac{qI_c}{2kg_m^2 R_g} , \quad (5.4)$$

The noise temperature is inversely proportional to the transconductance squared, so even a reduction in g_m by 70% will lead to a doubling in the minimum noise temperature. In fact, inspection of figure 5.9 and 5.10 reveals that equation (5.4) is a very good approximation¹⁷ of the shot noise contributions of the CITST1 and CITST2 devices at cryogenic temperatures. In other words, β is so high that the base shot noise may be ignored.

With the importance of g_m clearly demonstrated, its value at low frequency was measured using an HP3577 VNA from 100 kHz to 200 MHz. The transconductance may be determined from low frequency measurements of $|S_{21}|$ using the following relation:

$$|S_{21,LF}| \approx 2Z_l g_m , \quad (5.5)$$

where Z_l is the load resistance (50Ω for all VNA measurements), and it is assumed that the generator resistance is much smaller than the input impedance of the HBT; and the HBT’s input capacitance does not yet influence S_{21} . Subsequent measurements reveal that a reduction in g_m is visible at these frequencies, comparing static (DC) measurements with those determined from equation (5.5). This

¹⁷ Assuming $R_g=50\Omega$ and $J_c \approx 1 \text{ mA}/\mu\text{m}^2$.

is illustrated in figure 5.12, where the effect is shown for the $2.5 \mu\text{m}^2$ CITST2 device at 19 K physical temperature and a collector current of 2 mA. Note that the ripple in S_{21} between 50–200 MHz, of approximately 2 dB peak to peak amplitude. This feature was found to decrease in amplitude with increasing bias and is also observable, to a smaller degree, at room temperature.

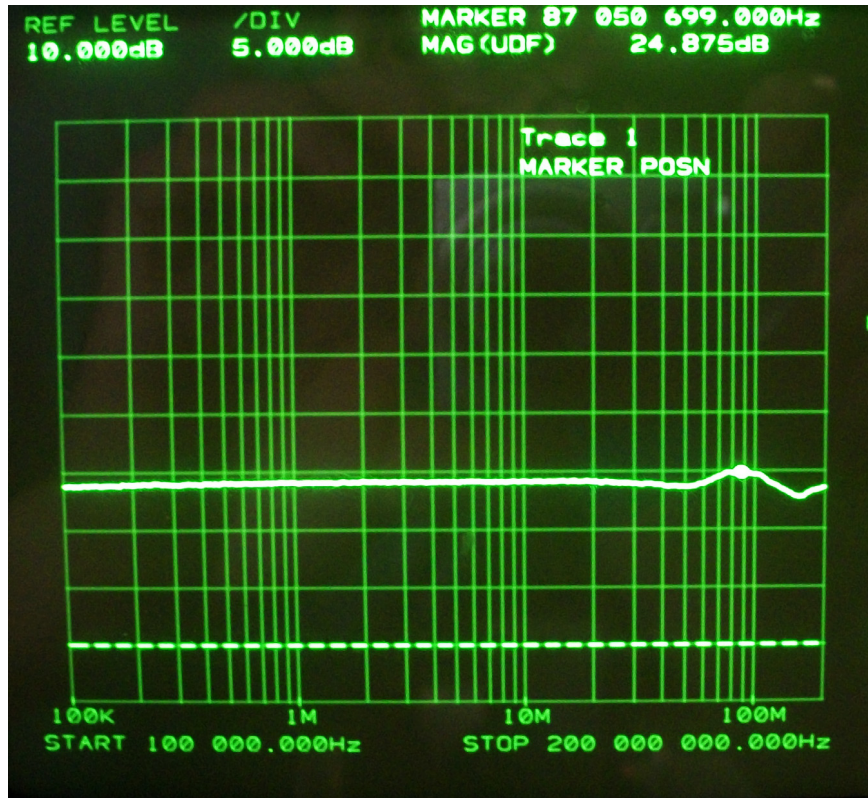


Figure 5.12: Low frequency $|S_{21}|$ measured on a $2.5 \mu\text{m}^2$ device at 19 K physical temperature and $I_c=2$ mA. The resulting dynamic transconductance, determined from equation (5.5) is 89% of its static value.

The reduction in g_m is plotted in figure 5.13 for devices within each reticle and is normalized to each device's static g_m from DC measurements. It is striking that there is a clear distinction in behavior between reticles, and between device sizes within a reticle. For the $2.6 \mu\text{m}^2$ device within the CITST1 reticle, the deviation between DC and dynamic g_m increases with increasing current density. The opposite is true for the 2.5 and $5 \mu\text{m}^2$ devices within the CITST2 reticle. Oddly, the 9.8 and $31.2 \mu\text{m}^2$ devices within the CITST2 reticle do not show the same behavior, even when run at equivalent current densities to the smaller devices. The transconductance frequency dispersion for these SiGe HBTs obviously is obviously a function of both germanium (Ge) content¹⁸ and warrants further investigation.

¹⁸The higher β of the CITST2 run was accomplished by a change to the Ge content and grading within the base of the HBT.

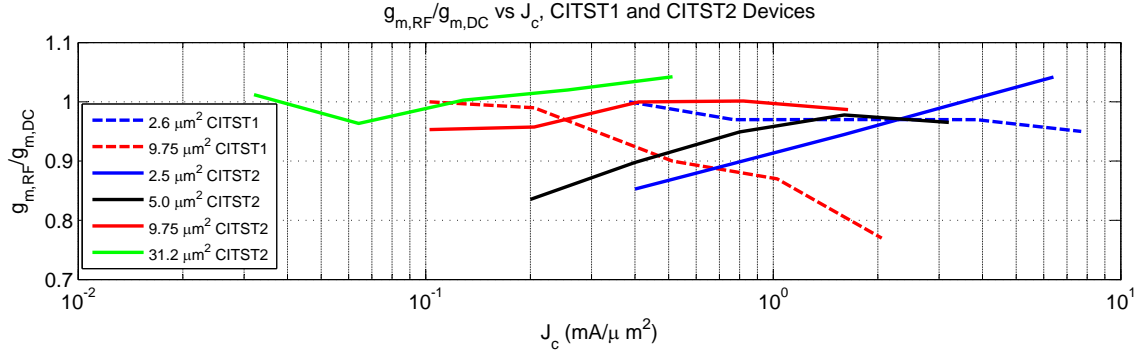


Figure 5.13: Correction to g_m , for CITST1 and CITST2 devices, due to low frequency dispersion. The static g_m is greater than the dynamic g_m determined from low frequency VNA measurements. The corrected g_m must be used in the HBT small signal model to accurately model noise and S-parameters.

5.3.1.3 Polynomial Fitting of DC Parameters

The dynamic g_m must be used in equation (5.3) to accurately model the input noise temperature of the device. To facilitate construction of a small signal model, both β and g_m are treated to polynomial fitting over a collector current range of 1–16 mA, provided in equation (5.6) and (5.7) below. For β , J_{cln} is the natural logarithm of the collector current density in millamps per micron squared. The expression for g_m uses I_{cln} , which is the natural logarithm of the collector current in mA, for the first half of the expression. The second half of equation (5.7) provides correction for dynamic g_m , where I_c is in mA, based on its average value between 100 kHz and 10 MHz.

$$\beta = \sum_{x=1}^6 C_x J_{c,ln}^x \quad (5.6)$$

$$g_m = \sum_{x=1}^6 D_x I_{c,ln}^x \sum_{x=1}^5 E_x I_c^x \quad (5.7)$$

The coefficients for equation (5.6) and (5.7) are given in tables 5.2 – 5.4 in the following pages. It should be noted that the static components of these terms are valid over a wider range of current, 100 μ A–20 mA.

5.3.1.4 S-Parameter Measurements

The remaining small signal parameters are determined by manually fitting measured S-parameter data for each device, taken at collector currents of 1, 2, 4, 8, and 16 mA. Although by no means as thorough as other characterization methods, such as those demonstrated in [10], it is possible to obtain models of sufficient fidelity for design purposes to \sim 8 GHz. The resulting, scalable, small

Table 5.2: β polynomial coefficients for CITST1 and CITST2 runs at 19 K.

| Size (μm^2) | Run | β Coefficients for equation (5.6) | | | | | | |
|-----------------------|--------|---|----------|------------|------------|------------|------------|-----------|
| | | C_6 | C_5 | C_4 | C_3 | C_2 | C_1 | C_0 |
| 2.6 | CITST1 | 2.71e-4 | 3.906e-3 | 1.7997e-2 | 1.37e-3 | -3.2161e-1 | -8.5468e-1 | 9.5172 |
| 9.75 | CITST1 | 2.45e-4 | 4.316e-3 | 2.4649e-2 | 2.6791e-2 | -2.8645e-1 | -8.954e-1 | 9.1150 |
| 31.2 | CITST1 | 4.0e-6 | 8.5e-5 | -1.5e-4 | -2.1547e-2 | -2.9194e-1 | -1.0849 | 8.4731 |
| 2.5 | CITST2 | 3.79e-4 | 2.313e-3 | -5.088e-3 | -6.9474e-2 | -2.9537e-1 | -3.2648e-2 | 1.0566e+1 |
| 5.0 | CITST2 | -5.4e-5 | -1.59e-3 | -1.4328e-2 | -6.5139e-2 | -2.6431e-1 | -8.5482e-2 | 1.0524e+1 |
| 9.75 | CITST2 | 2.0e-5 | 2.52e-4 | -3.87e-4 | -1.8305e-2 | -1.2574e-1 | 1.6591e-1 | 1.0426e+1 |
| 31.2 | CITST2 | -8.6e-5 | -2.03e-3 | -1.8262e-2 | -8.0205e-2 | -2.1545e-1 | 1.5863e-1 | 1.0382e+1 |

Table 5.3: g_m polynomial coefficients for CITST1 and CITST2 runs.

| Size (μm^2) | Run | DC g_m Coefficients for equation (5.7) | | | | | | |
|-----------------------|--------|--|----------|-----------|------------|------------|-----------|---------|
| | | D_6 | D_5 | D_4 | D_3 | D_2 | D_1 | D_0 |
| 2.6 | CITST1 | -3.9e-5 | -3.6e-4 | -2.068e-3 | -7.645e-3 | 2.231e-3 | 9.7454e-1 | -2.3593 |
| 9.75 | CITST1 | -7.9e-5 | 1.33e-4 | 1.243e-3 | -5.4e-3 | 9.473e-3 | 1.006 | -2.2583 |
| 31.2 | CITST1 | -2.42e-4 | 2.116e-3 | 3.895e-3 | -8.846e-3 | -1.3536e-2 | 9.7999 | -2.1033 |
| 2.5 | CITST2 | 2.36e-4 | 1.319e-3 | -8.289e-3 | -1.7218e-2 | 7.9351e-2 | 6.4237e-1 | -2.2322 |
| 5.0 | CITST2 | -1.02e-3 | 1.111e-3 | 1.4295e-2 | -2.8978e-2 | 1.1585e-2 | 6.8683e-1 | -2.0546 |
| 9.75 | CITST2 | -1.24e-4 | -5.12e-4 | 1.659e-3 | 4.17e-3 | -1.7787e-2 | 7.9149e-1 | -2.0078 |
| 31.2 | CITST2 | -4.9e-5 | -6.76e-4 | -1.59e-4 | 1.0679e-2 | -5.89e-3 | 7.9007e-1 | -1.802 |

Table 5.4: g_m polynomial coefficients for CITST1 and CITST2 runs.

| Size (μm^2) | Run | Correction Coefficients for Dynamic g_m equation (5.7) | | | | |
|-----------------------|--------|--|------------|------------|------------|------------|
| | | E_5 | E_4 | E_3 | E_2 | E_1 |
| 2.6 | CITST1 | 9.4388e-5 | -2.8461e-3 | 2.6626e-2 | -9.1376e-2 | 1.0675 |
| 9.75 | CITST1 | -2.0238e-4 | 5.5952e-3 | -4.3750e-2 | 8.5119e-2 | 9.5324e-1 |
| 31.2 | CITST1 | -2.42e-4 | 2.116e-3 | 3.895e-3 | -8.846e-3 | -1.3536e-2 |
| 2.5 | CITST2 | -4.9132e-5 | 1.5666e-3 | -1.6865e-2 | 8.6285e-2 | 7.8181e-1 |
| 5.0 | CITST2 | -7.5168e-5 | 2.4244e-3 | -2.6521e-2 | 1.2606e-1 | 7.3340e-1 |
| 9.75 | CITST2 | 1.0129e-4 | -2.8054e-3 | 2.1644e-2 | -4.2365e-2 | 9.7652e-1 |
| 31.2 | CITST2 | 2.5234e-4 | -7.3968e-3 | 6.5673e-2 | -1.9759e-1 | 1.1512 |

signal model parameters are given in table 5.5, where models for the CITST1 and CITST2 devices are provided, compared against the G4 (experimental) devices characterized in [10]. Although C_{be} and C_{bc} are themselves functions of bias, the value corresponding to $J_c = 1 \text{ mA}/\mu\text{m}^2$ is used to simplify the model. This value of current density corresponds to that of the minimum noise temperature of the device, as will be shown in the next section.

The largest shortcoming of this approach, with regards to noise modeling, is in the determination of the base resistance, R_b . The S-parameters of the small signal model are relatively insensitive to R_b , its determination needs to be augmented by data collected from subsequent noise measurements. With this simplified modeling approach, a reduction in base resistance by a factor of approximately 4 between CITST1 and CITST2 devices was observed. The scalable small signal model can be imported into a microwave simulator for design purposes. The simulated results provided for the MMICs in section 5.5 are made with these small signal models. The agreement between simulated and measured results is extremely good, validating the approach described here.

Table 5.5: Scalable small signal model parameters, based on a $10 \mu\text{m}$ emitter stripe length.

| ST Run | R_b (Ω/Stripe) | R_c (Ω/Stripe) | R_e (Ω/Stripe) | C_{be} ($f\text{F}/\mu\text{m}^2$) | C_{bc} ($f\text{F}/\mu\text{m}^2$) |
|--------|-------------------------------------|-------------------------------------|-------------------------------------|---|---|
| ST-G4 | 6 | 2.58 | 0.94 | 54.8 | 18.3 |
| CITST1 | 21.7 | 4.8 | 0.50 | 41.2 | 18.5 |
| CITST2 | 4.50 | 5.40 | 0.55 | 61.9 | 15.7 |

5.3.2 Device Sizing and Bias

The bias and size (emitter area) of the device used in a LNAs first stage must be optimized for the lowest noise and the highest gain possible. To do so, the appropriate small signal model is imported into a circuit simulator, so that noise parameters T_{min} and R_{opt} may be determined for a unit sized device. These quantities are plotted versus J_c , at the highest frequency the amplifier performance is to be specified at. The optimum current density, $J_{c,opt}$ corresponds to the value of J_c at minimum T_{min} . The value of R_{opt} corresponding to $J_{c,opt}$ is then determined. Optimum device size is found by multiplying the area of the unit sized device by $K = \Re(Z_g)/R_{opt}(J_{c,opt})$ [62], where Z_g is the generator impedance. This is illustrated in figure 5.14, based on the CITST1 small signal model, for a $1 \mu\text{m}^2$ device at several frequencies. At 4 GHz, $J_{c,opt}$ corresponds to $\approx 1.0 \text{ mA}/\mu\text{m}^2$, with the corresponding value of R_{opt} being 650Ω . For a 50Ω generator, this corresponds to $K = 650/50$, or a $13 \mu\text{m}^2$ device. The collector current the device should be operated at, the total transconductance, and the device capacitances are determined by multiplying their respective unit area values by K as well. Device resistances are determined by dividing the the values presented in table 5.5 by the

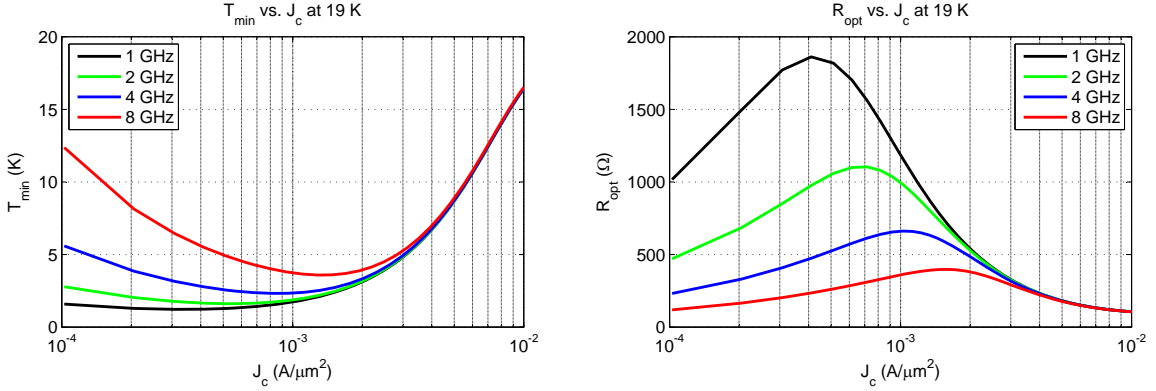


Figure 5.14: T_{min} and R_{opt} vs J_c at 19 K, for devices within the CITST1 reticle, at 2, 4, and 8 GHz. The R_{opt} values are for a $1 \mu\text{m}^2$ device, the device size should be scaled to obtain a lower R_{opt} . For example, at 4 GHz a $10 \mu\text{m}^2$ device would be near optimum for a 50Ω generator at a I_c of 20 mA.

total number of emitter stripes used to obtain the necessary device size.¹⁹ This procedure provides a good starting point for device sizing. It is especially valid in the low GHz range, the focus of this work, where the gain of the HBTs is relatively high. If this were not the case, than $J_{c,opt}$ should be selected for minimum noise measure [68].

5.3.3 Resistive Feedback

Resistive feedback between the collector and base of the HBT offers the benefits of ease of biasing, low return loss, gain flattening, and improved stability. Due to the high β of cryogenically cooled SiGe, the base to collector is effectively zero biased, even with several kilohms of feedback resistance employed. This in turn helps ensure that effects such as carrier multiplication, a potential consequence of a large reverse bias between base and collector, is not observed. The influence of resistive feedback on the low frequency S-parameters may be calculated using Middlebrook's and Blackman's formulas. Referring to the simplified small signal model of figure 5.15, the S-parameters are given by

$$\begin{aligned}
 S_{11} &= \frac{r_\pi (R_f + R_l - R_g) - R_g (R_f + \beta R_g)}{r_\pi (R_f + R_l + R_g) + R_g (R_f + \beta R_g)}, \\
 S_{21} &= 2 \frac{-R_f g_m + 1}{1 + R_g g_m + (R_f + R_g)/R_l}, \\
 S_{12} &= 2 \frac{R_g}{R_l (1 + g_m R_g) + R_f + R_g}, \\
 S_{22} &= \frac{R_f + R_g - R_l - g_m R_l R_g}{R_f + R_g + R_l + g_m R_l R_g}.
 \end{aligned} \tag{5.8}$$

¹⁹Additional scaling must be performed if the emitter stripe length selected deviates from the $10 \mu\text{m}$ length the values in table 5.5 are provided for.

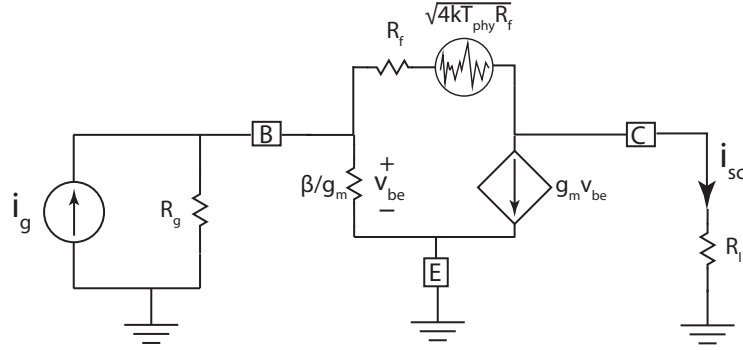


Figure 5.15: Simplified model for noise and S-parameter calculations of the use of resistive feedback. For noise calculations, $R_l \rightarrow 0$, and the expected value of the mean square short circuited output current, $|\bar{i}_{sc}|^2$, due to i_g , is compared to that from R_f .

If $r_\pi \gg R_g$ then both input and output can be matched with $R_f = g_m R_l R_g$. The presence of R_f can greatly improve the stability of the device as well.

As suspected, resistive feedback does contribute to the stages effective noise temperature. The effect of which can be analyzed with the same methods as described in Section 5.2.3. To simplify the derivation presented here, $R_b = R_c = R_e = 0$ is assumed. Referring to Fig 5.15, the expected value of the mean square, short circuited output current, due to generator and feedback resistances are

$$\begin{aligned} |\bar{i}_{sc}(i_g)|^2 &= \frac{4kT_n}{R_g} \left(\beta \frac{R_g \parallel R_f}{R_g \parallel R_f + R_\pi} - \frac{R_g \parallel R_\pi}{R_g \parallel R_\pi + R_f} \right)^2 \\ &\approx 4kT_n R_g g_m^2 \quad \text{assuming } R_f \gg R_g \text{ and } R_\pi \gg R_g, \end{aligned} \quad (5.9)$$

$$\begin{aligned} |\bar{i}_{sc}(e_{R_f})|^2 &= 4kT_{phy} R_f \left(\frac{g_m R_\pi \parallel R_g + 1}{R_f + R_g \parallel R_\pi} \right)^2 \\ &\approx 4kT_{phy} R_f \left(\frac{g_m R_g + 1}{R_f} \right)^2. \end{aligned} \quad (5.10)$$

Equating these contribution provides T_{n,R_f} , the noise temperature contribution from R_f .

$$\begin{aligned} T_{e,R_f} &= T_{phy} \frac{(g_m R_g + 1)^2}{R_g g_m^2} \frac{R_f}{(R_f + R_g)^2} \\ &\approx T_{phy} \frac{R_g}{R_f} \quad \text{assuming that } R_g g_m \gg 1 \end{aligned} \quad (5.11)$$

If $R_g = 50 \Omega$, $T_{phy} = 20 \text{ K}$, and g_m is sufficiently large, then a $1 \text{ k}\Omega$ resistor adds 1 K to the noise temperature, dropping to $\approx 0.2 \text{ K}$ when the LNA is operated at LHE temperatures. For design purposes, R_f should first be selected to satisfy input match and stability requirements. The impact

on noise should then be assessed, based on the final physical temperature the amplifier is to be operated at, and R_f adjusted accordingly.

5.3.4 On-Chip Passive Elements

Foundry supplied design kits do not provide accurate models for cryogenic design purposes. The designer must estimate the impact of temperature on passive devices from knowledge of their physical makeup. This is especially true of on-chip resistors and capacitors. Salicided resistors, for example, are formed by covering polysilicon with a thin layer of titanium or cobalt, thus lowering the effective sheet resistance [69]. Although this decreases the width of small valued resistors, it results in a tremendous temperature coefficient, as the loss in pure metals is roughly proportional to temperature. Likewise, poly n- and p-well (varactor) capacitors may potentially suffer from freeze-out effects, depending on the doping levels involved. For characterization purposes, “test structures” should be included within the reticles containing the MMIC designs, the test structure for the CITST2 reticle shown in figure 5.16.

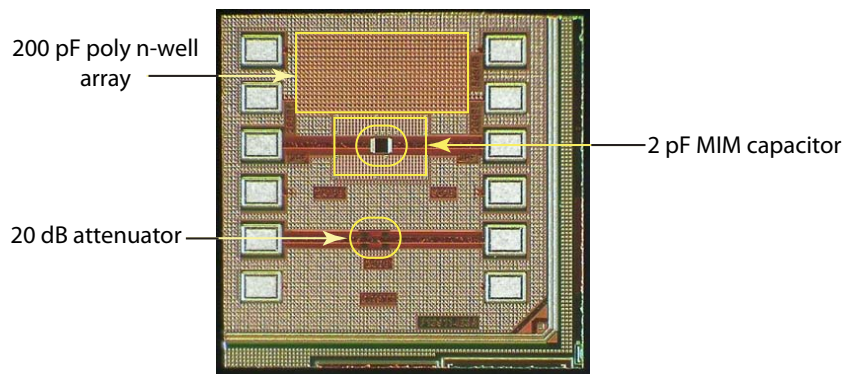


Figure 5.16: Test structures for the cryogenic characterization of passive components contained within the CITST2 reticle. Note the difference in area between the 200 pF poly n-well array and the 2 pF MIM capacitor. The rectangle around the MIM capacitor represents the metal density design rule requirement about the MIM capacitor. This severely limits the use of MIM devices for bypass. Individual salicide and polysilicon resistor on test structure are obscured by metal fill. Size after dicing is $\approx 800 \mu\text{m} \times 800 \mu\text{m}$.

Table 5.6 summarizes the results of cryogenic testing of the passive elements within the CITST1 and CITST2 reticles. Measurements were made with the test structure mounted in a connectorized 50Ω fixture, similar to that shown in figure 5.7. Tests on poly n-well capacitors reveal that at 0 V bias the capacitance had decreased by 80% from its value at room temperature, likely a result of carrier freeze out. Increasing the reverse bias across the capacitor to 1 V had restored its capacitance to its room temperature value. The most plausible cause being charge ionization [70] of carriers with increasing bias. This dependence on voltage and temperature limits the use of n-well capacitors to bypass purposes. Fortunately metal-insulator-metal (MIM) capacitors have an excellent temperature

response, with no observable change in capacitance. The only drawback to the use of MIM capacitors is their low capacitance density of $\sim 2.1 \text{ fF}/\mu\text{m}^2$ vs. $\sim 6.5 \text{ fF}/\mu\text{m}^2$ for n-well devices. Their size and spacing are also limited by design rules from the foundry, making values larger than 5–10pF impractical. MIM capacitors are therefore good candidates for AC coupling and matching purposes in the GHz range, but not for large values of supply bypass.

Table 5.6: Summary of changes to passive elements with cooling to 19 K.

| Element | Change 300 to 19 K |
|-----------------------|--|
| Poly N-Well Capacitor | 80% decrease at 0V bias |
| | no change at $>1\text{V}$ reverse bias |
| MIM Capacitor | no change |
| Salicided Resistors | $\sim 65\%$ decrease |
| Polysilicon Resistors | $\sim 2\%$ decrease |
| Substrate Resistivity | $\sim 2000\%$ increase |

Salicide resistor tests confirmed a large ($\sim 65\%$), negative dependance of resistance with temperature. The use of such resistors should be avoided, except for applications requiring course values, such as to limit the Q of on chip bypass networks. Conversely, the polysilicon resistors characterized showed only 2% change in resistance with cooling.

Also included on the test structure was a pair of active contacts, $\sim 300 \mu\text{m}$ apart, with all adjacent metalization removed. This provided a means of testing the change in substrate resistivity with temperature. figure 5.17 shows the result of this test. Not surprisingly, the substrate resistivity increases strongly at cryogenic temperatures. This is again attributed to freeze out, as the lower thermal energy severely limits the number of electrons reaching the conduction band. The substrate may be considered “frozen out,” and loss within the substrate ignored at cryogenic temperatures.

5.3.5 Layout

Referring to the sample BiCMOS metal stackup of figure 5.18, metal layer M6 is typically used in the routing RF interconnects, due to its height above the ground plane, itself typically comprised of layers M1 and M2. This results in 50Ω microstrip line widths on the order of $12 \mu\text{m}$, comparable in size to the HBTs they are connected to. The interconnects between the M6 and the M1 layer, the metal layer connected to the HBTs terminals in figure 5.6, is made through a series of vias. Many vias are typically used, beyond the number required for current handling capability, due to their resistance. Individual via resistance on the lower metal layers can be as high as 5Ω . Increasing the number of vias, particularly for the base contact of the input stage, ensures that the noise contribution will be minimized.

Unfortunately, the layout and ultimate packaging of the MMIC are often left out of the initial

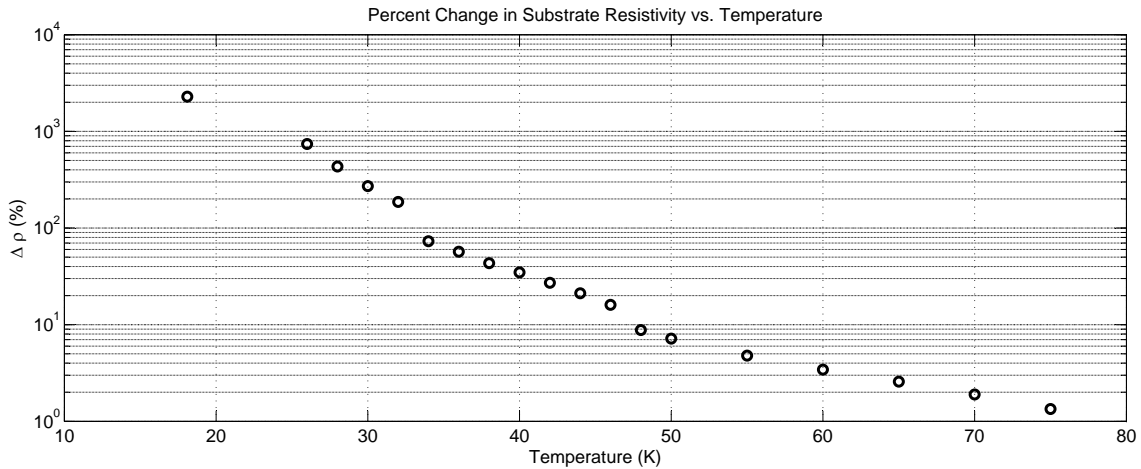


Figure 5.17: CITST1 substrate resistivity versus temperature, expressed as percent change from its room temperature value. The dramatic increase in resistivity at cryogenic temperatures indicates that carrier freeze-out within the substrate is at play.

design phase. This can have dire consequences, especially since silicon does not have a native backside ground plane. Unlike GaAs and InP technologies that benefit from low inductance grounds through on-chip vias and thinned substrates, all connections to Si MMICs must be made with bond wires. Subsequently, the layout of the circuit and its grounding become crucial to performance and, more importantly, to the stability of the amplifier. If a low impedance path to off-chip ground cannot be formed, return currents from each stage are allowed to circulate on chip, leading to potential instability. Room temperature amplifiers use on chip bypass capacitance to mitigate this problem. Care must be exercised in including on-chip bypass for cryogenic operation, due to the potential temperature response of these elements, as mentioned earlier. This work uses a double-pronged approach to solve these potential issues:

1. For multistage amplifiers, the emitter of each stage is pulled out to its own bond pad. This breaks, at lower frequencies at least, the feedback loop that would be otherwise present if the emitters were tied directly to chip ground. It also allows for some degree of noise and impedance tuning through adjustment in the length of the bondwire used.
2. Bypass capacitance is implemented through the use of a combination of n-well capacitors and parasitic capacitance formed by interdigitating metal layers M2 through M6. This bypass scheme is laid out in a unit cell of $18 \times 18 \mu\text{m}^2$, with 1 pF and 84 fF of n-well and parasitic capacitance respectively. The total capacitance contained within the layout is selected to stabilize the amplifier with the parasitic capacitance alone. In series with this capacitance cell is a $\sim 5 \Omega$ poly resistor, to lower the Q of the composite capacitor, and therefore avoid unfavorable interactions with the off-chip bias network.

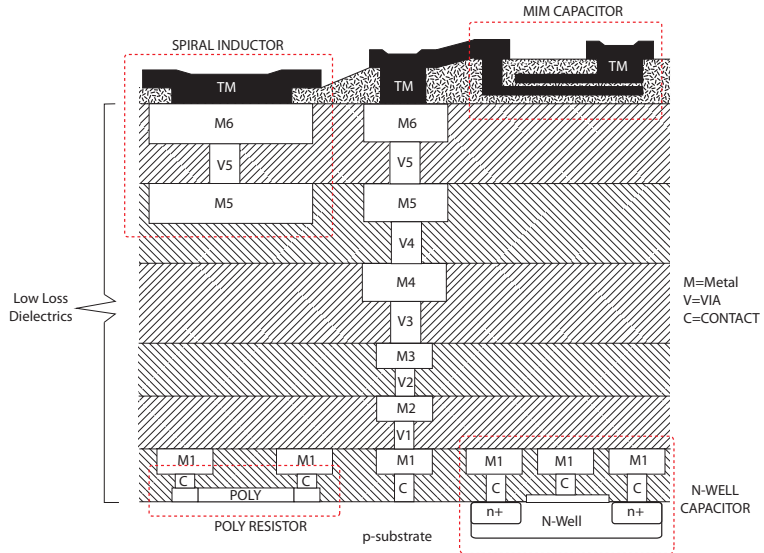


Figure 5.18: Simplified example of BiCMOS metal stackup and passive device location. Metal layers M1-M3 are thinner than those above them, and their associated vias (V1-V2) have a higher resistance. Layers M5 and M6 are used to form spiral inductors. The top layer (TM) is usually aluminum and is used in the construction of MIM capacitors. Poly resistors and n-well capacitors are fabricated directly onto the native substrate, and are reached through active contacts made from the metal 1 (M1) layer. Dielectrics with $\epsilon_r \approx 4-8$ are used to isolate the various metal layers.

Experimentally, the author has found it difficult to obtain <250 pH of inductance for a single bondwire, and <80 pH of inductance for multiple bondwires, limited primarily by mutual coupling and chip size. With these limitations, the above approach to the layout and grounding of the MMIC has been found to provide sufficient stability for SiGe amplifiers operating below 10 GHz at cryogenic temperatures.

The layout of all designs presented here was done using the Cadence IC 5²⁰ design tool. Post layout extraction of parasitic capacitances was performed using Mentor Graphic's²¹ Calibre tool. Simulations of the amplifiers presented in section 5.5, using AWR's²² Microwave Office, contain these parasitic capacitances. Although their effects on the inband performance is rather small, their out of band effect, particularly on stability of the amplifier, can be large. It is therefore essential that parasitics be extracted, instantiated within the simulation, and modifications to the design and or layout made accordingly.

²⁰Cadence Design Systems, Bagshot Road, Bracknell Berkshire, RG12 0PH U.K.

²¹Mentor Graphics, 8005 SW Boeckman Road, Wilsonville OR, 97070 U.S.A.

²²AWR Corporation, 1960 East Grand Avenue, El Segundo CA, 90245 U.S.A.

5.4 Measurement of Cryogenic-Low Noise Amplifiers

Solid state noise sources, such as Agilents N4007A smart noise source (SNS) cannot be directly employed to measure the noise temperature of cryogenic amplifiers for several reasons. To begin with, these noise sources need to be mounted outside of the cryostat containing the DUT, a semi-rigid coaxial cable connecting the two. The uncertainty in the physical temperature²³ of this cable places a sizable systematic error in the measurement of the DUT's noise temperature. Additionally, the excess noise temperature of these noise sources is often too high in comparison to the amplifier's noise temperature, making the measurement susceptible to errors due to compression of the DUT and nonlinearity of the receiver's (NFAs) detector during Y-factor measurements. Finally, the uncertainty in the ENR of the noise source itself typically imparts a large uncertainty in the noise temperature measurement. To put this in perspective, measurement of a 10 K amplifier, with a 6 ± 0.15 dB²⁴ noise source, would produce ~ 12 K of uncertainty in the measured noise.

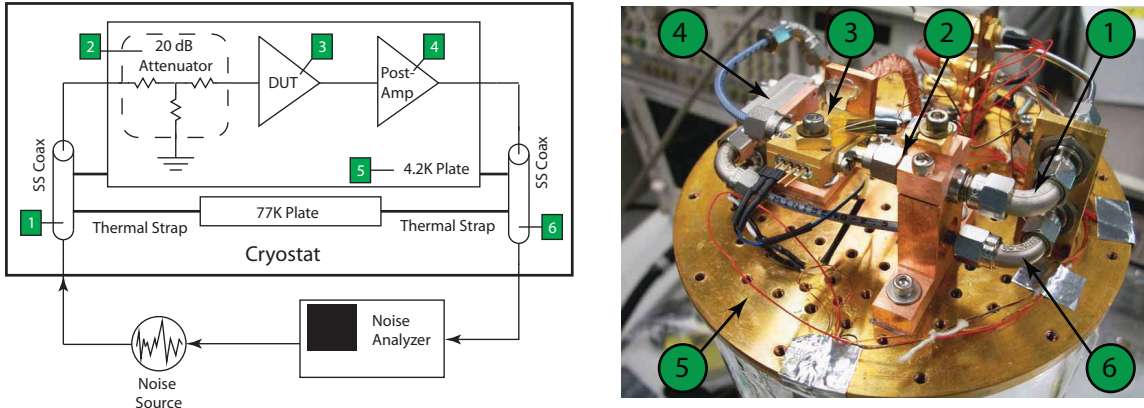


Figure 5.19: Noise temperature test setup based on the cold attenuator method [50]. The setup shown here is contained within a small LHE cryostat from Infrared Laboratories. All brackets are machined from OFHC and mounted to the cold plate with indium gaskets to minimize the temperature drop between the component and cold plate.

These measurement problems are alleviated by the use of the “cold attenuator method” [49], [50], the test setup for which is shown in figure 5.19. A ≈ 20 dB attenuator is mounted in between the input of the DUT and the coaxial cable connected to the external noise source. The attenuator itself is strapped to the same cold plate as the DUT, along with a temperature sensor. The resulting Y-factor of the measurement, when solved for the noise temperature of the DUT, T_{dut} , is given by (5.12). For simplicity, it is assumed that the gain of the DUT is sufficiently high, so that the noise introduced by the output coaxial line does not significantly impact the measured noise temperature.

²³Itself a function of distance along the cable.

²⁴This is the stated uncertainty for Agilent's N4000A noise source, used for the measurement of low noise devices from 0.010 to 18 GHz.

$$T_{dut} = \frac{T_{ext,ns}G_{coax}G_{att}}{Y - 1} - (T_{phy,ns}G_{coax}G_{att} + (1 - G_{coax})G_{att}T_{coax} + (1 - G_{att})T_{att,phy}) \quad (5.12)$$

$T_{ext,ns}$ and $T_{phy,ns}$ are the excess noise temperature and physical temperature of the external noise source respectively, G_{coax} and T_{coax} are the available gain and physical temperature of the coaxial cable respectively, and G_{att} and $T_{att,phy}$ are the available gain and physical temperature of the cooled attenuator respectively. The combination of G_{coax} and G_{att} can usually be measured to sufficient accuracy by replacing the DUT with a short and measuring the return loss of the combination with a VNA during a separate cool down. $T_{phy,ns}$ is usually also known to sufficient accuracy from the sensors now built into modern noise sources. The effect of the uncertainty in the measurement due to the remaining terms may be analyzed by taking the appropriate partial derivatives of equation (5.12). The resulting uncertainty, ΔT_n is given below in equation (5.13).

$$\Delta T_n = \sqrt{\Delta T_{ext,ns}^2 \left(\frac{G_{coax}G_{att}}{Y - 1} \right)^2 + \Delta T_{coax}^2 ((G_{coax} - 1)G_{att})^2 + \Delta T_{att}^2 (1 - G_{att})^2} \quad (5.13)$$

Note that the uncertainty in both the external noise source's excess noise temperature and temperature of the coaxial cable have been reduced by G_{att} . Assuming that $G_{att} \approx -20$ dB and that a high accuracy temperature sensor is used for the attenuator, uncertainties of <1 K are obtained. In addition to the above benefits, the cooled attenuator also lowers the impact of other systematic errors on the measurement, such as those due to changes in reflection coefficient of the noise source between on and off states, as detailed in section 4.4 and 4.6.2. The cooled attenuator method described above will be used in the measurement of all IFLNAs presented in the next section.

5.5 Examples

In this section several IFLNA examples are presented, where the tradeoffs between noise, bandwidth, and DC power consumption are explored.

5.5.1 WBA23. Low Power IFLNA for Large SIS Mixer Arrays

Future terahertz arrays employing thousands of pixels will require solving many of the problems associated with integration of the superconducting mixer, IFLNA, and related components to make manufacturing feasible. *The Kilopixel Array Pathfinder Project* ((KAPPA), refer to table 1.1) aims to tackle many of these problems, moving past the 1-D packaging approach, of current state of the art terahertz arrays, to 2-D integration. A conceptual illustration of the packaging approach

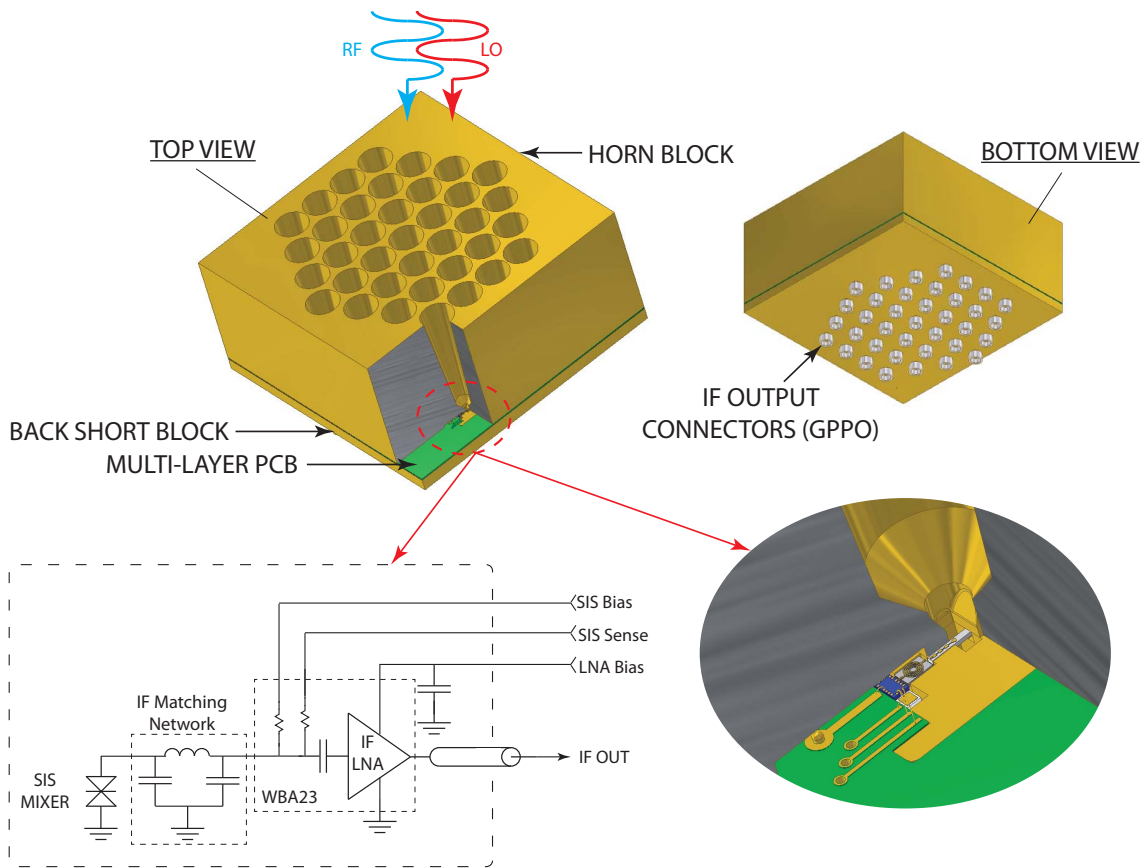


Figure 5.20: Conceptual packaging illustration for *The Kilopixel Array Pathfinder Project (KAPPa)*. The “Horn Block” feeds incoming RF and quasi-optically combined LO signals down to the SIS device below. SIS device, IF matching network, and IFLNA are mounted below each feed in the “Back short block,” which, among other things, provides the back short for the SIS assemblies’s waveguide probe. A multilayer PCB routes IFLNA outputs and DC connections. Gilbert²⁶ GPPO connectors at the back of the block provide connections to IFLNA IF outputs. Pixel spacing is ~ 6 mm \times 6 mm.

taken by KAPPA is shown in figure 5.20, where SIS mixer, IF matching network, and IFLNA reside adjacent to each other on a common block. This block also serves to; mount a multilayer printed circuit board (PCB) which routes DC and IF connections, provide a backshort for the SIS mixer's waveguide probe, and to mount the IF output connectors. Incoming LO and 650 GHz RF signals are combined quasi-optically and imaged onto an array of feedhorns machined into a common block of metal, mounted above the PCB. These horns are machined from a custom high speed machine tool, allowing rapid manufacturing of large arrays of feeds, already demonstrated at 700 GHz [71].

Integrating the IFLNA with the superconducting mixer requires that the amplifiers power dissipation be strictly minimized for two reasons: to limit heating of the mixer which is typically at LHE temperatures; and to ease the design of the cryogenics. The former is necessitated by the close proximity of the mixer and IFLNA, and the requirement that the mixer have a low loss thermal path to the cold finger. The later being limited by the capacity of modern cryocoolers, such as Sumitomo's RDK-415D capable of cooling 1.5 W at 4.2 K. In addition, the IFLNA should be as small as possible and require as few external components as possible, to minimize the spacing (pitch) between adjacent pixels. These requirements fed the development of the WBA23 IFLNA, with design goals listed in table 5.7.

Table 5.7: WBA23 design goals and drivers for operation at 4.2 K physical temperature.

| Parameter | Goal | Driver |
|-------------|--------------------|---|
| Bandwidth | 0.5–4.5 GHz | Spectral line width |
| Noise | <7 K | System noise <175 K |
| Gain | >15 dB | Noise contribution from postamplification |
| Return Loss | <-10 dB | Minimize reflections between SIS and IFLNA |
| DC Power | <2 mW | Temperature of SIS mixer and # of cryocoolers |
| Size | <1 mm ² | 6 mm × 6 mm pixel footprint |

The schematic and photo of the WBA23 IC are shown in figure 5.21. To meet the DC power requirement only a single stage could be employed. The device was sized according to the procedure presented in section 5.3.2, using the ST-G4 small signal model (ref. table 5.5). This required some tradeoff between the requirements for the IF matching network²⁷ and the IF impedance of the SIS mixer. If the real part of the mixer's impedance were close to 50Ω , then a device size of $\sim 10 \mu\text{m}^2$ would be required, operated at a collector current of $\sim 5 \text{ mA}$, as can be seen from the design curves of figure 5.14. Assuming the use of resistive feedback between base and collector, the resulting collector to emitter voltage is $\approx 1 \text{ V}$ at cryogenic temperatures, implying that 10 mW of DC power would be required to bias the device. Fortunately, Dr. Jacob Kooi²⁸ was able to design the SIS junctions with a large $R_n \approx 135 \Omega$, offering almost a factor of 3 reduction in device size and power for minimum

²⁷Between the mixer and IFLNA.

²⁸Dr. Kooi is with the Submillimeter Astronomy and Instrumentation Group, California Institute of Technology.

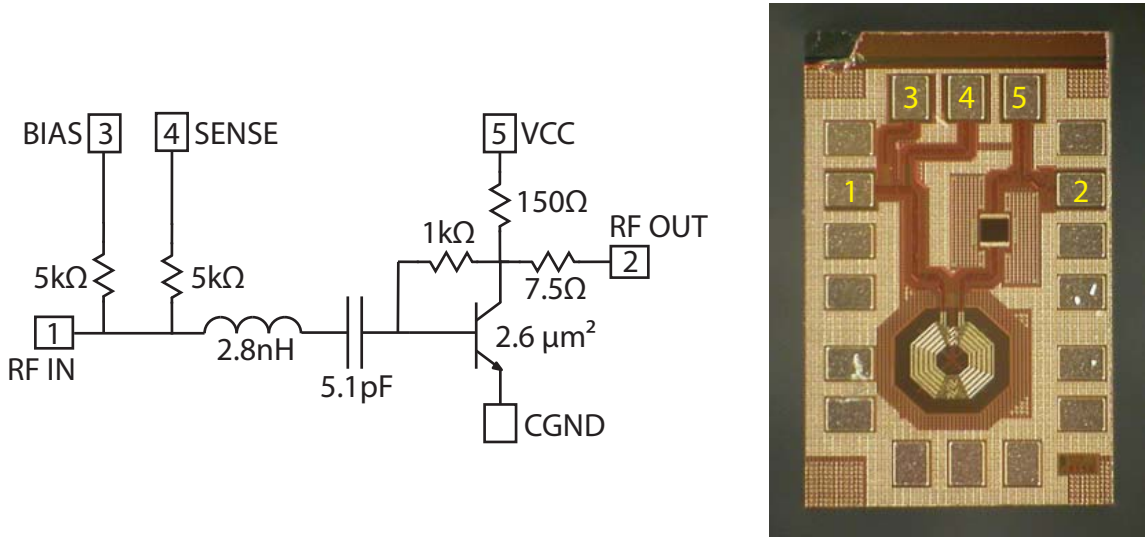


Figure 5.21: (Left) WBA23 Schematic. (Right) Photograph of fabricated IC. Dimensions after dicing are $550 \mu\text{m} \times 925 \mu\text{m}$.

noise. Following optimization, the final device size selected was a slightly smaller $2.6 \mu\text{m}^2$ operated at a collector current of 1.5 mA. The relatively small device required a feedback resistor of 1 kΩ to satisfy input match requirements, per equation (5.8), and contributes approximately 0.5 K noise as predicted by equation (5.11).

Another byproduct of the small device size was that the input of the HBT needs to see a relatively large inductance to compensate for its value of X_{opt} , which is inversely proportional to the device's input capacitance [62]. This is compounded by the reactive component of the mixers IF impedance, which is about 300 fF, only 100 fF of which is attribute to the SIS junction; the remainder associated with the IF bond pad and mounting of the SIS device. To help provide compensation for both X_{opt} and the capacitance of the SIS device, a 2.8 nH spiral inductor is included in the WBA23's input. Additional inductance is added externally, mounted between the IFLNA and mixer.

To facilitate biasing of the SIS mixer, a bias-tee is integrated into the input of the WBA23. It is comprised of two 5 kΩ shunt resistors, contributing $T_{phy} \cdot 2\Re(Z_{IF})/R_{shunt} \approx 0.23 \text{ K}$ at 4.2 K. One of the resistors is used to source bias current ($\approx 100 \mu\text{A}$) to the mixer, and the other providing feedback to the bias circuit for stabilization. The completed IC is $550 \mu\text{m} \times 925 \mu\text{m}$ after dicing (drawn dimensions are $500 \mu\text{m} \times 800 \mu\text{m}$), easily fitting within the pixel's 6 mm × 6 mm footprint. It was included within both the CITST1 and CITST2 runs.

The WBA23 MMIC was packaged into a 50Ω connectorized module for measurement of its noise and S-parameters. Although different from the impedance presented by the SIS device, the use of a 50Ω package greatly eases characterization. The module schematic and photograph are shown in figure 5.22. Measurements of the modules noise temperature at 19 K for the CITST1 and CITST2

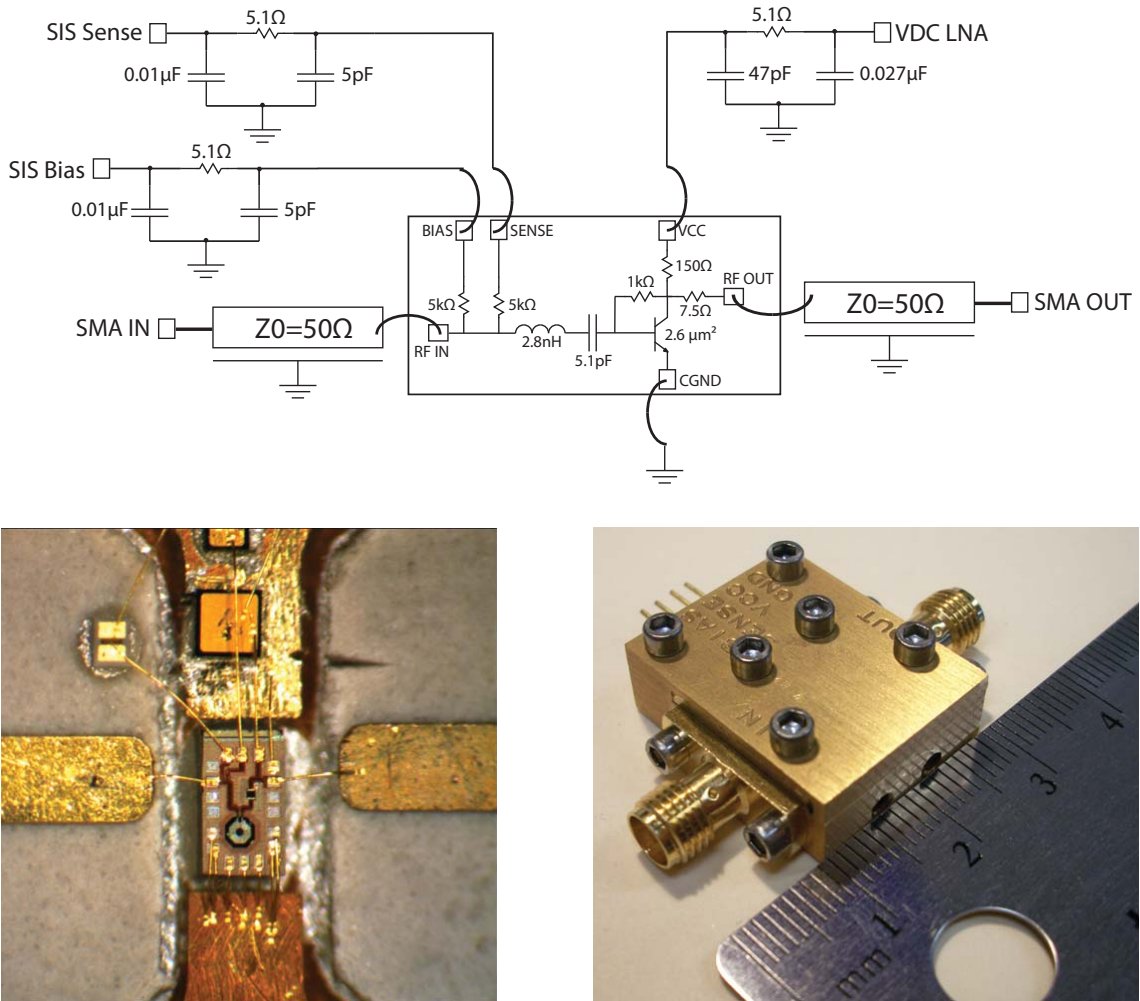


Figure 5.22: (Top) Schematic of WBA23 within 50Ω test module. (Bottom Left) Photograph of MMIC mounting within package. (Bottom Right) Module photograph. Pins at the top of the module provide bias to the MMIC and route lines to the integrated bias-tee.

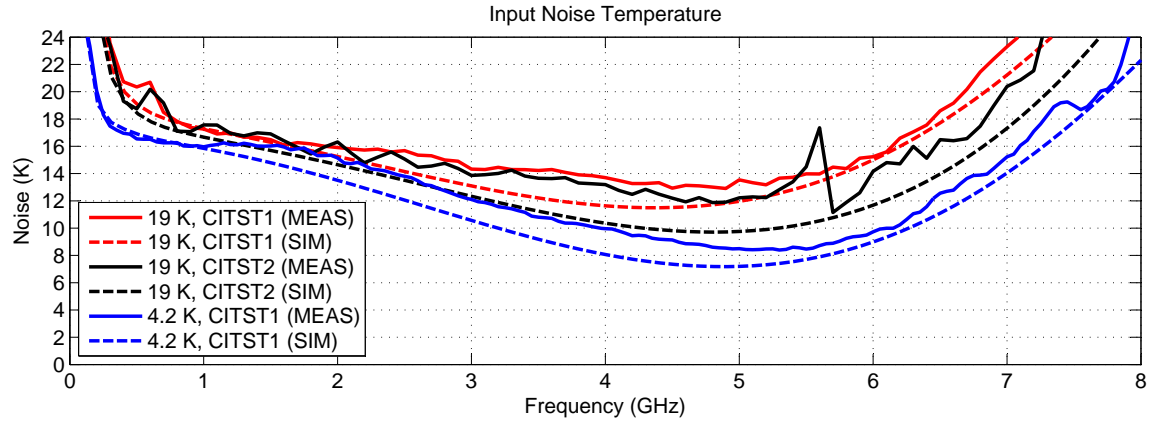


Figure 5.23: WBA23 noise temperature at 19 K and 4.2 K physical temperatures. Bias conditions are $V_{cc} = 1.289$ V @ 1.5 mA and $V_{cc} = 1.333$ V @ 1.5 mA at 19 K and 4.2 K respectively. The agreement between measurement and simulation is excellent, with less than 2 K of difference over most of the 0.5–4.5 GHz operating band. Simulations are based on the CIST1 and CITST2 small signal models.

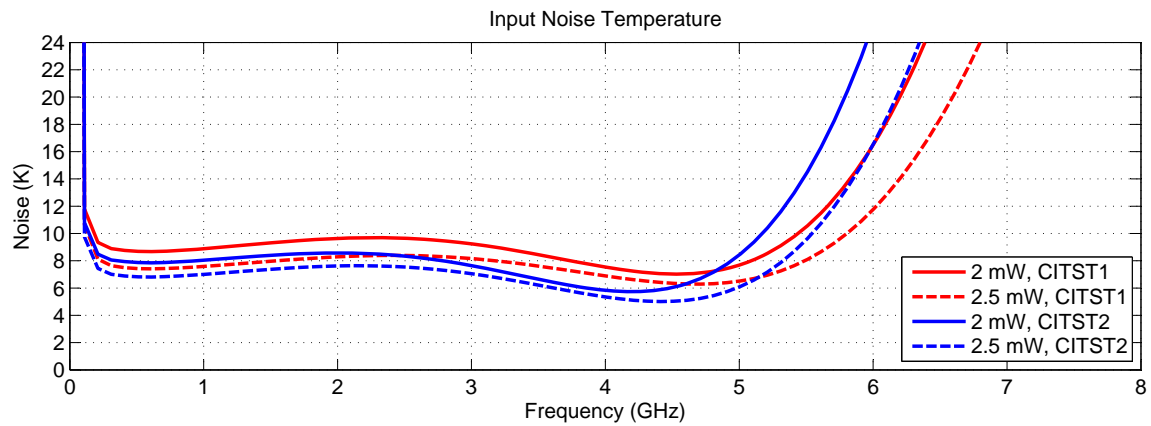


Figure 5.24: Predicted noise temperature for the WBA23, from CITST1 and CITST2 reticles, at 4.2 K when the MMIC is presented with the IF matching network and impedance of the SIS mixer. Using a slightly higher power consumption of 2.5 mW lowers the WBA23 noise temperature from the CITST2 device to ≈ 7 K over most of the band.

runs, and 4.2 K for the CITST1 run, are shown in figure 5.23. Both sets of measurements were made using the cold attenuator method, the setup for the 4.2 K measurements shown in figure 5.19. These are compared against simulation, using the appropriate small signal model from section 5.3.1, and parasitic extraction of the layout using Calibre. The measured vs. simulated noise temperatures are in good agreement, within 2 K of each across 0.5–4.5 GHz. Comparison of the noise between the CITST1 (standard β) and CITST2 (enhanced β) WBA23 designs shows only a small improvement in the noise with the CITST2 chips. This is in agreement with the predicted improvement to the low frequency noise of ~ 0.1 K, made by evaluation of equation (5.3) using the relevant small signal model. Although β is larger for the CITST2 run, its contribution is much smaller than that due to g_m , which is unfortunately lower for the CITST2 run. The small improvement in noise is believed to be due to the reduction in R_b between the two runs. The noise performance of the WBA23 at 4.2 K, when driven by the IF impedance of the SIS mixer in series with a 2.8 nH inductor for IF matching, is shown in figure 5.24. At 2 mW, both CITST1 and CITST2 iterations are below 10 K of noise, the CITST2 run being close to 8 K over the majority of the band. Although this is slightly higher than the 7 K design goal, it will still conform to the 170 K system requirement, assuming the SIS mixer has a noise temperature (DSB) of approximately 4.5 times the quantum limit and gain of ~ 8 dB. This also assumes negligible noise contribution from the post amplification.

Using a slightly higher DC power of 2.5 mW, the CITST2 sourced WBA23 MMIC is predicted to achieve ≈ 7 K of noise over the entire band. Even at this higher power, only two Sumitomo RDK-415D 4.2 K cryocoolers would be required to cool a 1000 element focal plane array. Figure 5.25 demonstrates the trade-off between noise, gain, and DC power at 1.5 GHz, for a $50\ \Omega$ generator impedance. This plot confirms diminishing returns in noise with increasing DC power above current densities of $\approx 1\ mA/\mu m^2$, corresponding to 3 mW for the entire MMIC. It also reveals that device heating is playing at most a minor role at these power levels, as the noise temperature continues to gently fall with increasing power. Obviously the improvement to g_m with increasing collector current is stronger than the self-heating observed within figure 5.11.

Finally, measurements of the modules S-parameters are compared against simulation in figure 5.26, along with the predicted performance at 4.2 K when integrated with the SIS mixer and IF matching inductor. Note the excellent agreement between measurement and simulation at 19 K, providing further validation of the modeling effort of section 5.3.1. At 4.2 K, with the inclusion of a 2.8 nH inductor for IF matching, the WBA23 MMIC is predicted to satisfy the remainder of its design goals, with the exception of $|S_{11}|$ between 4 and 4.5 GHz.

5.5.2 WBA24. Medium Power IFLNA

The main drawbacks to the WBA23 are its moderate gain and bandwidth. The KAPPA design will require careful attention to the design of the IF interconnects between the output of the WBA23 and

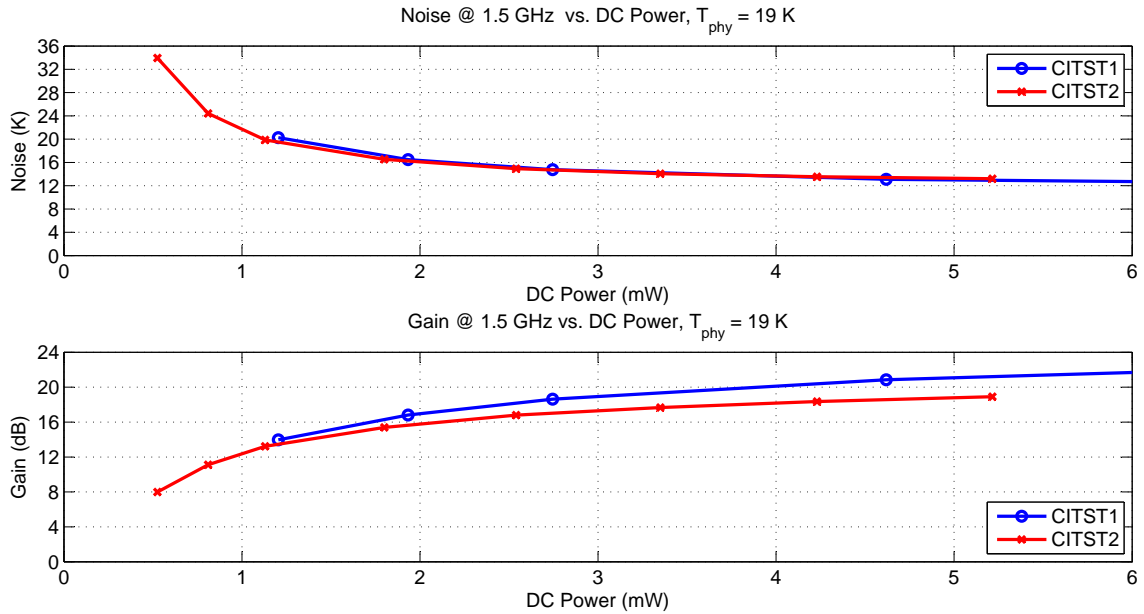


Figure 5.25: Measured WBA23 noise temperature vs. DC power at 19 K for the CITST1 and CITST2 wafer runs. The fact that the noise does not increase with increasing DC power suggests that base heating is not responsible for the additional noise shown in figure 5.23

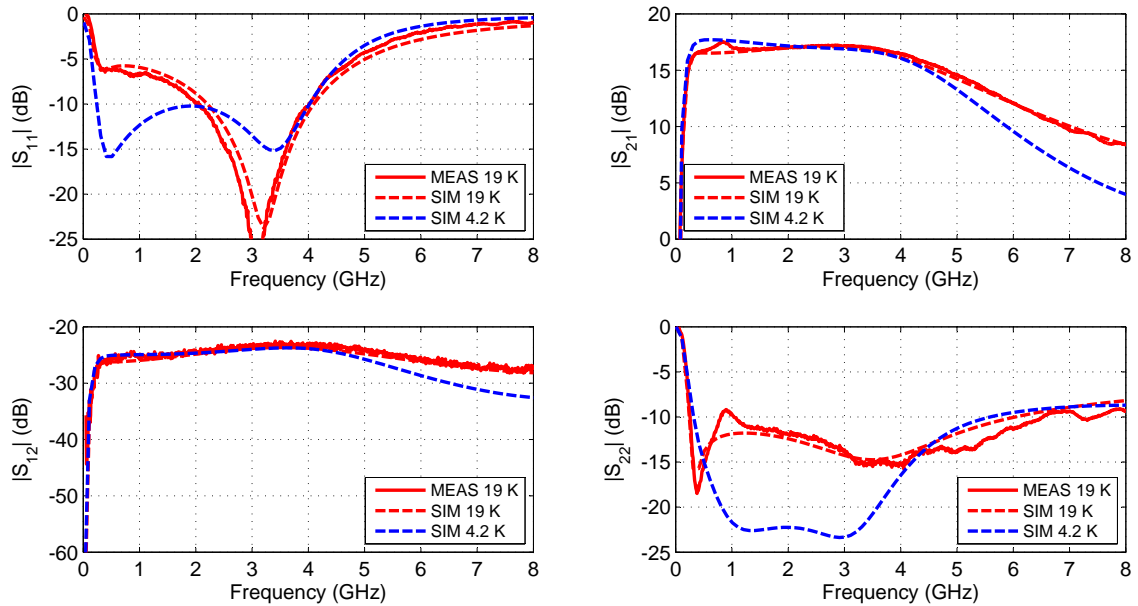


Figure 5.26: WBA23 measured and simulated $|S|$ at 19 K. Bias conditions are $V_{cc} = 1.289$ V @ 1.5 mA. The simulated results at 4.2 K are with a 2.8 nH IF matching inductor and a generator impedance equal to that presented by the IF port of the SIS mixer, approximately $135\ \Omega$ in parallel with 300 fF.

subsequent postamplification to limit the contribution from backend noise. The WBA23's use of a small device operated at low current density limits the bandwidth, due to the high value of X_{opt} . Both of these parameters are improved by increasing the current density through the transistor, at the cost of higher power consumption.

The WBA24 was designed to improve on the gain, bandwidth, and noise of the WBA23 through implementation of a two-stage amplifier with larger devices. It is intended for superconducting mixers, with $\approx 50 \Omega$ input impedance, operating between 2 and 4 GHz. The schematic and photograph of the completed MMIC are shown in figure 5.27. The first stage utilizes a $5.5 \mu\text{m}^2$ device, sized for slightly more than 4 GHz of bandwidth. A $5 \text{ k}\Omega$ feedback resistor provides minimum noise, but limits the low frequency return loss due to its high value.²⁹ The emitter of the first stage is pulled out to its own bond pad to eliminate feedback between the two stages, as discussed in section 5.3.5. Interstage matching between the two stages is accomplished through a 1.3 pF MIM capacitor and by using a low value feedback resistor for the second stage, reducing its input impedance. A 5 nH spiral inductor in the collector of the second stage provides additional frequency compensation.

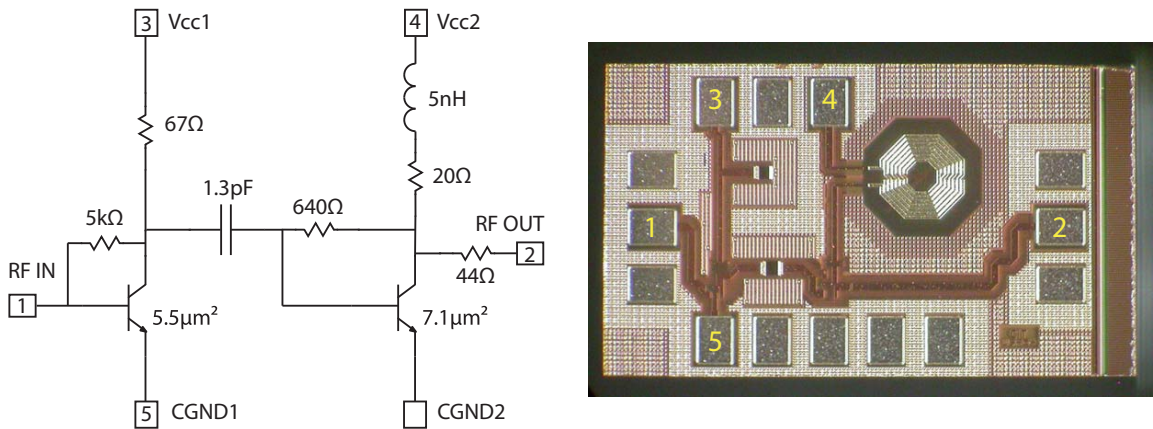


Figure 5.27: WBA24 schematic and IC photograph. Unmarked pads in photograph are CGND2. Chip dimensions after dicing are $570 \mu\text{m} \times 920 \mu\text{m}$.

The WBA24 MMIC design was included in the CITST1 run only, and subsequently packaged in a 50Ω module for testing. The schematic and photograph of the completed amplifier is shown in figure 5.28. Noise testing at 19 K physical temperature reveals good agreement between measurement and simulation, as demonstrated in figure 5.29. The best trade-off between noise and power is achieved at a DC power consumption of 8.3 mW ,³⁰ while still delivering $<8 \text{ K}$ of noise at 4 GHz. Cooling to 4.2 K is estimated to reduce the noise temperature by almost 2 K, due to the large base resistance associated with the CITST1 run. The same improvement at 19 K physical temperature may

²⁹Reducing this feedback resistor to $1.5 \text{ k}\Omega$ would improve the input match to $<-10 \text{ dB}$ at 500 MHz, with a modest increase in noise.

³⁰ $V_{cc1}=1.4 \text{ V} @ 4 \text{ mA}$ and $V_{cc2}=1.3 \text{ V} @ 2 \text{ mA}$

be obtained by approximately doubling the DC power³¹ to the device. Finally, the trade-off between noise, gain, and power is illustrated in figure 5.30. As with the WBA23, there is a diminishing return in noise with increased power, this time at about 12 mW, again at a current density of $\sim 1 \text{ mA}/\mu\text{m}^2$ through the first stage.

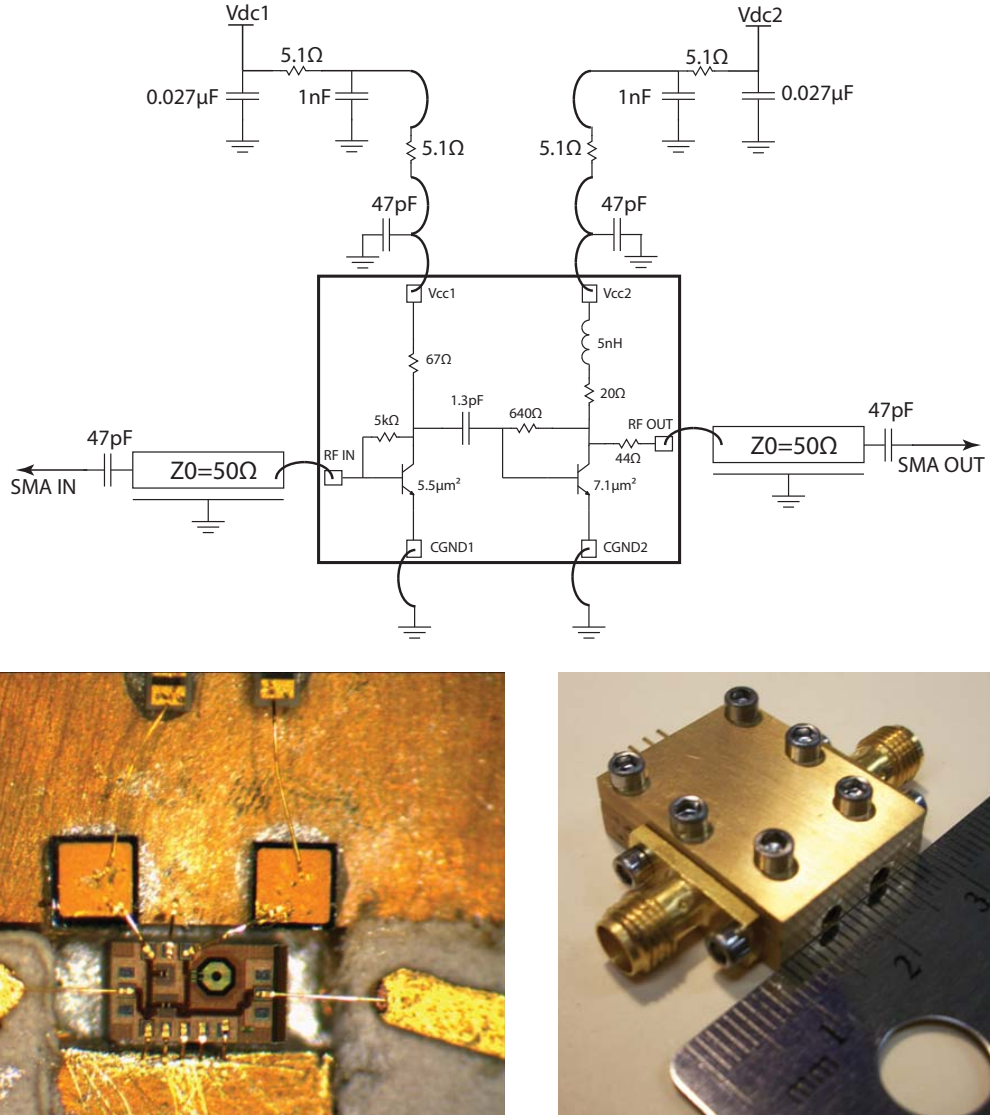


Figure 5.28: (Top) Schematic of packaged WBA24 amplifier. (Bottom Left) Mounting of MMIC within module. (Bottom Right) Photograph of completed module. Dimensions are 37.6 mm \times 24.1 mm \times 7 mm. Connectors are SMA male.

S-parameter measurements were made at the bias levels equivalent to those used for noise measurements, the results shown in figure 5.31 at 19 K physical temperature. Agreement between measurement and simulation is again excellent, with the WBA24 delivering more than 25 dB of

³¹ $V_{cc1}=1.8 \text{ V}$ @ 8 mA, $V_{cc2}=1.3 \text{ V}$ @ 2 mA

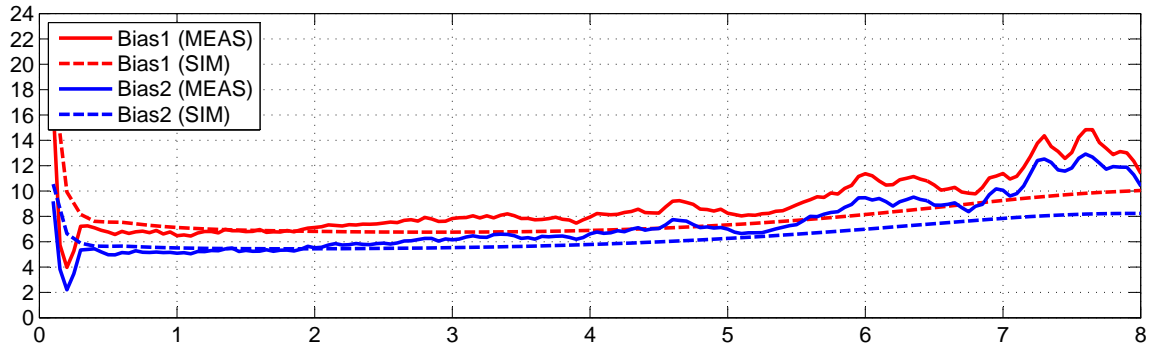


Figure 5.29: WBA24 measured and simulated noise temperature at 19 K physical temperature. Bias conditions are $V_{cc1}=1.4$ V @ 4 mA, $V_{cc2}=1.3$ V @ 2mA and $V_{cc1}=1.8$ V @ 8 mA, $V_{cc2}=1.3$ V @ 2mA for Bias1 and Bias2 settings respectively.

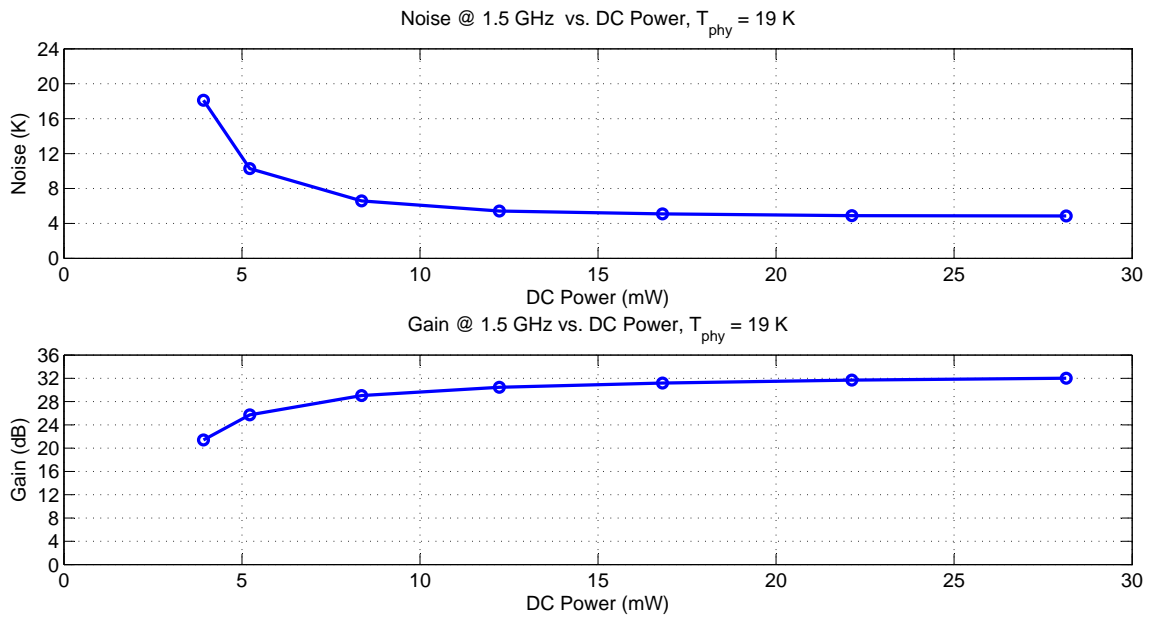


Figure 5.30: WBA24 noise temperature vs. DC power at 19 K. There is a diminishing return in performance above 12 mW, corresponding to $J_c \approx 1$ mA/ μm^2 through the first stage.

gain when operated at 8.3 mW. At this gain level it is possible for all post amplification to be done at room temperature, simplifying the system design. Post amplifiers with noise temperatures of ~ 150 K for example, would only contribute 0.5 K to the noise temperature of the IFLNA.

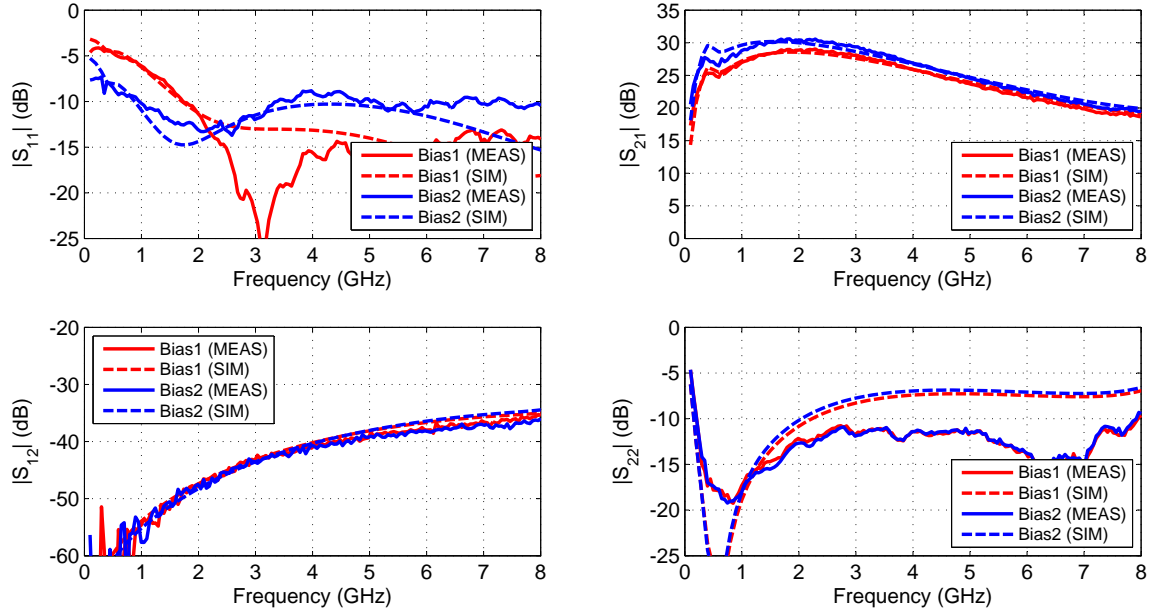


Figure 5.31: WBA24 measured and simulated S-parameters at 19 K. Bias1 and Bias2 correspond to the same bias used for the noise temperature measurements of figure 5.29.

Even with the lower noise and higher gain of the WBA24, its increased power would limit the size of THz arrays. To circumvent this problem, it is possible to thermally isolate the superconducting mixer from the IFLNA with a short section of stainless steel coax. figure 5.32 demonstrates this scheme for a single pixel, where 1 cm section of UT-47 stainless steel coaxial cable separates the mixer assembly (4.2 K) from the LNA (20 K). It should be noted that a larger semirigid cable could also be used, such as UT-85, but the factor of ≈ 1.8 improvement in loss [72] is accompanied by a factor of 3.6 increase in cross-sectional area. The added cross-sectional area implies that the length needs to be increased by the same amount for a given thermal transfer, thus offsetting any improvement in loss. This short section of coax would transfer 1 mW of heat into the mixer block, with a 0.57 K increase in the effective noise temperature of the IFLNA. Cooling a 1000 element array of superconducting mixers would therefore be possible with a single Sumitomo 4.2 K cryocooler. The IFLNA would be cooled with a separate cryocooler,³² such as Sumitomo's SRDK-408S2 which is capable of removing 13 W at 20 K. The second stage of this cooler could then be used to provide an intermediate heat sink to the UT-47 cable from the output of the IFLNA to further postamplification at 300 K. The

³²The RDK0415D's first stage could be used for this function, but its corresponding temperature would be ≈ 33 K. The result would be an increase the noise of the WBA24 by 1.6 K.

cost of isolating the WBA24 from the superconducting mixer is the additional complexity introduced by the semirigid coaxial cables and the additional cryocooler required. The advantage, however, is that cryogenically cooled postamplification is not required, as is with the WBA23.

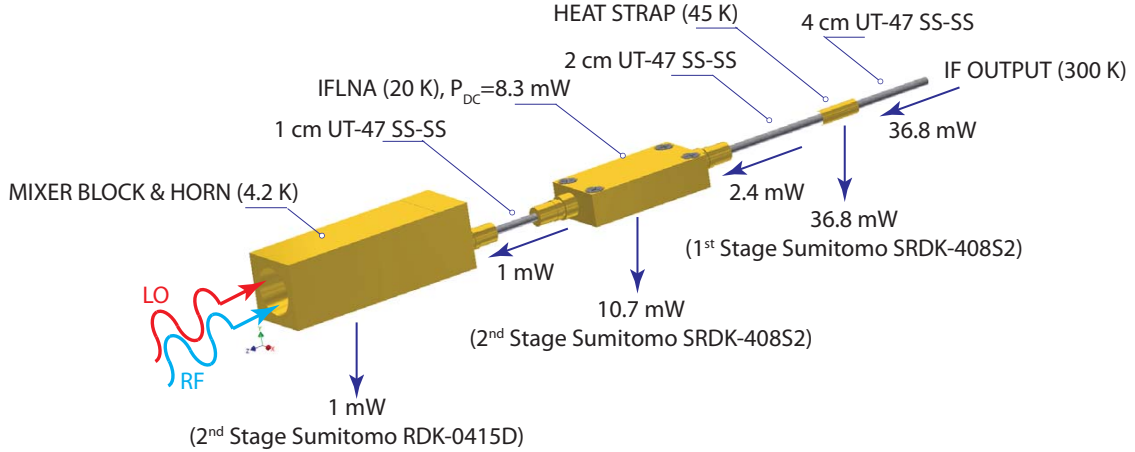


Figure 5.32: Packaging concept for medium power IFLNA module. Horn and superconducting mixer assembly is thermally isolated from the IFLNA through a 1 cm section of stainless steel UT-47 semirigid coaxial cable. When the IFLNA is adequately heat sunk to the 20 K stage of its cryocooler, only 1 mW of heat is transferred to the mixer's 4.2 K stage.

5.5.3 WBA25. High Power IFLNA

As a final example, the capabilities of an IFLNA are explored, without concern for DC power consumption. The WBA25, whose schematic and IC photograph are shown in figure 5.33, was designed with this in mind and included on the CITST2 reticle only. The initial design goals were to develop an IFLNA with <10 K of noise and 30 dB of gain over a bandwidth of 1–6 GHz. The first stage was designed using the same device size as the WBA24, but with a smaller value of feedback resistor to aide in low frequency return loss. A smaller device was selected for the second stage, to improve its high-frequency response. The interstage matching network, consisting of a spiral inductor and MIM capacitor, was designed to provide flat gain over the design bandwidth. Additional gain compensation is provided by peaking inductors in the collectors of each stage and a parallel RC network in the MMIC's output. The emitters for each device were pulled out to their own bondpads, allowing some tuning of noise and power match.

At the time of the design, the passives within the CITST1 reticle had not been fully tested, and it was not yet known if the n-well capacitors would suffer from freeze-out. Assuming a $10\times$ reduction in n-well capacitance at cryogenic temperatures, >100 pF of bypass capacitance was added to the supply pad of each stage. Metal layers 2–6, above the n-well bypass were interdigitated, providing additional capacitance. This ensured that at least 10 pF of on-chip capacitance would be available

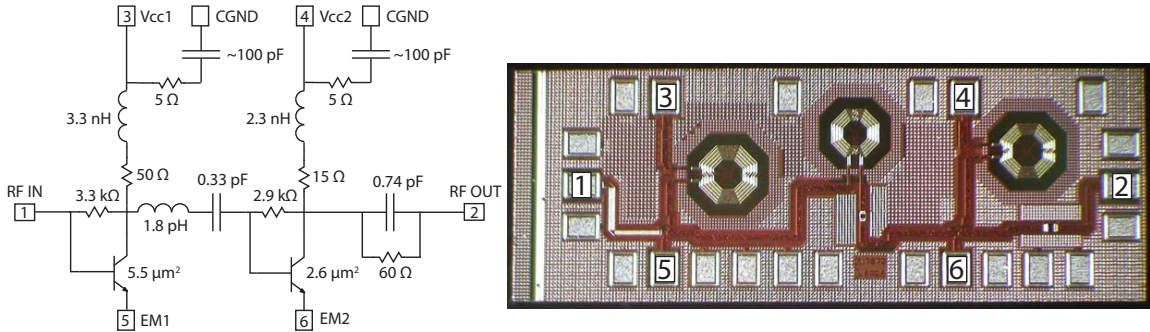


Figure 5.33: WBA25 schematic and IC photograph. Unmarked pads in photograph are CGND. Chip dimensions after dicing are $570 \mu\text{m} \times 1500 \mu\text{m}$.

to help stabilize the amplifier, regardless of the temperature dependence of the capacitors. Freeze out turned out not to be a concern at the supply voltages the MMIC is run at, so each stage has $\approx 100 \text{ pF}$ of bypass capacitance associated with it.

Design simulations using the small signal CITST1 model revealed that the amplifier would deliver the desired performance at 15 mW of DC power consumption. The completed CITST2 MMICs measured $570 \mu\text{m} \times 1500 \mu\text{m}$, the length of the IC driven by the size of the on chip spiral inductors and associated metal density rules. Figure 5.33 reveals the schematic and photographs of the packaged amplifier prior to testing.

Unfortunately, all of the CITST2 multistage amplifiers³³ suffered from what appeared to be biasing problems of the second and subsequent stages at cryogenic temperatures. For the WBA25, this manifested itself in low-gain from 1 to 4 GHz, with a large positive slope. Only reducing the transconductance of the output stage to $\sim 30\%$ of that determined from the discrete characterization allowed reasonable agreement between measurement and simulation. Figure 5.35 illustrates measurement vs simulation for two bias conditions: those from the design values; and that at a slightly higher current density through the second stage. Note that there is a $>10 \text{ dB}$ jump in the low frequency gain between the Bias 1 and Bias 2 levels, even though the current has only increased 1 mA through the second stage. What was somewhat surprising is that the bias conditions where low gain was observed did not appear to correspond to instability of the amplifier, as oscillations were not observed with subsequent tests with a spectrum analyzer to 26.5 GHz. It is possible that this is a manifestation of the transconductance frequency dispersion, attributed to by the presence of fast traps, and deserves further investigation. Although a reduction of g_m by $\approx 20\%$ was observed on discrete devices within the CITST2 reticle, it is suspected that this problem may be more extensive than first thought.

Not regarding with the problems associated with the cryogenic operation of the WBA25, it does

³³Refer to table 5.8 for a summary of CITST2 designs.

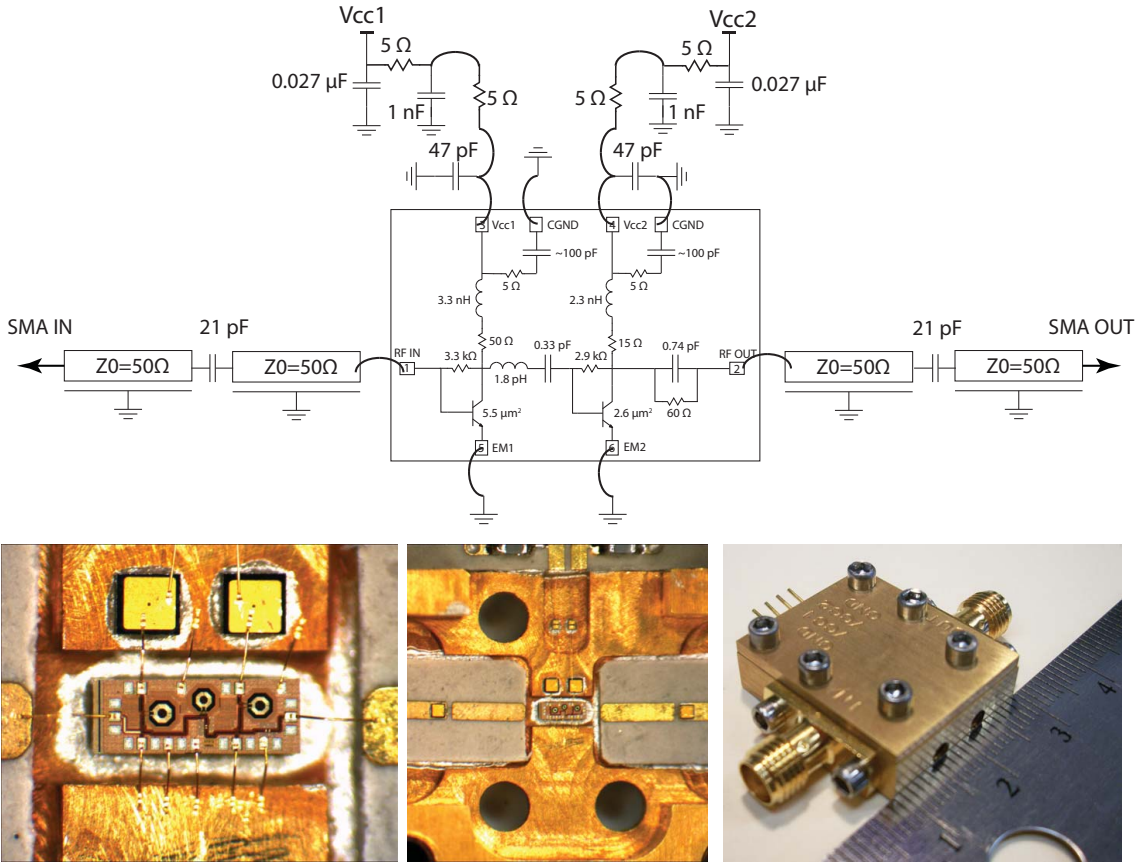


Figure 5.34: WBA25 MMIC packaged within a $50\ \Omega$ module. (Top) Schematic of packaged module. (Bottom Left) Mounting of MMIC within module. (Bottom Middle) Overview of module interior. There is a small cover, that fits over the MMIC to prevent feedback from the output to input of the chip, that has been removed for this photo. (Bottom Left) Photograph of completed module. Dimensions are $37.6\text{ mm} \times 24.1\text{ mm} \times 7\text{ mm}$.

achieve $<8\text{ K}$ of noise from 1 to 10 GHz at the higher bias condition, with a minimum of 4.5 K at 5 GHz. This is illustrated in figure 5.36 along with the noise temperature for the design at several bias levels. Test results at Bias 3 in figure 5.35 and 5.36 were made at a power of only 13.3 mW , and reveal that the amplifier has $<6\text{ K}$ of noise from 4 to 8 GHz, along with high gain and low mismatch. With the appropriate thermal isolation scheme in place, this amplifier would make an attractive alternative to InP LNAs used for SIS receivers within this frequency range.

It is believed that the problems associated with the CITST2 MMICs are associated with a yet unidentified solid state effect within the HBTs that shows up at cryogenic temperatures. Indeed, the room temperature performance of all the CITST2 MMICs were very close to their simulations. The WBA25, in fact, is a fairly good room temperature LNA, as shown in figure 5.37 and figure 5.38. Room temperature measurements were made at current densities of 3 times their cryogenic design values, to compensate for the reduction in transconductance. The corresponding noise temperature

was approximately 80 K over 1–7 GHz, with 25 dB gain, and -10 dB match on input and output.

5.6 Suggestions for Future Work

Future work on cryogenic SiGe LNAs should be focused on the characterization and modeling of a single process. The increase in β for the HBTs of CITST2 was not warranted by the marginal increase in noise performance given the cost of lower transconductance and frequency dispersion issues. It is very possible that all designs from the CITST2 reticle, summarized in table 5.8 would perform satisfactorily if the enhanced β had not been requested. Using the standard β would also have tested the repeatability of the process, for cryogenic operation, an important factor in the development of IFLNAs for very large arrays.

Work should continue on reducing the power consumption of the IFLNA. Although thermal isolation schemes are possible, as presented in section 5.5.2, they add complexity to the packaging.

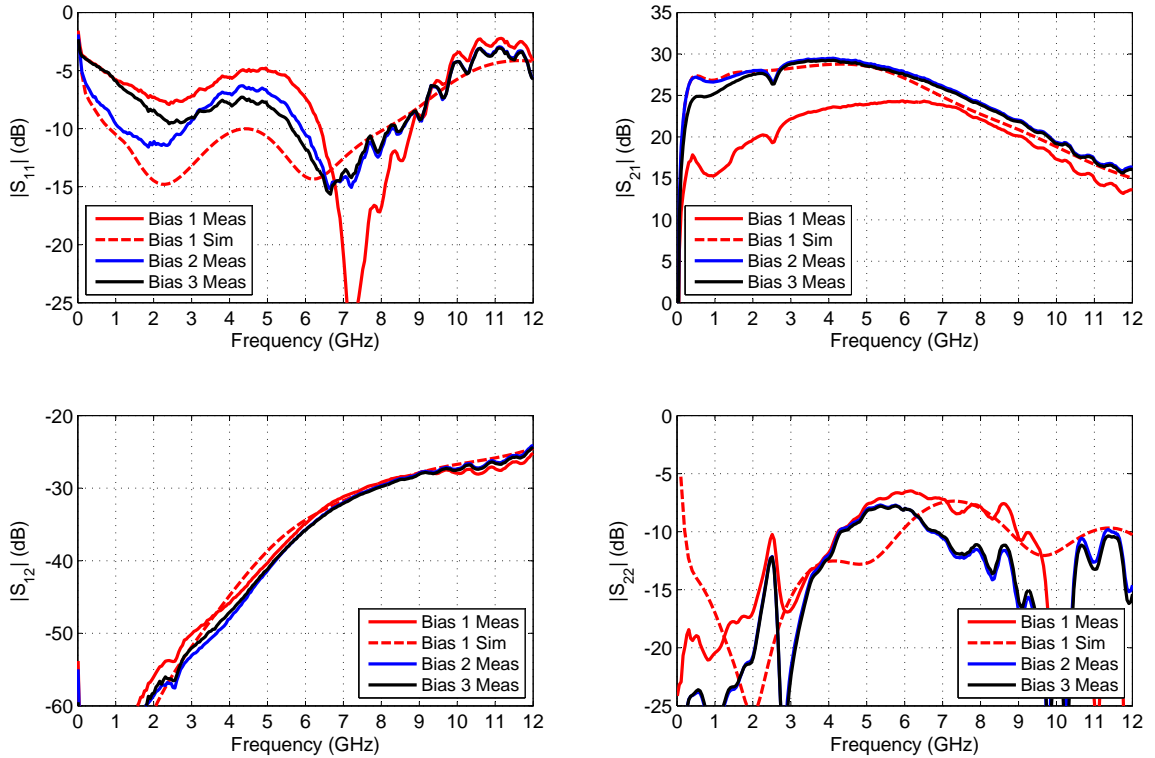


Figure 5.35: WBA25 measured and simulated S-parameters at 21 K physical temperature. Bias 1 ($V_{cc1}=1.57$ V at 10 mA, $V_{cc2}=1.10$ V at 5 mA) represents the optimal noise temperature predicted by simulation. Bias 2 ($V_{cc1}=1.56$ V at 10 mA, $V_{cc2}=1.16$ V at 6 mA) reveals a dramatic change in performance with only a 1 mA increase in the current through the second stage. Bias 3 ($V_{cc1}=1.27$ V at 5 mA, $V_{cc2}=1.16$ V at 6 mA) represents the best trade-off in noise vs. power for operation between 4 and 8 GHz.

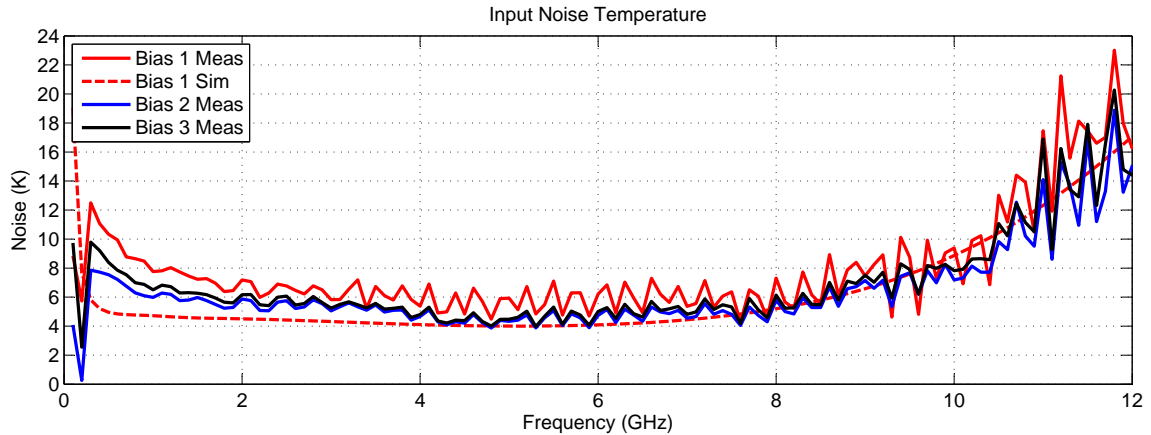


Figure 5.36: WBA25 measured and simulated noise temperature at 21 K physical temperature. Bias conditions are identical to those given in figure 5.35. The IFLNA demonstrates <8 K of noise between 1 and 10 GHz.

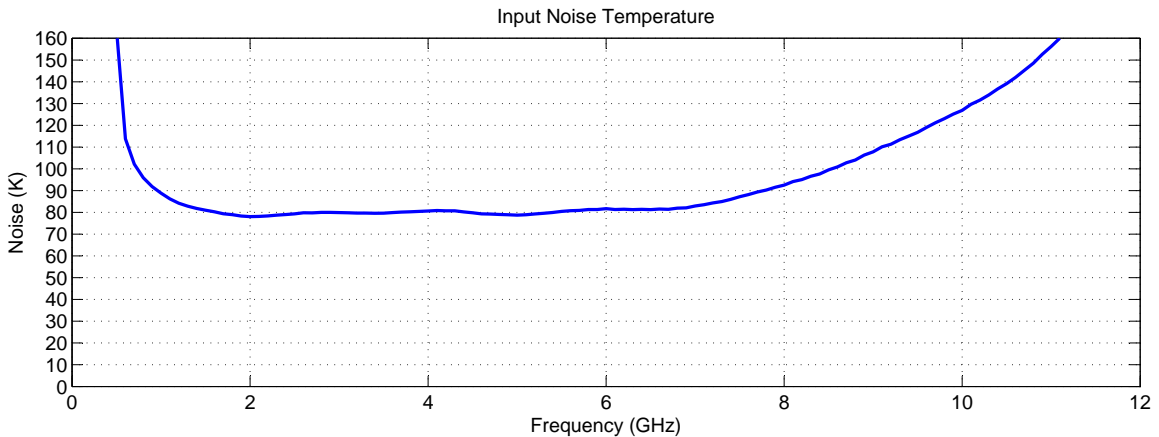


Figure 5.37: Measured noise temperature of WBA25 MMIC at room temperature. The device is biased at ($V_{cc1}=2.84$ V at 30 mA, $V_{cc2}=1.31$ V at 15 mA), an increase by a factor of 3 from the cryogenic design values to compensate for the drop in transconductance.

A slight improvement in the power consumption may be afforded by running the collector voltage slightly (~ 0.2 V) below the base. This would reduce power consumption per HBT by approximately 20% at cryogenic temperatures. Alternate schemes for bias and low frequency return loss would have to be devised as a result. The development of IFLNAs employing III-V based HEMTs should continue, as these devices have the potential for very low power operation. This is due to the fact that they can be operated at very low drain voltages, ~ 300 mV, opposed to the collector of a SiGe that must remain >800 mV for forward active mode. InP LNAs with noise temperatures as low as 2.4 K, using only 1 mW of DC power, have been reported in the 4–8 GHz band [73]. These are fairly large, discrete transistor amplifier modules, however. Further work will be necessary in the

miniaturization of these discrete designs and/or MMIC realization for use in large focal plane arrays. Although the use of HEMTs is feasible for SIS mixers where the IF bandwidth may be adjusted, the same is not true of HEB mixers whose upper IF frequency is limited by the thermal time constant of the superconducting film bridge. In such cases SiGe HBT designs afford the low frequency return loss necessary to suppress thermoelectric feedback. Although isolators may be used between the mixer and IFLNA, these complicate the design and add noise of their own.

As the f_t of future generations of SiGe improves, R_b will necessarily improve as a result. This in turn, will increase the frequency at which SiGe offers similar noise to its III-V counterparts, currently in the neighborhood of 5 GHz. SiGe largest strength, will continue to be the high yield afforded by 50+ years of rigorous development in Si processing. The same cannot be said of the III-V technologies, which have only seen commercialization starting in the mid 1990s. The path towards very large focal plane arrays for THz receivers will undoubtedly require the utilization of high yield technologies.

Unfortunately, most of the MMICs within the CIST2 reticle suffered from low frequency instability in the 50–300 MHz range. This problem was not observed at room temperature, even with the amplifiers operating at 3 times their cryogenic current density to compensate for the increase in transconductance with cooling. Oddly, this problem also effected most of the single stage amplifiers

³⁴Differential design.

³⁵CITST1 and CITST2 reticles.

³⁶Requires IF matching network.

³⁷CITST2 reticle.

³⁸CITST1 reticle.

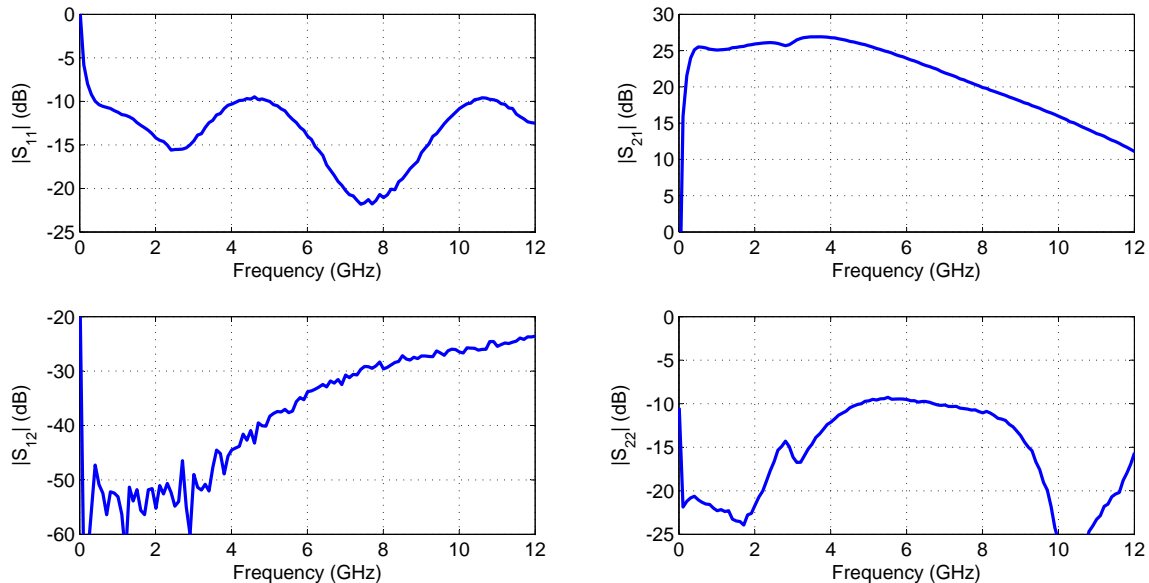


Figure 5.38: S-parameters of the WBA25 MMIC at room temperature. Bias conditions are equivalent to those of figure 5.37.

Table 5.8: Status of SiGe MMIC designs from CITST1 and CITST2 reticles.

| Design | Design Status | | | | | Status/Results |
|-------------------------|---------------|-----------|--------------------|-----------|--------|---|
| | Design Goals | | | | | |
| | BW (GHz) | Gain (dB) | Input (Ω) | Noise (K) | P (mW) | |
| WBA22 ^{35,37} | 0.5–15 | 31 | 200 | 9 | 25 | BW \approx 14 GHz. Noise \sim 15K at 1 GHz (meas) |
| WBA23 ^{36,37} | 0.5–4.5 | 17.5 | 100 | 7 | 2 | Noise \sim 8 K at 4.2 K (est.), 2 mW DC power. |
| WBA23B ^{37,38} | 0.5–4.5 | 16.5 | 50 | 7.5 | 3 | \approx 9 K at 19 K (meas), 3 mW of DC power. |
| WBA23C ^{37,38} | 0.5–4.5 | 17.5 | 100 | 7 | 2 | Functional at room temperature, unstable/low gain at cryogenic temperatures. |
| WBA23D ^{37,38} | 0.5–4.5 | 29.5 | 100 | 7 | 4 | Functional at room temperature, unstable/low gain at cryogenic temperatures. |
| WBA23E ^{37,38} | 0.5–4.5 | 28 | 50 | 8 | 5 | Functional at room temperature, unstable/low gain at cryogenic temperatures. |
| WBA24 ^{37,39} | 2–4 | 30 | 50 | 10 | 10 | Noise $<$ 8 K 0.5–4 GHz. 8.3 mW of DC power. |
| WBA25 ³⁸ | 0.5–6 | 30 | 50 | 4.5 | 22.5 | $<$ 8 K noise 1–10 GHz, $<$ 6 K 4–8 GHz. Gain 30 dB BW \approx 6 GHz. (meas) |
| WBA26 ³⁸ | 1–11 | 30 | 50 | 8 | 25 | Functional at RT. Cryogenically, low gain 1–5 GHz, traced to possible g_m /biasing issue in final stages. |

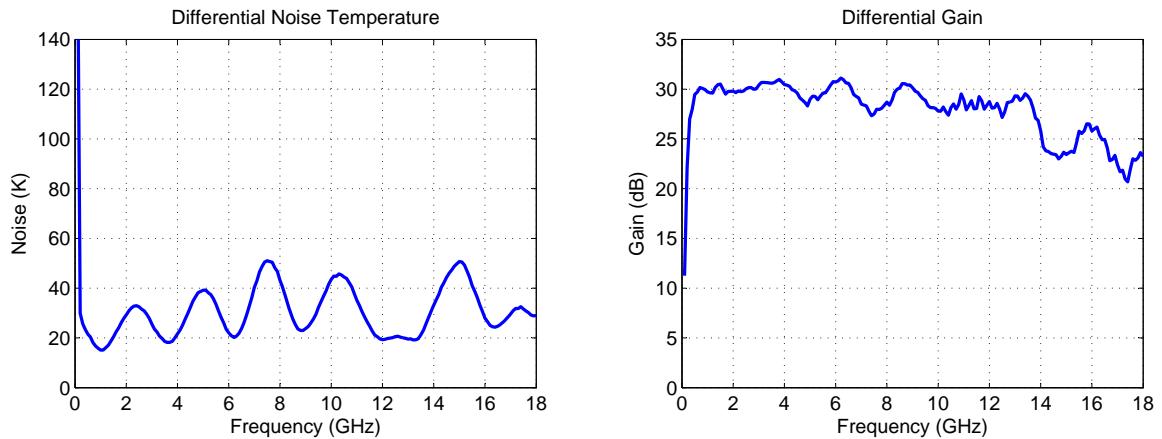


Figure 5.39: Measured differential noise and gain of WBA22 MMIC at 19 K. Bias conditions are $V_{cc1}=1.57$ V @ 4 mA, $V_{cc2}=1.85$ V @ 11 mA. The WBA22 is 2-stage differential amplifier, included on the CITST1 reticle, with a 200 Ω differential input impedance. Problems with the packaging of the MMIC are responsible for the ripple in the measured noise temperature and gain.

in the CITST2 reticle, which in principle should be harder to induce instability within. This behavior has also been observed to some extent in the discrete devices contained within the CITST2 reticle, tested within discrete amplifiers. Although the DC network contained within the packaged amplifiers was suspected, due to the low frequencies involved, extensive analysis revealed that they were not the source of the problem. Curiously, the frequency at which the instability occurs is similar to that of the ripple in transconductance shown in figure 5.12.

The WBA22 MMIC, included on the CITST1 reticle only (refer to 5.1), also warrants further work. It is a 500 MHz–15 GHz differential amplifier, designed to work with wide-band feeds requiring a $\sim 200 \Omega$ differential, low noise amplifier [74], [75]. Preliminary test data taken on the packaged MMIC is shown in figure 5.39, at a physical temperature of 19 K. Difficulties with the packaging resulted in the ripple in the noise temperature and gain. The first stage of the amplifier utilizes a differential pair consisting of small, $1.3 \mu\text{m}^2$ devices, to meet bandwidth requirements. As discussed in section 5.3.1, the smaller CITST1 devices resulted in higher noise than originally expected, from low transconductance and high base resistance. The noise minima of the WBA22 are roughly 10 K higher than initial simulations predicted³⁹ as a result. Future revisions of the WBA22 should incorporate larger devices, taking advantage of both higher transconductance and lower base resistance. Additional gain compensation with frequency will be required accordingly. Noise temperatures of ≈ 10 K to 10 GHz should be possible with such an approach.

5.7 Summary

In this chapter, the design and testing of low power, SiGe, IFLNAs for use in large terahertz arrays of superconducting mixers has been discussed. The basic operating principles of superconducting mixers and their limitations were presented, followed by the requirements they impose on the design of the IFLNA. Section 5.3 outlined the design of IFLNAs, focused on MMIC realization, through a detailed discussion of device modeling, cryogenic performance of passive elements, the use of resistive feedback, and design layout. Examples of IFLNAs for terahertz arrays were presented in section 5.5. One of these, the WBA23, consumes only 2 mW of power and will be utilized within KAPPa, a thousand-pixel terahertz array pathfinder project currently under development. The trade-offs between power, noise, and bandwidth were explored with two additional IFLNAs described in this work. Although they consume more power, they demonstrated the capability of providing less than 8 K of input noise temperature to 10 GHz. The thermal isolation scheme of these higher power designs was discussed, allowing their use in large focal plane arrays cooled by a few cryocoolers.

³⁹Based on the original ST-G4 HBT models from Bardin.

Chapter 6

Conclusions

Three technological advancements, necessary for the development of the thousands of LNAs for radio-astronomy's future instruments, have been presented. Their development, testing, limitations, and suggestions for future work have been clearly addressed. The cryogenic probe station presented in chapter 2 is the first of its kind, capable of performing automated testing of 100 mm InP wafers below 20 K. This station is already in use at Caltech, screening MMICs for new, as well as existing instruments. Similarly, the system presented in chapter 4 provides a key capability of measuring device noise parameters cryogenically. It does so using a robust, easily produced variable impedance noise source that works in concert with existing noise analyzers. Finally, the low noise, SiGe IFLNAs detailed in chapter 5 will pave the way for the manufacturing of extremely large focal plane arrays of superconducting terahertz mixer receivers. Its use of SiGe provides noise comparable to more exotic III-V technologies as well as offering the inherent benefits of high yield silicon processing.

Over the course of this work, I have become convinced that employing highly manufacturable elements within tomorrow's instruments is essential for their successful completion. Manufacturability can no longer be an afterthought, but a design variable, weighted with increasing importance as the number of elements grows. Indeed, with today's economic climate, successful completion of each project milestone is necessary to secure (but not guarantee) future funding. I have also become convinced that technologies that provide for great research papers should not, by default, be employed in future instrumentation. This is especially true in radio-astronomy, where the benefits of the sheer number of receiving elements allows for its own performance advantages. The use of technologies with lesser performance capabilities, but higher manufacturability, might quite possibly make better performing instruments through the power of numbers alone. Finally, although technology continues to advance, instruments in the design phase should not count on a given technology making a necessary advance, even if prophesied by industry. Only technologies with clear development paths (and clear lines of funding!) should be implemented within a design. Those projects which embrace such ideas shall make the most of today's dwindling financial resources and provide the scientific community with the most capable of instruments.

Bibliography

- [1] J. Kraus, *Radio Astronomy*. Powell, OH: Cygnus-Quasar Books, 1986, ch. 7, p. 12.
- [2] S. Weinreb, R. Lai, N. Erickson, T. Gaier, and J. Wielgus, “W-Band InP Wideband MMIC LNA with 30K Noise Temperature,” in *1999 IEEE MTT-S International Microwave Symposium Digest*, vol. 1, 1999, pp. 101–104.
- [3] E. Bryerton, X. Mei, Y. Kim, W. Deal, W. Yoshida, M. Lange, J. Uyeda, M. Morgan, and R. Lai, “A W-band Low-Noise Amplifier with 22 K Noise Temperature,” in *2009 IEEE MTT-S International Microwave Symposium Digest*, 2009, pp. 681–684.
- [4] S. Pan, A. Kerr, M. Feldman, A. Kleinsasser, J. Stasiak, R. Sandstrom, and W. Gallagher, “An SIS Mixer for 85-116 GHz Using Inductively Shuted Edge-Transitions,” pp. 465–468, 1988.
- [5] J. Condon and S. Ransom, “Recombination lines,” National Radio Astronomy Observatory, Tech. Rep., Apr. 2007, available on line at <http://www.cv.nrao.edu/course/astr534/PDFfiles/Recombination.pdf>.
- [6] C. Walker, C. Groppi, D. Golish, C. Kulesa, A. Hungerford, K. Jacobs, U. Graf, C. Martin, and J. Kooi, “PoleSTAR: A 4-Pixel 810 GHz Array Receiver for AST/RO,” San Diego, CA, pp. 540–552, 2001.
- [7] C. Groppi, C. Walker, C. Kulesa, D. Golish, P. Pütz, P. Gensheimer, A. Hedden, S. Bussmann, S. Weinreb, G. Jones, J. Bardin, H. Mani, T. Kuiper, J. Kooi, A. Lichtenberger, T. Cecil, and G. Narayanan, “SuperCam: A 64 pixel superheterodyne camera,” Pasadena, CA, pp. 264–269, 2007.
- [8] A. Kerr, S. Baker, E. Bryerton, T. Crowe, N. Erickson, P. Goldsmith, C. Gottlieb, C. Groppi, J. Hesler, T. Hunter, A. Lichtenberger, G. Narayanan, S. Padin, S. Pan, A. Russell, S. Srikanth, P. Thaddeus, C. Walker, J. Weber, B. Weikle, A. Wootten, L. Ziurys, and J. Zmuidzinas, “In Support of Instrument Technology Development for THz Astronomy,” Mar. 2009, a white paper submitted to the RMS and EOS panels of The Astronomy & Astrophysics Decadal Survey Committee Astro2010. Available online at <http://www8.nationalacademies.org/astro2010/DetailFileDisplay.aspx?id=493>.

- [9] A. Mellberg, N. Wadefalk, I. Angelov, E. Choumas, E. Kollberg, N. Rorsman, P. Starski, J. Stenarson, and H. Zirath, “Cryogenic 2-4 GHz ultra low noise amplifier,” Fort Worth, TX, pp. 161–163, 2004.
- [10] J. Bardin, “Silicon-Germanium Heterojunction Bipolar Transistors for Extremely Low-Noise Applications,” Ph.D dissertation, California Institute of Technology, Dept. Elect. Eng., Pasadena, CA, 2009.
- [11] S. Weinreb, J. Bardin, and H. Mandi, “Design of Cryogenic SiGe Low-Noise Amplifiers,” *IEEE Transactions on Microwave Theory and Techniques*, vol. 55, no. 11, pp. 2306–2312, Nov. 2007.
- [12] D. Russell, K. Cleary, and R. Reeves, “Cryogenic Probe Station for On-Wafer Characterization of Electrical Devices,” *Review of Scientific Instruments*, vol. 83, no. 4, pp. 044703–1–044703–10, Apr. 2012.
- [13] D. Russell and S. Weinreb, “Cryogenic Self-Calibrating Noise Parameter Measurement System,” *IEEE Transactions on Microwave Theory and Techniques*, vol. 60, no. 5, pp. 1456–1467, May 2012.
- [14] ——, “Low-Power Very Low-Noise Cryogenic SiGe IF Amplifiers for Terahertz Mixer Receivers,” *IEEE Transactions on Microwave Theory and Techniques*, vol. 60, no. 6, pp. 1641–1648, Jun. 2012.
- [15] A. Wexler, “Evaporation Rate of Liquid Helium,” *Journal of Applied Physics*, vol. 22, no. 12, pp. 1463–1470, 1951.
- [16] E. Marquardt, J. Le, and R. Radebaugh, “Cryogenic Material Properties Database,” in *Proceedings of the 11th International Cryocooler Conference*, vol. 12, no. 6. Springer, 2000, pp. 1–7.
- [17] R. Barron, *Cryogenic Systems*, 2nd ed. New York, NY: Oxford University Press, 1985, pp. 386–391.
- [18] F. Incropera, D. Dewitt, T. Bergman, and A. Lavine, *Introduction to Heat Transfer*, 5th ed. Hoboken, NJ: John Wiley and Sons, 2007, pp. 772–793.
- [19] G. Petencin, “Plating the Inside of Stainless Steel Waveguide to Reduce RF Losses While Retaining the Thermal Isolation,” National Radio Astronomy Observatory, Charlottesville, VA, Tech. Rep., Jul. 2005, ALMA DOC FEND-40.02.06.00-140-A-PRO.
- [20] B. Shank, J. Heilman, and A. Dahm, “Metallic Plating of WR-10 Stainless-steel Waveguide,” *Microwave Journal*, Aug. 2007.

- [21] A. Kerr and N. Horner, "The Low Temperature Thermal Resistance of High Purity Copper and Bolted Copper Joints," National Radio Astronomy Observatory, Charlottesville, VA, Electronics Division Technical Note 163, Aug. 1991.
- [22] A. Kerr and R. Groves, "Measurements of Copper Heat Straps Near 4 K With and Without Apiezon-N Grease," National Radio Astronomy Observatory, Charlottesville, VA, Electronics Division Technical Note 204, Oct. 2006.
- [23] T. Tomaru, T. Suzuki, T. Haruyama, T. Shintomi, A. Yamamoto, T. Koyama, and R. Li, "Vibration Analysis of Cryocoolers," *Cryogenics*, vol. 44, no. 5, pp. 309–317, May 2004.
- [24] W. Nash, *Metals Engineering Design*, 2nd ed. McGraw-Hill, 1965, pp. 174–179.
- [25] R. Green, *Machinery's Handbook*, 24th ed. New York, NY: Industrial Press, 1992, pp. 256–258.
- [26] *Parker O-Ring Handbook*, Parker Hannifin Corp., O-Ring Div., 2360 Palumbo Drive, Lexington, KY 40509, 2001, available online at www.parker.com/o-ring.
- [27] G. Ediss, F. Johnson, D. Koller, and A. Kerr, "WR-10 Waveguide Vacuum Feedthrough for the ALMA Band-6 Cartridge," National Radio Astronomy Observatory, Charlottesville, VA, ALMA Memo 536, Sept. 2005.
- [28] L. Samoska, A. Fung, D. Pukala, P. Kangaslahti, R. Lai, S. Sarkozy, X. Mei, and G. Boll, "On-wafer measurements of S-MMIC amplifiers from 400–500 GHz," in *2011 IEEE MTT-S International Microwave Symposium Digest*, 2011, pp. 1–4.
- [29] H. Rothe and W. Dahlke, "Theory of Noisy Fourpoles," *Proceedings of the IRE*, vol. 44, no. 6, pp. 811–818, 1956.
- [30] H. Nyquist, "Thermal Agitation of Electric Charge in Conductors," *Physical Review*, 1928.
- [31] J. Lange, "Noise Characterization of Linear Twoports in Terms of Invariant Parameters," *IEEE Journal of Solid-State Circuits*, 1967.
- [32] M. Pospieszalski, "On the Measurement of Noise Parameters of Microwave Two-Ports," *Microwave Theory and Techniques, IEEE Transactions on*, vol. 34, no. 4, pp. 456–458, Apr. 1986.
- [33] ——, "Modeling of Noise Parameters of MESFETs and MODFETs and Their Frequency and Temperature Dependence," *Microwave Theory and Techniques, IEEE Transactions on*, vol. 37, no. 9, pp. 1340–1350, Sept. 1989.
- [34] ——, "On Certain Noise Properties of Field-Effect and Bipolar Transistors," in *Microwave, Radar, and Wireless Communications, 2006, MIKON 2006, International Conference on*, 2006, pp. 1127–1130.

- [35] P. Penfield, "Wave Representation of Amplifier Noise," *Circuit Theory, IRE Transactions On*, vol. 9, no. 1, pp. 84–86, Mar. 1962.
- [36] R. Meys, "A Wave Approach to the Noise Properties of Linear Microwave Devices," *Microwave Theory and Techniques, IEEE Transactions on*, vol. 26, no. 1, pp. 34–37, Jan. 1978.
- [37] S. Wedge and D. Rutledge, "Noise Waves and Passive Linear Multiports," *IEEE Microwave and Guided Wave Letters*, vol. 1, no. 5, pp. 117–119, May 1991.
- [38] ——, "Wave Techniques for Noise Modeling and Measurement," *IEEE Transactions on Microwave Theory and Techniques*, vol. 40, no. 11, pp. 2004–2012, Nov. 1992.
- [39] J. Randa and D. Walker, "Amplifier Noise-Parameter Measurement Checks and Verification," in *ARFTG Conference Digest*, 2004, pp. 41–46.
- [40] R. Lane, "The Determination of Device Noise Parameters," *Proceedings of the IEEE*, vol. 57, no. 8, pp. 1461–1462, Aug. 1969.
- [41] ——, "A Microwave Noise and Gain Parameter Test Set," *Solid-State Circuits Conference. Digest of Technical Papers. 1978 IEEE International*, vol. XXI, pp. 172–173, Feb. 1978.
- [42] D. Gu, D. Walker, and J. Randa, "Noise-Parameter Measurements with Automated Variable Terminations," *IEEE Transactions on Instrumentation and Measurement*, vol. 58, no. 4, pp. 1072–1077, Apr. 2009.
- [43] R. Hu and S. Weinreb, "A Novel Wide-Band Noise-Parameter Measurement Method and Its Cryogenic Application," *IEEE Transactions on Microwave Theory and Techniques*, vol. 52, no. 5, pp. 1498–1507, May 2004.
- [44] G. Caruso and M. Sannino, "Computer-Aided Determination of Microwave Two-Port Noise Parameters," *Microwave Theory and Techniques, IEEE Transactions on*, vol. 26, no. 9, pp. 639–642, Sept. 1978.
- [45] D. Pozar, *Microwave Engineering*. New York, NY: Wiley, 1998, ch. 12, pp. 681–683.
- [46] P. Bevington and D. Robinson, *Error Analysis*. New York, NY: McGraw-Hill, 2003, ch. 3, pp. 36–46.
- [47] M. Pospieszalski, "Interpreting Transistor Noise," *IEEE Microwave Magazine*, vol. 11, no. 6, pp. 61–69, Oct. 2010.
- [48] S. Weinreb, J. Bardin, H. Mani, and G. Jones, "Matched Wideband Low-Noise Amplifiers for Radio-Astronomy," *Review of Scientific Instruments*, vol. 80, no. 4, pp. 44702–44702(–5), Apr. 2009.

- [49] J. Gallego and M. Pospieszalski, "Accuracy of Noise Temperature Measurement of Cryogenic Amplifiers," National Radio Astronomy Observatory, Charlottesville, VA, Electronics Division Internal Report 285, Apr. 1991.
- [50] J. Fernandez, "A Noise-Temperature Measurement System Using a Cryogenic Attenuator," Jet Propulsion Laboratory, Pasadena, CA, TMO Progress Report 42-135, Nov. 1998.
- [51] S. Weinreb, "Very Low Noise Ambient-Temperature Amplifiers for the 0.6 to 1.6 GHz Range," The Square Kilometre Array, Memo 137, 2011.
- [52] J. Pandian, L. Baker, G. Cortes, P. Goldsmith, A. Deshpande, R. Ganesan, J. Hagen, L. Locke, N. Wadefalk, and S. Weinreb, "Low-Noise 6-8 GHz Receiver," *IEEE Microwave Magazine*, vol. 7, no. 6, pp. 74–84, Dec. 2006.
- [53] T. Philips, "The Role of Heterodyne Detection in Future Space Missions," in *Far-IR Sub-MM and MM Detector Technology Workshop*, Apr. 2002, available on line at www.sofie.usra.edu.
- [54] A. Maestrini, J. Ward, J. Gill, H. Javadi, E. Schlecht, G. Chattopadhyay, F. Maiwald, N. Erickson, and I. Mehdi, "A 1.7-1.9 THz Local Oscillator Source," *IEEE Microwave and Wireless Components Letters*, vol. 14, no. 6, pp. 253–255, Jun. 2004.
- [55] S. Shiba, Y. Irimajiri, T. Yamakura, H. Maezawa, N. Sekine, I. Hosako, and S. Yamamoto, "3.1-THz Heterodyne receiver Using an NbTiN Hot-Electron Bolometer Mixer and a Quantum Cascade Laser," *IEEE Transactions on Terahertz Science and Technology*, vol. 2, no. 1, pp. 22–26, Jan. 2012.
- [56] J. Zmuidzinas and P. Richards, "Superconducting Detectors and Mixers for Millimeter and Submillimeter Astrophysics," *Proceedings of the IEEE*, vol. 92, no. 10, pp. 1597–1616, Oct. 2004.
- [57] A. Karpov, D. Miller, F. Rice, J. Stern, B. Bumble, H. LeDuc, and J. Zmuidzinas, "Low Noise 1 THz-1.4 THz Mixers Using Nb/AlN/NbTiN SIS Junctions," *IEEE Transactions on Applied Superconductivity*, vol. 17, no. 2, pp. 343–346, 2007.
- [58] W. McGrath, A. Skalare, B. Karsik, D. Prober, and I. Siddiqi, "Superconductive Hot-Electron Bolometer Mixers," in *Far-IR Sub-MM and MM Detector Technology Workshop*, Apr. 2002, available on line at www.sofie.usra.edu.
- [59] S. Maas, *Microwave Mixers*. Dedham, MA: Artech House, 1986, ch. 5, pp. 135–145.
- [60] J. Kooi, J. Baselmans, M. Hajenius, J. Gao, and T. Klapwijk, "IF Impedance and Mixer Gain of NbN Hot Electron Bolometers," *Journal of Applied Physics*, vol. 101, no. 4, pp. 044511–044511–8, 2007.

- [61] A. V. der Ziel, *Noise*. New York, NY: Preintice-Hall, 1954, pp. 1–50.
- [62] J. Cressler and G. Niu, *Silicon-Germanium Heterojunction Bipolar Transistors*. Boston, MA: Artech House, 2003, ch. 7, pp. 280–287, 383–391.
- [63] R. Anholt, *Electrical and Thermal Characterization of MESTFETs, HEMTs, and HBTs*. Norwood, MA: Artech House, 1995, ch. 10, pp. 230–232.
- [64] H. Kawasaki and J. Kasahara, “Low-Frequency Dispersion of Transconductance in GaAs JFET’s and MESFET’s with an Ion-Implanted Channel Layer,” *IEEE Transactions on Electron Devices*, vol. 37, no. 8, pp. 1789–1795, Aug. 1990.
- [65] B. Klepser and W. Patrick, “Determination of Dispersion of Output Conductance and Transconductance of InP HEMTs Using Low frequency S-parameter Measurements,” *Electronics Letters*, vol. 31, no. 5, pp. 1294–1295, Jul. 2012.
- [66] A. Rafei, G. Callet, G. Mouginot, J. Faraj, S. Laurent, M. Prigent, R. Quere, O. Jardel, and S. Delage, “DC (10 Hz) to RF (40 GHz) Output Conduction Extraction by S-parameters Measurements for In-Depth Characterization of AlInN/GaN HEMTs, Focusing on Low Frequency Dispersion Effects,” Manchester, England, pp. 5–8, 2011.
- [67] I. Kallfass, T. Brazil, B. OhAnnaidh, P. Abele, T. Hackbarth, M. Zeuner, U. Konig, and H. Schumacher, “Large-Signal Modelling Including Low-Frequency Dispersion of N-Channel SiGe MODFETs and MMIC Applications,” *Solid-State Electronics*, vol. 48, pp. 1433–1441, Jan. 2004.
- [68] H. Haus and R. Adler, “Optimum Noise Performance of Linear Amplifiers,” *Proceedings of the IRE*, vol. 46, no. 8, pp. 1517–1533, 1958.
- [69] R. Jacob, *CMOS Circuit Design, Layout, and Simulation*. Hoboken, NJ: Wiley-Interscience, 2008, ch. 7, pp. 199–200.
- [70] A. Gutierrez, M. Deen, and C. Claeys, *Low Temperature Electronics Physics, Devices, Circuits, and Applications*. San Diego, CA: Academic Press, 2001, ch. 1, pp. 53–61.
- [71] J. Leech, B. Tan, G. Yassin, P. Kittara, and S. Wangsuya, “Experimental Investigation of a Low-Cost, High Performance Focal-Plane Horn Array,” *IEEE Transations on Terahertz Science and Technology*, vol. 2, no. 1, pp. 61–70, Jan. 2012.
- [72] S. Weinreb, “Cryogenic Performance of Microwave Terminations, Attenuators, Absorbers, and Coaxial Cable,” National Radio Astronomy Observatory, Charlottesville, VA, Eletronics Division Internal Report 223, Jan. 1982.

- [73] N. Wadefalk, A. Mellberg, I. Angelov, M. Barsky, S. Bui, E. Choumas, R. Grundbacher, E. Kollberg, R. Lai, N. Rorsman, P. Starski, J. Stenarson, D. Streit, and H. Zirath, “Cryogenic Wide-Band Ultra-Low-Noise IF Amplifiers Operating at Ultra-Low DC Power,” *IEEE Transactions on Microwave Theory and Techniques*, vol. 51, no. 6, pp. 1705–1711, Jun. 2003.
- [74] G. Cortes, “Novel Non Planar Ultra Wide Band Quasi Self-Complementary Antenna,” in *Antennas and Propagation Society International Symposium*, 2007, pp. 5733–5736.
- [75] J. Yang, M. Pantaleev, P. Kildal, and L. Helldner, “Design of Compact Dual-Polarized 1.2-10 GHz Eleven Feed for Decade Bandwidth Radio Telescopes,” *IEEE Transactions on Antennas and Propagation*, vol. 60, no. 5, pp. 2210–2218, May 2012.